

# Multidimensional Phononics In Driven



## Dissertation

Zur Erlangung des Doktorgrades and der Fakultät für Mathematik,

Informatik und Naturwissenschaften

Fachbereich Physik

der Universität Hamburg

Vorgelegt von

**Niloofer Taherian Hosseinabadi**

Hamburg

2025

Gutachter/innen der Dissertation:

Prof. Dr. Andrea Cavalleri  
Prof. Dr. Nils Huse

Zusammensetzung der Prüfungskommission:

Prof. Dr. Andrea Cavalleri  
Prof. Dr. Nils Huse  
Prof. Dr. Michael Rübhausen  
Prof. Dr. Guido Meier  
Prof. Dr. Ludwig Mathey

Vorsitzende/r der Prüfungskommission:

Prof. Dr. Ludwig Mathey

Datum der Disputation:

15.05.2025

Vorsitzender des Fach-Promotionsausschusses PHYSIK:

Prof. Dr. Wolfgang J. Parak

Leiter des Fachbereichs PHYSIK:

Prof. Dr. Markus Drescher

Dekan der Fakultät MIN:

Prof. Dr.-Ing. Norbert Ritter

## Declaration on oath

I hereby declare and affirm that this doctoral dissertation is my own work and that I have not used any aids and sources other than those indicated.

If electronic resources based on generative artificial intelligence (gAI) were used in the course of writing this dissertation, I confirm that my own work was the main and value-adding contribution and that complete documentation of all resources used is available in accordance with good scientific practice. I am responsible for any erroneous or distorted content, incorrect references, violations of data protection and copyright law or plagiarism that may have been generated by the gAI.

08-01-2025

Date



Signature of doctoral candidate

*In memory of **Amir** and **Mohamad-Reza**...*

*May there be comfort in knowing that someone so special will never be forgotten.*



# Abstract

Quantum materials exhibit many phases with exotic and potentially useful properties, including superconductivity, charge ordering and various forms of magnetism. In many cases, these exotic phases compete with one another on comparable energy scales. The close proximity of the energy scales results in a scenario where even small perturbations can change the dominant phase. This energetic proximity also often gives rise to large fluctuations. Whilst these fluctuations typically act as a prohibiting factor in establishing a certain ordered state in equilibrium, they may also hold the key to establishing a desired state out of equilibrium through some form of pulsed excitation or periodic driving. In fact, a range of experiments have recently demonstrated that, by resonantly driving the normal modes of the crystal structure (known as phonons) with intense mid-infrared or Terahertz light pulses, it is possible to actively stabilize the fluctuations and hence induce or enhance desired orders at temperatures where they are not accessible in thermal equilibrium, even far above the critical temperature  $T_c$ . Non-equilibrium ferroelectricity, magnetism, insulator-to-metal transitions and superconductivity are some of the most relevant examples.

This thesis focuses on the case of  $\text{YBa}_2\text{Cu}_3\text{O}_{6+x}$ , a high- $T_c$  Cuprate compound, in which the superconducting state is formed by dispersive tunneling modes of Cooper pairs across the stacked  $\text{CuO}_2$  layers, known as Josephson plasmon polaritons. In

equilibrium, superconducting fluctuations were found far above  $T_c$ . Various experiments have demonstrated that, in underdoped compounds from this family, large amplitude resonant phonon excitation results in the emergence of transient macroscopic superconducting-like properties at temperatures far exceeding  $T_c$ , and even up to room temperature. These initial observations sparked a wave of follow-up experiments aimed at further characterizing this transient state and understanding the underlying microscopic mechanism which leads to its formation. Recent one-dimensional mid-infrared pump and time-resolved second-harmonic generation-probe (tr-SHG) experiments have revealed phonon-mediated amplification of the Josephson plasmon polaritons, a phenomenon likely to underpin the mysterious superconducting-like macroscopic properties. However, these one-dimensional experiments could not provide a conclusive picture of the coupling between the optically excited phonons and the Josephson plasmon polaritons.

The study presented in this thesis addresses this problem by reporting the development and use of a new form of two-dimensional spectroscopy, with the aim of obtaining an improved understanding of the microscopic dynamics in the driven state of  $\text{YBa}_2\text{Cu}_3\text{O}_{6+x}$ . This method involves sequentially exciting apical oxygen phonons with two carrier-envelope-phase-stable mid-infrared pump pulses and probing the time delay dependent changes in the second-order nonlinear optical susceptibility, which is sensitive to the coherent motion of both the infrared-active phonon and plasmon modes. The findings suggest that the driven phonons amplify coherent pairs of opposite-momentum Josephson plasma polaritons via a four-mode mixing process, generating a squeezed state of the inter-layer phase fluctuations. The identification of this squeezed state of the inter-layer tunneling modes not only offers a potential pathway towards manipulating the superconducting order parameter at temperatures higher than  $T_c$ , but also provides critical insights into the microscopic

physics underpinning "*photoinduced superconductivity*" in Cuprates and similar materials.

# Zusammenfassung

Quantenmaterialien weisen viele Phasenzustände mit exotischen und potenziell nützlichen Eigenschaften auf, darunter Supraleitfähigkeit, Ladungsordnung und verschiedene Formen von Magnetismus. In vielen Fällen konkurrieren diese exotischen Phasen auf vergleichbaren Energieskalen miteinander. Die enge Nachbarschaft der Energieskalen führt zu einem Szenario, in dem selbst kleine Störungen die dominante Phase ändern können. Diese energetische Nähe führt häufig auch zu großen Fluktuationen. Während diese Fluktuationen in der Regel ein Hindernis für die Etablierung eines bestimmten geordneten Gleichgewichtszustands darstellen, können sie auch der Schlüssel zur Erzeugung eines gewünschten Phasenzustands außerhalb des Gleichgewichts durch eine Form der gepulsten Anregung oder des periodischen Antriebs sein. Eine Reihe von Experimenten hat kürzlich gezeigt, dass es möglich ist, durch resonante Anregung der Normalmoden der Kristallstruktur (bekannt als Phononen) mit intensiven Lichtpulsen im mittleren Infrarot- oder Terahertzbereich die Fluktuationen aktiv zu stabilisieren und damit die gewünschten Zustände bei Temperaturen zu erzeugen oder zu verstärken, bei denen sie im thermischen Gleichgewicht nicht zugänglich sind, sogar weit oberhalb der kritischen Temperatur  $T_c$ . Nicht-Gleichgewichts-Ferroelektrizität, Magnetismus, Isolator-Metall-Übergänge und Supraleitung sind einige der wichtigsten Beispiele.

Diese Arbeit befasst sich mit  $\text{YBa}_2\text{Cu}_3\text{O}_{6+x}$ , einem kupferbasierten Hochtemper-

atursupraleiter, bei der supraleitende Zustand durch dispersive Tunnelmoden von Cooper-Paaren durch die gestapelten  $\text{CuO}_2$ -Schichten, die als Josephson-Plasmon-Polaritonen bekannt sind, gebildet wird. Im Gleichgewicht wurden supraleitende Fluktuationen weit über  $T_c$  festgestellt. Verschiedene Experimente haben gezeigt, dass in den unterdotierten Verbindungen dieser Familie die resonante Anregung von Phononen großer Amplitude zum Auftreten vorübergehender makroskopischer supraleitungsähnlicher Eigenschaften bei Temperaturen führt, die weit über  $T_c$  und sogar Raumtemperatur liegen. Diese ersten Beobachtungen lösten eine Welle von Folgeexperimenten aus, die darauf abzielten, den vorübergehenden Zustand weiter zu charakterisieren und den mikroskopischen Mechanismus zu verstehen, der zu seiner Entstehung führt. Kürzlich durchgeführte eindimensionale Anrege-Abfrage-Experimente, mit optischer Anregung im mittleren Infrarot und Detektion der Zweiten Harmonischen nahinfraroter Lichtpulse, haben eine durch Phononen vermittelte Verstärkung der Josephson-Plasmon-Polaritonen nachgewiesen, ein Phänomen, das wahrscheinlich den mysteriösen supraleitungsähnlichen makroskopischen Eigenschaften zugrunde liegt. Diese eindimensionalen Experimente konnten jedoch kein schlüssiges Bild der Kopplung zwischen den optisch angeregten Phononen und den Josephson-Plasmon-Polaritonen liefern.

Die in dieser Arbeit vorgestellte Studie hat zum Ziel, ein besseres Verständnis der mikroskopischen Dynamik im optisch angeregten Zustand von  $\text{YBa}_2\text{Cu}_3\text{O}_{6+x}$  zu erhalten, und berichtet über die Entwicklung und Anwendung einer neuen Form der zweidimensionalen Spektroskopie. Bei dieser Methode werden die Phononen, welche die Bewegung der apikalen Sauerstoffatome der Kupratverbindung beinhalten, nacheinander mit zwei optisch phasenstabilen Lichtpulsen im mittleren Infrarot angeregt, und die zeitabhängige Änderung der nichtlinearen optischen

Suszeptibilität zweiter Ordnung gemessen, die auf die kohärente Bewegung sowohl der infrarotaktiven Phonon- als auch der Plasmonmoden anspricht. Die Ergebnisse deuten darauf hin, dass die direkt angeregten Phononen kohärente Paare von Josephson Plasma Polaritonen mit entgegengesetztem Impuls über einen Vier-Moden Mischprozess verstärken und einen gequetschten Zustand der Phasenfluktuationen zwischen den Schichten erzeugen. Die Identifizierung dieses gequetschten Zustands der Zwischenschicht-Tunnelmoden bietet nicht nur einen potenziellen Weg zur Manipulation des supraleitenden Ordnungsparameters bei Temperaturen oberhalb von  $T_c$ , sondern liefert auch wesentliche Einblicke in die mikroskopische Physik, die der *”photoinduzierten Supraleitung”* in den Kupraten und ähnlichen Materialien zugrunde liegt.



# Contents

<b>Introduction</b>	<b>1</b>
<b>1 Light Matter Interaction</b>	<b>10</b>
1.1 Introduction . . . . .	10
1.2 Lattice Degrees of Freedom . . . . .	11
1.3 Optical Properties of Phonon-Polaritons . . . . .	15
1.4 Electronic Degrees of Freedom . . . . .	17
1.5 Optical Properties of Plasmon-Polaritons . . . . .	18
1.6 Beyond the Harmonic Approximation . . . . .	19
1.6.1 Linear Excitation . . . . .	21
1.6.2 Cubic Nonlinearities: Displacive Excitation . . . . .	24
1.6.3 Quartic Nonlinearity: Squeezed Excitation . . . . .	27
1.7 Squeezed State . . . . .	31
1.8 Linear and Nonlinear Polarization . . . . .	33
1.9 Summary and Outlook . . . . .	35
<b>2 Josephson Plasma Waves in Layered Superconductors</b>	<b>36</b>
2.1 Introduction . . . . .	36
2.2 Emergence of the Superconducting state . . . . .	37
2.3 Theory of Superconductivity . . . . .	39

## Contents

---

2.4	Josephson Effect . . . . .	46
2.5	sine-Gordon Equation . . . . .	49
2.5.1	Single Josephson Junction . . . . .	49
2.5.2	Stack of Josephson Junctions . . . . .	51
2.6	Optical Signatures of Josephson Plasma Waves . . . . .	54
2.6.1	Single-layer System Optical Properties . . . . .	54
2.6.2	Bi-layer System Optical Properties . . . . .	57
2.6.3	Summary and Outlook . . . . .	61
<b>3</b>	<b>Photo-induced Superconductivity in <math>\text{YBa}_2\text{Cu}_3\text{O}_{6+x}</math></b>	<b>63</b>
3.1	Introduction . . . . .	63
3.2	High $T_c$ Cuprates Layered Superconductors . . . . .	64
3.2.1	General Properties of Cuprates . . . . .	65
3.3	Equilibrium Properties of $\text{YBa}_2\text{Cu}_3\text{O}_{6+x}$ . . . . .	69
3.3.1	Crystal Structure and Phase Diagram . . . . .	69
3.3.2	THz c-axis Optical Properties . . . . .	71
3.3.3	Far-Infrared c-axis Optical Properties . . . . .	72
3.3.4	Plasmon Signature and Phonons Anomaly in the Pseudogap Phase . . . . .	75
3.4	Photo-Induced Superconducting-Like State of $\text{YBa}_2\text{Cu}_3\text{O}_{6.5}$ . . . . .	78
3.4.1	THz c-axis Photo-Induced Optical Properties . . . . .	78
3.4.2	Far-Infrared c-axis Photo-Induced Optical Properties . . . . .	82
3.4.3	Lifetime of the Photo-Induced State . . . . .	83
3.4.4	Expulsion of Magnetic Field in the Photo-Induced State . . . . .	85
3.5	Summary and Outlook . . . . .	88
<b>4</b>	<b>Phonon Driven Coherent Dynamics in <math>\text{YBa}_2\text{Cu}_3\text{O}_{6+x}</math></b>	<b>90</b>

4.1	Introduction . . . . .	90
4.2	Probing Symmetry-Even Vibrational Modes . . . . .	91
4.2.1	Raman Scattering . . . . .	91
4.2.2	Time-Resolved Polarization Rotation . . . . .	92
4.2.3	Experimental Setup . . . . .	95
4.3	Coherent Dynamics of the Raman-Active Phonons in $\text{YBa}_2\text{Cu}_3\text{O}_{6+x}$ . . . . .	97
4.4	Probing Symmetry-Odd Vibrational Modes . . . . .	100
4.4.1	Second-Order Nonlinear Optical Effects . . . . .	100
4.4.2	Hyper-Raman Scattering . . . . .	101
4.4.3	Electric-Field Induced Second Harmonic Generation . . . . .	102
4.4.4	Time-Resolved Second Harmonic Generation . . . . .	104
4.4.5	Detection of Time-Resolved SHG . . . . .	104
4.4.6	Experimental Setup . . . . .	110
4.5	Coherent Dynamics of the Symmetry-Odd modes in $\text{YBa}_2\text{Cu}_3\text{O}_{6+x}$ . . . . .	110
4.6	Doping and Temperature Dependence . . . . .	114
4.7	Summary and Outlook . . . . .	116
<b>5</b>	<b>Multidimensional Phononics in <math>\text{YBa}_2\text{Cu}_3\text{O}_{6+x}</math></b>	<b>118</b>
5.1	Introduction . . . . .	118
5.2	Two-Pulse Excitation . . . . .	119
5.3	Two-Dimensional Mid-IR Nonlinear Spectroscopy . . . . .	121
5.3.1	Experimental Setup . . . . .	123
5.4	Multidimensional tr-Polarization Rotation In $\text{YBa}_2\text{Cu}_3\text{O}_{6+x}$ . . . . .	125
5.5	Multidimensional tr-SHG In $\text{YBa}_2\text{Cu}_3\text{O}_{6+x}$ . . . . .	128
5.6	Doping and Temperature Dependence . . . . .	134
5.7	Summary and Outlook . . . . .	137

<b>6 Squeezed Josephson Plasmon Amplification</b>	<b>139</b>
6.1 Introduction . . . . .	139
6.2 Dynamics of Driven Phonons . . . . .	140
6.2.1 Single-Pulse Excitation . . . . .	141
6.2.2 Two-Dimensional Nonlinear Spectroscopy . . . . .	145
6.3 Phonon-Plasma Polariton Dynamics . . . . .	148
6.3.1 Single-Pulse Excitation . . . . .	149
6.4 Probing Amplified Josephson Plasmon Polariton Fluctuations . . . . .	153
6.4.1 Two-Dimensional Nonlinear Spectroscopy . . . . .	156
6.5 Photo-Induced Reflectivity Edge Calculations . . . . .	159
6.6 Phonon-Phonon Dynamics . . . . .	161
6.6.1 Single-Pulse Excitation . . . . .	163
6.6.2 Two-Dimensional Nonlinear Spectroscopy . . . . .	164
6.7 Summary . . . . .	165
<b>Summary and Outlook</b>	<b>168</b>
<b>List of Publications</b>	<b>175</b>
<b>Appendices</b>	<b>178</b>
<b>A Derivation of Squeezed State EOM</b>	<b>178</b>
A.1 Derivation of Squeezed State EOM . . . . .	178
<b>B Nonlinear Circuit Model of Josephson Junction</b>	<b>181</b>
B.1 Modeling the Josephson Junction . . . . .	181
<b>C Establishment of a Local Oscillator</b>	<b>184</b>
C.1 Experimental Development of a Local Oscillator . . . . .	184

<b>D Numerical Simulations Parameters</b>	<b>187</b>
D.1 Mid-Infrared Electric Field Parameters . . . . .	187
D.2 Time-Resolved SHG Simulations Parameters . . . . .	187
D.3 Time-Resolved Polarization Rotation Simulations Parameters . . . . .	188
<b>E Analytical Model For Nonlinear Mode Coupling</b>	<b>190</b>
E.1 Analytical Model For Nonlinear Mode Coupling . . . . .	190
E.2 Single-Pulse Excitation . . . . .	192
E.3 Two-Dimensional Nonlinear Spectroscopy . . . . .	193
<b>F Squeezed Plasmons Dynamics</b>	<b>197</b>
F.1 Squeezed Plasmons Dynamics . . . . .	197
<b>Bibliography</b>	<b>203</b>



# Introduction

## Fluctuating Orders in Quantum Materials

In recent decades, the study of various fascinating classes of materials which exhibit physical phenomena that cannot be captured by conventional theories, has become a prominent frontier of condensed matter physics. In these systems, which are commonly referred to as *quantum materials*, the nontrivial physical properties largely originate from an interplay between inherently quantum mechanical effects and strong particle correlations [1–3]. High-temperature superconductivity [4, 5], topology [6–12], unconventional magnetism [13–16], insulator to metal transitions [17, 18] and many other phenomena, are all examples of such material systems. Another common feature of such systems is their high sensitivity to various tuning parameters, such as electromagnetic fields, pressure, changes in chemical doping and more [2]. This sensitivity is manifested in the rich phase diagrams of these materials, which often show that through tuning these parameters multiple exotic orders can be accessed within the same material.

One key objective is to go beyond only understanding these properties, by developing methods to exert active *control* over them for use in future technological applications such as quantum computing and energy-efficient devices. Owing to the delicate balance between the competing energy scales of different phases, both

quantum and thermal fluctuations can play a key role in establishing or prohibiting the formation of orders in quantum materials. This is especially significant close to the phase boundaries. In such cases, the use of intense pulses of laser-light has recently emerged as a promising tool for selectively enhancing or reducing fluctuations and thereby enforcing desired orders along with their associated macroscopic properties [19–22]. Understanding the precise mechanisms by which the microscopic dynamics which follow photo-excitation can alter or reduce fluctuations remains a key research goal.

One key ingredient in many cases is seemingly the resonant driving of structural normal modes (known as phonons). This can be understood intuitively as arising from the high sensitivity of the quantum materials macroscopic properties to the precise details of the crystal structure. Consequentially, even small structural distortions can be expected to affect and rearrange other degrees of freedom such as magnetic and electronic orders [23–25].

Various experiments have shown that coherent distortions of the crystal structure can be achieved through the excitation of an infrared-active crystal lattice vibrational mode (phonon) via intense light pulses, which are tuned to be resonant with the natural frequency of the mode [26–31]. As will be explained in detail throughout *Chapter 1*, this type of selective and coherent control opens up pathways through which new non-equilibrium atomic arrangements and hence new desired properties can be accessed, which in some cases can even survive for much longer than the duration of the drive [19, 32–34].

Three representative examples of quantum material systems which host strong fluctuations in equilibrium are shown in Figs.1 (a-c). The first system is the rare earth titanate  $\text{YTiO}_3$ , which is ferromagnetic in equilibrium below the Curie temperature

of  $T_c = 27$  K, although strong spin-orbit-lattice fluctuations cause the magnetization to saturate below the ideal spin-half limit value of  $1 \mu_B$  for  $T < T_c$ . The Curie temperature itself is also suppressed with respect to the mean-field predicted value of 50 K [35–37].

From the same rare-earth titanate family,  $\text{SrTiO}_3$  is a quantum paraelectric in equilibrium which possesses structural inversion symmetry. Below 105 K the system undergoes an antiferrodistortive (AFD) structural transition (from cubic to tetragonal), whilst nevertheless maintaining its inversion center. Upon cooling down to even lower temperatures, there is a tendency to form a ferroelectric phase as evidenced by the softening of a polar phonon mode and an increase in the dielectric function [38, 39]. However, macroscopic ferroelectric order never emerges, even at the lowest temperatures, due to quantum fluctuations of the ionic positions between the competing antiferrodistortive and ferroelectric phases. As illustrated by the phase diagram in Fig.1 (b), the application of strain tips the balance between the competing structural phases in favor of ferroelectric order [40].

The final, and arguably most mysterious example, which forms the subject of *Chapter 2* and *3* in this thesis, is the superconducting state in  $\text{YBa}_2\text{Cu}_3\text{O}_{6+x}$ , a member of the famous high-temperature superconducting Cuprate family. As shown in Fig.1 (c), this material exhibits long-range superconducting order with  $T_c$  as high as  $\approx 93$  K for the optimal hole doping level. As the temperature increases, another mysterious phase, known as the pseudogap, is established for the compounds with lower doping levels. Whilst in the pseudogap phase there exist no macroscopic superconductivity, there are some pieces of experimental evidence which hint towards the interpretation of this phase as hosting strong superconducting fluctuations [41–55].

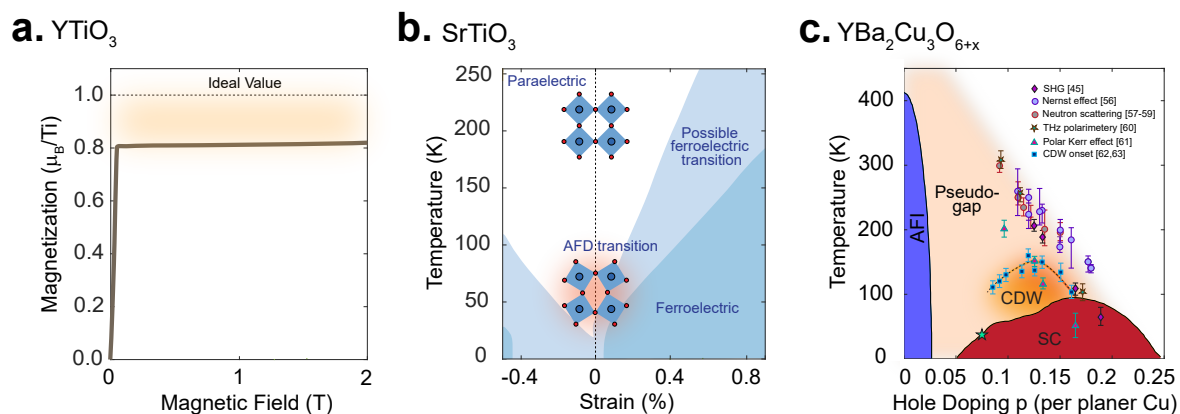


**Figure 1:** (a). Magnetization of  $\text{YTiO}_3$  as a function of applied magnetic field for  $T \ll T_c$ , representing a saturated magnetization of  $0.8 \mu_B$  per Ti, below the theoretically calculated value of 1. (b). Phase diagram of bulk  $\text{SrTiO}_3$  as a function of strain and temperature.  $\text{SrTiO}_3$  is paraelectric at finite temperature in the absence of strain. Around 105 K, it undergoes an antiferrodistortive (AFD) transition from cubic to tetragonal, although, remaining inversion symmetric. Application of any small amount of strain enforces a ferroelectric transition. (c). Phase diagram of  $\text{YBa}_2\text{Cu}_3\text{O}_{6+x}$  as a function of temperature and chemical hole doping. Figures and captions are adopted from Refs.[19, 33, 45, 56–63]

## Light-Based Suppression of the Fluctuations

In all these three exemplary cases discussed above, resonant phonon driving has been shown to either enhance or induce the desired order [19, 22, 33, 64–68], presumably by somehow effectively reducing the fluctuations which dominate in equilibrium. These results are summarized in Figs.2 (a-b) and Fig.3.

In the case of  $\text{YTiO}_3$ , resonant excitation of a  $B_{2u}$  symmetry, IR-active phonon mode at a frequency of 9 THz (chosen due to its strong spin-lattice coupling) was shown to suppress anti-ferromagnetic fluctuations and hence enhance ferromagnetism.

The magnetization measured after photo-excitation is plotted as a function of external applied magnetic field in Fig.2 (a), accompanied by the equilibrium value. The

enhancement of the saturated magnetization to the theoretical maximum value signifies that the fluctuations responsible for the suppression of equilibrium magnetization are reduced upon photoexcitation. Temperature dependence measurements, further demonstrated that applying this photo-excitation protocol in the high temperature non-ferromagnetic phase, induces long-ranged metastable ferromagnetic order, up to a temperature scale three times higher than  $T_c$  [19]. This effect was attributed to a quasi-static shift in the orbital levels, which couple to the square of the driven phonon amplitude  $Q_{\text{drive}}^2$ , effectively favouring ferromagnetism over the competing anti-ferromagnetic order [69].

Similarly, in the case of  $\text{SrTiO}_3$ , resonant excitation of an IR-active lattice vibrational mode at 20 THz with  $A_{2u}$  symmetry has been shown to exert a strong lattice distortion which in turn facilitates the establishment of long-range polar order [20, 33].

As shown in Fig.2 (b), this photoinduced ferroelectric order was observed via the measurement of a long-lived second harmonic generation from probe pulses after mid-IR photoexcitation. Note that in the equilibrium state where ferroelectricity is absent, the second harmonic generation is zero at all temperatures due to the presence of inversion symmetry [33]. A plausible explanation for the generation of this metastable polar state involves the nonlinear coupling between the resonantly driven phonon mode and an acoustic phonon mode, which induces strain within the lattice, estimated to be as high as 0.2%. This strain, in turn, effectively suppresses the AFD fluctuations, favoring the stabilization of the ferroelectric order [20].

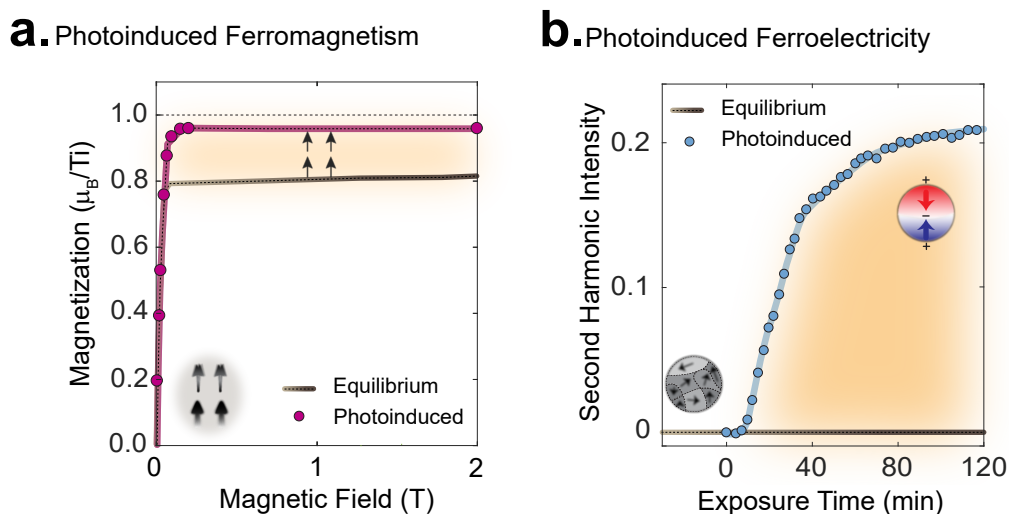


**Figure 2:** (a). Equilibrium magnetization (in grey) and maximum non-equilibrium magnetization (magenta circles) extracted from pump-probe experiments as a function of applied magnetic field measure in  $YTiO_3$  at the base temperature of 5 K well below  $T_c \propto 27$  K. The saturated magnetization is enhanced reaching the ideal value through suppression of antiferromagnetic fluctuations obtained after photoexcitation [70]. (b). Total time-delay independent second harmonic generation in equilibrium (in gray) and after mid-IR photoexcitation (blue circles) as a function of exposure time, measured in  $SrTiO_3$  at a base temperature of 4 K. The breaking of the inversion symmetry and hence generation of second harmonic intensity after mid-IR photoexcitation with respect to the inversion symmetric equilibrium phase is indicated by the yellow shading [33].

Turning finally to the case of  $YBa_2Cu_3O_{6+x}$ , resonant excitation of the IR-active  $B_{1u}$  symmetry apical oxygen phonon modes has been shown to induce macroscopic superconducting-like properties at temperatures well above  $T_c$ . These properties include a  $1/\omega$  divergence in the imaginary part of the complex optical conductivity [64–67] and the expulsion of a statically applied magnetic field [68], as illustrated in Fig.3. These photo-induced responses have been shown to survive on a temperature scale that matches that of the pseudogap phase. A detailed review of these experiments focusing on the macroscopic properties of the photoinduced superconducting-like state in  $YBa_2Cu_3O_{6+x}$  is given in *Chapter 3*.

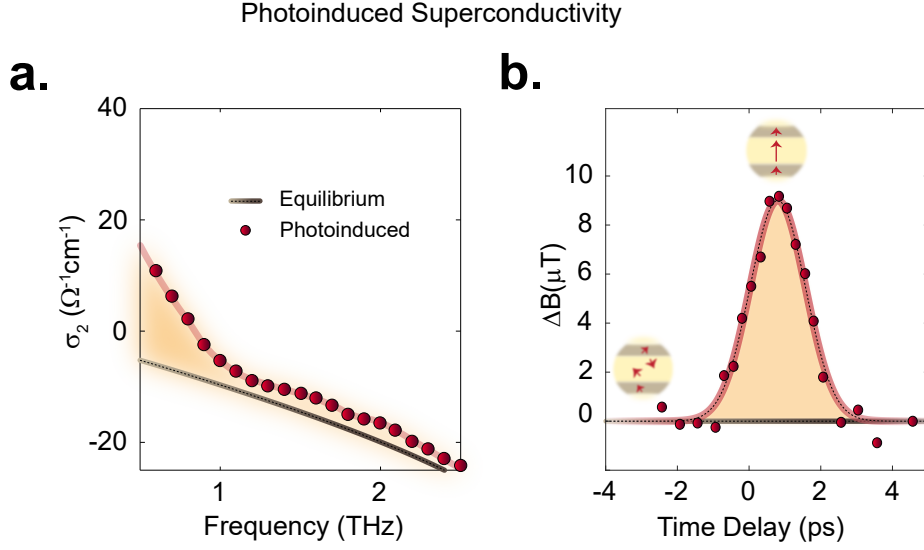


**Figure 3:** (a). The reconstructed imaginary part of the optical conductivity  $\sigma_2(\omega)$  measured via phase and time-resolved THz spectroscopy in  $\text{YBa}_2\text{Cu}_3\text{O}_{6.5}$  at the base temperature of 60 K (above  $T_c$ ) in equilibrium (gray shaded curve) and after mid-IR photoexcitation (red circles). The  $1/\omega$  divergence induced after mid-IR pump is shaded in yellow [64–67]. (b). The change in the magnetic field  $\Delta B$  measured on the edge of  $\text{YBa}_2\text{Cu}_3\text{O}_{6.48}$  at base temperature of 100 K (above  $T_c$ ) in equilibrium and after mid-IR photoexcitation with the same color coding as in (a). A positive change has been observed as a function of mid-IR pump and probe time delay which is absent in the equilibrium state. This positive change at the edge of the sample was interpreted as corresponding to a negative change at the top of the sample, suggestive of Meißner effect [68].

Various pump-probe experiments have been carried out to observe the microscopic dynamics which follow this photo-excitation with the aim of understanding the mechanism through which the superconducting-like properties emerge. Earlier experiments were primarily concerned with the nonlinear lattice dynamics [71–73], however, more recent experiments, as will be thoroughly discussed in *Chapter 4*, have linked the emergence of these properties to the dynamics of amplified Josephson plasmon modes [22], which are associated with superconducting tunneling currents. Although a theoretical framework describing the microscopic nature of this photo-induced state has been proposed [74] based on these findings, a defini-

tive explanation remains elusive.

In all these experiments, a single pump pulse was used to excite the system, and the resulting photo-induced dynamics were captured by a time-delayed probe pulse. Whilst the modeling and conclusions drawn from these one-dimensional experiments offer many insights into the underlying mechanism, they cannot unambiguously disentangle the precise nature of the coupling between the various excited modes.

One particularly effective experimental approach to resolving this ambiguity and thereby unlocking a full understanding of the dynamics which enable the creation of light-induced orders, is to probe the photo-induced dynamics using higher dimensional spectroscopic techniques.

In multidimensional experiments, the information is resolved across more than one time (or equivalently frequency) axis, with the number of axes corresponding to the number of dimensions. In this multidimensional space, the interactions between different modes draw particular spectral patterns which depend on, and hence reveal, the specific types of inter-mode coupling [75–85]. In *Chapter 5* of this thesis, we explain the development of a brand new form of multi-dimensional spectroscopy which is tailored towards understanding the dynamics of coherently-driven quantum materials. The results of applying this technique to the case of phonon-driven  $\text{YBa}_2\text{Cu}_3\text{O}_{6+x}$  are then presented.

In *Chapter 6*, numerical simulations which accurately reproduce the multidimensional experimental data are presented, revealing the true nature of the coupling between the driven phonons and the amplified plasmons. The theoretical consequences of this coupling are then explored in detail, revealing the generation of a highly novel squeezed state of finite-momentum Josephson plasmon pairs. This

## *Introduction*

---

squeezed state provides both a natural explanation for how the phonon-driving can result in reduced fluctuations of pre-existing superconducting carriers, whilst also quantitatively accounting for the non-equilibrium THz-frequency optical properties which were measured in previous studies.

# Chapter 1

## Light Matter Interaction

### 1.1 Introduction

In order to describe various optical phenomena in solids, we first need to understand their so-called *optical properties*. To do so, first the parameters by which these optical properties can be explained and understood, must be defined. Two important response functions determining the propagation of light in the medium are the complex refractive index  $\tilde{n}(\omega)$  and complex dielectric constant  $\tilde{\epsilon}_r(\omega)$ . In this chapter, we start by introducing various degrees of freedom through which the material can interact with light, before describing this interaction using the classical dipole oscillator model (otherwise known as the Lorentz Model), to derive a simple expression for the frequency-dependent response of the medium [86].

The simple Lorentz model will then be extended via the introduction of a more general framework known as *non-linear phononics* which enables higher order light-matter interactions to be captured. This theory of non-linear phononics forms the basis for understanding the light-matter interactions observed in the experiments described in Chapters 3, 4 and 5. The Chapter will conclude with a detailed

review of three specific types of non-linear mode couplings that are crucial to the interpretation of those experiments.

## 1.2 Lattice Degrees of Freedom

When the ions in a crystal are displaced from their equilibrium positions, they experience a restoring force, resulting in their harmonic collective motion. These collective oscillations are described by the normal modes of the crystal lattice, the quanta of which are referred to as *phonons*. Figure 1.1(a) illustrates this phenomenon with a ball undergoing harmonic oscillation around its equilibrium position within a parabolic potential. The oscillations of ions within a primitive unit cell can occur either in-phase (referred to as *Acoustic* mode) or out-of-phase (referred to as *Optical* mode). Additionally, these oscillatory motions have a propagation direction characterized by their wave vector  $\tilde{k}$  and a characteristic frequency  $\Omega$  [87–90]. Figure 1.1 panel (a) inset and panel (b) depict these two modes of oscillation along and their dispersion within the first Brillouin zone, respectively.

If the phonon modes carry an electric dipole moment, and hence couple to light, they are known as *IR-active* phonon modes. On the other hand, the modes which do not carry a dipole moment and hence do not couple to light, but can instead modify the polarizability of the lattice are known as *Raman-active* phonon modes [91]. Selection rules, determined by Group Theory and crystal symmetry known as Neumann’s principle, dictate which phonons are IR- or Raman-active. Importantly, the Hamiltonian of the system with all the interaction terms must obey the crystal point group symmetry. For instance, in the case of an inversion-symmetric system (which will be the case for the system studied in this thesis), any given mode is either IR-

active or Raman-active but not both<sup>1</sup>. The inversion symmetry operation not only disentangles the symmetry-odd IR-active modes from symmetry-even Raman-active modes, but also requires their coupling to remain symmetry-even [92–94].

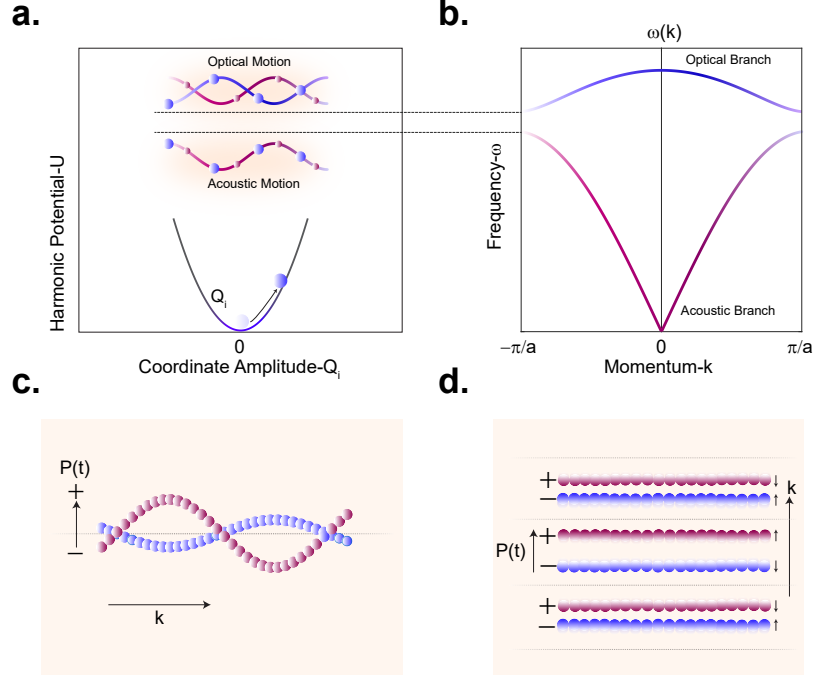


**Figure 1.1:** (a). The harmonic potential as a function of a normal mode of the crystal coordinate amplitude represented by  $Q_i$ . The harmonic oscillations of the crystal along this normal mode is indicated by the movement of the ball back and forth in the parabolic potential. The inset depicts the in-phase and out-of-phase motion of the diatomic chain, corresponding to acoustic and optical modes, respectively. (b). Phonon dispersion within the first Brillouin zone. Red and blue shaded curves represent the acoustic and optical branches respectively. (c). and (d). Respectively, transverse and longitudinal representation of the atomic motions in the presence of a driving field  $E(t)$  where  $P(t) \parallel \tilde{E} \perp \tilde{k}$  for transverse and  $P(t) \parallel \tilde{E} \parallel \tilde{k}$  for longitudinal. Panels (b), (c) and (d) are adapted from [86, 92, 95].

Depending on the relative alignment of the vibrations propagation direction  $\tilde{k}$  with respect to the orientation of the electric field  $\tilde{E}$ , the phonons can then be divided

<sup>1</sup>Some modes are neither IR- nor Raman active, and such modes are referred to as *silent*. These modes are not relevant to the results discussed in this thesis.

into **transverse** when  $\tilde{E} \perp \tilde{k}$  and **longitudinal** when  $\tilde{E} \parallel \tilde{k}$ . In fact, the electric field of light can only couple to the IR-active transverse optical phonons (TO phonons) (see Fig. 1.1(c) and (d)) [86].

The optical response of the TO phonon modes is described using the Lorentz oscillator model. According to this model, considering the excitation electric field to be  $E(t) = E_0 \sin(\omega_d t)$  - with  $\omega_d$  being the electric field frequency-, the equation of motion for the collective ionic displacement, indicated by coordinate amplitude  $Q_{\text{IR}}$  reads;

$$\ddot{Q}_{\text{IR}} + 2\gamma\dot{Q}_{\text{IR}} + \Omega_{\text{TO}}^2 Q_{\text{IR}} = \frac{Z^*}{\mu} E(t) \quad (1.1)$$

Here  $Z^* = \frac{\partial P_{\text{IR}}}{\partial Q_{\text{IR}}}$  is the Born effective charge of the phonon mode,  $\mu$  is the effective mass of the oscillator,  $\gamma_{\text{IR}}$  is the damping which accounts for the phonon life time and  $\Omega_{\text{TO}}$  is the natural frequency of the TO phonon. The solution to this equation of motion is of the form  $Q_{\text{IR}} = Q_{\text{IRO}} e^{-i\Omega_{\text{TO}} t}$ , where

$$Q_{\text{IRO}} = \frac{Z^* E_0 / \mu}{\Omega_{\text{TO}}^2 - \omega^2 - i\gamma_{\text{IR}} \omega} \quad (1.2)$$

This displacement creates a local time-varying electric dipole moment for the phonon denoted by  $p(t)$ , from which the macroscopic polarization is derived as follows;

$$P(t) = Np(t) = \frac{NZ^{*2}}{\mu} \frac{E(t)}{\Omega_{\text{TO}}^2 - \omega^2 - i\gamma_{\text{IR}} \omega} \quad (1.3)$$

The polarization is not negligible once the driving frequency is tuned to be at resonance with the TO phonon frequency i.e.  $\omega_d = \Omega_{\text{TO}}$ .

The polarization, derived from the Lorentz model in Eq.1.3, gives rise to a new propagating mode resulting from the hybridization of light photons with the lattice vibrational modes which is referred to as **Phonon-Polariton**. In essence, polaritons

possess a character distinct from both photons and phonons.

Now we have developed a model for the microscopic interaction between the phonons and the light field, we aim to understand how this interaction modifies the macroscopic optical properties of the sample. We start with the definition of the electric displacement  $D$ , which is given by a combination of the electric field and polarization:

$$D = \epsilon_0 E(t) + P \quad (1.4)$$

if we assume that the polarization is linear in the applied field, we can write  $P = \epsilon_0 \chi E(t)$ , where  $\chi$  is defined as the medium polarizability (susceptibility). Note that, here  $P$  accounts for all the resonant excitations. There exist also contributions to  $D$  from non-resonant, background excitations which will be considered later on. From this the complex Dielectric Function,  $\epsilon_r$  is defined as follows;

$$\epsilon_r = 1 + \chi \quad (1.5)$$

Using Eq.1.5 the Eq.1.4 can be rewritten as

$$D = \epsilon_0 \epsilon_r E(t) \quad (1.6)$$

As mentioned in the beginning of this Chapter, the second parameter from which we can study the optical properties of the material is the Complex Refractive Index  $\tilde{n}$ . This complex quantity determines the absorption and reflection of the medium and is connected to the complex dielectric function as follows;

$$\tilde{n} = \sqrt{\epsilon_r} \quad (1.7)$$

Following the complex refractive index, the reflectivity is calculated as following

[86] ;

$$R = \left| \frac{\tilde{n} - 1}{\tilde{n} + 1} \right|^2 \quad (1.8)$$

### 1.3 Optical Properties of Phonon-Polaritons

The complex dielectric function determining the optical properties of the phonon-polaritons is obtained by combining the result in Eq.1.3 with the definition of the permittivity from Eq.1.5 as follows:

$$\epsilon_r(\omega) = 1 + \frac{Ne^2}{\epsilon_0 m_0} \frac{1}{(\Omega_{\text{TO}}^2 - \omega^2 - i\gamma\omega)} \quad (1.9)$$

It can be seen that from the equation above, for the case of  $\omega = 0$ ,  $\epsilon_0 = \epsilon_r(0) = 1 + \frac{Ne^2}{\epsilon_0 \mu \Omega_{\text{TO}}^2}$ . On the other hand, in the limit of  $\omega \rightarrow \infty$ ,  $\epsilon_r(\infty) = 1$ <sup>2</sup> Based on these responses the Eq.1.9 can be rewritten as below:

$$\epsilon_r(\omega) = \epsilon_\infty + (\epsilon_0 - \epsilon_\infty) \frac{\Omega_{\text{TO}}^2}{(\Omega_{\text{TO}}^2 - \omega^2 - i\gamma\omega)} \quad (1.10)$$

As shown in Fig.1.2(a), for frequencies below  $\Omega_{\text{TO}}$ , the real  $\epsilon_1$  and imaginary  $\epsilon_2$  parts of the dielectric function are constant. Close to the resonance frequency  $\Omega_{\text{TO}}$ ,  $\epsilon_2$  becomes positive and  $\epsilon_1$  changes sign, respectively. This indicates the strong interaction between the photons with TO phonons. Above the TO frequency,  $\epsilon_1$  becomes negative for a certain frequency range. In this frequency range, because of destructive interference between the electric field and the oscillatory phonon field, light can not propagate inside the medium and is completely reflected until  $\epsilon_1(\omega)$  approaches zero or becomes positive. The frequency at which  $\epsilon_1(\omega)$  is exactly zero

---

<sup>2</sup>In reality, as mentioned earlier, there are also non-resonant, background contributions which will add up to a value defined as  $\epsilon_\infty$ , which we now introduce to the equations.

### 1.3. Optical Properties of Phonon-Polaritons

is known as longitudinal frequency ( $\Omega_{LO}$ ). Above  $\Omega_{LO}$  frequency the light can again propagate into the medium. The relation between  $\Omega_{TO}$  and  $\Omega_{LO}$  can be derived from Eq.1.10 as  $\frac{\Omega_{LO}^2}{\Omega_{TO}^2} = \frac{\epsilon_0}{\epsilon_\infty}$  (assuming  $\gamma \simeq 0$ ) and is known as *Lydanne-Sachs-Teller* (LST) relationship. The frequency dependent reflectivity can be calculated using Eqs.1.7 and 1.8 and is displayed in Fig.1.2 (b). As explained, throughout the frequency range between  $\Omega_{TO}$  and  $\Omega_{LO}$  where  $\epsilon_1(\omega) < 0$ , the reflectivity is close to unity. This feature is known as the *Reststrahlen band* [86, 88].

Due to the strong interaction between TO phonons and photons, the light entering a medium is heavily dispersed. The dispersion relation of the phonon-polaritons propagating inside the medium can be obtained from the relation  $\omega^2 = \frac{c^2 k^2}{n(\omega)^2}$ , which using Eqs.1.7 and 1.10 for  $\gamma \simeq 0$  gives:

$$\omega^2(k) = \frac{\epsilon_0 \Omega_{TO}^2 + c^2 k^2}{2\epsilon_\infty} \pm \frac{\sqrt{(\epsilon_0 \Omega_{TO}^2 + c^2 k^2)^2 - 4c^2 k^2 \epsilon_\infty \Omega_{TO}^2}}{2\epsilon_\infty} \quad (1.11)$$

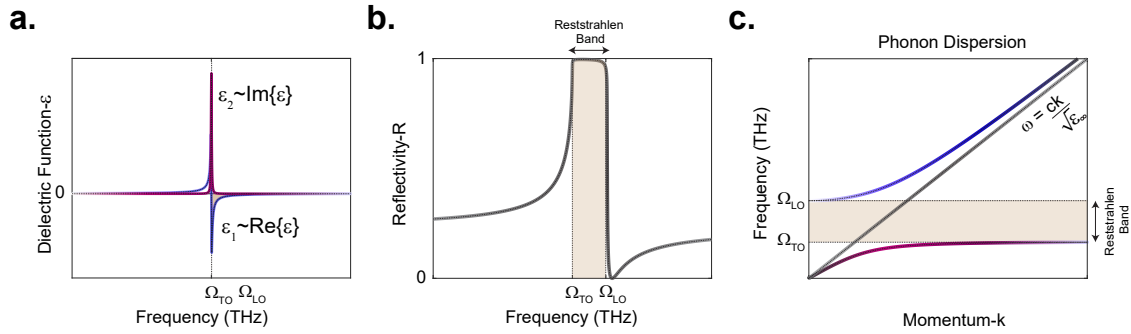


**Figure 1.2:** Exemplary complex optical properties of the phonon-polaritons derived from Lorentz model (see the text for details). (a). Real ( $\epsilon_1$  - shaded in blue) and imaginary ( $\epsilon_2$ -shaded in purple) parts of the complex dielectric function for phonon-polaritons plotted using Eq.1.10. (b). Exemplary reflectivity using Eq.1.8. The light shaded area indicates the Reststrahlen band. (c). Phonon-polariton dispersion plotted using Eq.1.11, with the same light shading as in panel (b). The grey line represents the dispersion of light in the medium.

As shown in Fig.1.2 (c) and can be seen from this equation, there are two dispersion branches, spaced by the splitting of the  $\Omega_{\text{TO}}$  and  $\Omega_{\text{LO}}$  or the so-called Reststrahlen band.

## 1.4 Electronic Degrees of Freedom

The collective motion of the conduction band electrons in a solid are known as plasma oscillations. The quanta of these oscillations are called **plasmons**. Unlike phonons, described above, the oscillatory motion of the plasma does not have a restoring force, because the electrons are not bound to a specific equilibrium position. Therefore we can model the plasma response with the following equation of motion, which is very similar to eq.1.1, including the same oscillatory electric field:

$$\ddot{Q}_p + 2\gamma_e \dot{Q}_p = \frac{e}{\mu_e} E(t) \quad (1.12)$$

Here  $Q_p$  represents the amplitude response of the plasma and upon solving the equation of motion we obtain:

$$Q_p(t) = \frac{-eE(t)/\mu_e}{\omega^2 + i\gamma_e\omega} \quad (1.13)$$

and consequently the polarization due to the plasma dipole moment is given by  $P(t) = -NeQ_p(t)$ :

$$P(t) = \frac{-ne^2E(t)/\mu_e}{\omega^2 + i\gamma_e\omega} \quad (1.14)$$

Here  $\Omega_p = \sqrt{\frac{Ne^2}{\mu_e\epsilon_0}}$  is the so-called plasma frequency [86, 88]. In the absence of any external field, the electron charges are uniformly distributed. In the presence of any driving field interacting with the material, if the frequency of this field is below the plasmon frequency ( $\omega_d < \Omega_p$ ), the charge carriers immediately respond to the

electric field, oscillate at the same frequency as the driving field frequency and reflect back the electric field totally. Therefore in this frequency range the electric field of light is screened from entering the bulk of the material. On the other hand, if the frequency is above the plasmon frequency ( $\omega_d > \Omega_p$ ), the charge carriers can not respond to the light electric field quickly enough and therefore the light can easily propagate through the material and be transmitted. For the case when the frequency is precisely at the plasmon frequency ( $\omega_d = \Omega_p$ ), the wavelength of light in the medium diverges to infinity, causing a longitudinal excitation of the plasma which results in finite absorption. These will be discussed illustratively in the next sections.

## 1.5 Optical Properties of Plasmon-Polaritons

The plasmon-photon interaction can be described following a similar approach to that discussed above for the case of the phonon-photon interaction, except with  $\Omega_{TO} = 0$  in the complex dielectric function in Eq.1.10. This procedure gives us the plasmon complex dielectric function which describes the optical properties of the free charge carriers<sup>3</sup>;

$$\epsilon_r(\omega) = \epsilon_\infty - \frac{\Omega_p^2}{\omega^2 + i\gamma\omega} \quad (1.15)$$

---

<sup>3</sup>Note that the optical properties of the free-charge carriers can also be represented by the *complex Optical Conductivity*  $\sigma$ , given by:  $\epsilon_r(\omega) = \epsilon_\infty + \frac{i\sigma(\omega)}{\epsilon_0\omega}$ .

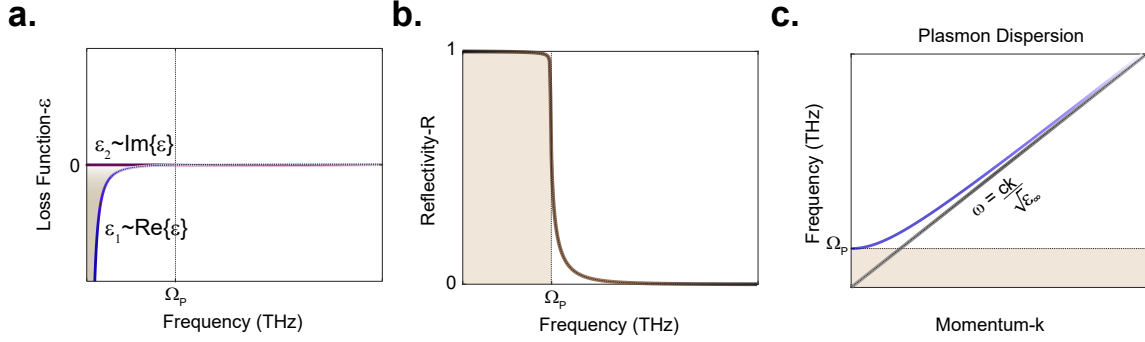


**Figure 1.3:** Exemplary complex optical properties plasmon-polaritons (see the text for detailed explanation). **(a).** Real ( $\epsilon_1$ - shaded in blue) and imaginary ( $\epsilon_2$  - shaded in purple) parts of the complex dielectric function for plasmon-polaritons plotted using Eq.1.15. **(b).** Exemplary reflectivity of the plasmon-polaritons using Eqs.1.15 and 1.8. The light shaded area indicates the region where the light is screened (Reststrahlen band). **(c).** Dispersion plot of plasmon-polaritons representing the hybrid state of photons with solids electronic degrees of freedom plotted using Eq.1.16. The grey line represents the dispersion of light in the medium. In the plots shown here the  $\epsilon_\infty$  is set to one.

The real and imaginary parts of Eq.1.15 and the reflectivity of the charge carriers for the case of  $\gamma \simeq 0$  are shown in Fig.1.3 (a) and (b). Comparing Figs.1.2 and 1.3 demonstrates the similar optical properties for phonon-polaritons and plasmon-polaritons, with the major difference being that the TO frequency of the plasmon-polaritons is zero. Similar to above, the dispersion relation for the plasmon-polaritons is obtained as in Eq.1.16 and is displayed in Fig.1.3 (c);

$$\omega(k)^2 = \frac{c^2 k^2 + \Omega_P^2}{\epsilon_\infty} \quad (1.16)$$

## 1.6 Beyond the Harmonic Approximation

So far, the motion of the phonons in the crystal lattice were modelled using the *harmonic approximation*, which is valid under the assumption that the ionic displacements in the crystal lattice are small with respect to the inter-ionic distances.

## 1.6. Beyond the Harmonic Approximation

---

However, this assumption breaks down when the lattice vibrations are large enough, either due to high temperature in equilibrium or strong external excitation. Indeed, this approximation fails to describe various well-known phenomena in solids such as the violation of the high-temperature Dulong and Petit law of specific heat, thermal expansion, thermal conductivity and phonon mode life times. To capture these phenomena, higher order corrections (*an-harmonic* terms) must be included in the Hamiltonian.

Intuitively, this can be understood as follows, the motion of a phonon in the crystal lattice, distorts the periodicity and hence scatters another phonon. The energy transfer due to this scattering can occur through various nonlinear phonon-phonon couplings, the an-harmonic terms, which explain the finite life time of the phonons as well as the thermal expansion and thermal conductivity of the material [87, 90].

To model these phenomena, the lattice potential can be expanded as harmonic part (discussed earlier) denoted by  $V_{\text{harmonic}}$  and an-harmonic part denoted by  $V_{\text{an-harmonic}}$  as a function of the displacement of the different normal modes of the crystal. Using this notation, the lattice potential for a given system, driven by an external field  $E(t)$  can be written as below [24–26]:

$$\begin{aligned}
 V_{\text{lattice}} &= V_{\text{harmonic}} + V_{\text{an-harmonic}} + \sum_i Z_i^* Q_i E(t) \\
 V_{\text{harmonic}} &= \frac{1}{2} \sum_i \omega_i^2 Q_i^2 \\
 V_{\text{an-harmonic}} &= \sum_{i,n} \frac{1}{n} \alpha_{i,n} Q_i^n + \sum_{ijk} \beta_{ijk} Q_i Q_j Q_k + \sum_{ijkl} \lambda_{ijkl} Q_i Q_j Q_k Q_l + \dots
 \end{aligned} \tag{1.17}$$

Where  $\sum_i Z_i^* Q_i E(t)$  only sums over IR-active phonon modes. In the last expression

in Eq.1.17, starting from the left, the first term accounts for the self-anharmonicity and the next two terms represent third-order and fourth-order nonlinearities, respectively. The stronger the driving field becomes, the more important the contributions of the nonlinear terms in the anharmonic potential [26]. Crucially, the Hamiltonian of the system, and thus the an-harmonic phonon-phonon coupling terms, must obey the symmetry constraints dictated by the crystal lattice.

For example, in a centro-symmetric medium the Hamiltonian must remain even with respect to the inversion operation. This means that the coupling of different IR-active or Raman-active modes is only allowed if their tensor product is part of the  $A_g$  totally symmetric irreducible representation.

In general, the *nonlinear phononics*, provide a selective framework for the dynamical manipulation as well as the non-equilibrium study of the crystal lattice [19–23, 26–28, 30, 33, 70, 96–99]. The rest of this chapter is devoted to describing the dynamics which may arise when different non-linearities are driven by an external electric field. We will focus only on non-linearities which may be present in a centro-symmetric system, as that will be the case for the system studied in the later chapters of this thesis.

### 1.6.1 Linear Excitation

As already discussed in Section 1.2 from the Lorentz model, the light electric field can couple to the lattice IR-active modes and excite these modes resonantly [86]. The lowest order excitation is the linear term in the Hamiltonian denoted by  $\sum_i Z_{\text{IR},i}^* Q_{\text{IR},i} E(t)$ . The derivative of this linear term ( $F_i = -\frac{\partial V_{\text{lattice}}}{\partial Q_{\text{IR},i}}$ ) acts as a resonant force for the respective IR-active mode with the coordinate amplitude  $Q_{\text{IR},i}$ . The Hamiltonian of the system is given below, which can be expected to accurately capture the phonon dynamics provided that the drive strength is weak enough that

the higher order terms remain negligible.

$$V_{\text{linear}} = \frac{1}{2}\omega_{\text{IR},0}^2 Q_{\text{IR}}^2 + Z_{\text{IR}}^* Q_{\text{IR}} E(t) \quad (1.18)$$

The dynamical motion of this mode is then obtained by solving the equation of motion derived from this Hamiltonian<sup>4</sup>:

$$\ddot{Q}_{\text{IR}} + 2\gamma_{\text{IR}}\dot{Q}_{\text{IR}} + \omega_{\text{IR},0}^2 Q_{\text{IR}} = Z_{\text{IR}}^* E(t) \quad (1.19)$$

Here  $\gamma_{\text{IR}}$  is the phenomenological damping which accounts for the life-time of the IR-active mode and  $\Omega_{\text{IR},0}$  is the eigenfrequency. Figs.1.4 (a-c) summarize the dynamics which arise from solving Eq.1.19 for a driving field consisting of a Gaussian pulse with its center frequency tuned to be resonant with the natural frequency of the IR mode  $\Omega_{\text{IR},0}$ .

$$E(t) = E_0 \exp\left(-\frac{(t-t_0)^2}{2\sigma_{\text{pump}}^2}\right) \sin(\omega_{\text{pump}}(t-t_0)) \quad (1.20)$$

The harmonic oscillations observed from the mode displacement can be visualized as the oscillatory motion of the ball in the parabolic potential shown in Fig.1.4(c).

For larger driving fields, the nonlinear terms in the lattice potential can no longer be ignored. Due to the effect of the nonlinear terms the parabolic shape of the potential is modified which in turn affects the motion of the ball and hence the dynamics of the phonon mode. The first type of nonlinear correction is the self-anharmonic terms  $\sum_{i,n} \frac{1}{n} \alpha_{i,n} Q_i^n$ . For a centro-symmetric medium, the lowest-order symmetry-allowed correction to the harmonic potential is the fourth-order self-anharmonicity

---

<sup>4</sup>All the equations of motions presented and solved in this thesis are treated classically, as the intense driving regime of the experiments ensure large mean phonon occupation numbers.

$\propto Q_{\text{IR}}^4$ . The nonlinear dynamics obtained by accounting for this term are then given by solving the equation of motion:

$$\ddot{Q}_{\text{IR}} + 2\gamma_{\text{IR}}\dot{Q}_{\text{IR}} + \omega_{\text{IR},0}^2 Q_{\text{IR}} = Z_{\text{IR}}^* E(t) - \alpha_1 Q_{\text{IR}}^3 \quad (1.21)$$

Figure 1.4 (d-e) displays the result of simulating this equation of motion. As can be seen from both the equation of motion itself, and the simulation results, the mode self-anharmonicity effectively renormalizes the mode eigen frequency  $\omega_{\text{IR}}^2 = (\omega_{\text{IR},0}^2 + \alpha_1 Q_{\text{IR}}^2)$ . Since  $Q_{\text{IR}}^2$  is always positive, the sign of  $\alpha_1$  determines if the frequency increases or decreases. As shown in Fig. 1.4 (f), for a positive or negative sign of  $\alpha_{\text{IR}}$ , the ball moves in a steeper or wider potential, respectively. In this model there are two forces exerted on the phonon mode coordinate, one due to the external field  $E(t)$  with phase  $\phi_1$ , which lasts as long as the drive is present and the other by the nonlinear term proportional to  $\alpha_{\text{IR}} Q_{\text{IR}}^3(t)$  and with the phase  $\phi_2$ , which lasts for the duration of  $Q_{\text{IR}}^3(t)$ . Due to these differing phases and timescales, the coordinate oscillates with different phases in different windows in time (given by the duration of pump and the an-harmonic force). This gives rise to interference in the response, visible in the Fourier spectrum shown in Fig. 1.4 (e).

By observing the phonon dynamics which result from intense driving, the higher order non-linear terms in the Hamiltonian can be measured, allowing the instantaneous Hamiltonian to be mapped out [99] which also provides insight into the possible energy pathways for further targeted manipulation of the system's functional properties.

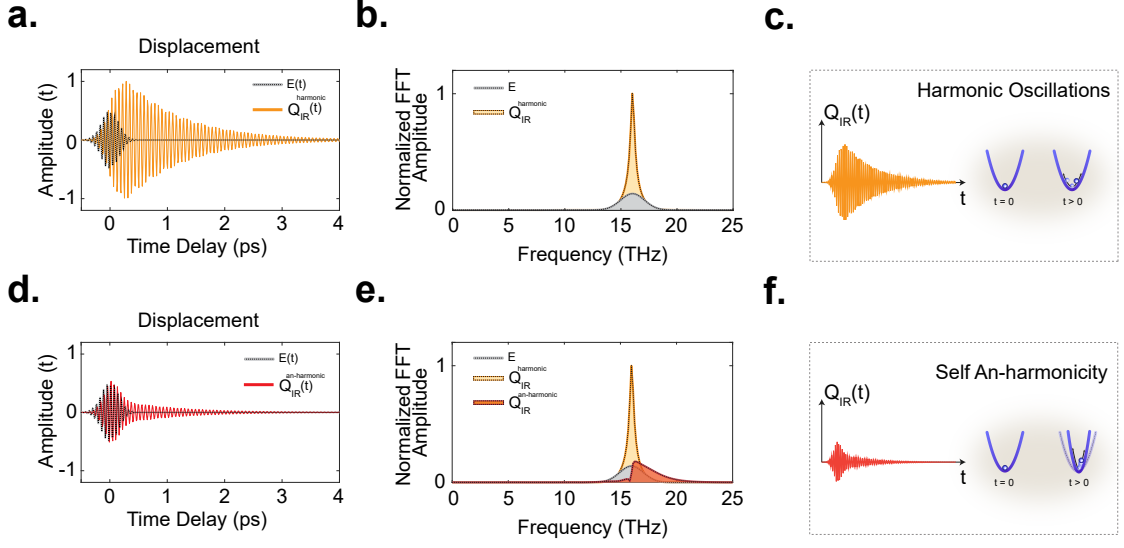


**Figure 1.4:** (a). Displacement of resonantly excited IR-active phonon mode with coordinate amplitude  $Q_{\text{IR}}$  (yellow curve) via electric field  $E(t)$  (black dashed curve), simulated using Eq.1.19. Both curves are normalized to  $Q_{\text{IR}}$  maximum value. (b). Normalized Fourier transform amplitude of electric field (shaded in grey) and driven phonon (shaded in yellow). Both FFT amplitudes are normalized to maximum value of the driven phonon FFT amplitude. (c). Resonant Excitation of the  $Q_{\text{IR}}$  by electric field results in a harmonic motion of the ball in the parabolic potential and decays on the time scale of phonon life time. (d). Same as in (a) with  $Q_{\text{IR}}$  being the orange curve, this time for the effect of phonon mode self-anharmonicity, simulated using Eq.1.21. (e). Same as in (b), for harmonic oscillations (shaded in yellow) and anharmonic oscillations (shaded in orange). All the FFT amplitudes are normalized to the maximum value of  $Q_{\text{IR}}^{\text{harmonic}}$  (f). The effect of self-anharmonicity on the driven phonon parabolic potential. For  $\alpha_1 > 0$ , the frequency of  $Q_{\text{IR}}$  is renormalized which results in a motion of the ball in a steeper potential. The change in the frequency and oscillations amplitude can also be seen from (d) and (e).

### 1.6.2 Cubic Nonlinearities: Displacive Excitation

So far the discussion was limited to the dynamics of a single IR-active phonon mode. However, as pointed out earlier, the motion of one phonon mode can affect other modes via different non-linear mode-mixing corrections. The lowest order non-linear term is the **Cubic** coupling mentioned in Eq.1.17. The lattice potential describing the mixing of two phonon modes of the system with coordinate amplitudes

denoted by  $Q_{\text{IR}}$  and  $Q_{\text{c}}$ , respectively, via such a cubic nonlinearity reads:

$$V_{\text{cubic}} = \frac{1}{2}(\omega_{\text{IR}0}^2 Q_{\text{IR}}^2 + \omega_{\text{c}0}^2 Q_{\text{c}}^2) + Z_{\text{IR}}^* Q_{\text{IR}} E + \beta_1 Q_{\text{IR}}^2 Q_{\text{c}} + \beta_2 Q_{\text{IR}} Q_{\text{c}}^2 \quad (1.22)$$

Here  $\beta_i$  and  $\omega_{\text{c}0}$  are the coupling coefficients and coupled mode natural frequency. For a non centro-symmetric medium, both symmetry-odd and even modes are allowed to mix via a cubic nonlinearity. However, in an inversion symmetric medium which is considered here, with the assumption that  $Q_{\text{IR}}$  and  $Q_{\text{c}}$  are, respectively, IR-active with  $B_{1u}$  symmetry and Raman-active with  $A_g$  symmetry, the term  $\beta_2 Q_{\text{IR}} Q_{\text{c}}^2$  is forbidden due to symmetry constraints<sup>5</sup>. In this case, the only symmetry-allowed cubic term which couples the two modes is  $\beta_1 Q_{\text{IR}}^2 Q_{\text{c}}$  ( $\beta_1 \neq 0$ ), because the tensor product of  $I(Q_{\text{IR}}) \times I(Q_{\text{IR}}) \times I(Q_{\text{c}})$  produces irreducible representation of  $A_g$  and is therefore totally symmetric.

According to the cubic coupling term the driven phonon mode exerts a force proportional to  $F_{\text{c}} = -\frac{\partial(Q_{\text{IR}}^2 Q_{\text{c}})}{\partial Q_{\text{c}}} \propto -Q_{\text{IR}}^2$  on the coupled Raman mode coordinate. This force consists of two components, one oscillating at  $2\omega_{\text{IR}0}$  and one non-oscillatory rectified envelope (see Fig.1.5 (b)). As a result of this envelope component, the force is unidirectional and therefore displaces the minimum of the coupled mode potential. This displacement follows the envelope of  $Q_{\text{IR}}^2$ . If the envelope of the force is shorter than the period of the coupled mode, the mode is impulsively excited via the non-oscillatory rectified force and oscillates in the displaced potential at its natural frequency (see Fig.1.5 (e) and (f)).

---

<sup>5</sup>Note that the phonon modes self-anharmonicities are neglected here in order to isolate the effective dynamics which arise only due to the cubic inter-mode coupling, but they would be present in any real physical system.

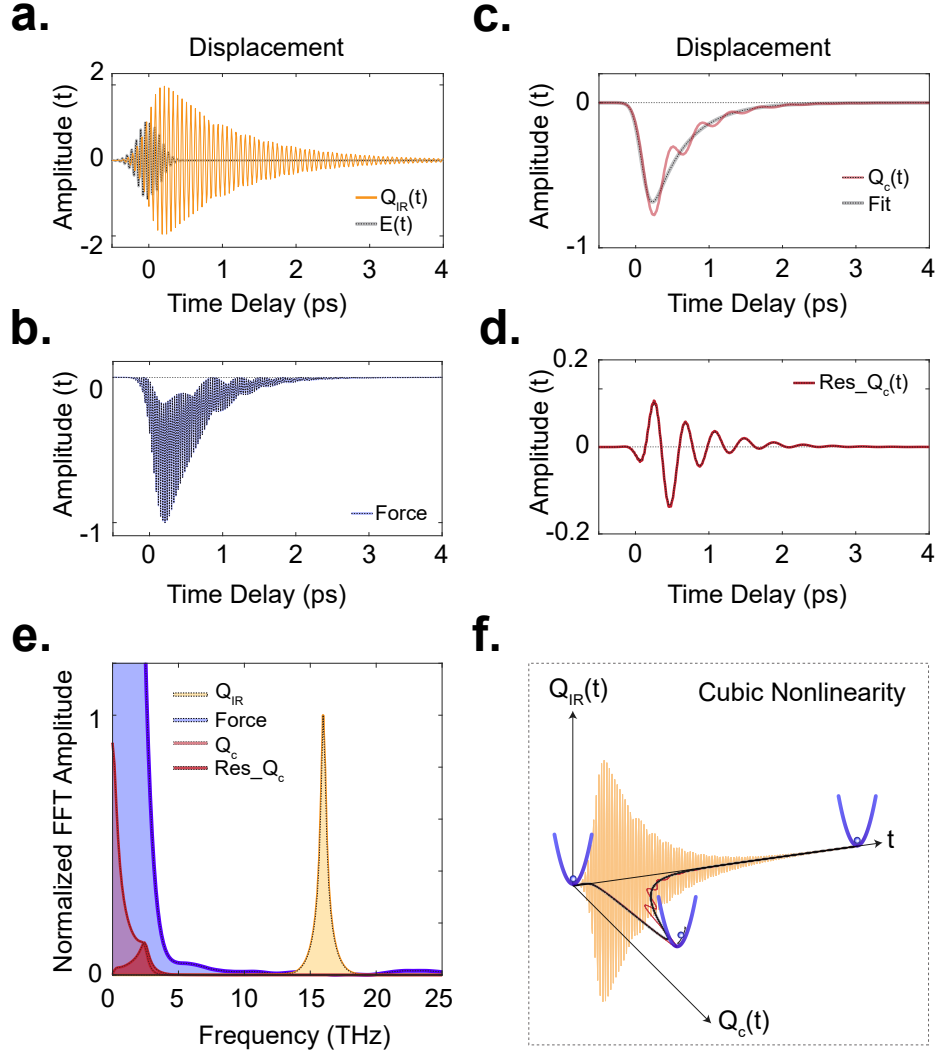


**Figure 1.5:** (a). Displacement of resonantly excited IR-active phonon mode with coordinate amplitude  $Q_{\text{IR}}$  (yellow curve) via electric field  $E(t)$  (black dashed curve), simulated using Eq.1.23. Both curves are normalized to  $Q_{\text{IR}}$  maximum value. (b). The displace force  $-Q_{\text{IR}}^2$  exerted on the Raman mode coordinate with two frequency components of  $2\omega_{\text{IR},0}$  and 0. (c). and (d). Coupled mode displacement, driven via cubic coupling with and without the force envelope, respectively. (e). Normalized FFT amplitude of panels (a-d) with the same color coding. The sharp peaks at 16 THz and 2.5 THz denote the  $\omega_{\text{IR},0}$  and  $\omega_{\text{c},0}$  frequency responses, respectively. (f). Due to the force  $-Q_{\text{IR}}^2$ , the minimum of the coupled mode parabolic potential is displaced following the envelope of the force. At the same time, the rectified component of the drive impulsively excite the coupled mode which results in motion of the ball in the parabolic potential at its natural frequency as discussed in the text.

The coupled equations of motion for these two phonon modes read:

$$\begin{aligned}\ddot{Q}_{\text{IR}} + 2\gamma_{\text{IR}}\dot{Q}_{\text{IR}} + \omega_{\text{IR}0}^2 Q_{\text{IR}} &= Z_{\text{IR}}^* E(t) - \beta_1 Q_{\text{IR}} Q_{\text{c}} \\ \ddot{Q}_{\text{c}} + 2\gamma_{\text{c}}\dot{Q}_{\text{c}} + \omega_{\text{c}0}^2 Q_{\text{c}} &= -\beta_1 Q_{\text{IR}}^2\end{aligned}\tag{1.23}$$

Where  $\gamma_{\text{c}}$  is the phenomenological damping of the coupled Raman mode accounting for its lifetime. Figure 1.5(a) illustrates the time domain displacement of the resonantly excited  $Q_{\text{IR}}$  which was already discussed earlier. The dispersive dynamics of the coupled Raman mode  $Q_{\text{c}}$  are then shown in Figs. 1.5(c-e).

Dynamics discussed here, illustrate how the cubic nonlinearity can be exploited to induce time-averaged distortions of the crystal structure and thereby manipulate different functional properties. This framework has been already shown to be an effective approach for example for photo-induced ferroelectric switching [20, 21, 29, 33], photo-induced magnetism [70] and also to study the coherent dynamics of the lattice on an ultra-fast time scale [22, 28, 72].

### 1.6.3 Quartic Nonlinearity: Squeezed Excitation

Whilst in many systems the cubic nonlinearity dominates the lattice dynamics, in an inversion-symmetric system this term is forbidden for the mixing of symmetry-odd (IR-active) modes. In these systems, the lowest order symmetry-allowed anharmonic correction to the lattice potential is a fourth order non-linearity known as **Quartic** coupling, as already was discussed in the Section 1.6.1 for the case of a single mode.

The lattice potential which describes the nonlinear dynamics of a system including quartic coupling between two IR-active phonon modes with coordinate amplitudes

## 1.6. Beyond the Harmonic Approximation

---

$Q_{\text{IR}}$  and  $Q_{\text{c}}$ , respectively, is as follows;

$$V_{\text{Quartic}} = \frac{1}{2}(\omega_{\text{IR}0}^2 Q_{\text{IR}}^2 + \omega_{\text{c}0}^2 Q_{\text{c}}^2) + Z_{\text{IR}}^* Q_{\text{IR}} E + \lambda_1 Q_{\text{IR}}^3 Q_{\text{c}} + \lambda_2 Q_{\text{IR}}^2 Q_{\text{c}}^2 + \lambda_3 Q_{\text{IR}} Q_{\text{c}}^3 \quad (1.24)$$

Here  $\lambda_i$  are the coupling coefficients. For the case that  $\lambda_1, \lambda_3 \approx 0$ , the dynamics of the system are dominated by the  $Q_{\text{IR}}^2 Q_{\text{c}}^2$  term where both  $Q_{\text{IR}}$  and  $Q_{\text{c}}$  are assumed to be IR-active  $B_{1u}$  modes. Based on this quartic term in the potential, the force on the coupled mode coordinate  $Q_{\text{c}}$  is proportional to  $-2\lambda_2 Q_{\text{IR}}^2 Q_{\text{c}}$ . This force is nonzero provided that there exist finite, nonzero fluctuations of the coordinate  $Q_{\text{c}}$ .

When the electric field resonantly excites the  $Q_{\text{IR}}$  coordinate, the frequency of the coupled mode  $\omega_{\text{c}}$  is immediately renormalized due to the quartic interaction,  $\omega_{\text{c}} = \sqrt{\omega_{\text{c}0}^2 - 2\lambda_2 Q_{\text{IR}}^2}$  - note that here we restrict the discussion to the case where  $\omega_{\text{c}0} > Q_{\text{IR}}^2$  and the lattice remains stable. The frequency renormalization occurs as fast as the rise time of the  $Q_{\text{IR}}^2$  and decays to its initial value following the  $Q_{\text{IR}}^2$  decay time.

In a real solid, there are many different modes corresponding different values of momentum  $q$  which can be coupled by a quartic nonlinearity. Therefore, the generalized version of the excitation term discussed above can be written as  $Q_{\text{IR}}^2 Q_{\text{c},q} Q_{\text{c},-q}$ , where  $\pm q$  is required to conserve the total crystal momentum. Here we need only to consider the  $Q_{\text{IR}}$  mode at  $q \approx 0$ , because it is excited directly by the light field which has negligible momentum. Such an excitation then leads to the generation of pairs of fluctuating  $Q_{\text{c}}$  with equal and opposite momenta  $\pm q$ . The generalized

coupled equations of motion now read:

$$\begin{aligned}
 \ddot{Q}_{\text{IR}} + 2\gamma_{\text{IR}}\dot{Q}_{\text{IR}} + \omega_{\text{IR}0}^2 Q_{\text{IR}} &= Z_{\text{IR}}^* E - \lambda_2 Q_{\text{IR}} Q_{c,q} Q_{c,-q} \\
 \ddot{Q}_{c,+q} + 2\gamma_c \dot{Q}_{c,+q} + \omega_{c0}^2 Q_{c,+q} &= -\lambda_2 Q_{\text{IR}}^2 Q_{c,+q} \\
 \ddot{Q}_{c,-q} + 2\gamma_c \dot{Q}_{c,-q} + \omega_{c0}^2 Q_{c,-q} &= -\lambda_2 Q_{\text{IR}}^2 Q_{c,-q}
 \end{aligned} \tag{1.25}$$

Here we have again reintroduced  $\gamma_c$  as the phenomenological damping of the coupled mode (see Appendix A.1 for the detailed derivation of the Eqs.1.25). As discussed earlier and from the equations above, it is necessary that  $Q_c$  has a fluctuating initial amplitude otherwise the coordinate remains zero. On the other hand, the fluctuating amplitude results in a phase fluctuating force on the coordinate and therefore phase fluctuating amplified coordinate.

The fixed phase of the drive ( $Q_{\text{IR}}^2$ ) however, fixes the zero-crossings of the coupled mode oscillating coordinate  $Q_c$ , but the amplitude remains fluctuating from positive to negative sign. This means that, averaged over many excitation pulses which is the case in the experiments, the coordinate response oscillating at  $\omega_{0c}$  averages to zero  $\langle Q_{c,\pm q} \rangle = 0$ . However, the variance of the coupled modes at  $\pm q$ , which oscillates at  $2\omega_{0c}$ , remains non-zero  $\langle Q_{c,q} Q_{c,-q} \rangle \neq 0$  (see Fig.1.6 (c) and (d)). Figures 1.6 (a-f) summarize the dynamics of these opposite-momenta pairs of phase fluctuating phonon modes.

These dynamics discussed here resemble a specific state which will be defined below, known as a **squeezed state**. Consequently, the excitation which leads to the generation of this state is called **squeezed excitation**, and the product of the amplified modes (or equivalently the variance of the modes at  $\pm q$ ,  $\pm q$ )  $\langle Q_{c,q} Q_{c,-q} \rangle$  is called a **squeezed mode** [20, 100–103]. The squeezed excitation is of particular interest, because through this excitation, coupling to the fluctuations is provided.

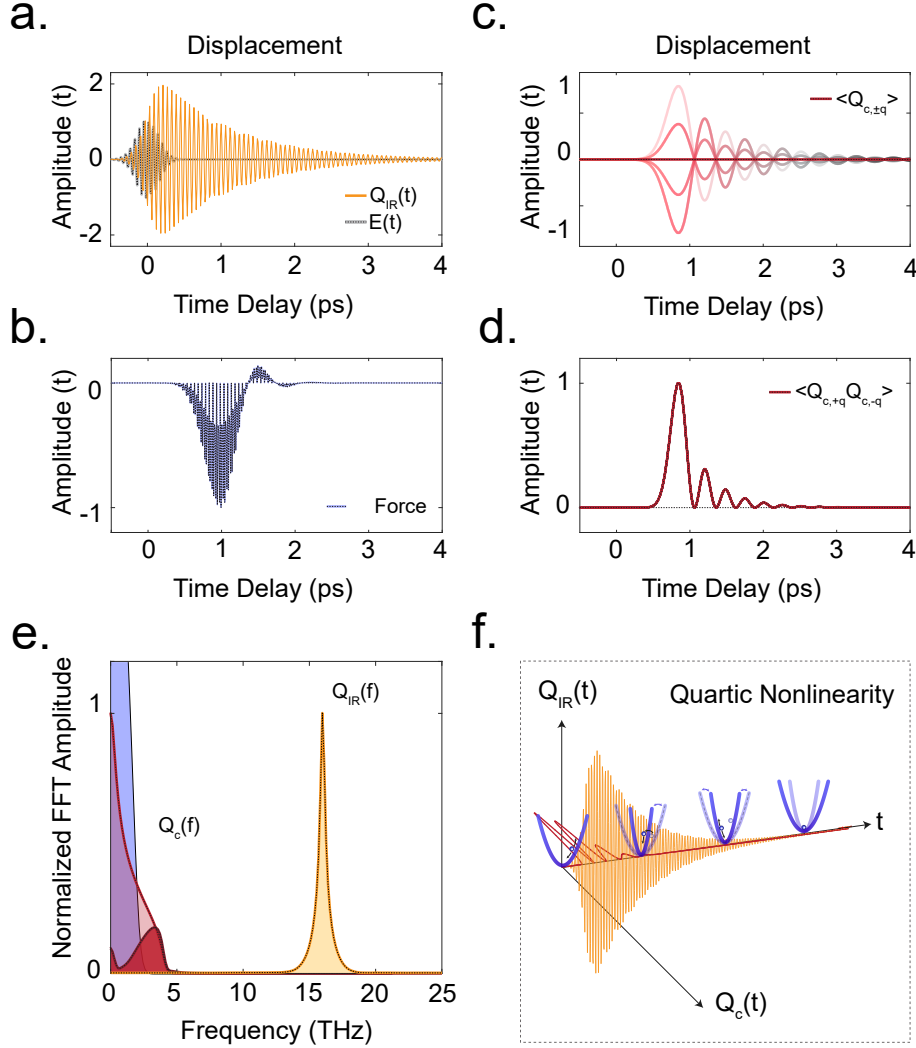


**Figure 1.6:** (a). Displacement of resonantly excited IR-active phonon mode with coordinate amplitude  $Q_{\text{IR}}$  (yellow curve) via electric field  $E(t)$  (black dashed curve), simulated using Eq.1.25. Both curves are normalized to  $Q_{\text{IR}}$  maximum value. (b). Time-domain representation of the  $-Q_{\text{IR}}^2 Q_c$  Force. (c). Displacement of the fluctuating  $Q_c$  coordinate for a number of initial amplitudes along with the zero averaged response. (d). Non-zero displacement of the squeezed mode  $\langle Q_{c,+q} Q_{c,-q} \rangle$  for the same initial amplitudes shown in (c). As can be seen, the product term (squeezed mode) has a fixed phase as oppose to an each individual coordinate. (e). Normalized FFT amplitude of the both resonantly driven mode  $Q_{\text{IR}}$  (in yellow), the  $-Q_{\text{IR}}^2 Q_c$  force (in blue) and the coupled mode  $Q_c$  (without and with the D.C. background subtraction in light and dark red, respectively). All components are normalized to the driven phonon FFT amplitude.

**Figure 1.6: (f).** The effect of quartic nonlinearity on the coupled mode parabolic potential. As the driven phonon  $Q_{\text{IR}}$  oscillates, the frequency of the coupled mode is re-normalized such that the coupled mode oscillates (as indicated by the motion of the ball) in a steeper potential and slowly relaxes back to its equilibrium value. This is correct under the assumption that the ball is not stationary in the potential and has non-zero fluctuations. Note that this picture only applies to the case of one excited mode and cannot be extended to the case of squeezing which involves pairs of modes.

---

## 1.7 Squeezed State

The squeezed state can be understood intuitively, by starting from a coherent harmonic oscillations of an ensemble of harmonic oscillators  $\hat{Q} = \sum_i A_i \cos(\omega_0 t + \phi_i)$  with equal Gaussian statistical noise on both the amplitude  $A_i$  and phase  $\phi_i$ . In phase space (coordinate  $\hat{Q}$  and momentum  $\hat{P}$  where  $\hat{P} = \dot{\hat{Q}}$ ), such an ensemble is represented by a circle shifted by  $\langle A \rangle$  from zero, as shown in Fig.1.7 (a). As time advances, this circle orbits the origin. As the circle maintains its shape, the noise in both the amplitude and phase is constant as a function of time. Extending this picture to the case of a squeezed state, we can imagine either squeezing the amplitude or the phase noise, which results in an ellipse elongated either along  $\hat{Q}$  or  $\hat{P}$ , as illustrated in Fig.1.7 (b) and (c), respectively. It can be seen that the phase and amplitude squeezed states give rise to different noise profiles in the coordinate response which repeats with a frequency of  $2\omega_0$ . The concept of squeezing has been extensively used in metrology to reduce noise and redistribute fluctuations [100–102, 104].

The picture of a coherently oscillating squeezed state described above can be extended to an in-coherent, vacuum state where there is no harmonic response to start with. In phase space, this is represented by a Gaussian distribution of fluctuations centered around zero (see Fig.1.7 (d)). Once again, the phase and amplitude

can be squeezed by distorting the circle into an ellipse, which in this case gives rise to harmonic modulation of the noise that also repeats with a frequency of  $2/\omega_0$  as illustrated in Fig.1.7 (e).

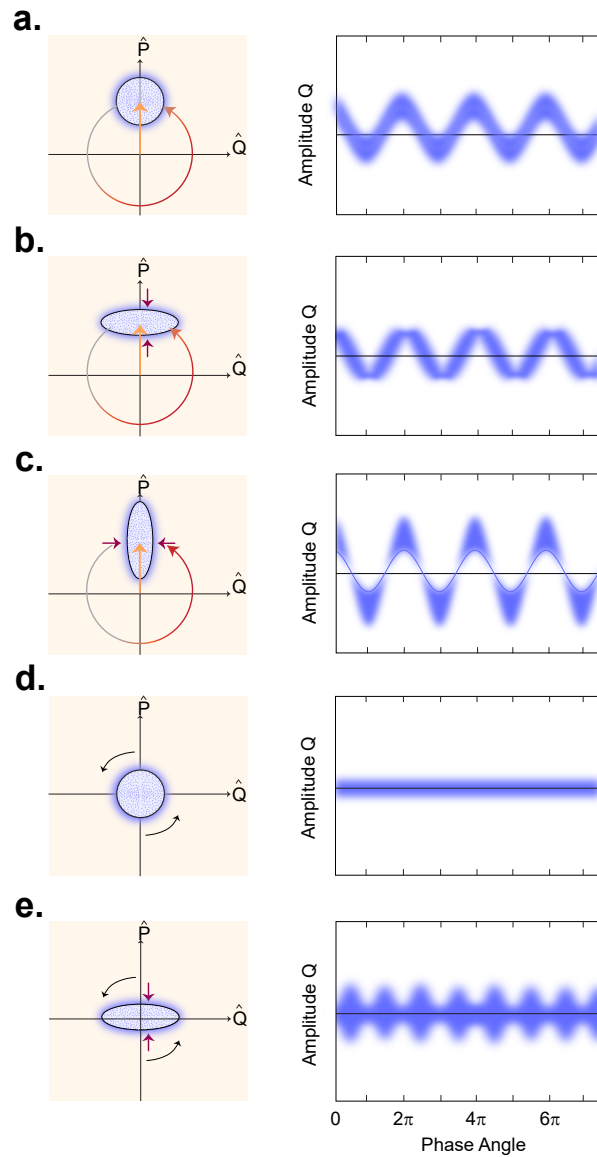


**Figure 1.7:** (a). From left to right: representation of a weakly displaced coherent state (yellow arrow) in the phase-space denoted by  $\hat{Q}$  (position) and  $\hat{P}$  (momentum). The circle indicates the quantum uncertainty/fluctuations. The rotation of this circle in the phase-space is mapped out in the plot on the right Amplitude-phase angle.

**Figure 1.7:** (b). Same as in (a) but corresponding to an *amplitude squeezed* state. As depicted in the plot on the right, at certain phase angles ( $n\pi$ ), the uncertainty on the amplitude is reduced and the uncertainty on the phase is maximized. (c). Same as in (a) but corresponding to a *phase squeezed* state. As oppose to (b), at certain phase angles, the uncertainty on the amplitude is maximized and the uncertainty on the phase is reduced. (d). Same as in (a) but for an in-coherent state. Correspondingly, the uncertainty on the amplitude and phase is around zero. (e). Squeezed state of an in-coherent state. Note that here, there cannot be any comparison for the phase-squeezed or amplitude squeezed, since there is no coherent state to start with. Figure is adapted from ref.[101].

---

From the discussion above, the squeezed state can be defined as a state with a modified noise (fluctuations) profile [100, 101].

In the case of the quartic coupling  $Q_{\text{IR}}^2 Q_{c,q} Q_{c,-q}$  discussed above, the squeezed state of the coupled modes was generated from an in-coherent, fluctuating state and therefore corresponds to panel (e) in Fig.1.7.

## 1.8 Linear and Nonlinear Polarization

As introduced in Sections 1.3 and 1.5, the interaction of the electromagnetic fields with different degrees of freedom in the medium results in the manifestation of a macroscopic time-varying dipole moment. Previously we considered the case in which the polarization is linearly proportional to the electric field, but in general higher order terms may also be present, and become important if the field is large. To capture this behaviour, the macroscopic polarization can be expanded as power series of the electric field  $E(t)$ :

$$\begin{aligned} P_i(t) &= \epsilon_0 [\chi_{ij}^{(1)} E_j(t) + \chi_{ijk}^{(2)} E_j E_k(t) + \chi_{ijkl}^{(3)} E_j(t) E_k(t) E_l(t) + \dots] \\ &= P_i^{(1)}(t) + P_i^{(2)}(t) + P_i^{(3)}(t) + \dots \end{aligned} \quad (1.26)$$

Here  $\chi_{ij}^{(1)}$  is the polarizability representing the linear contribution,  $\chi_{ijk}^{(2)}$  and  $\chi_{ijkl}^{(3)}$  are the hyper-polarizability and second hyper-polarizability, respectively, which give rise to the nonlinear contributions. In general, these polarizability tensors can be frequency dependent [105].

Via the excitation and hence motion of a lattice vibrational mode which is represented by the coordinate amplitude  $Q$ , the polarizability of the medium can be modulated, giving rise to different types of scattering processes. For example, the modulation of the  $\chi_{ij}^{(1)}$  results in **Raman scattering** [91, 106–108] which is represented by the expansion below:

$$\chi_{ij}^{(1)} = \chi_{ij,eq}^{(1)} + \left( \frac{\partial \chi_{ij}^{(1)}}{\partial Q_l} Q_l \right) \quad (1.27)$$

Here the  $\chi_{ij,eq}^{(1)}$  term is responsible for elastic Rayleigh scattering, and the  $\frac{\partial \chi_{ij}^{(1)}}{\partial Q_l}$  term gives rise to Raman scattering [107, 109–113]. Similarly, modulation of the quadratic hyper-polarizability term is described by the expression below:

$$\chi_{ijk}^{(2)} = \chi_{ijk,eq}^{(2)} + \left( \frac{\partial \chi_{ijk}^{(2)}}{\partial Q_m} Q_m \right) \quad (1.28)$$

where now  $\chi_{ijk,eq}^{(2)}$  and  $\frac{\partial \chi_{ijk}^{(2)}}{\partial Q_m}$  are known as **hyper-Rayleigh** and **hyper-Raman scattering**, respectively. Considering these ionic contributions to the macroscopic polarization, we can re-write Eq.1.25 as follows:

$$\begin{aligned} P_i(t) = \epsilon_0 & [\chi_{ij}^{(1)} E_j(t) + \left( \frac{\partial \chi_{ij}^{(1)}}{\partial Q_l} Q_l \right) E_j(t) \\ & + \chi_{ijk}^{(2)} E_j(t) E_k(t) + \left( \frac{\partial \chi_{ijk}^{(2)}}{\partial Q_m} Q_m \right) E_j(t) E_k(t) + \chi_{ijkl}^{(3)} E_j(t) E_k(t) E_l(t) + \dots] \end{aligned} \quad (1.29)$$

The Raman and hyper-Raman scattering processes discussed here are of central importance to the experiments described in Chapters 4 and 5 of this thesis, where a more detailed explanation is given.

## 1.9 Summary and Outlook

This chapter highlighted that lattice vibrational modes (known as phonons) provide efficient pathways for light to interact with a system both linearly and non-linearly. The linear interaction largely determines the equilibrium optical properties in the vicinity of the natural frequencies of these modes, whilst the non-linear interactions provide a framework through which these optical properties can be modified or manipulated. The framework established here will form the foundation for the following chapters, where the discussion will be focused on the study of one of the most interesting and yet mysterious dynamical states of the matter, the non-equilibrium superconducting state.

# Chapter 2

## Josephson Plasma Waves in Layered Superconductors

### 2.1 Introduction

From the discussion in Chapter 1, it was concluded that nonlinear phononics may provide an efficient, selective mechanism through which material properties can be modified or induced. The rest of this thesis is concerned with understanding how this method has been applied to the case of superconductivity.

In this chapter we first provide a brief introduction to the concept of superconductivity, beginning with conventional superconductors. The concept of the complex order parameter will be introduced, emphasizing that both Cooper pairing and phase coherence are equally crucial ingredients for establishing the macroscopic superconducting state. A fascinating phenomenon arising from the quantum tunneling of the Cooper pairs across the insulating barrier, the Josephson effect, will then be discussed in detail. The chapter concludes by solving the sine-Gordon differential equations for a stack of coupled Josephson junctions, enabling both the

linear optical properties, and the plasma wave dispersion relations of such a system to be derived.

These derivations form the basis for understanding the physics of the high- $T_c$  Cuprate superconductors, which structurally resemble such a stack of Josephson junctions. This family of compounds, in particular  $\text{YBa}_2\text{Cu}_3\text{O}_{6+x}$ , are the subject of the rest of this thesis.

## 2.2 Emergence of the Superconducting state

In a metal electronic resistance arises from three different sources, electron-electron interactions, electron-phonon interactions and residual scattering from impurities. These effects, which add together to give the total resistivity, can be disentangled through their different temperature dependencies, which reads:

$$\rho(T) = \rho_0 + \alpha T^2 + \beta T^5 \quad (2.1)$$

In this equation,  $\rho_0$  arises from impurity effects whilst the second and third terms are due to electron-electron and electron-phonon interactions, respectively [114]. In 1911, H. Kammerling Onnes observed a surprising resistivity curve for mercury which deviated strongly from this functional form, upon cooling down below 4 K. At very low temperatures the resistivity abruptly dropped to zero [115]. This **zero-resistance** state (**perfect conductivity**) was in fact the first observation of a new state of matter: **superconductivity**. The temperature at which this thermodynamic phase transition occurs is known as the critical temperature, denoted as  $T_c$ . Figure 2.1(a) represents a generic normal metal (NM) to superconducting state (SC) phase transition.

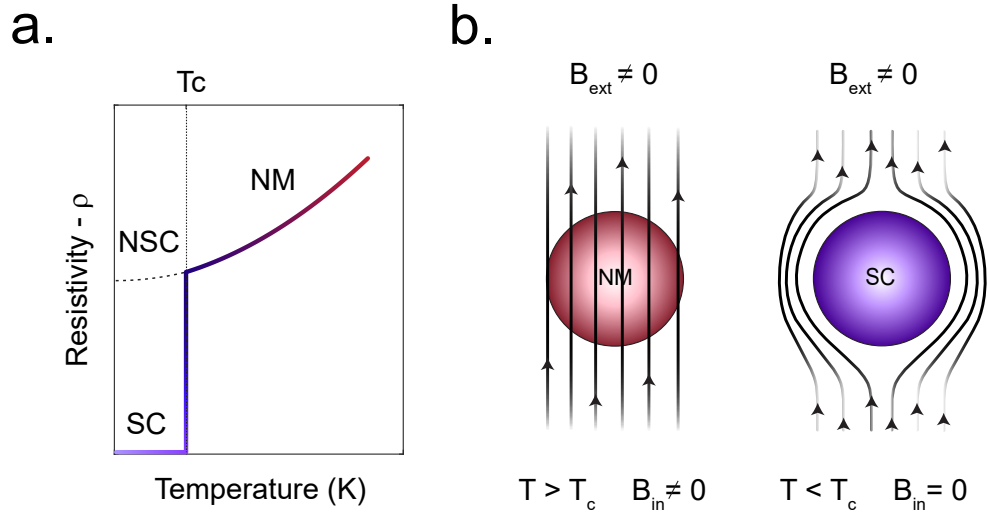


**Figure 2.1:** (a). Resistivity curve as a function of temperature for a typical metal. The resistivity follows the  $\rho_0 + \alpha T^2$  curve in case of normal metal with finite resistivity at all temperatures. For a superconducting material, however, starting from temperatures above  $T_c$ , the resistivity follows the NM curve and at  $T = T_c$  abruptly drops to zero and remains exactly zero for all temperatures below  $T_c$ . (b). The demonstration of Meißner-Ochsenfeld effect for a superconducting material. For temperature above  $T_c$  in the normal state and in the presence of a magnetic field, the field uniformly penetrates into the material and hence the field inside is the same as the applied field  $B_{in} = B_{ext}$ . On the other hand, below  $T_c$  in the superconducting state, material expels the magnetic field and therefore the field does not reach the inside  $B_{in} = 0$ . The figure was adapted from [114].

About 20 years after this initial discovery, Meißner and Ochsenfeld demonstrated that in a superconductor, not only is the resistance zero, but so is the magnetic field inside the superconductor (*perfect diamagnetism*). This phenomenon came to be known as the *Meißner effect*, which is specifically associated with superconductivity. In the normal state above  $T_c$ , and in the presence of an externally applied magnetic field, the field penetrates uniformly into the material ( $B_{in} \neq 0$ ) as depicted in Fig.2.1(b). However, upon cooling below  $T_c$  and entering the superconducting state, regardless of whether the magnetic field was applied before or after cooling and provided that the field strength remains below the critical value above

which the superconducting state is destroyed, the material expels the magnetic field ( $B_{\text{in}} = 0$ ), thus demonstrating the Meißner effect [114, 116].

## 2.3 Theory of Superconductivity

After the discovery of superconductivity, attempts to understand this novel state of matter commenced. Bardeen, Cooper and Schrieffer were the pioneering figures to propose a microscopic explanation of the superconducting state (**BCS theory**) [117]. According to the BCS theory, below the critical temperature, an electron-phonon interaction results in an attractive, effective electron-electron interaction, resulting in the formation of bound pairs of electrons with opposite spins and momenta, known as **Cooper pairs**, no matter how weak the force is. All these Cooper pairs together then form a single quantum coherent state<sup>1</sup>. This coherent state is represented by a complex **macroscopic wave function**  $\psi(r) = |\psi_0(r)|e^{i\theta(r)}$ , referred to as the BCS ground state wave function, which has a fixed phase  $\theta$ - note that the total number of the supercharge carriers is given by  $n_s = \psi_0(r)\psi_0(r)^*$ .

The formation of Cooper pairs opens an energy gap at the Fermi surface which is denoted as the **superconducting gap**  $\Delta$ , corresponding to the binding energy which must be overcome in order to break a Cooper pair and excite two quasiparticles from this ground state. For conventional superconductors in the weak coupling limit, the BCS theory predicts the relationship between the value for the gap at zero temperature and  $T_c$  as  $2\Delta(T = 0) = 3.52k_B T_c$ , which is known as the BCS gap equation [114, 116, 117]. A significant deviation from this value ( $\approx 3.5$ ) suggests unconventional superconductivity. This may indicate that the pairing mechanism is not phonon-mediated, and also that the normal state may deviate from that of

---

<sup>1</sup>A quantum coherent state is identified by a definite phase  $\theta$  and complex amplitude  $\alpha$  and is given by:  $\alpha = |\alpha|e^{i\theta}$  [114].

a conventional metal. In fact, a comprehensive theoretical framework for unconventional superconductors remains elusive, highlighting the complexity of these materials. Figure 2.2 (a) summarizes the fundamental features of the BCS theory.

The emergence of macroscopic superconducting properties relies on firstly, the formation of Cooper pairs ( $|\psi_0(r)| > 0$ ), and secondly the establishment of the quantum coherent state with a well-defined phase ( $\theta(r)$ ). Consequently, the superconducting state can be destroyed by either losing the phase coherence, depairing of the Cooper pairs or both. Based on this argument, one can assume that there exist two temperature scales which are both upper bounds on  $T_c$ , the first of which is set by  $T'$ , below which the pairing forms locally. The second temperature scale is set by  $T_\theta^{\max}$ , below which the phase fluctuations are suppressed and long-range phase coherence is established, assuming the existence of formed Cooper pairs. The  $T_\theta^{\max}$ , which is calculated for a given material according to various experimentally measured parameters such as penetration depth and superconducting coherence length<sup>2</sup>, can then be compared to  $T_c$ , in order to understand which process may be chiefly responsible for the loss of superconductivity at  $T_c$ .

Under normal circumstances for conventional materials, it is found that  $T_\theta^{\max} \gg T_c$ , which shows that Cooper pairs are extremely coherent all the way up to  $T_c$ , and the phase transition into the normal state occurs because the Cooper pairs themselves are thermally destroyed (depairing). In some rare cases,  $T_\theta^{\max}/T_c$  is actually close to unity, making it plausible that Cooper pairs are surviving above  $T_c$ , although their mutual coherence is lost.

---

<sup>2</sup>Superconducting coherence length  $\xi$  is defined as a typical length scale over which the order parameter may vary. In the weak-coupling BCS limit, the coherence length refers to the physical size of the Cooper pairs bound state and is related to the superconducting gap as follows:  $\xi_0 = \frac{\hbar v_F}{\pi \Delta(0)}$ —here  $v_F$  is the electron band velocity at the Fermi surface [114].

Table 2.1 displays the estimated ratio of  $T_{\theta}^{\max}/T_c$  for various classes of superconductors [118]. Of particular interest to this thesis, is that (as will be explained more thoroughly later) the classes of superconductors in which photo-excitation has been shown to establish signatures of superconductivity above  $T_c$  all exhibit ratios  $T_{\theta}^{\max}/T_c \approx 1$ . This suggest that these compounds may host pre-existing, phase fluctuating Cooper pairs and are therefore potential candidates for photo-induced phase-stabilization at temperatures above  $T_c$ .

Superconductor	$T_c$	$T_{\theta}^{\max}/T_c$
Pb	7	$2 \times 10^5$
Nb <sub>3</sub> Sn	18	$2 \times 10^3$
K <sub>3</sub> C <sub>60</sub> <sup>†</sup>	18	17
(BEDT) <sub>2</sub> Cu(NCS) <sub>2</sub> <sup>†</sup>	8	1.7
La <sub>2-x</sub> Sr <sub>x</sub> CuO <sub>4+δ</sub> <sup>†</sup>	28	1
YBa <sub>2</sub> Cu <sub>3</sub> O <sub>6+x</sub> <sup>†</sup>	92	1.4

**Table 2.1:** The list of  $T_c$  and the calculated ratio of  $T_{\theta}^{\max}/T_c$  for different classes of superconductors [118]. ”<sup>†</sup> indicates that photo-excitation has been observed to induce superconducting-like properties above  $T_c$  in this family of compounds”.

The microscopic physics of the conventional superconductors in the weak-coupling limit can very well be described using the BCS theory discussed above. However, this theory has its limitations and cannot account for all the phenomena even within this category as well as the unconventional superconductors. For such cases, a phenomenological macroscopic theory, established by Ginzburg and Landau, known as *Ginzburg-Landau theory (GL)* [116, 119] provides a more useful framework. In fact, this macroscopic GL theory can be obtained from the BCS theory in a suitable limit [120].

Considering the macroscopic wave function defined in the BCS theory as a complex order parameter, Ginzburg and Landau were able to describe the superconducting

phase transition in terms of this complex order parameter using the free energy landscape. Consequently, close to the phase transition temperature  $T_c$  (where the order parameter is small,  $|\psi(r)| \rightarrow 0$ ), the difference between the Helmholtz free energy of the superconducting state  $F_s$ , and the normal state  $F_n$ , can be expanded as a power series of  $|\psi(r)|^2$  as follows:

$$F_s - F_n = \alpha |\psi(r)|^2 + \frac{\beta}{2} |\psi(r)|^4 + \frac{\hbar}{2m^*} \left| \left( \nabla - \frac{ie^*}{\hbar c} A(r) \right) \psi(r) \right|^2 + \frac{H^2}{8\pi} \quad (2.2)$$

Here  $\alpha$  and  $\beta$  are expansion parameters that can be determined both from BCS theory and experiment.  $A(r)$ ,  $H$ ,  $e^*$  and  $m^*$  represent the vector potential, external magnetic field, effective charge and mass of the supercarriers, respectively. In the absence of electromagnetic fields and spatial gradients, the third and fourth terms on the right hand side are zero. We can find stationary points in the free energy landscape by taking the derivative of  $F_s - F_n$  with respect to  $\psi(r)$ ;

$$\frac{\partial(F_s - F_n)}{\partial\psi(r)} = 2|\psi(r)|(\alpha + \beta|\psi(r)|^2) = 0 \quad (2.3)$$

The Eq.2.3 has three solutions given by  $|\psi(r)| = 0$  and  $|\psi(r)|^2 = -\frac{\alpha}{\beta}$ . From this and as shown in Fig.2.2(b), in the normal state ( $T > T_c$ ), parameters  $\alpha$  and  $\beta$  are both positive and therefore the free energy has only one stable minimum at exactly  $|\psi_0| = 0$ . As the temperature gradually approaches  $T_c$ , the parameter  $\alpha$  reaches zero (at  $T_c$ ,  $\alpha = 0$ ). In the superconducting state ( $T < T_c$ ),  $\alpha$  becomes negative and the potential develops two stable minima at  $|\psi_0|^2 = -\frac{\alpha}{\beta}$ , whilst the stationary point at  $|\psi_0| = 0$  becomes an unstable local maximum.

Furthermore, the dynamics of the supercurrent in the presence of a magnetic field is discussed via the third term in Eq.2.2, which shows that in the presence of a magnetic vector potential it becomes energetically favorable for the order parameter to

vary as a function of position [114, 116].

The electrodynamics of a superconductor with the macroscopic wave function defined in the BCS and GL theories can be obtained by solving the Schrödinger equation for charged particles in the presence of an electromagnetic field:

$$i\hbar \frac{\partial \psi(r, t)}{\partial t} = \frac{1}{2m^*} \left( \frac{\hbar}{i} \nabla - e^* A(r, t) \right)^2 \psi(r, t) + e^* \phi(r, t) \psi(r, t) \quad (2.4)$$

$\phi(r, t)$  refers to the electrostatic potential. By analogy with the expression for the probability current from the Schrödinger equation, the supercurrent density  $J_s$  is given by:

$$J_s(r, t) = \frac{e^* \hbar}{2m^* i} (\psi(r, t)^* \nabla \psi(r, t) - \psi(r, t) \nabla \psi(r, t)^*) - \frac{e^{*2}}{2m^*} \psi(r, t) \psi(r, t)^* A(r, t) \quad (2.5)$$

By substituting the definition of the order parameter ( $\psi(r, t) = \sqrt{n_s(r, t)} e^{i\theta(r, t)}$ ) into Eq. 2.5, we obtain the following expression for the supercurrent density,

$$J_s(r, t) = e^* n_s(r, t) \left( \frac{\hbar}{m^*} \nabla \theta(r, t) - \frac{e^*}{m^*} A(r, t) \right) \quad (2.6)$$

The time-dependent changes of the supercurrent are obtained by taking the time derivative of both sides of Eq.2.6:

$$\begin{aligned} \frac{\partial J_s}{\partial t} &= e^* n_s(r, t) \left( \frac{\hbar}{m^*} \nabla \left( \frac{\partial \theta(r, t)}{\partial t} \right) - \frac{e^*}{m^*} \frac{\partial A(r, t)}{\partial t} \right) \\ &= \frac{1}{\Lambda} E - \frac{1}{n_s^* e^*} \nabla \left( \frac{1}{2} J_s^2 \right) \end{aligned} \quad (2.7)$$

where the last expression was obtained by firstly assuming  $n_s(r, t) = n_s$  is constant, and introducing the coefficient  $\Lambda = \frac{m^*}{n_s^* e^{*2}}$  and using the relations  $-\hbar \frac{\partial \theta(r, t)}{\partial t} = \frac{\Lambda J_s(r, t)^2}{2n_s^2} + e^* \theta(r, t)$  and  $E = -\frac{\partial A}{\partial t} - \nabla \theta$  [116, 121]. In Eq.2.7 the second term on the

right ( $\frac{1}{n_s^* e^*} \nabla \cdot (\frac{1}{2} J_s^2)$ ) indicates dissipation which for a superconductor is zero, since the current experiences no dissipation (perfect conductivity-zero-resistance effect). Therefore, Eq.2.7 reduces to the equation below which is known as the **first London equation** which relates the current and the electric field in a superconductor.

$$\frac{\partial J_s}{\partial t} = \frac{1}{\Lambda} E \quad (2.8)$$

The spatial dependence of the supercurrent density in response to the electromagnetic field is determined by taking curl of both sides of the Eq.2.6<sup>3</sup>.

$$\nabla \times J_s = -\frac{1}{\Lambda} B \quad (2.9)$$

Eq.2.9 is known as the **second London equation**. From Maxwell's equation  $J_s = \frac{1}{\mu_0} \nabla \times B$ , so taking curl of the Eq.2.9 one more time yields;

$$\nabla^2 B = \frac{1}{\lambda_L^2} B \quad (2.10)$$

Solving Eq.2.10 for an applied external magnetic field while considering the boundary conditions reveals that the magnetic field inside the superconductor decays exponentially (Meißner-Ochsenfeld effect), expressed as  $B_z(x) = B_{z0} e^{-x/\lambda_L}$ , over a length scale known as the London penetration depth, given by  $\lambda_L^2 = \frac{\mu_0}{\Lambda}$  [121–123] (see Fig.2.2(c)).

---

<sup>3</sup>Note that  $\nabla \times \nabla \theta = 0$  and  $\nabla \times A = B$ .

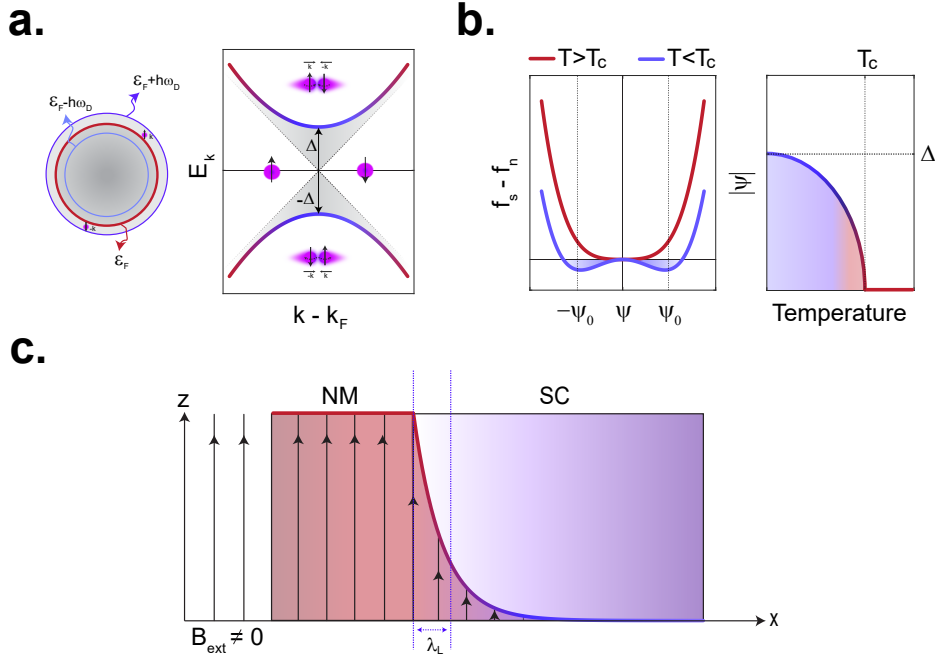


**Figure 2.2:** (a). Left plot: Illustrative condensation of the Cooper pairs with opposite momenta and spin at the Fermi surface via the attractive force due to electron-phonon coupling from BCS model which results in formation of the superconducting gap  $\Delta$ . Right plot: Energy eigenvalues  $E_k$  as a function of  $k$  near the Fermi wave vector  $k_F$ . The grey-dashed lines indicate the energy levels of electron and holes at  $\epsilon_k - \epsilon_F$  and  $\epsilon_F - \epsilon_k$  in the normal metal. In the superconducting state these states become hybridized which leads to opening of a gap  $\Delta$  relative to  $\epsilon_F$  (shown by arrows and grey shading) (b). Left plot: Ginzburg-Landau free energy ( $F_s - F_n$ ) as a function of superconducting order parameter  $\psi$  for  $T > T_c$  (red curve) and  $T < T_c$  (blue curve). Upon phase transition from normal state, two minima in the free energy are developed, minimizing the free energy for the ordered state. right plot: Temperature dependence of superconducting order parameter obtained from GL model. Note that the zero temperature order parameter amplitude  $|\psi_0|^2$  is the same as the superconducting gap  $\Delta$  introduced by BCS. (c). Penetration of magnetic field  $B_{\text{ext}}(z)$  as a function of distance ( $x$ ) inside a normal metal and a superconductor. The magnetic field inside the normal metal (red section) is the same as the external field. In a superconductor, however, the external magnetic field penetration is followed by London's equation and it decays exponentially on the length scale of London's penetration depth  $\lambda_L$ . Panels (a) and (b) are adopted from [114, 116].

## 2.4 Josephson Effect

An important physical phenomenon by which the macroscopic quantum coherence of the superconducting state manifests itself is the **Josephson Effect**. When two superconductors with macroscopic wave functions denoted by  $\psi_1(r, t) = \sqrt{n_{s,1}^*} e^{i\theta_1(r,t)}$  and  $\psi_2(r, t) = \sqrt{n_{s,2}^*} e^{i\theta_2(r,t)}$  are weakly coupled via an insulating barrier as depicted in Fig.2.3(a), the Cooper pairs macroscopic wave function tunnels across the insulating barrier. Due to this tunneling, a zero-voltage current density is established which depends on the phase difference of the macroscopic wave functions on each side of the junction and decays exponentially as a function of the barrier's thickness. This phenomenon was first predicted by Brian D. Josephson in 1962 and the superconductor-insulator-superconductor configuration is therefore known as the **Josephson Junction** [114, 116, 124, 125].

The expression for the tunneling current (also known as the **Josephson current**, and here denoted as  $J_s$ ) which flows through the Josephson junction can be derived by calculating the gauge-invariant phase difference across the junction  $\Delta\theta^*(r, t)$  (from Eq.2.6), assuming that the insulating layer is thin enough to guarantee homogeneous current density throughout the junction. The gauge-invariant phase difference is defined as:

$$\Delta\theta^*(r, t) = \int_1^2 (\nabla\theta(r, t) - \frac{2\pi}{\Phi_0} A(r, t)) \cdot dI = \theta_2(r, t) - \theta_1(r, t) - \frac{2\pi}{\Phi_0} \int_1^2 A(r, t) \cdot dI \quad (2.11)$$

Note that in the absence of an applied voltage across the junction, the third term is zero. We can derive a relationship between the gauge-invariant phase difference and the tunneling current by considering firstly that a  $2\pi$  phase shift in the phase difference obtained from Eq.2.11 must not change the tunneling current across the junction ( $J_s(\Delta\theta^*) = J_s(\Delta\theta^* + 2\pi n)$ ). Also, by symmetry, a reversal in the sign

of  $\Delta\theta^*$  should result in an equal current flowing in the opposite direction across the junction - i.e  $J_s(-\Delta\theta^*) = -J_s(\Delta\theta^*)$ . These two restrictions heavily restrict the functional form of  $J_s(\Delta\theta^*)$ , and further rigorous theoretical treatment can be used to show that:

$$J_s = J_c \sin(\Delta\theta^*) \quad (2.12)$$

This is the **first Josephson equation**, which gives rise to the **DC Josephson effect** whereby the Cooper pairs tunnel through the Josephson junction in the absence of any bias voltage. In Eq.2.12  $J_c = 2K \sqrt{n_{s,1}^* n_{s,2}^*} / \hbar$  is the maximum current density that can flow in the Josephson junction without dissipation, and is called the critical current density.

If now we consider the case where a voltage is applied across the junction, the third term in Eq.2.11 becomes non-zero, and the macroscopic wave functions on either side of the junction become time-dependent, evolving according to Eq.2.4<sup>4</sup>. By substituting the solutions for  $\theta_1(t)$  and  $\theta_2(t)$  into Eq.2.11 and simplifying, it can be shown that:

$$\Delta\theta^*(t) = \Delta\theta^*(0) + \frac{2eVt}{\hbar} \quad (2.13)$$

Where  $V$  is the voltage drop due to the dissipation. By substituting Eq.2.13 into Eq.2.12, the time-dependent current density is obtained:

$$J_s = J_c \sin\left(\Delta\theta^*(0) + \frac{2eVt}{\hbar}\right) \quad (2.14)$$

This is the **second Josephson equation**, which gives rise to the **AC Josephson effect**, in which, in response to a constant applied voltage, an oscillating current density flows through the Josephson junction. In Eq.2.11  $\nu = \frac{2eV}{\hbar}$  is the frequency of this

---

<sup>4</sup>From Eq.2.4 for  $\psi(r, t) = \sqrt{n_s^*(r, t)} e^{i\theta(r, t)}$  it reads:  $-\hbar \frac{\partial \theta}{\partial t} = \frac{1}{2n_s^*} \Lambda J_s^2 + e^* \Phi$

oscillating current which can be rewritten as  $= \frac{2\pi V}{\Phi_0}$  by using the definition of **flux quantum**  $\Phi_0 = \frac{h}{e^*}$ <sup>5</sup> [121, 124–126].

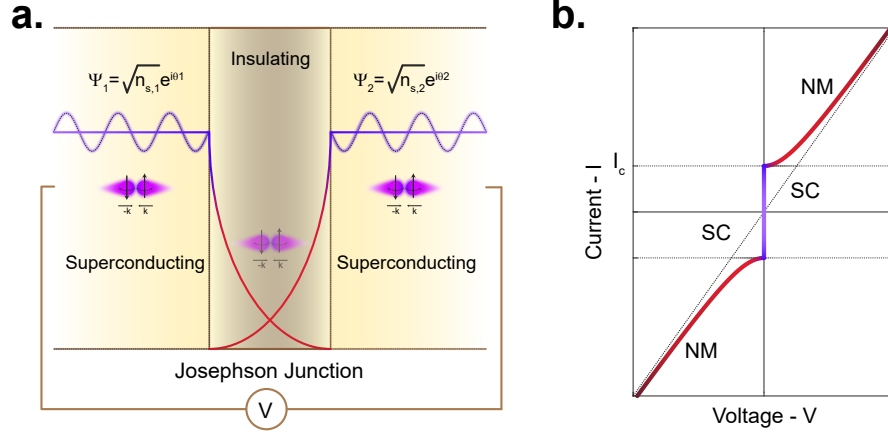


**Figure 2.3:** (a). Schematic of a Josephson junction consisting of two superconducting layers denoted by the macroscopic wave functions  $\psi_1$  and  $\psi_2$ , on the left and right, respectively, separated by an insulating layer. The phase difference of the macroscopic wave functions on each side of the barrier gives rise to tunneling of the supercarriers into the insulating layer (the so-called Josephson current) as described by Eq.2.12. (b). Josephson junction characteristic I-V curve. For  $I < I_c$ , the voltage drop across the junction is zero. For  $I > I_c$ , a voltage drop across the junction is developed which follows the ohmic I-V curve, adapted from [114].

In both the DC and AC Josephson effect, as long as  $J_s < J_c$ , the current flows without dissipation (the resistance is zero). However, as soon as  $J_s > J_c$ , the current density becomes dissipative and follows the ohmic behavior akin to that in a normal metal (see Fig.2.3 (b)).

<sup>5</sup>The experimental observation of the flux quantization was an important verification of the Cooper pairing (the bound state with  $e^* = 2e$  charges) and another manifestation of the complex nature of the superconducting order parameter as an inherently quantum phenomenon [Ref].

## 2.5 sine-Gordon Equation

As shown by the Josephson equations, the variation of the phase of the macroscopic wave function plays a crucial role in the microscopic physics of the Josephson Junction. The spatial and temporal evolution of the phase difference in the Josephson junction determines the dynamics of the current flowing across the junction. This temporal and spatial evolution of the phase can be studied via a nonlinear differential equation known as the *sine-Gordon equation*. In the following, we start with the derivation of the sine-Gordon equation for a single Josephson junction before extending the discussion to an array of Josephson junctions, which we will later see provides a useful model for the study of Cuprate superconductors.

### 2.5.1 Single Josephson Junction

The application of an external magnetic field results in spatial variation of the phase difference across the Josephson junction. From Eq.2.11 and for a magnetic field  $B$  applied perpendicular to the Josephson junction, the spatial variation of the phase is found to be [127, 128]:

$$\nabla_{xy}(\Delta\theta^*) = \frac{2\pi(2\lambda_L + d)}{\Phi_0} B \times \hat{z} \quad (2.15)$$

where the gradient is taken only in the lateral (planar) directions,  $\lambda_L$  is the London penetration depth for an isotropic superconductor,  $d$  is the thickness of the insulating layer and  $\Phi_0$  is the flux quantum defined above. For an applied external current, the total current going through the junction consists of both the Cooper pair tunneling current (2.14) and the ohmic current due to the quasiparticles:  $J_t = J_c \sin(\Delta\theta^*) + \sigma E$ , where  $\sigma$  is the quasiparticle conductivity. Combining the total current  $J_t$  with the Maxwell equation  $\nabla \times B = \frac{4\pi}{c} J_t + \frac{\epsilon}{c} \frac{\partial E}{\partial t}$ , the sine-Gordon

equation for a single Josephson junction is obtained which determines both the spatial and temporal evolution of the phase difference across the junction:

$$\nabla_{xy}^2(\Delta\theta^*) = \frac{1}{\lambda_J^2} \sin(\Delta\theta^*) + \frac{1}{c'^2} \frac{\partial^2(\Delta\theta^*)}{\partial t^2} + \frac{\beta'}{c'^2} \frac{\partial(\Delta\theta^*)}{\partial t} \quad (2.16)$$

Here  $\lambda_J$  is the *Josephson penetration depth*, given by  $\lambda_J^2 = \frac{c\phi_0}{8\pi^2 J_c(d+2\lambda_L)}$  and is typically found to be on the order of several  $\mu\text{m}$  [127, 129].  $c'$  is the *Swihart velocity* given by  $c'^2 = \frac{c^2}{\epsilon(1+2\lambda_L/d)}$ ,  $\beta' = 4\pi\sigma/\epsilon$  [127]. Equation 2.16 is in the form of a wave equation. To solve this equation, we first assume small  $\Delta\theta^*$ , such that  $\sin(\Delta\theta^*)$  can be replaced by  $\Delta\theta^*$ . Furthermore, we search for solutions for which  $\nabla_{xy}^2(\Delta\theta^*) = 0$ , in which case Eq.2.16 reduces to:

$$\frac{1}{\lambda_J^2}(\Delta\theta^*) + \frac{1}{c'^2} \frac{\partial^2(\Delta\theta^*)}{\partial t^2} + \frac{\beta'}{c'^2} \frac{\partial(\Delta\theta^*)}{\partial t} = 0 \quad (2.17)$$

which once again resembles the equation of motion of a damped harmonic oscillator, with  $\Delta\theta^*$  being the coordinate amplitude. An alternative and often used derivation of the Eq.2.14 based on modelling the Josephson junction with an equivalent nonlinear circuit model is given in Eq.B.2 for  $I_{\text{ext}} = 0$  in AppendixB.1. The solutions to the Eq.2.17 are longitudinal oscillations of the Cooper pairs through the Josephson Junction with the characteristic frequency  $\omega_{J,L} = \frac{c'}{\lambda_J}$ .

On the other hand, the solutions to the sine-Gordon equations when  $\nabla_{xy}^2(\Delta\theta^*) \neq 0$ , are transverse oscillations with a frequency of  $\omega_{J,T}$ , arising from the oscillatory motion of the Cooper pairs which is due to the in-plane changes of the phase. These solutions obey the following dispersion relation, where  $k$  is the in-plane wave-vector[127]:

$$\omega_{J,T}^2 = \omega_{J,L}^2 + c'^2 k^2 \quad (2.18)$$

## 2.5.2 Stack of Josephson Junctions

A regular pattern consisting of Josephson junctions interconnected along the z axis, as illustrated in Fig.2.4, is called a **stack of Josephson junctions**. In such a configuration, the behavior of each junction is affected by the neighbouring junctions, resulting in the emergence of collective electrodynamics across the whole stack. Depending on the type of coupling between adjacent junctions, different properties and phenomena may arise. In this section the spatial and temporal variation of the phase across the stack of Josephson junctions will be discussed which is given by the sine-Gordon equation for the case of strong inductive coupling<sup>6</sup>.

As illustrated in Fig.2.4 (a), the phase difference across the  $l$ th junction is determined by the changes in the current from  $l$  and  $l+1$  junction and the in-plane magnetic field contribution already mentioned in Eq.2.15 [127].

$$\nabla_{x,y}^l(\Delta\theta^*) = \frac{8\pi^2\lambda_{xy}^2}{c\Phi_0}(J_{l+1} - J_l) + \frac{2\pi s}{\Phi_0}B \times \hat{z} \quad (2.19)$$

Here  $\lambda_{xy}$  is the lateral magnetic penetration depth. The conservation of charge for in-plane and out-of-plane directions is expressed via the continuity equation  $\frac{\partial\rho}{\partial t} = \nabla \cdot J$ . In the absence of charging effects  $\frac{\partial\rho}{\partial t} = 0$  (i.e. in the strong inductive coupling), hence  $\nabla \cdot J = 0$ . Taking the gradient of both sides of this equation yields;

$$\frac{\partial}{\partial x}(J_{l+1}^x - J_l^x) + \frac{\partial}{\partial y}(J_{l+1}^y - J_l^y) = -\frac{1}{s}\Delta_d J_l^z \quad (2.20)$$

---

<sup>6</sup>In the strong inductive regime assumption, the charging effect is zero  $\frac{\partial\rho}{\partial t} = 0$ .

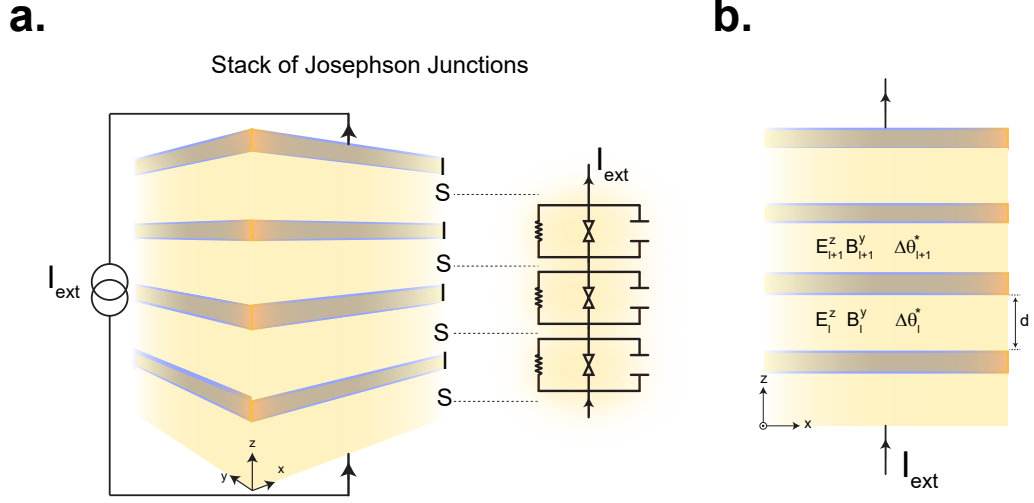


**Figure 2.4:** (a). Schematic of stack of Josephson junctions modeled as coupled RC shunted junctions (see Appendix B.1) where S and I denote the superconducting and insulating layers, respectively.  $I_{\text{ext}}$  is the externally applied current. (b). The schematic view of the stack of Josephson junctions with alternating intrinsic parameters and phase difference denoted by  $\Delta\theta_l^*$ . The electric and magnetic fields (which point in the  $z$  and  $y$  directions) for the  $l$ th layer are denoted by  $E_l^z$  and  $B_l^y$  respectively.

where the terms on the left correspond to spatial variation of the current in the  $xy$  plane and  $\Delta_d J_l^z$  is the discretized version of the second derivative of the tunneling current  $J_l^z$  with respect to  $z$  such that:  $\Delta_d J_l^z = J_{l+1}^z + J_{l-1}^z - 2J_l^z$ .

Here  $s$  denotes the separation between two neighboring junctions. Combining Eqs. 2.19 and 2.20 with Maxwell's equation (as we did in section 2.5.1 when treating the case of a single Josephson junction) then gives the sine-Gordon equation describing the phase dynamics across the stack of Josephson junctions;

$$\nabla_{xy}^2(\Delta\theta_l^*) = \frac{1}{\lambda_z^2} \left( 1 - \frac{\lambda_{xy}^2}{s^2} \Delta_d \right) (\sin(\Delta\theta_l^*) + \frac{4\pi\sigma\lambda_z^2}{c^2} \frac{\partial(\Delta\theta_l^*)}{\partial t} + \frac{\lambda_z^2}{c^2/\epsilon} \frac{\partial^2(\Delta\theta_l^*)}{\partial t^2}) \quad (2.21)$$

Note that for the stack of Josephson Junctions, the Swihart velocity reduces to  $c^2 = c^2/\epsilon$ . For typical layered superconductors which will be discussed in the present study,  $\lambda_{xy} \approx 400$  nm and  $\lambda_z \approx 200$   $\mu$ m and the Josephson penetration depth is modified as:  $\lambda_J = s\Gamma$  - where  $\Gamma = \frac{\lambda_z}{\lambda_{xy}}$  is the anisotropy factor [127].

Following the same argument discussed in section 2.5.1, the solutions to the Eq.2.21 can be found for small amplitudes which take the form of plane waves  $\Delta\theta^* \approx \Delta\theta_0^* e^{i(\vec{q}\cdot\vec{r}-\omega t)}$  known as **Josephson plasma waves** which are oscillatory pattern of Cooper pairs propagating along the stack of Josephson junctions either in the in-plane direction (*transverse mode* -  $q_z = 0, q_x, q_y \neq 0$ ) or in the out-of-plane direction (*longitudinal mode* -  $q_x = q_y = 0, q_z \neq 0$ ) as displayed in Figs.2.5 (a) and (b). The dispersion relation for the transverse plasmon modes is given below:

$$\omega^2 = \omega_J^2 + \frac{c^2}{\epsilon} q_x^2 \quad (2.22)$$

where the  $\omega_J^2 = c^2/\lambda_z^2\epsilon$ .

In some cases, the charging effect of the superconducting layers cannot be neglected ( $\frac{\partial\rho}{\partial t} \neq 0$ ) which then results in a capacitive coupling between the adjacent junctions and hence dispersion for the propagating longitudinal mode along the out-of-plane direction as shown in Eq.2.23. In most cases, since  $\lambda_{xy} \ll \lambda_z$ , the longitudinal modes disperse much less than the transverse modes.

$$\omega^2 = \omega_J^2 + \frac{c^2}{\lambda_z^2/\mu^2} q_z^2 \quad (2.23)$$

Here  $\mu$  is the *Debye length*. For negligible charging effect (thicker superconducting layers)  $\mu \approx 0$  and hence the longitudinal mode does not have dispersion, as was the case for the single Josephson junction [127, 130].

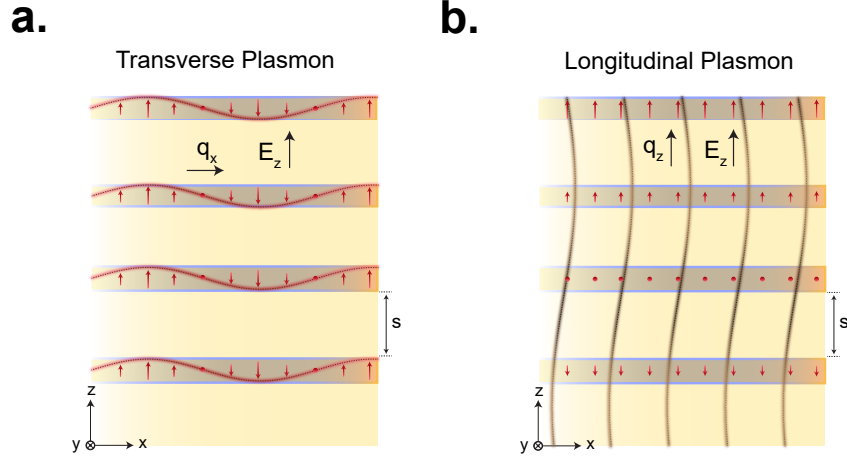


**Figure 2.5:** (a). Schematic illustration of transverse Josephson plasma oscillations in the stack of Josephson junctions. The propagation direction of the oscillating supercarriers and the applied electric field is denoted by  $q_x$  and  $E_z$ , respectively. (b). Same as in (a) but for longitudinal oscillations. The propagation direction of the oscillating supercarriers and the applied electric field is denoted by  $q_z$  and  $E_z$ , respectively. Figure adapted from [131]

## 2.6 Optical Signatures of Josephson Plasma Waves

High- $T_c$  Cuprate superconductors, which will form the subject of the rest of this thesis, can be modeled as a stack of Josephson junctions. Hence, by deriving the optical properties of such a stack of Josephson junctions, we can form an understanding of the characteristic optical features of Cuprates.

### 2.6.1 Single-layer System Optical Properties

Here, we begin by calculating the macroscopic complex dielectric function  $\epsilon(\omega)$  for a stack with uniform spacing, denoted by  $d$ , between each Josephson junction. This configuration is referred to as a single-layer system (see Fig.2.6(a)), because every individual layer in the stack is identical. The electrodynamics of such a system was already discussed in section 2.5.2. For each individual junction consisting of two

neighboring planes, the complex impedance  $Z_m$ , and hence the complex optical conductivity  $\sigma_m$ , is calculated [132, 133]. Accordingly, the complex dielectric function  $\epsilon_m = \frac{4\pi\sigma_m i}{\omega}$  can be written as in Eq.2.24, which includes the inductive response of the supercarriers (first term) as well as the resistive response of the quasiparticles (second term).

$$\epsilon_m = \epsilon_\infty \left(1 - \frac{\omega_{J,m}^2}{\omega^2}\right) + \frac{4\pi i \sigma_{qp,m}}{\omega} \quad (2.24)$$

Here  $\omega_{J,m}$  is the Josephson plasmon frequency corresponding to junction  $m$  and is proportional to the supercarrier density  $\sqrt{n_{s,m}^*}$ .  $\sigma_{qp,m}$  denotes the quasiparticle complex conductivity and is given by the Drude expression  $\sigma_{qp,m} = \frac{\sigma_{0,m}}{(1-i\omega\gamma_m)}$ . For a stack of Josephson junctions of length  $D$ , the macroscopic complex dielectric function is derived as follows;

$$\begin{aligned} \epsilon &= \left(\sum_m \frac{\alpha_m}{\epsilon_m}\right)^{-1} \\ &= \epsilon_\infty \left(1 - \frac{\omega_J^2}{\omega^2} - \frac{\omega_{qp}^2}{\omega(\omega + i\gamma)}\right) \end{aligned} \quad (2.25)$$

where  $\alpha_m$  is the weighting factor proportional to the separation of the planes and is given by;  $\alpha_m = \frac{d_m}{D}$ ,  $\omega_J$  is the longitudinal plasmon frequency,  $\omega_{qp} = \sqrt{4\pi\sigma_0}$  is the normal plasmon frequency and  $\gamma$  is the quasiparticles scattering rate [132–134].

The optical properties of a single-layer system including the real ( $\epsilon_1$ ) and imaginary ( $\epsilon_2$ ) parts of the complex dielectric function, the loss function ( $\text{Im}\{-1/\epsilon(r)\}$ ) and the reflectivity, are shown in Fig.2.6(c). In the limit of small quasiparticle density ( $n_n \rightarrow 0$ ), and hence  $\gamma \rightarrow 0$ , the dielectric function given by Eq.2.24 reduces to only the inductive response of the supercarriers:  $\epsilon = \epsilon_\infty \left(1 - \frac{\omega_J^2}{\omega^2}\right)$ . The plasmon modes of this system correspond to the solutions of the Sine Gordon equation derived in section 2.5.2, with the dispersion relations given by Eqs.2.22 and 2.23. Figure.2.7(a)

## 2.6. Optical Signatures of Josephson Plasma Waves

and (b) display the dispersion plots for the transverse and longitudinal plasmon-polariton branches, respectively.

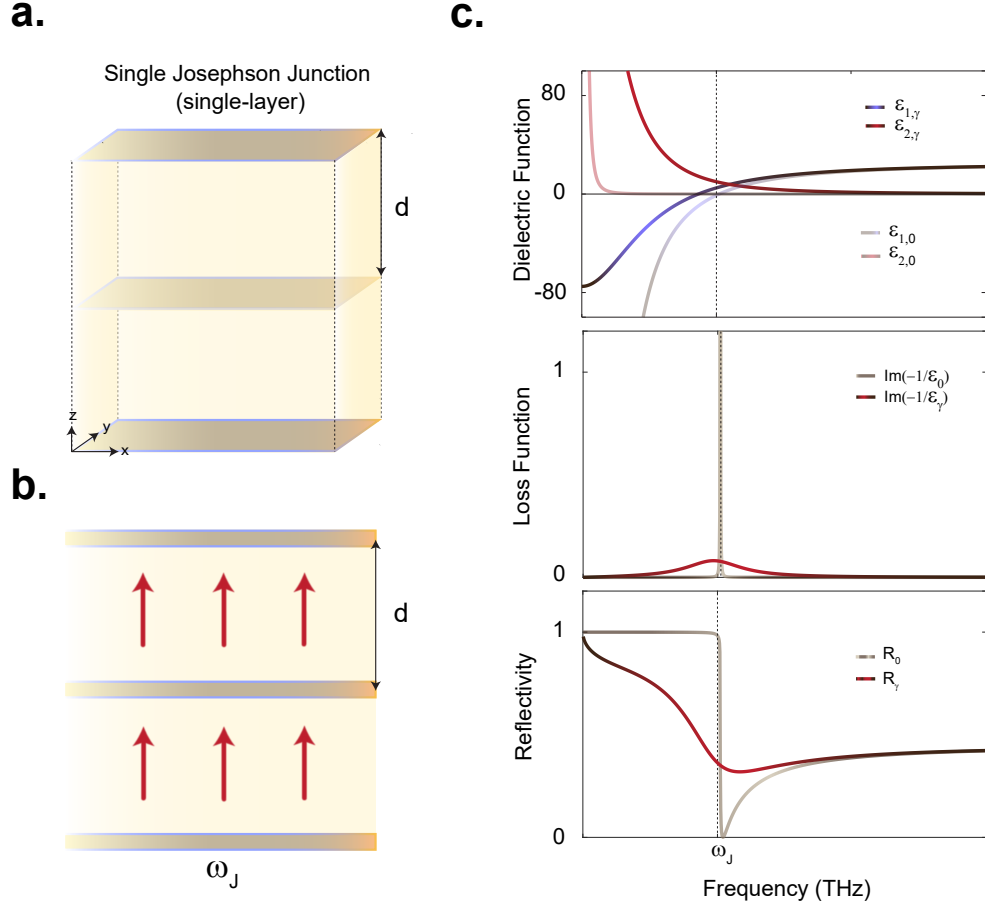


**Figure 2.6:** (a). The schematic of a stack of uniformly spaced Josephson junctions with  $d$  indicating the spacing, resembling the single-layer Cuprate superconductors. (b). The superconducting current flowing across the coupled junctions (along the  $z$ -axis) in the single-layer system with the Josephson plasmon frequency of  $\omega_J$ . (c). From top to bottom: simulated real and imaginary parts of complex dielectric function using Eq.2.26, loss function ( $\text{Im}\{-1/\epsilon(r)\}$ ) and reflectivity, for two limits of small dissipation, denoted by subscript 0 (light-shaded curves) and large dissipation, denoted by subscript  $\gamma$  (dark-shaded curves), respectively.

**Figure 2.6:** Bottom plot: Reflectivity of the single-layer system for the limits of negligible (in grey) and non-negligible (in red) dissipation. The Josephson plasmon frequency appears at the frequency where  $\text{Re}\{\epsilon(\omega)\} = 0$  which gives rise to a peak in the loss function and an edge in the reflectivity.

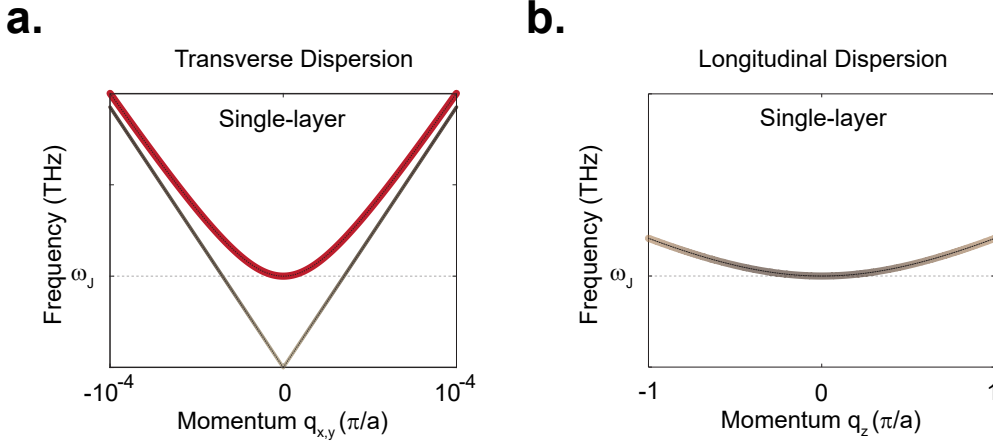


**Figure 2.7:** (a). Exemplary dispersion branch of the transverse Josephson plasmon-polariton mode for the single-layer system simulated using Eq.2.22. (b). Same as in (a), this time for the longitudinal branch, simulated using Eq.2.23.

---

### 2.6.2 Bi-layer System Optical Properties

The model discussed in section 2.6.1 for the single-layer system can easily be extended to a bi-layer system, where the spacing between the alternating coupled junctions varies as indicated by  $d_1$  and  $d_2$  and shown in Fig.2.8(a). This geometrical difference, compared to the single-layer case, not only modifies the coupling between the junctions and hence the overall optical properties, but also gives rise to a new transverse excitation between the coupled junctions. Figure.2.8(b) demonstrates all of the different types of plasma excitations which exist in the bi-layer coupled system [132, 135]. The total complex dielectric function for the bi-layer

system is derived using Eqs.2.24, which reads:

$$\begin{aligned}\epsilon(\omega) &= \left(\frac{\alpha_1}{\epsilon_1} + \frac{\alpha_2}{\epsilon_2}\right)^{-1} \\ &= \left(\frac{\alpha_1}{1 - \frac{\omega_{J1}^2}{\omega^2} - \frac{\omega_{qp,1}^2}{\omega(\omega+i\gamma_1)}} + \frac{\alpha_2}{1 - \frac{\omega_{J2}^2}{\omega^2} - \frac{\omega_{qp,2}^2}{\omega(\omega+i\gamma_2)}}\right)^{-1}\end{aligned}\quad (2.26)$$

where  $\alpha_1$  and  $\alpha_2$  are the weighting factors for the junctions with spacing  $d_1$  and  $d_2$ , respectively, and  $\epsilon_1$  and  $\epsilon_2$  are calculated using Eq.2.24. In the superconducting state, assuming no dissipation due to quasiparticles, the third term in the denominator of Eq.2.26 will be zero and therefore Eq.2.26 reduces to [132, 136]:

$$\epsilon(\omega) = \frac{\epsilon_\infty(\omega^2 - \omega_{J1}^2)(\omega^2 - \omega_{J2}^2)}{\omega^2(\omega^2 - \omega_{JT}^2)} \quad (2.27)$$

The frequencies  $\omega_{J1}$  and  $\omega_{J2}$  are longitudinal Josephson plasmon frequencies which correspond to the zero crossings of the real part of the complex dielectric function (and equivalently peaks in the loss function) and appear as edges in the reflectivity.  $\omega_{JT}$  is the transverse optical plasmon frequency and is given by:  $\omega_{JT}^2 = (d_2\omega_{J1}^2 + d_1\omega_{J2}^2)/(d_1 + d_2)$  [132, 136]. Figure 2.8(c) summarizes the optical properties of the bi-layer system for both negligible and large dissipation, with light and dark coloured curves, respectively. As shown, the reflectivity is modified close to the frequency of the transverse plasmon along with a peak in the imaginary part of the complex dielectric function at  $\omega_{JT}$ . The reflectivity is close to unity throughout the frequency range from  $\omega_{JT}$  to  $\omega_{J2}$ , as the fields are effectively screened. This closely resembles the Reststrahlen band phenomenon discussed for TO and LO phonon modes in sections 1.3 and 1.5.

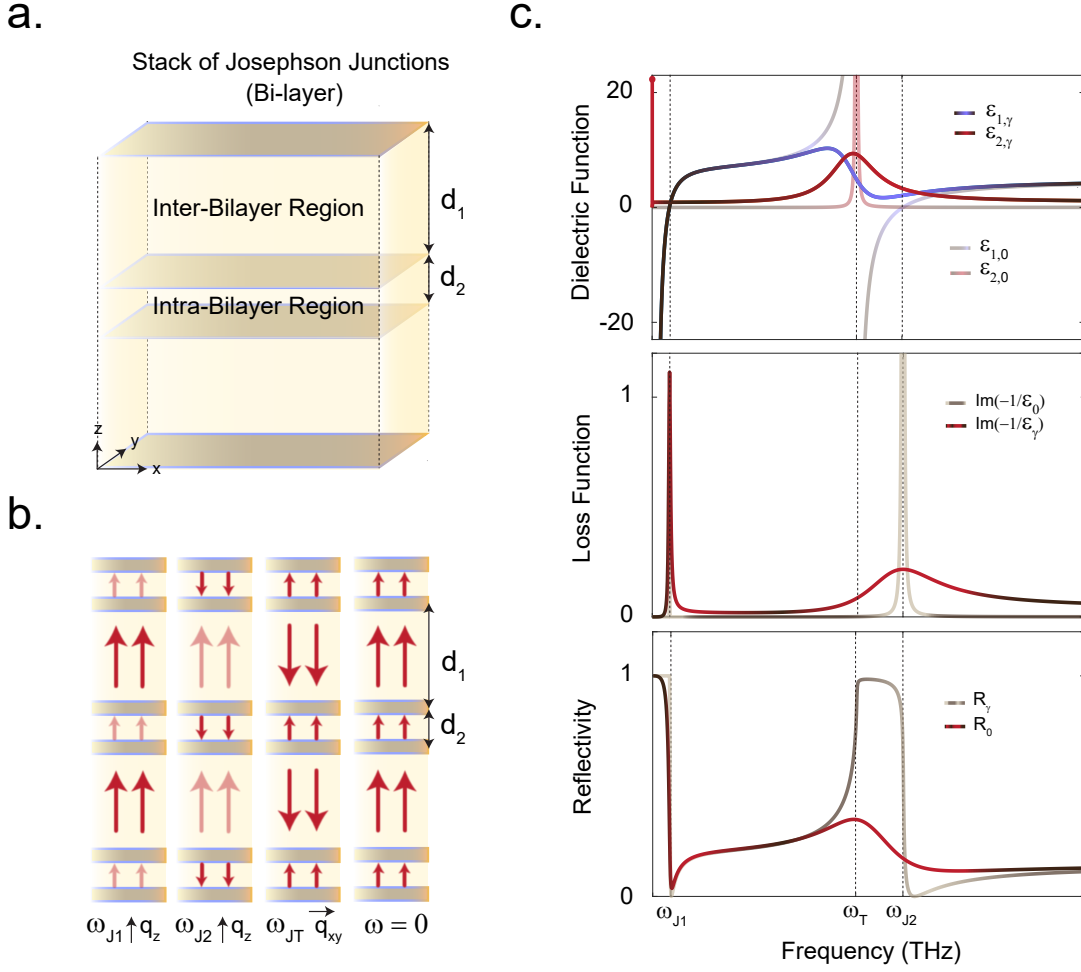


**Figure 2.8:** (a). Schematic of a bi-layer system, made of alternating coupled Josephson junctions with separations denoted by  $d_1$  and  $d_2$ . (b). Snapshots of the longitudinal (denoted by frequencies  $\omega_{J1}$  and  $\omega_{J2}$ ) and transverse Josephson plasmon (denoted by frequencies  $\omega_{JT}$  and  $\omega = 0$ ) currents (red arrows), denoted by  $\omega_{J1}$  and across the intrinsic Josephson junctions, along the  $z$  direction, perpendicular to the coupled junctions. (c). From top to bottom: simulated real and imaginary parts of complex dielectric function using Eq.2.26, loss function ( $\text{Im}\{-1/\epsilon(r)\}$ ) and reflectivity, for two limits of small dissipation, denoted by subscript 0 (light-shaded curves) and large dissipation, denoted by subscript  $\gamma$  (dark-shaded curves), respectively.

To generalize the optical responses of the bi-layer system to finite-momentum, same as in the case of single-layer system, the solutions to the sine-Gordon equation given

## 2.6. Optical Signatures of Josephson Plasma Waves

---

in Eq.2.21 must be found. The solutions are again plain plasma waves in the form of  $\Delta\theta^* \approx \Delta\theta_0^* e^{i(\vec{q}\cdot\vec{r}-\omega t)}$ . In the presence of electromagnetic fields with the electric field oriented along the z-direction, and for the case of strong inductive coupling between adjacent layers, the transverse solutions ( $q_z = 0, q_{x,y} \neq 0$  - *transverse configuration*) can be written as in Eq.2.28. For a full description of this modelling and the corresponding solutions see Ref.[137].

$$\omega^2(q_{xy}) = \left( \frac{\omega_{J1}^2 + \omega_{J2}^2 + q_{xy}^2 c^2 / \epsilon_\infty}{2} \right) \pm \sqrt{\left( \frac{\omega_{J1}^2 + \omega_{J2}^2 + q_{xy}^2 c^2 / \epsilon_\infty}{2} \right)^2 - \omega_{J1}^2 \omega_{J2}^2 - c^2 q_{xy}^2 / \epsilon_\infty} \quad (2.28)$$

Eq.2.28 represents two dispersion branches for the two Josephson plasmon modes  $\omega_{J1}$  and  $\omega_{J2}$  (derived earlier for zero momentum from the circuit model) which are associated with the variation of the order parameter phase in the lateral direction as illustrated in Fig.2.9(a). As shown, both upper and lower Josephson plasma-polariton branches experience a strong dispersion with  $q_{x,y}$ . Accordingly, the two Reststrahlen band regions which are indicated by grey shading, start from zero up to  $\omega_{J1}$  and  $\omega_{JT}$  up to  $\omega_{J2}$ , respectively (see also the reflectivity in Fig.2.8 (c)) [137, 138].

Similarly, the longitudinal solutions ( $q_{xy} = 0, q_z \neq 0$  - *longitudinal configuration*) give rise to two upper and lower plasmon-polariton branches, although these exhibit almost no dispersion (see Fig.2.9 (b)). These longitudinal modes correspond to the in-phase ( $\omega_{J1}$ ) and out-of-phase ( $\omega_{J2}$ ) solutions to the sine-Gordon equation for this configuration which are referred to as *inter-bilayer* ( $\omega_{J1}$ ) and *intra-bilayer* ( $\omega_{J2}$ ) Josephson plasmon modes for  $\omega_{J1}$  and  $\omega_{J2}$ .

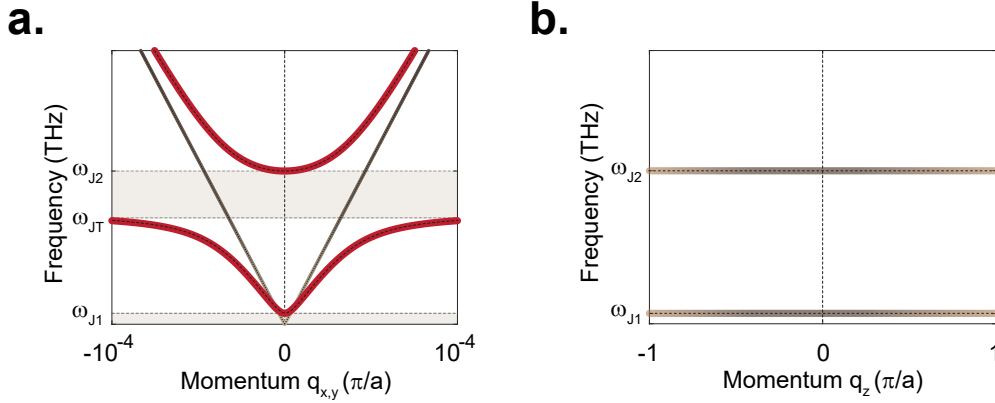


**Figure 2.9:** (a). Dispersion plot of the Josephson plasmon-polaritons of the bi-layer system in the in-plane direction ( $xy$ ) plane (red curves) and the dispersion of light (in grey lines). The grey shading indicates the Reststrahlen band. (b). Same as in (a), this time along the out-of-plane direction ( $z$ ), showing almost no dispersion across the whole range as oppose to the transverse configuration.

The microscopic physics and the optical properties of the stack of Josephson junctions discussed so far provide a basis for understanding the physics of one of the most mysterious, and complex classes of high- $T_c$  superconductors, the Cuprate compounds. A general overview of this class of materials will be given in the next chapter [137, 138].

### 2.6.3 Summary and Outlook

In this chapter we reviewed the fundamental physics of the superconducting state. We pointed out that, regardless of the microscopic pairing mechanism, the concept of the complex order parameter can be used to describe the macroscopic superconducting properties in both conventional and unconventional superconductors. Within this framework, the Cooper pairing and phase coherence as equally important ingredients for the establishment of macroscopic superconducting order were discussed, presenting the possibility that some compounds may host pre-formed,

## 2.6. *Optical Signatures of Josephson Plasma Waves*

---

phase in-coherent pairs above  $T_c$  with an important example being  $\text{YBa}_2\text{Cu}_3\text{O}_{6+x}$ .

Finally, the Josephson physics were introduced, and the optical properties of stacks of Josephson junctions were derived, along with the plasmon dispersion relations for such a medium. In the following chapters, we will relate the optical properties derived here for this model system, to the experimentally-measured c-axis optical properties of Cuprate superconductors, including  $\text{YBa}_2\text{Cu}_3\text{O}_{6+x}$ . The physics of the Josephson plasma waves particularly become important in the chapter 6, where we discuss a theoretical model which can describe the experimental results measured in  $\text{YBa}_2\text{Cu}_3\text{O}_{6+x}$  which will be presented in Chapters 3, 4 and 5.

# Chapter 3

## Photo–induced Superconductivity in $\text{YBa}_2\text{Cu}_3\text{O}_{6+x}$

### 3.1 Introduction

In recent years, superconducting-like properties have been transiently induced and observed in the compound  $\text{YBa}_2\text{Cu}_3\text{O}_{6+x}$  at temperatures far above  $T_c$  upon resonantly exciting certain IR-active c-axis phonon modes using intense pulses of mid-infrared light [22, 64–67]. The region of the phase diagram in which the non-equilibrium superconducting-like state has been observed in this compound coincides with that of the pseudogap phase where, even in equilibrium, indications of phase fluctuating pre-formed Cooper pairs have been observed experimentally via various probing techniques [41, 43–45, 48, 49, 51–54, 139, 140].

In this chapter, we begin with a general introduction to Cuprate physics and specifically the  $\text{YBa}_2\text{Cu}_3\text{O}_{6+x}$  family of compounds. Then we will focus on the equilibrium c-axis optical properties of two doping levels of  $\text{YBa}_2\text{Cu}_3\text{O}_{6+x}$ , which are the doping levels discussed in the rest of this thesis, restricting the discussion to those aspects

which appear to be most relevant to the non-equilibrium experiments. This is followed by an overall review of the non-equilibrium experiments in  $\text{YBa}_2\text{Cu}_3\text{O}_{6.48}$  in which macroscopic signatures of photo-induced superconductivity have been observed at temperatures above  $T_c$ .

## 3.2 High $T_c$ Cuprates Layered Superconductors

According to the BCS theory of superconductivity, one of the determining factors for increasing the transition temperature of the superconducting state is a large electron-phonon coupling, which is limited in conventional metallic superconductors due to excessive screening [114, 141]. The journey took a pivotal turn when Bednorz and Müller (1987 Nobel prize winners) made their ground-breaking discovery of high- $T_c$  superconductivity in the copper oxide compounds known as Cuprates [4, 5], where the mechanism of high- $T_c$  superconductivity defies explanation by conventional BCS theory.

The first Cuprate superconductor to be discovered was  $\text{La}_{2-x}\text{Ba}_x\text{CuO}_4$ , which exhibited a sudden drop in resistivity upon cooling below 35 K, accompanied by a Meißner effect. Although the  $\text{La}_{2-x}\text{Ba}_x\text{CuO}_4$  compound was the first high- $T_c$  superconductor to be discovered, its  $T_c$  would soon be dramatically surpassed by other Cuprate compounds. Following this initial discovery, more classes of Cuprate superconductors including compounds such as  $\text{YBa}_2\text{Cu}_3\text{O}_{6+x}$ , with a maximum  $T_c = 91$  K, and  $\text{HgBa}_2\text{Cu}_3\text{O}_{8+\delta}$  with  $T_c = 135$  K (the highest  $T_c$  for any superconductor at ambient pressure known to date) were discovered [141–143].

### 3.2.1 General Properties of Cuprates

Cuprate superconductors have a quasi-two dimensional layered perovskite structure in which the layers consist of conductive  $\text{CuO}_2$  planes, spaced by insulating blocks, and thus naturally form a stack of Josephson junctions. Consequently, their physics can be well modeled and explained by the same physics discussed in section 2.6. Depending on the number of unique  $\text{CuO}_2$  planes per unit cell, the compounds are referred to as single-layer ( $\text{L}_{2-x}\text{Sr}_x\text{CuO}_4$ ), bi-layer ( $\text{YBa}_2\text{Cu}_3\text{O}_{6+x}$ ) or tri-layer ( $\text{Hg}_{1-x}\text{Tl}_x\text{Ba}_2\text{Ca}_2\text{Cu}_3\text{O}_7$ ) [141], as depicted in the Fig.3.1(a).

The generic phase diagram of the Cuprates is shown in Fig.3.1(b). The undoped Cuprate parent compounds are anti-ferromagnetic with a high Néel temperature  $T_N$  (typically 300-500 K) [141]. Upon chemical doping (either electron or hole), the antiferromagnetic order is suppressed and superconducting order emerges with the transition temperature indicated by  $T_c$ . However, there is experimental evidence which points towards residual spin fluctuations surviving up to much higher doping levels, which might be an important ingredient in the formation of high- $T_c$  superconductivity in these compounds [144–161].

As the doping level is increased, the superconducting critical temperature is enhanced, reaching a maximum, before decreasing again. The doping with the highest  $T_c$  is called *optimally doped*. The compounds with doping levels below and above the optimum doping are called *underdoped* and *overdoped* compounds, respectively [3].

The electronic structure of cuprate compounds is determined though the strong interaction between the localized and itinerant electrons. In particular, the configuration of the oxygen and copper atoms in the  $\text{CuO}_2$  planes, which are the defining common characteristic of all the cuprates, give rise to hybridization between their

### 3.2. High $T_c$ Cuprates Layered Superconductors

---

orbitals [141]. As shown in Fig.3.1(c), the oxygen and copper orbitals are very close in energy which results in a strong  $pd\sigma$  orbital bonding between the Cu 3d ( $d_{x^2-y^2}$ ) orbital and O 2p ( $p_x$  and  $p_y$ ) orbitals, forming the governing electronic structure of these compounds [162, 163] (see Fig.3.1(d) upper panel).

The bandwidth of this hybridization is sensitive to the doping level. Whilst such electronic structure would normally be expected to give rise to metallic behavior, the undoped parent compounds are instead found to be insulating. This is because the Coulomb repulsion on the Cu 3d sites is much bigger than the hybridization bandwidth. Upon doping, the bandwidth increases, overcoming the Coulomb repulsion and resulting in metallic behavior in the overdoped region. In the underdoped region, above  $T_c$  and below certain temperature denoted as  $T^*$ , the cuprates exhibit anomalous physical properties coinciding with the opening of a gap in the electronic spectrum known as normal state *Pseudogap* [3, 55, 141, 162]. The Pseudogap is described in more detail below.

In the superconducting state below  $T_c$ , the measurement of flux quantization and Josephson effects directly confirmed the presence of bound Cooper pairs, regardless of the exact pairing mechanism, which is known to differ from conventional BCS pairing, but remains a source of debate [164–171]. The phase sensitive measurements such as scanning tunneling microscopy and scanning tunneling spectroscopy [141, 172] as well as ARPES measurements [42, 55, 173–175] demonstrated a *d-wave symmetry* for the superconducting gap with  $B_{1g}$  or  $B_{2g}$  symmetry, which has a lower symmetry than the Fermi surface and conventional *s-wave* superconductors with  $A_{1g}$  symmetry [141], as shown in Fig.3.2 (a) bottom panel. Unlike an *s-wave* gap, the *d-wave* gap changes sign for different  $k$  values and exhibits nodes along the diagonal lines and antinodes on the edges of the Fermi surface in the Brillouin zone [55, 141].

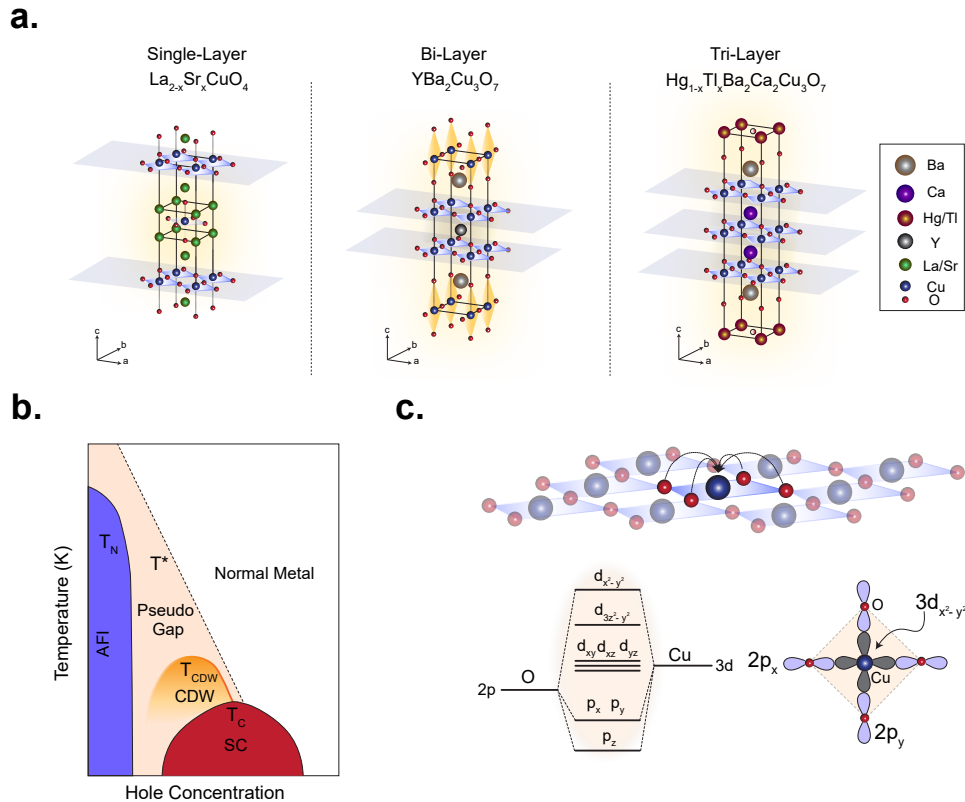


**Figure 3.1:** (a). Exemplary Cuprate systems with one, two and three  $\text{CuO}_2$  planes per unit cell, respectively, which are separated by insulating layers. (b). Schematic of typical temperature versus chemical hole-doping phase diagram of the cuprate compounds, various competing phases emerge from the anti-ferromagnetic parent compound. (c). Schematic of the conductive  $\text{CuO}_2$  planes. Schematic energy diagram for Cu 3d ( $d_{x^2-y^2}$ ) and O 2p ( $p_x$  and  $p_y$ ) orbitals. Strong orbital hybridization between Cu 3d and O 2p orbitals forms the governing electronic structure of these compounds.

**Pseudogap phase:** ARPES experiments have revealed that, for nearly all Cuprates, near the antinodal region, there can be found two co-existing energy scales [176] (see Fig.3.2 (b)). As shown, a sharp feature is measured at low energies, associated with the superconducting gap, on top of a broader feature which appears at higher energies, associated with the so-called pseudogap. The superconducting gap closes at  $T_c$ , whilst the pseudogap persists up to much higher temper-

### 3.2. High $T_c$ Cuprates Layered Superconductors

atures and eventually closes at  $T^*$ . The value of  $T^*$  is strongly doping-dependent such that in the heavily underdoped region it has a higher value, but gradually decreases with increasing doping and approaches  $T_c$  close to the optimum doping level [3, 42, 55, 141]. The presence of the pseudogap can also be observed via an unusual dependence of both the in and out-of-plane resistivity curves as a function of temperature [50, 52, 177].

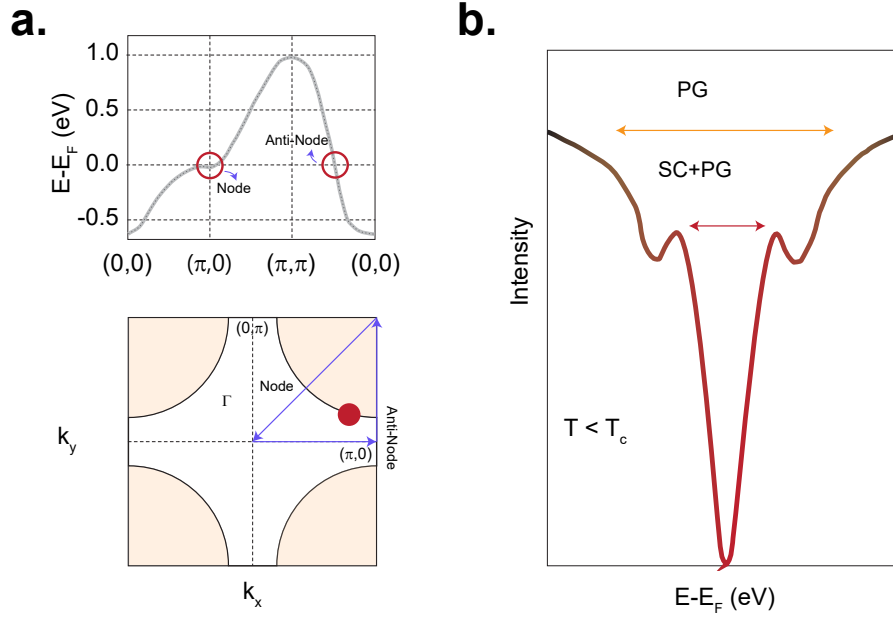


**Figure 3.2:** (a). Top plot: Cuprates reciprocal space band dispersion along the light blue arrows shown in the bottom plot. Red circles indicate the anti-node and node points, respectively. Bottom plot: Cuprates Fermi surface where the nodes and anti-nodes are determined. The pseudogap is identified in the anti-nodal region. (b). ARPES data measured in the most studied Cuprate compound  $\text{Bi}_2\text{Sr}_2\text{CaCu}_2\text{O}_{8+x}$  close to anti-nodal region at the Fermi surface below  $T_c$  which is shown by the red circle in (a) bottom plot. The lower energy sharp feature indicated by red arrow is associated with the superconducting gap and the broader higher energy feature is associated with the pseudogap. When measured above  $T_c$ , the superconducting gap closes whereas the pseudogap persists, representing two different temperature scales for the two gaps. This figure is adapted from [45, 173, 174].

Based on various experimental results [41–50, 52–55, 178], the pseudogap has been interpreted either as a precursor to superconductivity or as a new competing

order. Intriguingly, Nernst experiments have demonstrated residual superconducting vortices at temperature range above  $T_c$  [178], suggesting that even in the absence of phase coherence, fluctuating preformed Cooper pairs could be present in this temperature range, within the pseudogap region. This experimental evidence further supports the discussion in section 2.3 and in Refs.[118, 170, 179], which points towards thermal fluctuations of the phase, rather than depairing, being the relevant energy scale which determines  $T_c$  for these compounds.

Taken together, this is suggestive of a temperature scale above  $T_c$  which hosts pre-existing, phase-fluctuating Cooper pairs, especially in the compounds which exhibit a strong pseudogap, such as underdoped  $\text{YBa}_2\text{Cu}_3\text{O}_{6+x}$ .

## 3.3 Equilibrium Properties of $\text{YBa}_2\text{Cu}_3\text{O}_{6+x}$

### 3.3.1 Crystal Structure and Phase Diagram

$\text{YBa}_2\text{Cu}_3\text{O}_{6+x}$  single crystals are typically grown using a top-seeded solution growth method in Y-stabilized  $\text{ZrO}_2$  crucibles [180, 181]. To enable hole doping, the crystals are first annealed in an oxygen-rich environment and then rapidly cooled, facilitating controlled oxygen uptake [182, 183]. Upon doping, the compound undergoes a structural transformation from a tetragonal phase (in its undoped, parent state) to an orthorhombic structure, maintaining its center of symmetry. This transition coincides with changes in electronic behavior: the material evolves from an insulating, non-metallic state to a superconducting phase and ultimately to a metallic state, depending on the extent of doping [183]. The phase diagram of  $\text{YBa}_2\text{Cu}_3\text{O}_{6+x}$  is shown in Fig.3.3 (a).

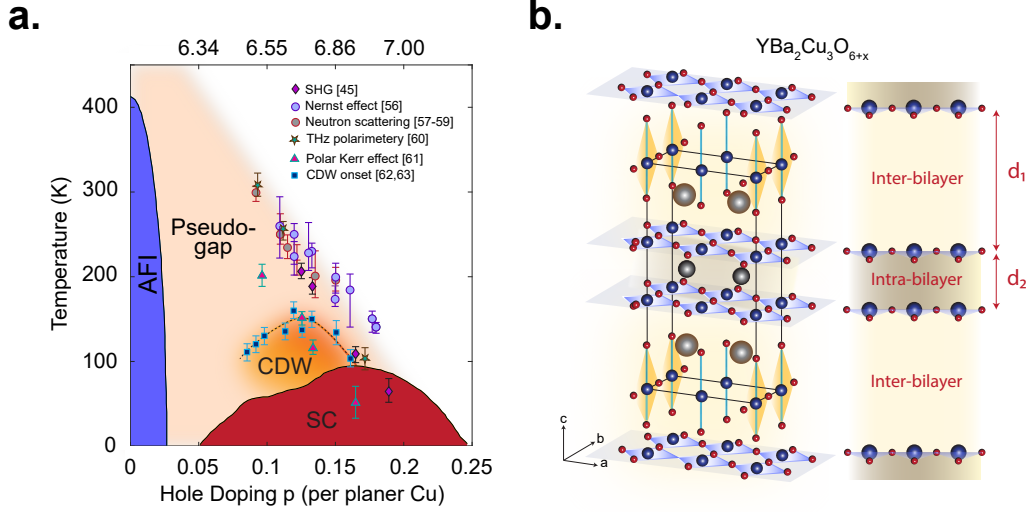


**Figure 3.3:** (a). Phase diagram of the hole-doped  $\text{YBa}_2\text{Cu}_3\text{O}_{6+x}$ . The light-range shading indicates the pseudogap phase in the underdoped region with the corresponding temperature scale denoted by  $T^*$ , determined by different probes. Error bars denote the uncertainty in the onset temperatures. (b).  $\text{YBa}_2\text{Cu}_3\text{O}_{6+x}$  orthorhombic unit cell. The  $\text{CuO}_2$  layers are separated by insulating layers including Yttrium (intra-bilayer) and charge reservoir layers containing Barium atoms (inter-bilayer). The doping of the  $\text{YBa}_2\text{Cu}_3\text{O}_{6+x}$  compounds is varied by the oxygen concentration of the inter-bilayer region along the chains. As shown to the right, the structure resembles the two coupled Josephson junctions with different spacing denoted by  $d_1$  and  $d_2$  (see also Fig.2.8).

In  $\text{YBa}_2\text{Cu}_3\text{O}_{6+x}$ , superconductivity occurs primarily within the  $\text{CuO}_2$  planes, while the Cu-O chains serve as charge reservoirs. Oxygen doping targets these Cu-O chains, which, through charge transfer mechanisms, control the electron density in the  $\text{CuO}_2$  planes. This charge modulation directly impacts the material's electronic and superconducting properties, including the critical temperature ( $T_c$ ), which strongly depends on the doping level [183]. In optimally doped compound, the anisotropic superconducting gap observed near the nodal region of the Fermi surface is around 7 THz, [184–186] which has been observed to increase as the doping is lowered [187].

In this bi-layer system, the two superconducting  $\text{CuO}_2$  planes separated by insulat-

ing Y atoms in the intra-bilayer region (with spacing  $d_2 \approx 4 \text{ \AA}$ ) and Cu-O chains in the inter-bilayer region (with spacing  $d_1 \approx 8 \text{ \AA}$ ), form the two coupled Josephson junctions (see Fig.3.3 (b)). Therefore, the c-axis optical properties of  $\text{YBa}_2\text{Cu}_3\text{O}_{6+x}$  compounds can be understood based on the model presented in section 2.6.2. In the rest of this thesis the discussion is mainly focused on the equilibrium and non-equilibrium optical responses of  $\text{YBa}_2\text{Cu}_3\text{O}_{6.48}$ , which has a critical temperature of  $T_c \approx 50 \text{ K}$  and a pseudogap which closes at a temperature of  $T^* \approx 380 \text{ K}$ .

### 3.3.2 THz c-axis Optical Properties

The superconducting transition is characterized by the transfer of spectral weight in the real part of the optical conductivity  $\sigma_1(\omega)$  from finite frequencies into a delta function at zero frequency, which corresponds to the infinite mobility of the supercarriers [188, 189]. Through Kramers-Kronig relations, this delta function also results in a  $1/\omega$  divergence in the imaginary part of the optical conductivity  $\sigma_2(\omega)$  approaching low frequencies, the coefficient of which is proportional to the number of supercarriers [190, 191]. In the case of  $\text{YBa}_2\text{Cu}_3\text{O}_{6+x}$ , these superconducting optical signatures are accompanied by a plasma edge in the low-frequency THz reflectivity, which also on-sets as the temperature crosses below  $T_c$  and is not present for temperatures above  $T_c$  (see also Fig.3.5(a) for more temperatures) [48, 64–66]. The c-axis equilibrium THz optical properties of  $\text{YBa}_2\text{Cu}_3\text{O}_{6.5}$  measured via THz spectroscopy below and above  $T_c$ , are shown in Fig.3.4 [65].

Here the low-frequency plasma edge observed in the reflectivity below  $T_c$  corresponds to the longitudinal Josephson plasmon frequency, associated with the inter-bilayer tunneling current ( $\omega_{\text{JP1}}$ ) [132, 133, 137, 138] and for the 6.5 doping is at the frequency of  $0.9 \text{ THz}$  ( $30 \text{ cm}^{-1}$ ) [48, 49, 64, 65].

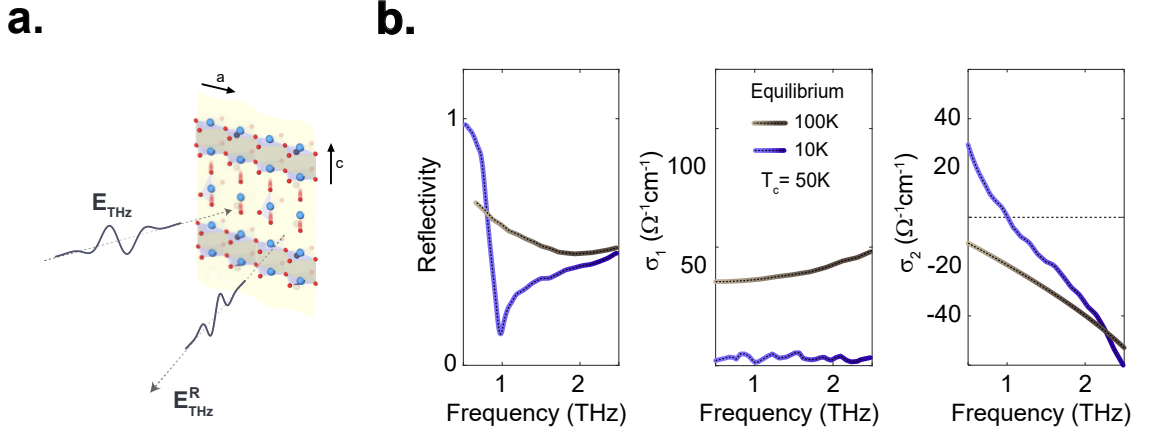


**Figure 3.4:** (a). Schematic of the THz probe measurement of the equilibrium c-axis optical properties of  $\text{YBa}_2\text{Cu}_3\text{O}_{6.48}$ . The low-frequency optical properties are sampled by a c-axis polarized THz probe pulses (grey). (b). From left to right; equilibrium c-axis terahertz-frequency reflectivity together with real and imaginary parts, denoted by  $\sigma_1(\omega)$  and  $\sigma_2(\omega)$ , respectively, of the optical conductivity in the superconducting state below  $T_c$  (in blue) and normal state above  $T_c$  (in grey).

### 3.3.3 Far-Infrared c-axis Optical Properties

Whilst the superconducting transition in  $\text{YBa}_2\text{Cu}_3\text{O}_{6+x}$  results in significant changes in the THz region to the reflectivity and optical conductivity, the far-infrared region in the range of 2-20 THz, where the IR-active c-axis phonon modes as well as the second longitudinal plasmon and transverse plasmon are found, also manifests strong effects both as a function of temperature and doping when approaching  $T_c$  [43, 48, 49]. The far-infrared c-axis reflectivity and the real part of the optical conductivity for the underdoped  $\text{YBa}_2\text{Cu}_3\text{O}_{6.5}$  and the near-optimally doped  $\text{YBa}_2\text{Cu}_3\text{O}_{6.95}$  compounds are shown in Fig. 3.5<sup>1</sup>. For  $\text{YBa}_2\text{Cu}_3\text{O}_{6.5}$ , as the temperature drops below a temperature of approximately  $\approx 150$  K (above  $T_c$ ) a second longitudinal Josephson plasma edge emerges at approximately 14.5 THz, repre-

<sup>1</sup>Note that these optical data are the closest available to the doping levels, 6.48 and 6.92, which are studied in Chapters 3 to 6 of this thesis.

senting the intra-bilayer mode ( $\omega_{J2}$ ). Below  $T_c$ , this mode is observed alongside the previously identified edge at around 1 THz, (see Fig.3.4 (b)) [132, 133, 135, 137, 138].

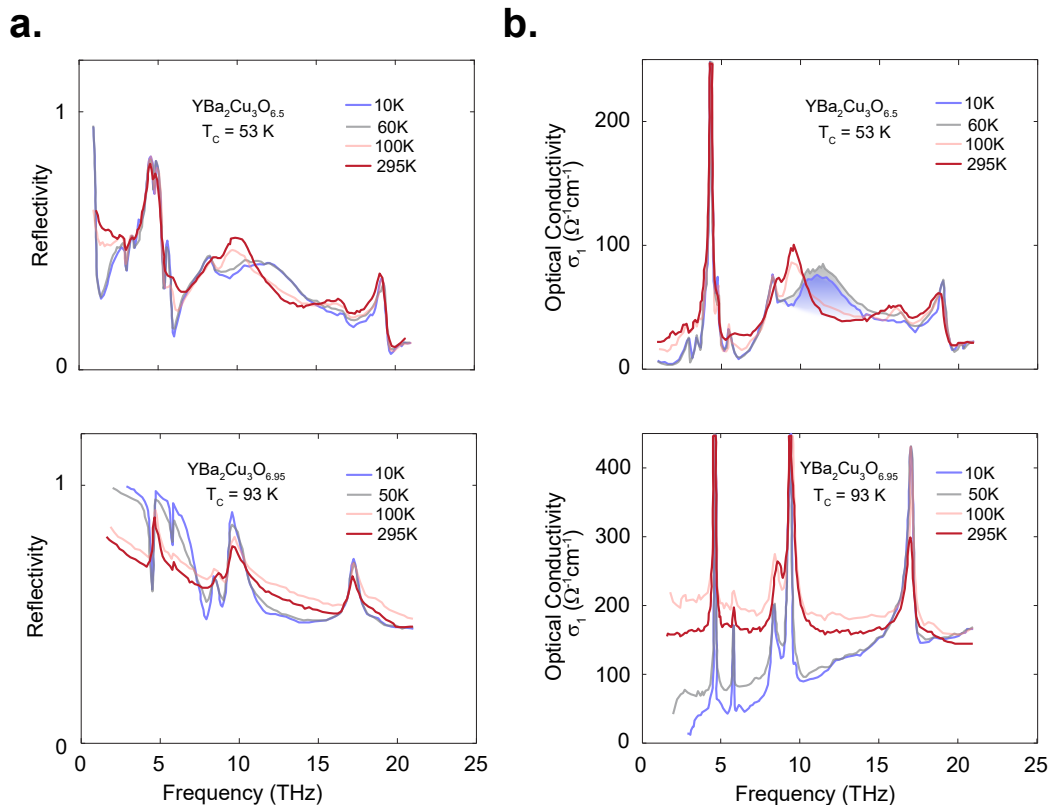


**Figure 3.5:** (a). From top to bottom:  $c$ -axis reflectivity for underdoped  $\text{YBa}_2\text{Cu}_3\text{O}_{6.5}$  ( $T_c = 53\text{ K}$ ) and overdoped  $\text{YBa}_2\text{Cu}_3\text{O}_{6.95}$  ( $T_c = 93\text{ K}$ ), respectively, for four different temperatures, starting from below  $T_c$  up to room temperature. (b). From top to bottom:  $c$ -axis real part of the optical conductivity  $\sigma_1(\omega)$  for the same doping levels and temperature range as in (a). The data shown in this figure were adapted from Ref.[48].

In addition to the two longitudinal modes, a broad peak in  $\sigma_1$  sets in also below a temperature of 150 K (at the same time as intra-bilayer mode), as indicated by the shaded region in Fig.3.5 (b). This feature is attributed to the transverse Josephson plasmon  $\omega_{JT}$ . The discussion of this mode and its relation to the potential presence

### 3.3. Equilibrium Properties of $\text{YBa}_2\text{Cu}_3\text{O}_{6+x}$

of phase fluctuating pre-existing Cooper pairs above  $T_c$  is postponed to the next section.

Turning now to the 6.95 doped compound, the frequencies of the longitudinal plasma edges are shifted relative to the underdoped compound. In this case the inter-bilayer Josephson plasmon is around 7.5 THz as also depicted in Fig.3.5 (a), whilst the upper longitudinal and the transverse plasmons are in the mid-infrared range, beyond the frequency range of the data presented in Fig.3.5 (see [48, 135] for extended data).

Also visible in the optical properties of Fig.3.5 are the  $B_{1u}$  phonons which are listed in the 3.1 for the underdoped and near optimally doped compounds, respectively. The high-frequency phonon mode at 17 THz in  $\text{YBa}_2\text{Cu}_3\text{O}_{6.95}$  is associated with the motion of apical oxygen atoms. In this compound, as the oxygen content is reduced, this mode splits into two disproportionate phonons with frequencies around 16.6 THz and 19.2 THz. In underdoped samples, the formation of the transverse plasmon mode is accompanied by spectral shift of neighboring phonon peaks toward this plasmon peak, significantly renormalizing the phonon modes line-shape [48, 49].

$\text{YBa}_2\text{Cu}_3\text{O}_{6.5}$	$\text{YBa}_2\text{Cu}_3\text{O}_{6.95}$
4.35	4.70
5.52	5.82
8.15	8.36
9.02	9.35
16.52	17.09
19.09	-

**Table 3.1:** The  $B_{1u}$  symmetry IR-active phonon modes found in the optical conductivity of the  $\text{YBa}_2\text{Cu}_3\text{O}_{6.5}$  and  $\text{YBa}_2\text{Cu}_3\text{O}_{6.95}$  in the units of THz.

In addition, the background conductivity changes significantly across both doping levels. In the  $\text{YBa}_2\text{Cu}_3\text{O}_{6.5}$  sample, the low-frequency region of conductivity, below approximately 7 THz ( $230 \text{ cm}^{-1}$ ), shows a continuous suppression as the temperature decreases from the normal to superconducting state. This suppression reflects the pseudogap opening. In the  $\text{YBa}_2\text{Cu}_3\text{O}_{6.95}$  sample, a gaped feature is also observed which is associated with the superconducting gap. Additionally, the normal state of the  $\text{YBa}_2\text{Cu}_3\text{O}_{6.95}$  compound exhibits metallic behavior, as seen from the increase in conductivity with decreasing temperature, different to the anomalous non-metallc behavior observed in the underdoped sample [49].

### **3.3.4 Plasmon Signature and Phonons Anomaly in the Pseudogap Phase**

The temperature dependence of the various c-axis optical features in  $\text{YBa}_2\text{Cu}_3\text{O}_{6+x}$  compounds could provide some insight into the underlying nature of the mysterious pseudogap phase. Whilst the lower longitudinal (inter-bilayer) plasmon only sets in below the superconducting critical temperature, the appearance of the transverse Josephson plasmon mode around 10-12.5 THz (as well as the intra-bilayer plasmon) in the underdoped compounds as mentioned starts at much higher temperatures, around 150 K. In addition, as the temperature is lowered the spectral weight of this mode increases at the expense of the neighboring 9.4 THz phonon mode (the oxygen bending mode), accompanied by a reshaping of the 16.8 THz and 18.9 THz apical oxygen phonon modes, as shown in Fig.3.6(a), such that the overall spectral weight is conserved at all temperatures [48, 49].

The presence of this mode and the neighboring phonon anomalies in the underdoped compounds were explained by a phenomenological model presented by Mun-

zar et al.[43]. According to this model, as the temperature approaches  $T_c$ , the local averaged field acting on the ions decreases which in turn results in their softening and spectral weight loss. Based on this model, the temperature dependence of this mode was further modeled by adding a damping to a Drude-like mode, which changes from zero THz to 9 THz. The temperature scale of this mode is compared to the lower longitudinal plasmon spectral weight and apical oxygen phonon modes at 16.6 THz and 19.2 THz, in Fig.3.6(c) and (d), respectively, showing that this mode already develops at temperatures above  $T_c$  in the pseudogap phase, which is suggestive of the presence of fluctuating pairs in the pseudogap region at least within the bi-layers [48, 49, 179, 192, 193].

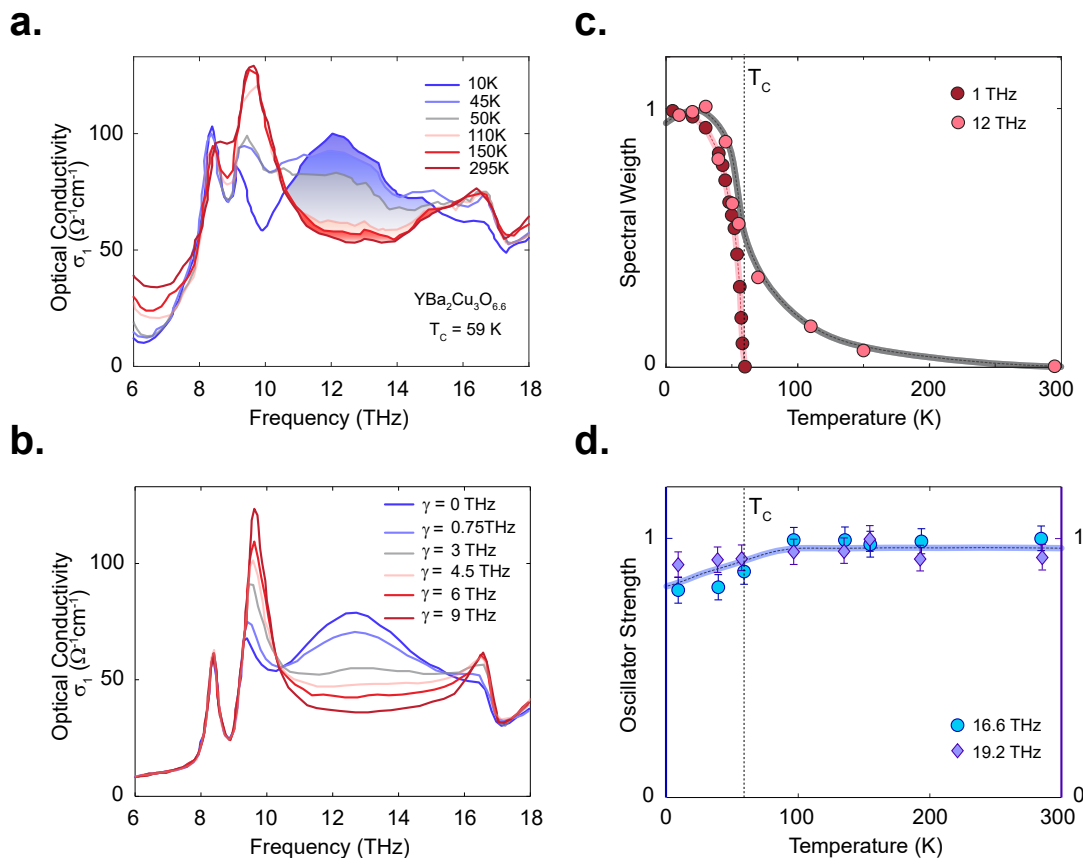


**Figure 3.6:** (a).  $c$ -axis optical conductivity for underdoped  $\text{YBa}_2\text{Cu}_3\text{O}_{6.6}$  ( $T_c = 59\text{ K}$ ) for five different temperatures starting from below  $T_c$  up to room temperature. The broad shaded peak in the frequency range of 10 to 15 THz centered at 12 THz indicates the transverse Josephson plasmon in this compound for each measured temperature. (b). Model calculation of (a) based on Munzar et. al. model [43], and the effect of the width of the broad peak as a function of damping of this mode, showing a good agreement with the measured data shown in (a) (c). The temperature dependence of the spectral weight of the loss-function peak at the frequency of the longitudinal lower plasmon (inter-bilayer plasmon  $\omega_{\text{JP1}}$ ) (dark red circles) and the spectral weight of the transverse Josephson plasmon peak centered at 12 THz ( $\omega_{\text{T}}$ ) in the optical conductivity (light red circles, emphasizing the different temperature scale for two plasmons (d). The temperature dependence of the oscillator strength for the two apical oxygen phonon modes in the underdoped  $\text{YBa}_2\text{Cu}_3\text{O}_{6.5}$  [192].

## 3.4 Photo-Induced Superconducting-Like State of $\text{YBa}_2\text{Cu}_3\text{O}_{6.5}$

### 3.4.1 THz c-axis Photo-Induced Optical Properties

As discussed above, the normal state of  $\text{YBa}_2\text{Cu}_3\text{O}_{6+x}$  retains some residual characteristics of fluctuating superconductivity. These characteristics present  $\text{YBa}_2\text{Cu}_3\text{O}_{6+x}$  as a promising candidate for somehow re-establishing superconducting order at temperatures above  $T_c$ . More specifically, the idea of using light to re-establish coherence between the phase fluctuating Cooper pairs which are thought to be present in the pseudogap phase is tantalizing.

In recent years, resonant mode-selective driving has been shown to induce transient optical properties reminiscent of superconductivity at temperatures above the transition temperature  $T_c$  in various materials, including certain molecular solids and cuprate compounds[22, 34, 64–67, 188, 194–196]. In underdoped  $\text{YBa}_2\text{Cu}_3\text{O}_{6.5}$ , the large-amplitude excitation of c-axis apical oxygen phonon modes using resonant mid-infrared pulses has been demonstrated to transiently induce optical properties that resemble those of an equilibrium superconductor [64–67]. As this non-equilibrium effect has not been observed in the higher-doped compound ( $\text{YBa}_2\text{Cu}_3\text{O}_{6.95}$ ) [188], the discussion in the rest of this Chapter will only be focused on  $\text{YBa}_2\text{Cu}_3\text{O}_{6.48}$ .

In the following sections, a summary of these photo-induced macroscopic superconducting-like properties in this compound is given, establishing the motivation for the main subject of this thesis, which is to develop a greater understanding of the microscopic dynamics which give rise to this effect.

As shown in Fig.3.7(a), the mid-infrared pulses resonantly excited the apical oxygen phonon modes, and the optical properties after photo-excitation were probed using time- and phase-resolved THz spectroscopy. The transient photo-induced c-axis low frequency THz reflectivity  $R(\omega)$  and optical conductivity  $\sigma_1(\omega)$  and  $\sigma_2(\omega)$  were calculated by measuring the pump-induced changes in the reflected THz electric field and adding these changes to the known equilibrium properties, taking into account the pump and probe penetration mismatch for the photo-excited volume [34]. The resulting photo-induced optical properties are compared to those in equilibrium and shown in Fig.3.7(b) and (c) for below and above  $T_c$ , respectively.

For base temperatures below  $T_c$ , a photo-induced edge at blue-shifted frequencies emerges, along with a reduction in the equilibrium Josephson plasma edge. The emergence of this photo-induced edge at 1.5-1.8 THz is accompanied by an enhancement of the  $1/\omega$  divergence in the imaginary part of the optical conductivity  $\sigma_2$ . The slight enhancement of the real part of the optical conductivity  $\sigma_1$  was attributed to heating of the quasiparticles by the mid-IR pump [197].

Unlike the equilibrium plasma edge, the photo-induced edge persists for temperatures far above  $T_c$  and even above room temperature, along with a  $1/\omega$  divergence in the imaginary part of the optical conductivity  $\sigma_2$  which closely resembles that of the equilibrium state below  $T_c$ . There is almost no change to the real part of the optical conductivity throughout the measured frequency range [65].

Importantly the frequency of the photo-induced edge in the reflectivity does not change as the temperature increases. The photo-induced edge does however blue-shift as the doping increases, as is the case for the equilibrium Josephson plasma resonances[65].

### 3.4. Photo-Induced Superconducting-Like State of $\text{YBa}_2\text{Cu}_3\text{O}_{6.5}$

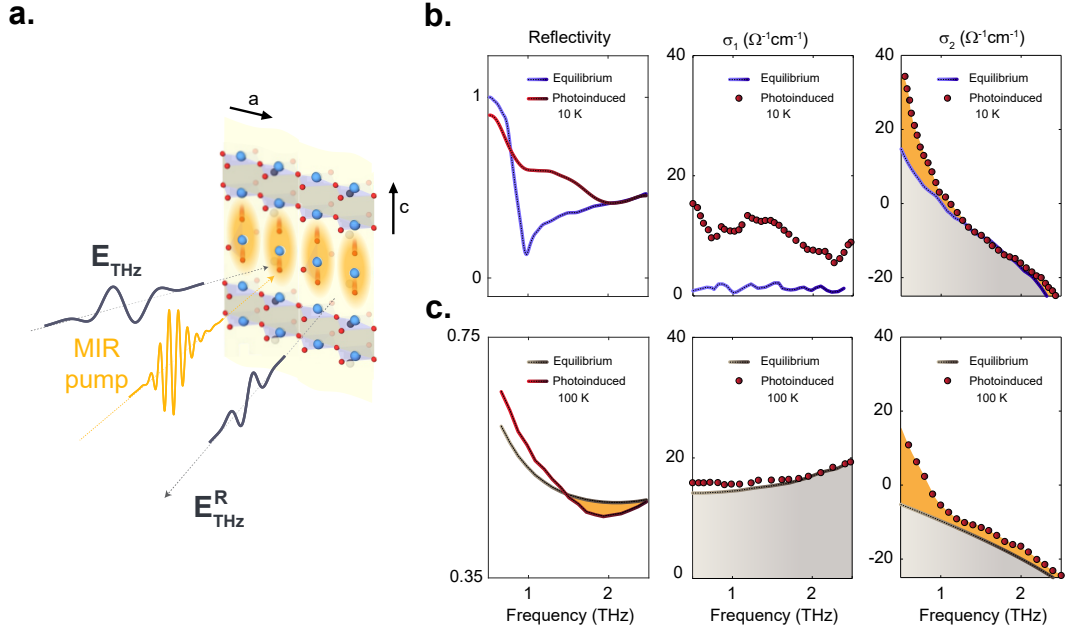


**Figure 3.7:** (a). Schematic of the mid-IR pump-THz probe experiment in  $\text{YBa}_2\text{Cu}_3\text{O}_{6.5}$ . The sample is excited by a mid-IR pump pulses (in yellow) polarized along the crystal c-axis, resonantly driving apical oxygen phonon modes as indicated inside the yellow shading. The subsequent changes in the low-frequency optical properties are sampled by a c-axis polarized THz probe pulses (in grey). (b). c-axis optical properties measured at a base temperature of 10 K below  $T_c$  ( $T_c = 50$  K) in equilibrium (blue) and after mid-IR photoexcitation (in red) (c). Same as in (b) but measured above  $T_c$  at a base temperature of 100 K. The changes in  $\sigma_1$  and  $\sigma_2$  before and after photo-excitation are indicated with grey and yellow shading, respectively [64, 65].

Further experiments, carried out using narrow-bandwidth excitation pulses, demonstrated that when the center frequency of the excitation pump was tuned to be resonant with each one of the c-axis phonon modes in turn. It was found that only large amplitude excitation of the apical oxygen phonon modes at 16.4 THz and 19.2 THz lead to the emergence of the photo-induced superconducting-like state in the measured THz optical properties, with all other phonon modes not showing a comparable effect<sup>2</sup>. Figure.3.8(a) shows the full frequency-dependence of the ex-

<sup>2</sup>Note that similar photo-induced superconducting-like signatures including  $1/\omega$  divergence of the

tracted photo-induced superfluid density.

The temperature dependence of the extracted superfluid density is shown for two pump frequencies in Fig.3.8(b). The excitation of the low frequency mode demonstrates no response, whereas driving the apical oxygen mode gives rise to a mean-field temperature dependence with a temperature scale which coincides with that of the pseudogap.

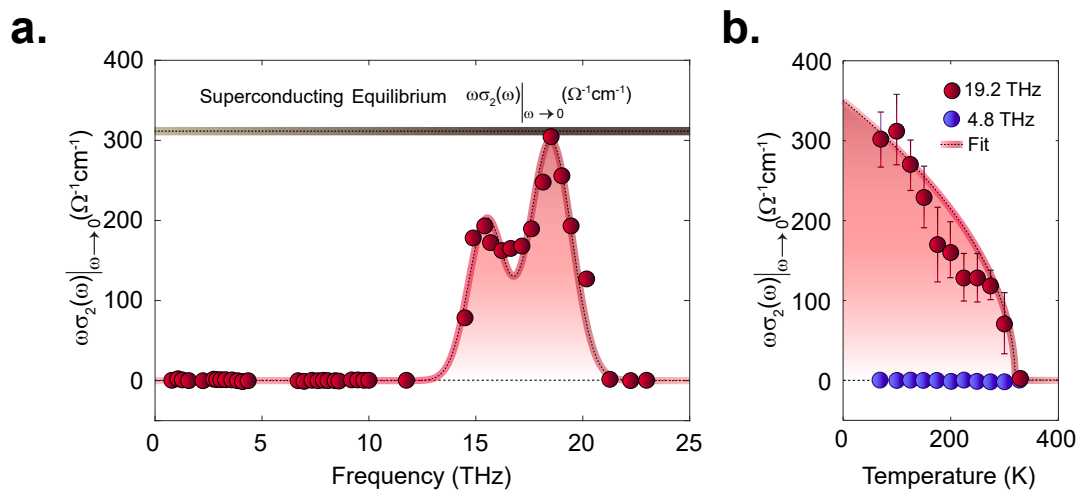


**Figure 3.8:** (a). Extracted photo-induced superfluid density (red circles) as a function of excitation pump frequency measured at a base temperature of 100 K (above  $T_c$ ) for excitation fluence of  $8 \text{ mJ.cm}^{-2}$ . The grey dashed-line represents the extracted equilibrium superfluid density measured at a base temperature of 10 K (below  $T_c$ ). The red-shaded fit indicates the resonant enhancement of the superfluid density at the apical oxygen phonon modes resonance frequency. (b). The same quantity as in (a) this time as a function of temperature for two excitation pump frequency resonant with c-axis 19.2 THz and 4.8 THz IR-active phonon modes. The red-dashed fit indicates the mean-field behavior of the data measured upon excitation of phonon modes at the frequency of 19.2 THz [66].

imaginary part of the optical conductivity  $\sigma_2(\omega)$  have been observed when pumping at much shorter wavelengths 800 nm [66, 193], however, in this thesis the discussion will be restricted only to the apical oxygen phonon-driven dynamics [22, 64–67].

### 3.4.2 Far-Infrared c-axis Photo-Induced Optical Properties

The photo-induced changes to the optical properties in the far-infrared frequency range have also been measured using the same excitation procedure but with a broader bandwidth time- and phase-resolved THz probe, providing data throughout the frequency range from 0.5-15 THz. The resulting reflectivity and the real part of the optical conductivity after photo excitation both below and above  $T_c$ , are shown in Fig.3.9.

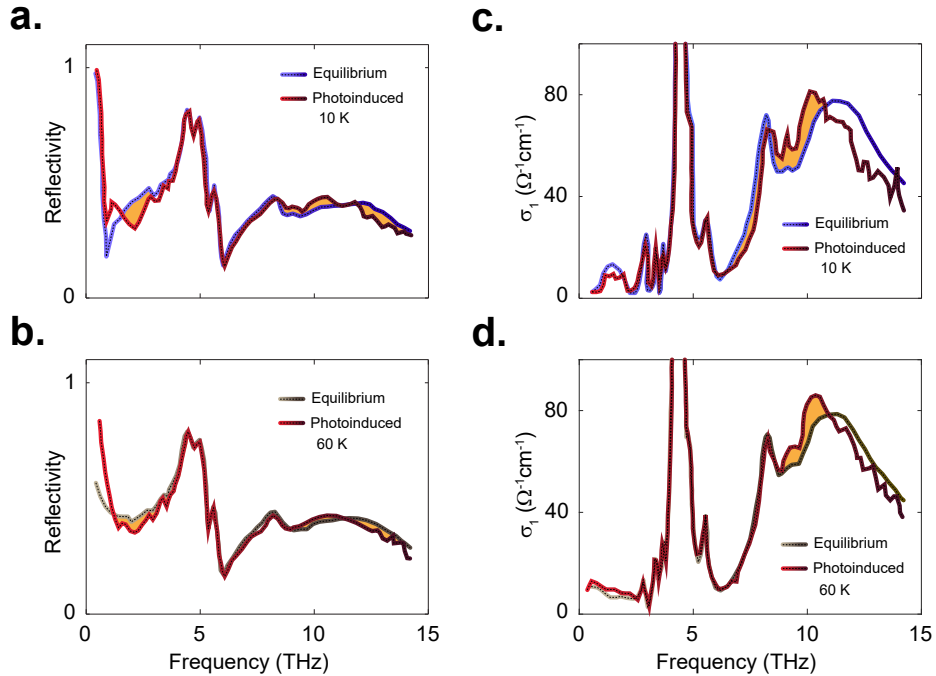


**Figure 3.9:** (a). The change in the reflected THz probe electric field before (in blue) and after photo-excitation via mid-IR pump at the peak of mid-IR pump-THz probe response (in red), measured at a base temperature of 10 K below  $T_c$  ( $T_c = 50 \pm 2$  K) in  $\text{YBa}_2\text{Cu}_3\text{O}_{6.5}$ . (b). Same as in (a) measured at the base temperature of 60 K above  $T_c$ . (c). Real part of the complex optical conductivity  $\sigma_1(\omega)$  calculated from reflectivity shown in (a) with the same color coding. (d). Same as in (c) but calculated from (b) with the same color coding. The photo-induced changes in the complex optical properties shown here are highlighted in yellow [64].

This data reveals that the appearance of the low-frequency photo-induced edge  $\omega_{\text{JP1LI}}$  and reduction of the equilibrium edge  $\omega_{\text{JP1}}$  (already observed in the previous experiments) are accompanied by changes in the spectrum of the far-infrared modes. A red-shifting of the upper longitudinal plasmon is visible in the reflectivity. In the optical conductivity, an accompanying red-shifting of both the transverse plasmon and the IR-active oxygen bending mode is observed. As discussed earlier in section 3.3.4, this oxygen bending mode is strongly influenced by the transverse plasmon. As a function of temperature, these photo-induced frequency shifts remain constant upon crossing  $T_c$ .

These observations were interpreted as a redistribution of the tunneling strength between the two coupled junctions and hence coherence transfer from intra-bilayer Josephson coupling associated with  $\omega_{\text{JP2}}$  to inter-layer Josephson coupling associated with  $\omega_{\text{JP1}}$  via the lattice modulation which is induced by the mid-IR pump. This interpretation could also explain the enhancement of the superfluid density observed at lower frequencies as well as the frequency red-shifts and phonon-sharpening in the higher frequency range [64].

### 3.4.3 Lifetime of the Photo-Induced State

In a recent series of experiments, the lifetime of this phonon-driven transient state was extended by increasing the excitation pulse duration from 0.15 ps to 4.3 ps (which is longer than the natural decay time  $\approx 1$  ps of the apical oxygen phonon modes) whilst keeping the peak electric field of the pulse constant. The subsequent transient photo-induced complex optical properties were again measured with a time- and phase-resolved THz probe. It was found that the phonon driven coherent state in  $\text{YBa}_2\text{Cu}_3\text{O}_{6+x}$  survives for as long as the driven phonon modes oscillate (see Fig.3.10(a)) and is therefore extended with the longer duration excitation pulses.

### 3.4. Photo-Induced Superconducting-Like State of $\text{YBa}_2\text{Cu}_3\text{O}_{6.5}$

In addition, it was shown that as the excitation pulse duration is extended (whilst maintaining a constant peak electric field), the transient dissipative response extracted from  $\sigma_1(\omega)$  increases, showing no saturation, whilst the transient photo-induced superfluid density extracted from  $\sigma_2(\omega)$  approaches a saturation limit which is equal to the equilibrium superfluid density at low temperatures (see Fig.3.10(b)).

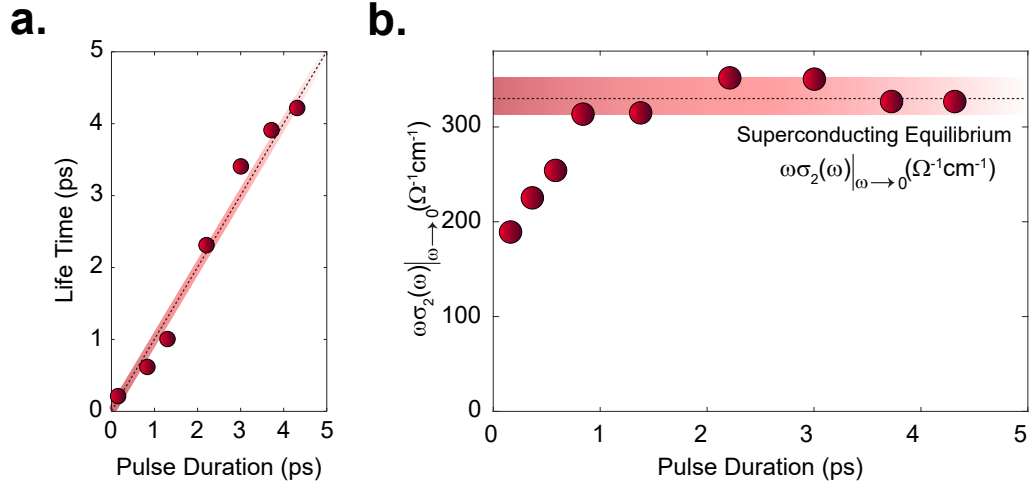


**Figure 3.10:** (a). The extracted photo-induced superfluid density  $\omega\sigma_2(\omega)$  measured in  $\text{YBa}_2\text{Cu}_3\text{O}_{6.48}$  at a base temperature of 10 K (below  $T_c$ ) as a function of mid-IR excitation pulse duration (in ps), representing a linear correspondence between the life-time of the transient superconducting-like state and the drive duration. (b). The extracted photo-induced superfluid density as a function of pulse duration. For pulse duration starting from 1 ps, this quantity reaches a saturation value (the thick red shading) which is the same quantity of the "zero-temperature" equilibrium superfluid density [67].

This suggests that the driven state cannot host more Cooper pairs than the equilibrium below  $T_c$  state. No matter how much energy is deposited into the system, the extra energy is being spent on quasiparticle heating and does not result in a higher superfluid density. Furthermore, the saturated photo-induced superfluid density being equal to the low-temperature equilibrium state provides further support to the idea that the excitation pulse effectively synchronizes the pre-formed phase fluctu-

ating Cooper pairs throughout the pseudogap.

These two competing effects have been speculated to arise from the presence of two types of quasiparticles, which reside in the nodal and antinodal regions of the Brillouin zone. In this picture the coherent response could arise from the antinodal regions, in which pre-formed Cooper pairs are thought to be present, whereas the dissipative response is attributed to the unpaired nodal quasiparticles [67].

#### **3.4.4 Expulsion of Magnetic Field in the Photo-Induced State**

Another major step towards characterizing the photo-induced superconducting-like state in  $\text{YBa}_2\text{Cu}_3\text{O}_{6.48}$  beyond the THz-optical measurements, was the determination of the (dia)magnetic response in the driven state in order to understand whether it is comparable to the equilibrium magnetic response of a superconductor. In a recent experiment [68],  $\text{YBa}_2\text{Cu}_3\text{O}_{6.48}$  was again photo-excited with 1 ps-duration mid-IR pulses to resonantly drive the apical oxygen phonon modes, this time in the presence of a static magnetic field. The dynamical magnetic response of the sample after photo-excitation was measured via ultra-fast magneto-optic probing, which makes use of the Faraday rotation in a magneto-optic crystal GaP placed in close proximity to the sample surface. The measured polarization rotation of the probe pulses is proportional to the magnetic field inside the magneto-optic crystal, such that changes in the polarization rotation induced when the sample is photo-excited report on how the photo-induced state disturbs the surrounding magnetic field (see Fig.3.11(a) for the details of the experimental schematic).

The results of these measurements are shown in Fig.3.11. As expected for a superconductor (and explained in Chapter 2), in equilibrium, when the superconducting

coherence is established, the magnetic susceptibility changes, resulting in an expulsion of magnetic field (Meissner-effect), giving rise to a reduction and enhancement of magnetic field in the center and on the edges of the sample, respectively. The time-resolved measurement of the change in magnetic field on the edge of the sample as it is photoexcited is shown in Fig.3.11(b), demonstrating an enhancement of the magnetic field with the time scale matching the driven phonon lifetime at temperatures well above  $T_c$  (100 K), as would be expected for a photo-induced transition into a superconducting state. The size of the diamagnetic susceptibility of the photo-excited state can be calculated under the assumptions that the photo-excited region is homogeneous and the changes in the susceptibility are slow, and was reported to be  $\approx -0.3$ , comparable with that of an equilibrium type-II superconductor.

Crucially, this response has been shown to persist as high as room temperature, which is consistent with the extracted photo-induced superfluid density temperature dependence from the THz-measurements (see Fig.3.11(c)), and remains consistent with the pseudogap phase. This on one hand draws a connection between the underlying nature of both observations, and on the other hand re-emphasises the potential importance of the pseudogap phase as a pre-cursor of the photo-induced superconducting-like state [68, 198].

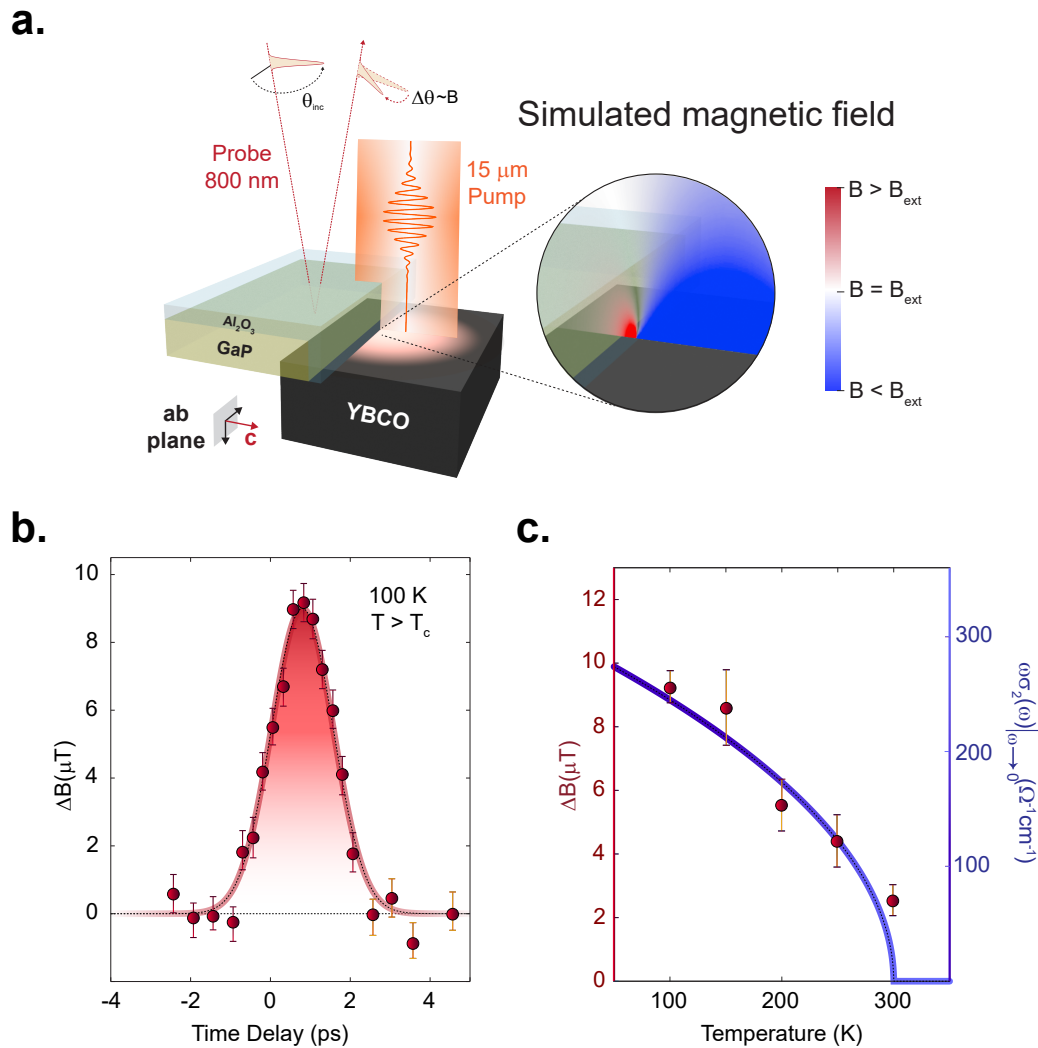


**Figure 3.11:** (a). Schematic of the experiment. A thin layer of  $\text{Al}_2\text{O}_3$  is placed on top and next to GaP detection crystal. This guarantees that mid-IR pump is reflected and no spurious nonlinear optical response in the detection crystal is generated. The thin  $\text{Al}_2\text{O}_3$  crystal also creates a well-defined edge in the mid-infrared pump beam, shaping the photo-excited region into a half-disc of about  $375 \mu\text{m}$  diameter. The zoomed in area represents the expected changes due to the local magnetic field expulsion on photo-excitation. The time-dependent magnetic field is sampled by probing the vicinity of the edge of the photo-excited region. (b). Photo-induced change in the magnetic field  $\Delta B$  measured at on the edge of photoinduced  $\text{YBa}_2\text{Cu}_3\text{O}_{6.48}$  as a function of mid-IR pump and probe delay at a base temperature of 100 K (above  $T_c$ ). (c). Photo-induced magnetic field expulsion as a function of temperature (red circles). The temperature dependence of the superfluid density extracted from the THz optical measurements is shown in blue curve for comparison, representing a similar mean-field temperature scaling for both observations. The figures and part of the caption were adapted from Ref.[68].

## 3.5 Summary and Outlook

This Chapter provided a detailed picture of the equilibrium superconducting and non-equilibrium superconducting-like properties of  $\text{YBa}_2\text{Cu}_3\text{O}_{6+x}$ . We began with a general introduction to the characteristics of the Cuprate superconductors which are most relevant to the interpretation of the non-equilibrium experiments with which this thesis is primarily concerned. These characteristics include the details of the crystal and electronic structures, their exotic phase diagram and the correlation of pseudogap and the superconducting phases. This was followed by an examination of the THz-frequency optical properties of  $\text{YBa}_2\text{Cu}_3\text{O}_{6.5}$  in equilibrium. It was explained that the optical properties along the c-axis (in the superconducting phase) are governed by the Josephson dynamics described extensively in Chapter 2, with a divergent imaginary part of the conductivity (typical of all superconductors) being accompanied by a characteristic edge in the reflectivity due to Josephson tunneling.

A thorough review of the recent non-equilibrium experiments was given, in which photo-excitation with mid-infrared pulses tuned resonant with the apical oxygen phonon modes was shown to induce both a similar divergence in the imaginary part of the optical conductivity, and a reflectivity edge, with a frequency slightly blue-shifted relative to that of the equilibrium edge. These observations were complemented by further experiments in which the same photo-excitation protocol was shown to result in the expulsion of a static applied magnetic field, reminiscent of the Meissner effect in an equilibrium superconductor. Intriguingly, both the superconducting-like THz-frequency optical properties and magnetic field expulsion were observed for base temperatures up to approximately  $T^*$ . Whether this short-lived non-equilibrium state has true microscopic features of a superconductor,

or is instead some other kind of exotic dynamical state is still open to a definitive answer.

In the next Chapter we present a series of experiments aimed at obtaining a microscopic understanding of the non-equilibrium dynamics which follow the mid-infrared excitation.

# Chapter 4

## Phonon Driven Coherent Dynamics in $\text{YBa}_2\text{Cu}_3\text{O}_{6+x}$

### 4.1 Introduction

Whilst the transient photo-induced optical properties and magnetic field expulsion measured in  $\text{YBa}_2\text{Cu}_3\text{O}_{6+x}$  provide macroscopic signatures of non-equilibrium superconductivity, the underlying mechanism explaining how this state is formed upon photo-excitation remains shrouded in mystery.

In this chapter, two earlier sets of single-pump-optical probe experiments which were aimed at addressing this mystery are reviewed in detail [22, 72]. These experiments studied the coherent microscopic dynamics which follow photo-excitation in  $\text{YBa}_2\text{Cu}_3\text{O}_{6+x}$ , leading to great insights into non-linear coupling between the resonantly driven phonon modes and other low frequency modes which could be ultimately responsible for the manifestation of the macroscopic superconducting-like properties described in Chapter 3. To improve on the understanding obtained by these experiments, we also present here new measurements carried out on a sec-

ond  $\text{YBa}_2\text{Cu}_3\text{O}_{6+x}$  compound with higher doping ( $\text{YBa}_2\text{Cu}_3\text{O}_{6.92}$ ), and describe a new analysis of all of the data taken together with the aim of achieving a more unified understanding. However, ambiguities in the interpretation of these results also highlight the shortcomings of the single-pump experiments, which are not able to uniquely determine the precise nature of this coupling mechanism[22, 199]. These shortcomings directly form the motivation for the multidimensional experiments described in chapters 5 and 6 of this thesis.

## 4.2 Probing Symmetry-Even Vibrational Modes

### 4.2.1 Raman Scattering

As discussed in the first chapter via Eq.1.29, harmonic oscillations of a Raman-active mode  $Q_{\text{R}}(t)$  can modulate the polarizability of the medium  $\chi_{ij}$  which gives rise to a polarization in the medium that reads:

$$P_i(t) = \epsilon_0 \left( \frac{\partial \chi_{ij}^{(1)}}{\partial Q_{\text{R}}} \right) Q_{\text{R}}(t) E_j(t) \quad (4.1)$$

This polarization results in a radiating field  $E_i(t) = \frac{dP_i}{dt}$  with a frequency which is shifted relative to that of the incoming field ( $\omega_{\text{pr}}$ ) by the frequency of the Raman mode ( $\omega_{\text{R}}$ ) according to the equation below:

$$Q_{\text{R}}(t) E_j(t) \propto \frac{1}{2} [\cos((\omega_{\text{pr}} + \omega_{\text{R}})t) - \cos((\omega_{\text{pr}} - \omega_{\text{R}})t)] \quad (4.2)$$

The possible inelastic processes are summarized in Fig.4.1(a) with the terms **Rayleigh**, **Stokes** and **Anti-Stokes**, describing scattering with no shift, red-shift and

## 4.2. Probing Symmetry-Even Vibrational Modes

blue-shift relative to the frequency of the incoming field, respectively. This further means that the emitted field reports on the frequency and symmetry of the Raman-active modes (see Fig.4.1(b)) and hence this technique can be used to probe the dynamics of these modes.

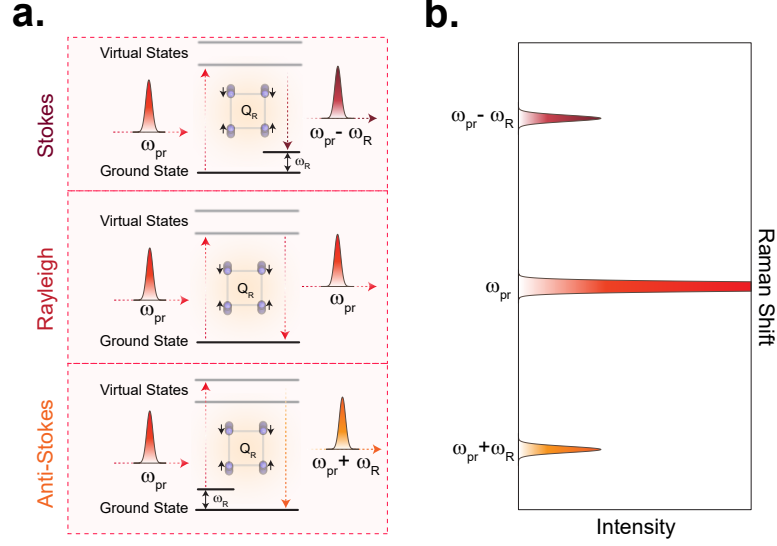


**Figure 4.1:** (a). Energy diagram describing the Raman and Rayleigh scattering processes. In the Raman scattering process the incident photons of light at a frequency of  $\omega_{pr}$  are scattered at slightly shifted frequencies:  $\omega_{pr} - \omega_R$  (stokes) and  $2\omega_{pr} + \omega_R$  (anti-stokes), generating the Raman side bands. Here  $\omega_R$  refers to a Raman-active excitation of the medium. In the Rayleigh scattering process, however, the scattered photons remain unaffected, leaving the medium at the frequency of  $\omega_{pr}$  as shown in the middle energy diagram. (b). Illustrative spectrum of the Rayleigh and Raman-scattering processes.

### 4.2.2 Time-Resolved Polarization Rotation

The physical mechanism underlying Raman scattering outlined in section 4.2 can also be exploited to measure the coherent motion of Raman modes in time-resolved pump-probe measurements.

If a Raman-active mode has been excited coherently inside a medium, the mode

oscillates as a function of real time  $t'$  denoted by  $Q_R(t')$ . The interaction of an incoming probing field with such an excitation is described by the following wave equation [110, 200]:

$$\left(\frac{\partial^2 E}{\partial z^2} - \frac{n^2}{c^2} \frac{\partial^2 E}{\partial t'^2}\right) = \frac{4\pi}{c^2} \left(\frac{\partial \chi^{(1)}}{\partial Q_R}\right) \frac{\partial^2}{\partial t'^2} (Q_R(t') E_{\text{pr}}(t' - t)) \quad (4.3)$$

Here  $E(z, t', t)$  is the propagating electric field inside the medium.  $E_{\text{pr}}$  refers to the probe electric field (with a Gaussian envelope), given by  $E_{\text{pr}}(t' - t) = \exp(-\frac{(t'-t)^2}{2\sigma_{\text{pr}}^2}) \sin(\omega_{\text{pr}}(t' - t))$ , with  $t$ ,  $\omega_{\text{pr}}$  and  $\sigma_{\text{pr}}$  being the relative pump-probe delay, probe frequency and pulse duration, respectively. For a weak probe field (neglecting the depletion or gain) and considering the boundary condition ( $E(z=0) = E_{\text{pr}}(z=0)$ ), the general solution is found as follows [201]:

$$E(z, t' - t) = E_{\text{pr}}(z, t' - t) - \frac{2\pi z}{cn} \frac{\partial \chi^{(1)}}{\partial Q_R} \frac{\partial}{\partial t} Q_R(z, t') E_{\text{pr}}(z, t' - t) \quad (4.4)$$

where  $Q_R(z, t') = Q_R(z) \sin(\omega_R t') \approx Q_{R,0} \sin(\omega_R t')$  (for a stationary excitation). This electric field is then sent to a slow detector which effectively integrates over time in the lab frame  $t'$ . Consequently, this detector measures a time-delay dependent response denoted by  $R(t)$  which is obtained by integrating Eq.4.4 [201].

$$R(t) \propto \int E(t', t) dt' \quad (4.5)$$

The time resolution of such measurement is determined via the probe field pulse duration  $\Delta\nu \approx \sqrt{\ln 2} \sigma_{\text{pr}}$  under the assumption that the probe pulse is transform limited. The highest frequency that a pulse with such bandwidth can resolve is up to  $\Delta\nu/2$  [202]. An intuitive illustration of time-resolved measurements and the effect of the pulse bandwidth is shown in Fig.4.2.

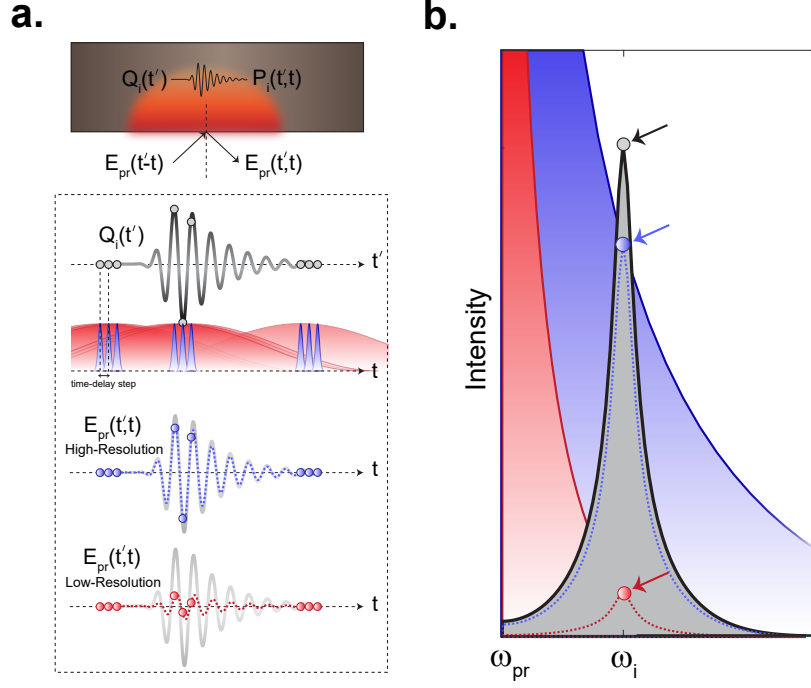


**Figure 4.2:** (a). Illustrative explanation of the time-resolved experiments. An excitation has been created in the system, oscillating in the lab time frame  $P_i(t')$  (black curve). The probe pulses with the time profile of  $\Delta t$  are centered at  $(t' - t)$ , with  $t$  indicating the pump-probe time delay, sample the oscillating field generated from the aforementioned polarization. If  $\Delta t$  is much shorter than the period of the oscillations (blue pulses) corresponding to a large bandwidth, the oscillations are measured almost with infinite resolution as shown in the blue curve. On the contrary, if  $\Delta t$  is much longer than the period of the oscillations (red pulses), corresponding to a short bandwidth, the oscillations are poorly resolved or not resolved at all, as shown by the red curve. (b). The overlap of the probe pulse bandwidth and the oscillatory component frequency denoted by  $\omega_i$  in the Fourier spectrum, for the case of high resolution (shaded in blue) and poor resolution (shaded in red).

The frequency content of the Eq.4.4 consists of three components, one with the probe fundamental frequency  $\omega_{pr}$  and two side-bands with respectively red- and blue-shifted frequencies,  $(\omega_{pr} - \omega_R)$  and  $(\omega_{pr} + \omega_R)$  due to the coherent oscillations of the Raman-active excitation which effectively modifies the polarizability of the system (via  $\frac{\partial \chi^{(1)}}{\partial Q_R}$ ). The change in the polarizability can be measured as a time-delay

dependent polarization rotation of the incoming probe field denoted as  $\Delta E_{PR}$ . Note that the subscript *PR* here refers to the polarization rotation not to be mistaken with *pr* which stands for probe.

### 4.2.3 Experimental Setup

In this and the following experiments, a 1-kHz repetition rate Ti:sapphire femtosecond amplifier system (800 nm wavelength, 30 fs pulse duration, 2 mJ output power) was used to pump two two-stage optical parametric amplifiers, seeded with the same white light continuum. The output signal pulses from the two OPAs, at 1235 nm ( $\approx 170 \mu\text{J}$ ) and 1326 nm ( $\approx 130 \mu\text{J}$ ), were overlapped in a 350  $\mu\text{m}$  thick GaSe crystal to generate CEP stable mid-IR pulses [203] via the nonlinear optical effect known as difference frequency generation (DFG). The mid-IR pump pulse duration ( $\approx 150$  fs), frequency ( $\approx 5$  THz bandwidth, centered at 18 THz) and  $\approx 1.6 \mu\text{J}$  (after generation) were characterized by electro-optic sampling in a second GaSe crystal ( $\approx 50 \mu\text{m}$  thickness) (see Fig.4.3(c)). The details of the optical setup are shown in Fig.4.3(a).

The generated mid-IR beam was then focused onto the sample with a spot size of  $\approx 70 \mu\text{m}$ . The pump polarization was fixed parallel to the  $\text{YBa}_2\text{Cu}_3\text{O}_{6+x}$  c-axis. The reflected probe pulses at 800 nm wavelength were collected with a dichroic mirror. The photoinduced time-resolved polarization rotation of the 800 nm probe was measured by sending this beam to a half-wave plate and a Wollaston prism and detecting the difference signal of two intensity-balanced photodiodes as highlighted by the red square in Fig.4.3(b).

## 4.2. Probing Symmetry-Even Vibrational Modes

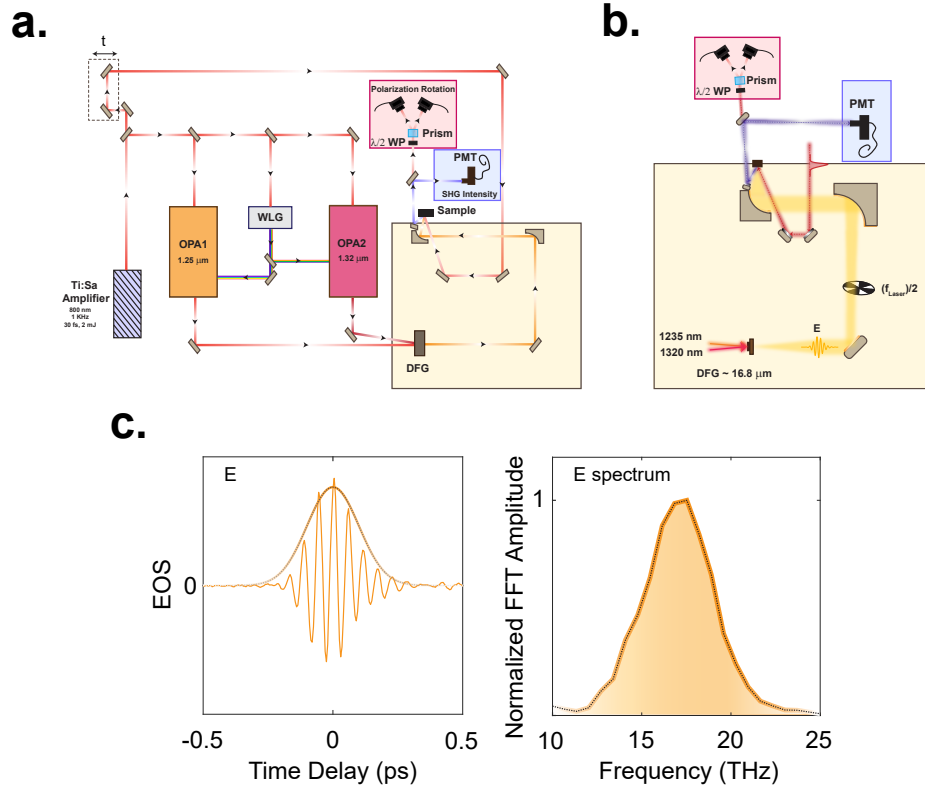


**Figure 4.3:** (a). An overview of the experimental setup used for single mid-IR pulse – polarization rotation and SHG probe experiments. See text for the details. (b). The generated mid-IR pulses were first collimated and then focused onto the sample. The photo-induced dynamics after mid-IR excitation were measured by time-resolved second harmonic generation of the 800 nm probe pulse (60 nJ) in non-collinear geometry and detected using a photomultiplier detector. The polarization rotation of the reflected 800 nm pulses was measured simultaneously using a half-wave plate and Wollaston prism combined with two balance photodiodes. (c). The mid-IR pump pulse duration and frequency spectrum were measured using electro-optic sampling in a second GaSe crystal (50 μm thickness) [199].

### 4.3 Coherent Dynamics of the Raman-Active Phonons in $\text{YBa}_2\text{Cu}_3\text{O}_{6+x}$

In  $\text{YBa}_2\text{Cu}_3\text{O}_{6+x}$ , the time-resolved polarization rotation probing technique discussed above, has been used to measure the coherent dynamics of the Raman-active modes which follow mid-IR photo-excitation. In this section, the previously reported data measured on  $\text{YBa}_2\text{Cu}_3\text{O}_{6.48}$  is presented [22] and then is compared to the new measurements conducted on  $\text{YBa}_2\text{Cu}_3\text{O}_{6.92}$ .

As sketched in Fig.4.4(a), the mid-IR pulses polarized along the c-axis resonantly excite the apical oxygen phonon modes. The subsequent dynamics of the Raman-active modes following photo-excitation are revealed by coherent oscillations which are superimposed on top of a slowly varying background in the time-delay dependent polarization rotation of the probe pulses measured at room temperature on both doping levels and shown in Fig.4.4(b). To isolate the coherent oscillations, the slowly varying envelope was fitted and subtracted away using the following functional form:

$$F_1(t) = \sum_i A_i \left[ \left( 1 + \operatorname{erf}\left(\frac{t - t_i}{s_i}\right) \right) \exp\left(-\frac{(t - t_i)}{\tau_i}\right) \right] \quad (4.6)$$

Here  $A_i$ ,  $t_i$ ,  $s_i$  and  $\tau_i$  denote the amplitude, time-zero, rise time and decay time, respectively and  $i$  sums over all the fitting functions. To extract the frequency components of the signal, the residuals following subtraction were then fitted using the function  $F_2(t)$  in Eq.4.7:

$$F_2(t) = \sum_j A_j \left[ \left( 1 + \operatorname{erf}\left(\frac{t - t_j}{s_j}\right) \right) \sin(\omega_j t) \exp\left(-\frac{(t - t_j)}{\tau_j}\right) \right] \quad (4.7)$$

### 4.3. Coherent Dynamics of the Raman-Active Phonons in $\text{YBa}_2\text{Cu}_3\text{O}_{6+x}$

---

Here  $A_j$ ,  $t_j$ ,  $s_j$ ,  $\omega_j$  and  $\tau_j$  denote the amplitude, time-zero, rise time, frequency and decay time of the  $j$ th component, respectively.

The analysis performed here shows that the signal measured on both compounds contains three dominant components at frequencies which match those of the known fully symmetric  $A_g$  phonon modes in  $\text{YBa}_2\text{Cu}_3\text{O}_{6+x}$ . After fitting the time-domain oscillations using Eq.4.7, the Fourier amplitude of each component was extracted individually from the fit and overlaid on top of the raw-data and is plotted in Fig.4.4(e) and (f) for both doping levels, respectively. It can be seen that the frequencies of the modes observed here do not change much as the doping increases.

The observations summarized here have previously been studied and explained in terms of third-order nonlinear coupling between the resonantly excited IR-active apical oxygen phonon modes and the  $A_g$  Raman modes, following the nonlinear phonon-phonon mechanism which was presented in Chapter 1, section 1.6.2. A direct measurement of the nonlinear coupling mechanism can be obtained by utilizing multidimensional mid-IR spectroscopy, as will be presented in the following chapters (section 5.4) together with a full theoretical analysis and numerical simulation for both one-dimensional and two-dimensional experiments (section 6.6).

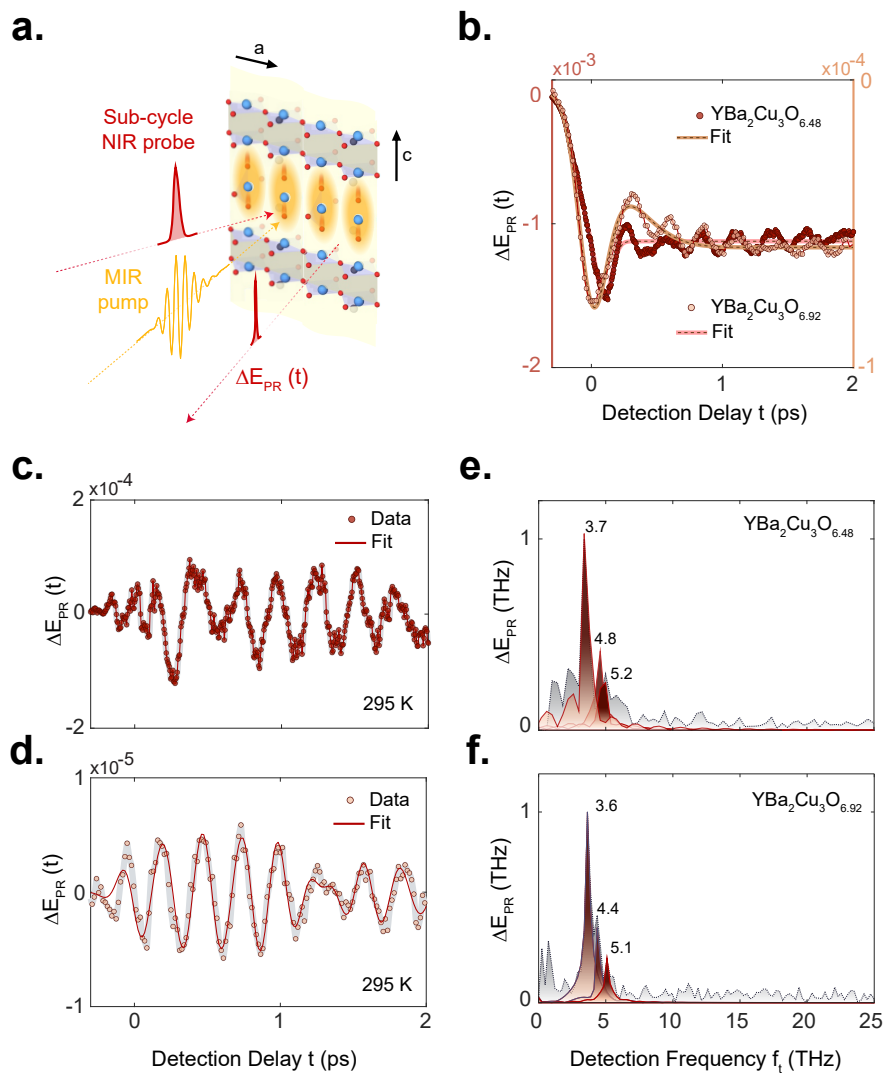


**Figure 4.4:** (a). Schematic of the mid-IR pump, polarization rotation (PR) experiment in  $\text{YBa}_2\text{Cu}_3\text{O}_{6+x}$ . The sample is excited by a mid-IR pump pulse (yellow) polarized along the crystal  $c$ -axis, resonantly exciting apical oxygen phonon modes as indicated by the yellow shading. The photo-induced changes of the polarization state of the reflected beam were sampled by a short near-infrared probe pulse at 800 nm wavelength (red). (b). The polarization rotation signal measured at a base temperature of 295 K (above  $T_c$ ) in  $\text{YBa}_2\text{Cu}_3\text{O}_{6.48}$  (dark red circles) and  $\text{YBa}_2\text{Cu}_3\text{O}_{6.92}$  (light-orange circles) reveals coherent oscillations of Raman-active phonons. The thick light red and orange lines are fits to the data. (c). and (d). The residual of the fitted data shown in (a) for 6.48 and 6.92 doping levels along with the fits to their oscillatory components, respectively. (e). and (f). Corresponding Fourier spectra of the experimental data (shaded in grey) and the fit for individual oscillatory component (shaded in brown). Three Ag Raman modes are found at the frequencies of 3.8 THz, 4.8 THz and 5.2 THz for  $\text{YBa}_2\text{Cu}_3\text{O}_{6.48}$  and 3.6 THz, 4.4 THz and 5.1 THz for  $\text{YBa}_2\text{Cu}_3\text{O}_{6.92}$ .

## 4.4 Probing Symmetry-Odd Vibrational Modes

### 4.4.1 Second-Order Nonlinear Optical Effects

When the intensity of the incoming electromagnetic waves entering a medium increases, higher order nonlinear processes become available, as described in Eq.1.17. In particular, for a given medium with broken inversion symmetry, the lowest order nonlinear term in the expansion of the polarization is associated with the second order nonlinear susceptibility  $\chi_{ijk}^{(2)}$ . Importantly,  $\chi_{ijk}^{(2)}$  is a tensor which obeys the symmetry of the system. The second order nonlinear contribution to the polarization in the medium can therefore be expressed as follows [204, 205]:

$$P_i(t) = \chi_{ijk}^{(2)} E_j(t) E_k(t) \quad (4.8)$$

For a degenerate incoming field with frequency  $\omega_1$ , the resulting polarization becomes  $P_i(t) = \chi_{ijj}^{(2)} E_j(t)^2$  which includes an oscillatory component with frequency  $2\omega_1$ , known as **second harmonic generation** (SHG) and a non-oscillatory rectified component at  $\omega = 0$  (D.C. effect) [205–207]. In the SHG process, two photons of the fundamental frequency are converted into a single photon at twice this frequency. The efficiency of this conversion is defined as the ratio between the incoming fundamental and outgoing SHG intensities  $\frac{I^{(2\omega)}}{I^{(\omega)}}$ . This efficiency is determined by size of the relevant components of the  $\chi_{ijk}^{(2)}$  tensor, as well as the interaction length inside the medium and the degree of phase matching between the fundamental and SHG fields.

In the case of two non-degenerate incident fields with frequencies  $\omega_1$  and  $\omega_2$ , the polarization will oscillate at both the sum frequency  $\omega_1 + \omega_2$  and the difference frequency  $\omega_1 - \omega_2$ . These processes are referred to as **sum frequency generation** and

*difference frequency generation* [204].

#### 4.4.2 Hyper-Raman Scattering

In the case of a centro-symmetric medium, the above second-order nonlinear processes are forbidden by symmetry constraints. This arises from the fact that in a system with inversion symmetry, the motion of the charges in the positive ( $+x$ ) and negative ( $-x$ ) direction with respect to the inversion center must be energetically equivalent  $U(x) = U(-x)$  [204]. Nevertheless, if the crystal structure is displaced along an IR-active mode  $Q_{\text{IR}}$ , inversion symmetry will necessarily be broken, allowing second-order nonlinear processes to take place. Consequently, if an excitation pulse coherently excites such a mode, the inversion symmetry will be transiently broken while the mode oscillates, modulating  $\chi^{(2)}$  and giving rise to a transient contribution to the polarization as written in Eq.4.9. Note that, in an inversion-symmetric system, all the IR-active (symmetry-odd) modes are hyper-Raman active.

$$P_i(t) = \epsilon_0 \left( \frac{\partial \chi_{ijk}^{(2)}}{\partial Q_{\text{IR}}} \right) Q_{\text{IR}}(t) E_j(t) E_k(t) \quad (4.9)$$

For the case of a degenerate incoming field  $E_{\text{pr}}(t)$  at frequency  $\omega_{\text{pr}}$ , the equation above reduces to:

$$P_i(t) = \epsilon_0 \left( \frac{\partial \chi^{(2)}}{\partial Q_{\text{IR}}} \right) Q_{\text{IR}}(t) E_{\text{pr}}(t)^2 \quad (4.10)$$

The equation above describes the process known as **Hyper-Raman scattering**. For an IR-active excitation which is oscillating such that  $Q_{\text{IR}}(t) = Q_{\text{IR},0} \sin(\omega_{\text{IR}} t)$ , this process generates **Stokes** and **Anti-Stokes** hyper-Raman side bands which are shifts of  $\pm \omega_{\text{IR}}$  relative to the frequency of the second harmonic generation from the incoming field, resulting in time-dependent polarization at frequencies  $2\omega_{\text{pr}} \pm \omega_{\text{IR}}$  [110] (see Fig.4.5 for an illustrative explanation of SHG and Hyper-Raman scattering).

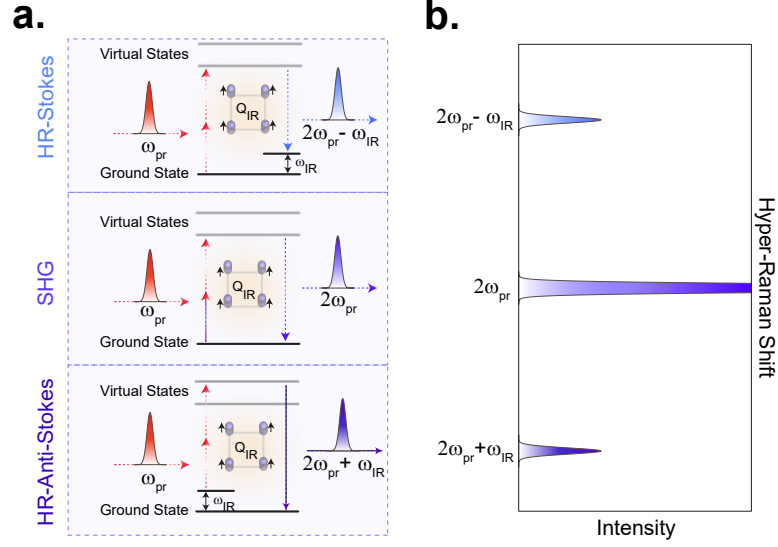


**Figure 4.5:** (a). Energy diagram describing the second harmonic generation (SHG) and hyper-Raman scattering processes. In the SHG process, two incident photons of light at a frequency of  $\omega_{pr}$  are converted to a photon at the frequency of  $2\omega_{pr}$  via second order nonlinear susceptibility. In the hyper-Raman scattering process, however, the scattered photons are at a frequencies of  $2\omega_{pr} - \omega_{IR}$  (hyper-Raman stokes) and  $2\omega_{pr} + \omega_{IR}$  (hyper-Raman anti-stokes), generating the hyper-Raman side bands. Here  $\omega_{IR}$  refers to an IR-active excitation of the medium. (b). Illustrative spectrum of the SHG and hyper-Raman processes.

As the IR-active mode frequencies are typically in the THz to mid-infrared range, and (for the experiments described in this thesis) the probing field frequency is in the near-infrared range, the relative frequency shift of the hyper-Raman side bands is very small. Consequently, the resulting polarization oscillates at frequencies very close to  $2\omega_{pr}$ . Therefore, in the following the term SHG is used instead of hyper-Raman scattering.

#### 4.4.3 Electric-Field Induced Second Harmonic Generation

The next term in the expansion of the macroscopic polarization in Eq.1.17 includes mixing of three fields via third-order nonlinear susceptibility  $\chi_{ijkl}^{(3)}$  which gives rise

to a polarization as follows [22, 204]:

$$P_i(t) = \chi_{ijkl}^{(3)} E_j(t) E_k(t) E_l(t) \quad (4.11)$$

Such a time-dependent polarization results in a radiating field  $E_i(t) = \frac{dP_i(t)}{dt}$  with its frequency components depending on the sum or difference frequencies of the incoming fields  $E_j(t)$ ,  $E_k(t)$  and  $E_l(t)$ , respectively.

In the time-resolved SHG experiments that form the subject of this thesis and will be discussed in the following, this nonlinear optical effect gives rise to a significant contribution to the early time-delay signal which arises from mixing the mid-IR pump field  $E_{\text{pump}}(t)$  at the frequency  $\omega_{\text{pump}} \approx 18$  THz with two contributions from the probe field  $E_{\text{pr}}(t)$  at the frequency  $\omega_{\text{pr}} = 374$  THz. Therefore, the Eq.4.11 reduces to the equation below:

$$P_i(t) = \chi^{(3)} E_{\text{pump}}(t) E_{\text{pr}}(t)^2 \quad (4.12)$$

The radiated field is given by  $E_i(t) = \frac{dP_i(t)}{dt}$  and has frequency components of  $2\omega_{\text{pr}} \pm \omega_{\text{pump}}$ . Because the pump frequency is very small compared to that of the probe second harmonic, the radiated photons are very close to second harmonic generation of the probe field, just as for the hyper-Raman scattering process. This process is therefore known as ***Electric Field Induced Second Harmonic Generation (EFISH)***  $E_{\text{EFISH}}(t)$ , and is only present at the earliest time delays when there is temporal overlap between the mid-infrared pump and near-infrared probe fields.

#### 4.4.4 Time-Resolved Second Harmonic Generation

The fact that SHG is symmetry-forbidden in centro-symmetric systems [204] makes it a powerful technique to effectively detect and investigate the dynamics of the inversion symmetry-breaking (odd) modes on an ultra-fast time scale. This technique has been extensively used to track such coherent dynamics in pump-probe experiments in different material systems as well as to map out the symmetry of different nonlinear optical properties via the second order nonlinear susceptibility tensor [22, 33, 45, 208–211]. Whilst time-resolved SHG provides critical microscopic-level information about the dynamics of driven material systems, it also poses practical challenges related to the detection process.

In the following sections, first the details of the detection scheme for performing time-resolved SHG pump-probe measurements (including the concepts of heterodyne and homodyne detection) are discussed, before the results of applying this technique to phonon-driven  $\text{YBa}_2\text{Cu}_3\text{O}_{6+x}$  are presented.

#### 4.4.5 Detection of Time-Resolved SHG

Before presenting the experimental data measured on  $\text{YBa}_2\text{Cu}_3\text{O}_{6+x}$ , it is important to understand the different types of contributions which can appear in the measured SHG signal in these experiments. In this section, the concepts of so-called homodyne and heterodyne detection are introduced. As will be shown, understanding whether the experiment is carried out in the homodyne or heterodyne limit (or perhaps in an intermediate regime) is critical to interpreting the results.

As discussed above in an inversion-symmetric system, the resonant excitation of IR-active, symmetry-odd modes with a mid-IR electric field  $E_{\text{pump}}(t)$  launches coherent oscillations of these modes ( $Q_{\text{IR}}$ ) which transiently break inversion sym-

metry and gives rise to a polarization via the hyper-Raman scattering process as in Eq.4.10. Here the assumption is that the hyper-Raman coefficient ( $\frac{\partial\chi^{(2)}}{\partial Q_i}$ ) of these modes are constant within the probe spectral bandwidth. In these experiments the probe can be well described as a Gaussian pulse with the electric field  $E_{pr}(t' - t) = \exp(\frac{-(t'-t)^2}{2\sigma_{pr}})\sin(\omega_{pr}(t' - t))$  and ( $\sigma_{pr} \approx 30$  fs,  $\omega_{pr}/2\pi \approx 375$  THz at 800 nm wavelength). Here  $t$  and  $t'$  refer to the pump-probe time delay and lab time frame, respectively, following the same notation as was used in section4.2.2.

The total SHG field ( $E_{SH,total}$ ) has contributions from both the hyper-Raman field  $E_{SH}$  due to the oscillating symmetry-odd mode and the nonlinear third-order mixing of the mid-IR pump with the probe electric fields (EFISH),  $E_{EFISH}$ :

Hyper-Raman Polarization :

$$P_i(t) = \epsilon_0 \frac{\partial\chi^{(2)}}{\partial Q_{IR}} Q_{IR}(t') E_{pr}^2(t' - t)$$

Third-order nonlinear polarization :

$$P^{(3)} = \epsilon_0 \chi^{(3)} E_{pump}(t') E_{pr}^2(t' - t) \tag{4.13}$$

Total emitted field :

$$E_{SH,total} = E_{SH} + E_{EFISH} = \frac{d(P_i + P^{(3)})}{dt}$$

In the absence of any other electric field on the detector, the generated field in Eq.4.13 is measured as the intensity (given by the modulus square of the SHG field), as a function of pump-probe time delay  $t$ . This intensity detection scheme is known as **Homodyne detection- $I_{Hom}$** , which results in the coherent oscillations of the mode  $Q_{IR}$  being detected at twice the fundamental frequency ( $I_{Hom}(t) \approx \cos(2\omega_{IR}t)$ ) along with a D.C. component ( $\omega = 0$ ). Via this detection procedure, the absolute phase of the coherent oscillations is lost and the double-frequency oscillations are ob-

served provided the probe pulse duration is sufficiently short. Figure 4.6(a) shows a schematic illustration of the homodyne detection.

In some circumstances it is useful to supply the detector with an auxiliary field at the SH frequency, in order to interfere with the SHG field from the sample. This auxiliary field is referred to as a **local oscillator**  $-E_{Lo}$  (see Appendix C.1 for an example), and the interference results in a beating contribution between the local oscillator field and the generated field in the sample  $E_{SH}$ . This is then detected as an intensity proportional to  $2E_{SH}E_{Lo}\cos(\phi)$  where  $\phi$  is the phase difference between the two fields. This interference term leads to phase-sensitive detection of the time delay dependent oscillations at the frequency of the oscillating mode  $\omega_{IR}$ . Such detection scheme is referred to as **Heterodyne detection**  $-I_{Het}$  (see Fig. 4.6(b)). Depending on the amplitude of  $E_{Lo}$ , the relative size of the homodyne and heterodyne contributions to the measured SH intensity  $I_{SH}$  can be adjusted [29, 205–207, 212–214], as can also be seen in Eq. 4.14.

$$\begin{aligned} I_{SH}(t) &= \int dt' |E_{SH}(t', t) + E_{Lo}(t')|^2 = |E_{SH}(t)|^2 + |E_{Lo}|^2 + 2E_{SH}(t)E_{Lo}\cos\phi \\ &= I_{Hom}(t) + I_{bg} + I_{Het}(t) \end{aligned} \quad (4.14)$$

Here  $I_{bg} = \int dt' |E_{Lo}(t')|^2$  and is the time-delay independent intensity generated by only the local oscillator at the detector.

In the heterodyne detection, the absolute phase of the oscillations can be captured, on the condition that the interference between the two fields at 400 nm is *phase-stable* down to a fraction of its 1.3 fs period. This phase-stabilization is technically challenging, making the establishment of a controllable heterodyne detection scheme difficult in practice. In the following, we present an example that highlights the importance of understanding whether the homodyne or heterodyne detection

is dominating the signal.

For a relevant comparison to the experiments that will be discussed in the following, here we explore the detected features in the cases of homodyne, heterodyne and intermediate (with contributions from both) detection via simulations. We choose a model consisting of two oscillatory modes with coordinate amplitudes  $Q_1$  and  $Q_2$  and eigenfrequencies of  $\omega_1$  and  $\omega_2$ , respectively. Each of these modes generates a separate hyper-Raman field, labeled as  $E_{SH,Q_1}$  and  $E_{SH,Q_2}$ . The total intensity measured by the detector (including the contribution of the local oscillator) can then be calculated using Eq.4.14 as follows:

$$\begin{aligned}
 I_{SH,Int}(t) &= \int dt' |E_{SH,Q_1}(t', t) + E_{SH,Q_2}(t', t) + E_{Lo}(t')|^2 \\
 &= |E_{SH,Q_1}(t)|^2 + |E_{SH,Q_2}(t)|^2 + 2|E_{SH,Q_1}(t)||E_{SH,Q_2}(t)| \\
 &\quad + 2E_{Lo}E_{SH,Q_1}(t)\cos\phi + 2E_{Lo}E_{SH,Q_2}(t)\cos\phi \\
 &= I_{SH,Hom}(t) + I_{SH,Het}(t) + I_{bg}
 \end{aligned} \tag{4.15}$$

where the second equality is correct under the assumption of infinite probe time resolution. In the limit of small or zero local oscillator, the term  $I_{SH,Hom}(t) = |E_{SH,Q_1}(t)|^2 + |E_{SH,Q_2}(t)|^2 + 2|E_{SH,Q_1}(t)||E_{SH,Q_2}(t)|$  dominates the detected signal. Accordingly, the first two terms in  $I_{SH,Hom}(t)$  give rise to two frequency components each, one oscillatory  $\cos(2\omega_i t)$  and one non-oscillatory D.C. component at 0. The third term mixes the two oscillatory fields and results in oscillatory detected responses of both  $\cos[(\omega_2 - \omega_1)t]$  and  $\cos[(\omega_1 + \omega_2)t]$ . These contributions are displayed in red in Figs.4.6 (c) and (d), in the time and frequency domains, respectively. Note that among all these frequency components, only those within the probe time resolution will be resolved in an experiment.

Next, we consider the heterodyne limit in which  $E_{Lo}$  is very large, causing the

#### 4.4. Probing Symmetry-Odd Vibrational Modes

---

terms  $2E_{\text{Lo}}E_{\text{SH},Q_1}(t)\cos\phi$  and  $+2E_{\text{Lo}}E_{\text{SH},Q_2}(t)\cos\phi$  to dominate the measured signal. In this limit, these terms overcome the homodyne contributions and recover *only* the oscillations of the modes at their eigenfrequencies  $\cos(\omega_i t)$ . This limit is also shown in Fig.4.6 (c) and (d) in light blue for comparison to the homodyne limit.

Turning now to the intermediate regime, in the presence of a local oscillator with comparatively small amplitude, all the terms in Eq.4.15 ( $I_{\text{SH,Int}}(t)$ ) may contribute roughly equally to the detected signal. Depending on the amplitude of the local oscillator, the relative contributions of homodyne and heterodyne in the measured signal differ. This intermediate limit is shown in dark blue in Fig.4.6 (c) and (d), which appears as a sum of the features from both extreme limits.

From the example discussed above it is clear that establishing a *phase-stable* local oscillator field for detection of the time-resolved SHG signal is essential in order to unambiguously understand the underlying dynamics which correspond to a measured signal. However, the implementation of this scheme is practically very challenging as discussed in Appendix C.1. The challenges are more pronounced in the case of a system with center of symmetry such as  $\text{YBa}_2\text{Cu}_3\text{O}_{6+x}$ , as there is no static SHG signal with which to establish temporal and spatial overlap with the local oscillator field on the detector, and the number of generated hyper-Raman photons is very small.

In the optical setup used for the time-resolved SHG experiments in  $\text{YBa}_2\text{Cu}_3\text{O}_{6+x}$ , which will be presented in the following sections, a weak, stray and uncontrollable SHG was present that acted as an  $E_{\text{Lo}}$  as measured and reported in [22].

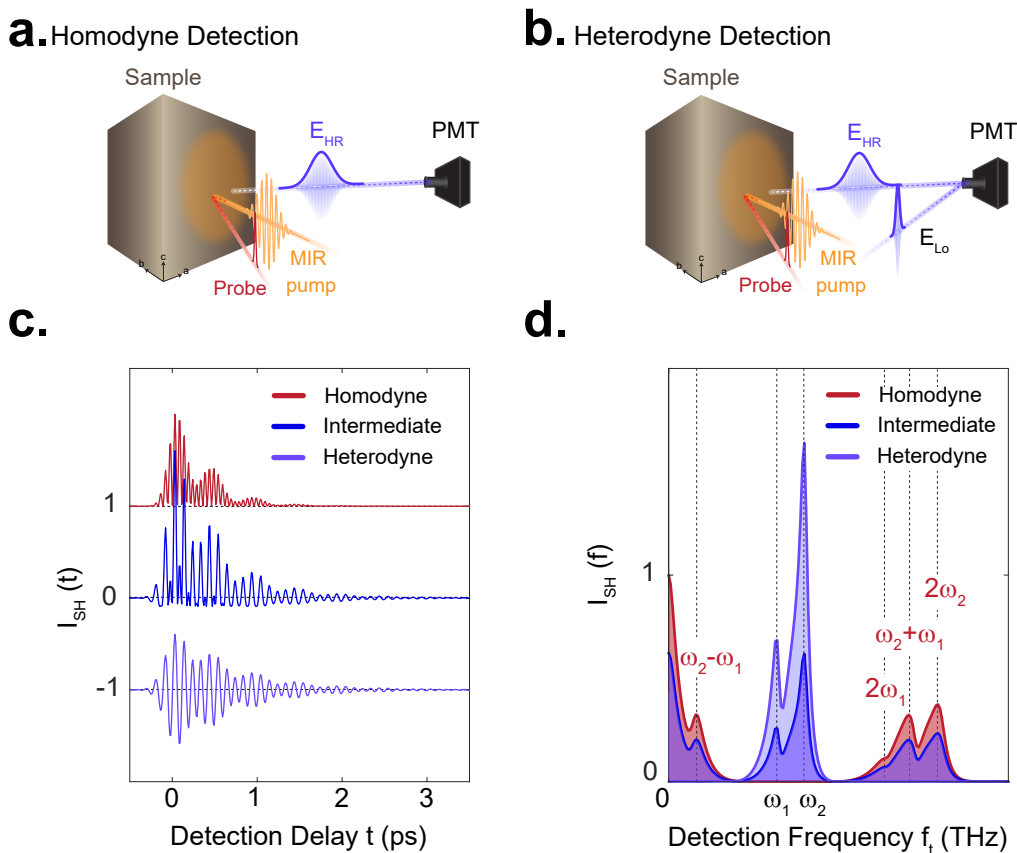


**Figure 4.6:** (a). Homodyne detection scheme: symmetry-breaking, IR-active modes of a centro-symmetric system were excited via mid-IR pump pulses. The resulting symmetry-breaking dynamics interact with the probe pulse, generating hyper-Raman field  $E_{\text{HR}}$  which is then measured by a PMT detector as an intensity signal. Without the presence of any other electromagnetic field at the detector, the detected intensity reflects the dynamics as described by the first term of Eq.4.14  $I_{\text{Hom}} \approx |E_{\text{SH}}|^2$ . (b). Heterodyne-detection scheme: Here, the hyper-Raman field generated in the sample is combined with a reference beam  $E_{\text{Lo}}$  on the detector. The interference between these two fields is measured, as captured by the second term of Eq.4.14  $I_{\text{HetSH}} E_{\text{Lo}} \cos(\phi)$ . (c) Exemplary time domain responses of two resonantly driven modes  $Q_1$  and  $Q_2$ , simulated for for three different values of  $E_{\text{Lo}}$ , as explained in the text. (d). The Normalized Fourier spectrum of (c).

## 4.5. Coherent Dynamics of the Symmetry-Odd modes in $\text{YBa}_2\text{Cu}_3\text{O}_{6+x}$

### 4.4.6 Experimental Setup

The experimental setup used for the mid-IR pump, time-resolved SHG probe experiments is the same as shown in Fig.4.3(a) and (b) for mid-IR generation (highlighted in yellow) and tr-SHG probe (highlighted in blue). The linearly polarized mid-IR pump pulses photo-excite the sample at normal incidence and the pump-induced dynamics in the sample were measured using time-resolved SHG of the 800 nm-wavelength probe pulses, which were focused to a spot diameter  $\approx 30 \mu\text{m}$  and overlapped with the mid-IR excitation pulses in a non-collinear geometry. Both mid-IR pump and probe pulses were polarized along the c-axis of here  $\text{YBa}_2\text{Cu}_3\text{O}_{6+x}$ , the studied sample in this thesis. The SH response was collected in reflection, whilst the fundamental beam was blocked by a high-pass filter. The SHG intensity was then measured using a photomultiplier (PMT) detector.

## 4.5 Coherent Dynamics of the Symmetry-Odd modes in $\text{YBa}_2\text{Cu}_3\text{O}_{6+x}$

The dynamics of  $\text{YBa}_2\text{Cu}_3\text{O}_{6+x}$  under the same phonon drive which was previously shown to induce superconducting-like macroscopic properties (as reviewed in Chapter 3) has recently been studied in single-pump time and SHG probe experiments [22]. The experimental schematic is shown in Fig.4.7(a). Concomitant with the mid-infrared excitation pulse which was polarized along the c-axis, a 30-fs ultrafast NIR probe pulse of center wavelength 800 nm and also polarized along the c-axis was incident on the sample, and the pump-induced SHG was measured. Because  $\text{YBa}_2\text{Cu}_3\text{O}_{6+x}$  is a centro-symmetric system, the equilibrium second harmonic signal is zero.

However, as explained in section 4.4.4, coherent motion of infrared-active modes (here the c-axis apical oxygen phonon modes), which dynamically break inversion symmetry twice per cycle, results in a time-delay dependent SHG intensity  $I_{\text{SH}}$ . An exemplary SH intensity response measured in the superconducting phase below  $T_c$  is displayed in Figs.4.7(b).

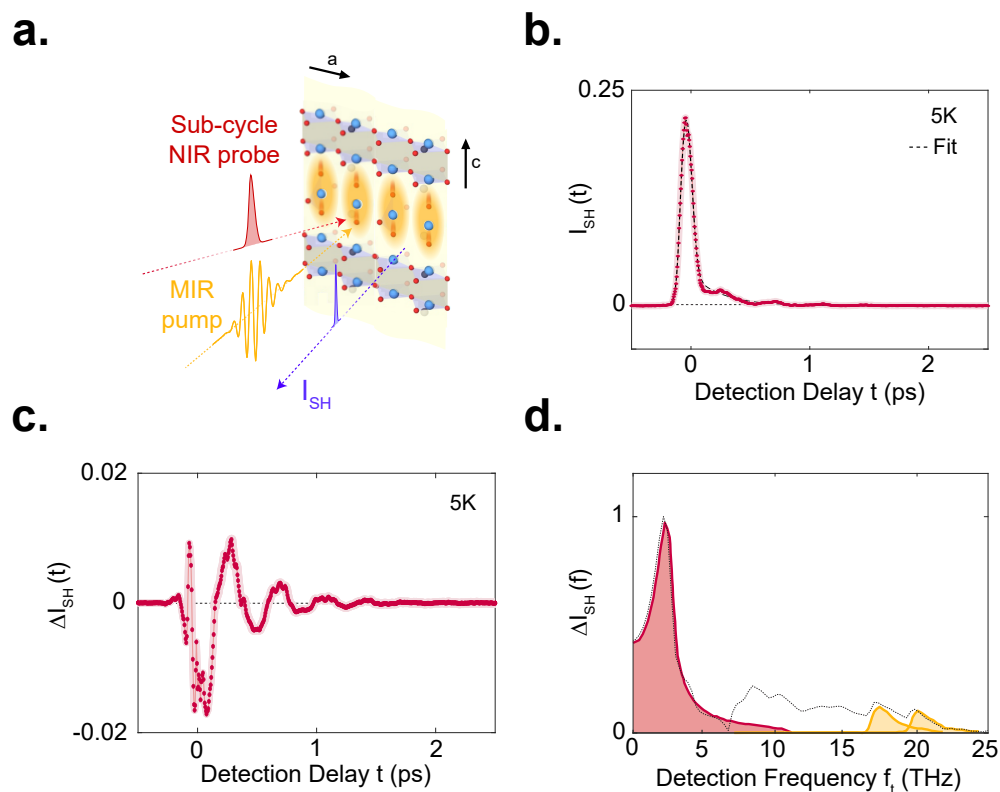


**Figure 4.7:** (a). Schematic of the mid-IR pump – time-resolved SHG probe experiment in  $\text{YBa}_2\text{Cu}_3\text{O}_{6.48}$ . Here, the CEP stable mid-IR pump pulses polarized along the crystal c-axis (shown in yellow) resonantly excite the apical oxygen phonon modes. The subsequent dynamics are probed by collecting the second harmonic intensity (blue) generated from a 800 nm femtosecond probe pulses (red), also polarized along the c-axis as a function of detection delay  $t$ . (b). and (c). Changes in the second harmonic intensity, respectively without and with D.C. background subtraction, as a function of pump-probe time delay measured at a base temperature of 5 K, below  $T_c$ . (d). Corresponding Fourier spectrum, highlighting the two resonantly excited apical oxygen phonons at 17 and 20 THz in yellow, and the low-frequency amplified Josephson plasmon polariton in red [22].

#### 4.5. Coherent Dynamics of the Symmetry-Odd modes in $\text{YBa}_2\text{Cu}_3\text{O}_{6+x}$

To better focus on the coherent oscillations, the D.C. background component in Figs.4.7(b) which originates from the homodyne contributions of the EFISH and all coherently excited modes, was removed as shown in Fig.4.7 panel(c), denoted as  $\Delta I_{\text{SH}}$ . As shown and highlighted in the corresponding Fourier spectrum in Fig.4.7(d), these coherent oscillations consist of three contributions at  $\omega/2\pi = 17$  THz, 20 THz and  $\approx 3$  THz.

The peaks at  $\omega/2\pi = 17$  THz and  $\omega/2\pi = 20$  THz were attributed to the response of the  $B_{1u}$ -symmetry apical oxygen phonon modes, driven resonantly by the mid-IR pump pulses (see table 3.1). Fluence-dependent measurements showed that these peaks are present even at lower pump fluences, and grow linearly as a function of pump electric field. The low-frequency mode has a frequency which does not coincide with any known IR-active phonon mode in  $\text{YBa}_2\text{Cu}_3\text{O}_{6.48}$  (see Fig.3.5 and refs.[48, 49]). This peak was characterized and attributed to a finite-momentum Josephson plasmon polariton (JPP). In this case, fluence-dependent measurements (plotted here in Fig.4.8(a)) showed that the amplitude of this mode grows exponentially as a function of the amplitude of the driven phonons. This was suggested to result from a parametric amplification process between the driven phonons and the low-frequency JPP [22, 74].

Figure.4.8(b) summarizes the temperature dependence of the driven phonon modes and the low-frequency JPP, revealing a mean-field behavior ( $\approx \sqrt{1 - T/T^*}$ ) for the JPP with  $T^* \approx 380$  K being the relevant temperature scale. This temperature scale also matched that of the photo-induced superconducting-like THz response observed under the same phonon drive (Fig.3.8(b)), drawing a connection between the two experimental observations [22, 64–66].

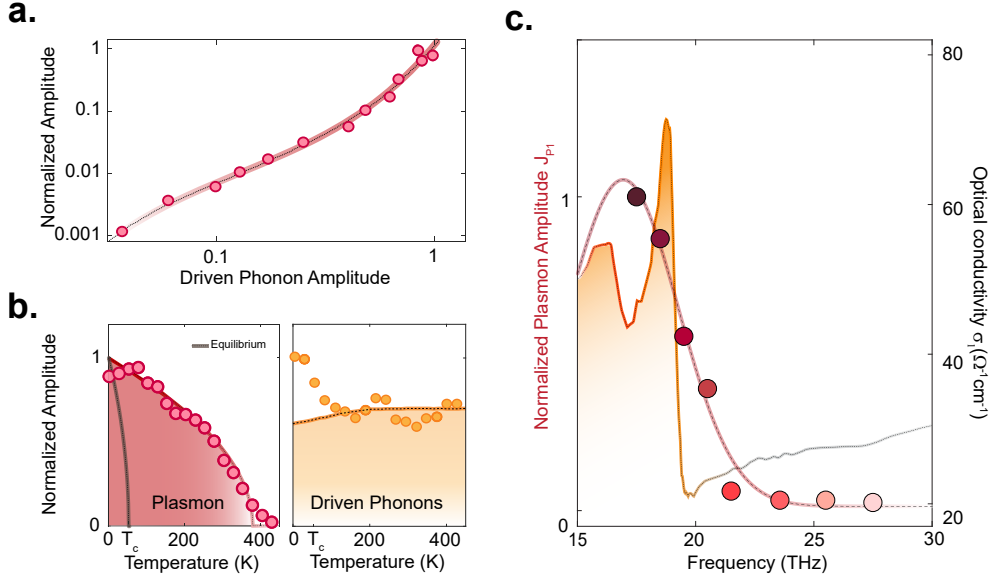


**Figure 4.8:** (a). Amplitude of the amplified JPP at  $\approx 3$  THz plotted as a function of apical oxygen driven phonon amplitude. These quantities were extracted from the measured time-domain response in  $\text{YBa}_2\text{Cu}_3\text{O}_{6.48}$  for different mid-IR pump driving field strength. The fit shown to the data points has a functional form of  $f = A\exp^{\alpha Q_d} - \beta$ . (b). Amplitude of the amplified JPP (left plot-red circles) and the driven phonon (right plot-yellow circles), extracted from measured time-domain SHG response as a function of temperature. The fit to the JPP temperature dependence has a mean-field functional form  $\approx \sqrt{1 - T/T^*}$ , with  $T^* = 380$  K. The fit to the driven phonon temperature dependence is taken from [192] and also shown in Fig.3.6(d). With some anomalies observed in the range below  $T_c$ , the driven phonon amplitudes were found to be temperature-independent. (c). The amplitude of the amplified JPP extracted from the Fourier spectrum of the SHG response measured for each pump frequency at a fixed peak field of 5 MV/cm and a base temperature of 295 K, plotted as a function of mid-IR pump center-frequency, overlaid on the real part of the optical conductivity  $\sigma_1$  for the same temperature taken from [48]. The fit to the data points is a Gaussian function centered at 18 THz between the two apical oxygen phonon modes [22].

The phonon-driven nature of the observed JPP response was further explored by varying the pump-frequency whilst maintaining a constant pump peak electric field of  $5 \text{ MV}\cdot\text{cm}^{-1}$ . From this data, the amplitude of the low-frequency JPP peak was extracted and plotted as a function of drive frequency, as shown in Fig.4.8(c). It

was observed that the pump-frequency dependence of the JPP peak observed in these measurements aligns with that of the photo-induced THz superconducting-like features (plotted in Fig.3.8(a)[66]). The coherent response of the JPP is found to be maximal when *both* apical oxygen phonon modes are efficiently excited within the pump bandwidth [22].

## 4.6 Doping and Temperature Dependence

The mid-IR pump, tr-SHG experiments discussed above and reported in [22] provided a valuable insights into photo-induced coherent dynamics. However, the pump-probe measurements fell short in identifying the exact coupling mechanism. This limitation was due to the intrinsic ambiguity of pump-probe techniques, compounded by the presence of an uncontrollable local oscillator, which rendered the interpretation of the data ambiguous.

The detection of driven phonon modes at their eigenfrequencies suggested the presence of a small, yet uncontrollable, local oscillator. Additionally, the dominance of homodyne contributions during the early time-delay signal (see Fig.4.7 (b)), characterized by a significant D.C. component, indicates that these experiments were conducted in the strong homodyne regime. While these observations validate the interpretation of the 3 THz peak as a JPP, it remained unclear, whether this peak corresponded to a  $2\omega$  or a  $\omega$  component, as discussed in section4.4.5. Furthermore, the driven phonon-beating contribution ( $\omega_2 - \omega_1$ ), expected from the homodyne mixing should also be around 3 THz. These uncertainties underscored the challenges in fully characterizing the exact coupling dynamic.

As a step further in understanding and hence better comparison, these single mid-IR pump, tr-SHG probe experiments were also performed on the higher doping com-

pound  $\text{YBa}_2\text{Cu}_3\text{O}_{6.92}$ , with  $T_c = 91$  K and  $T^* = 160$  K. In this doping no signatures of photoinduced superconductivity have been observed [188].

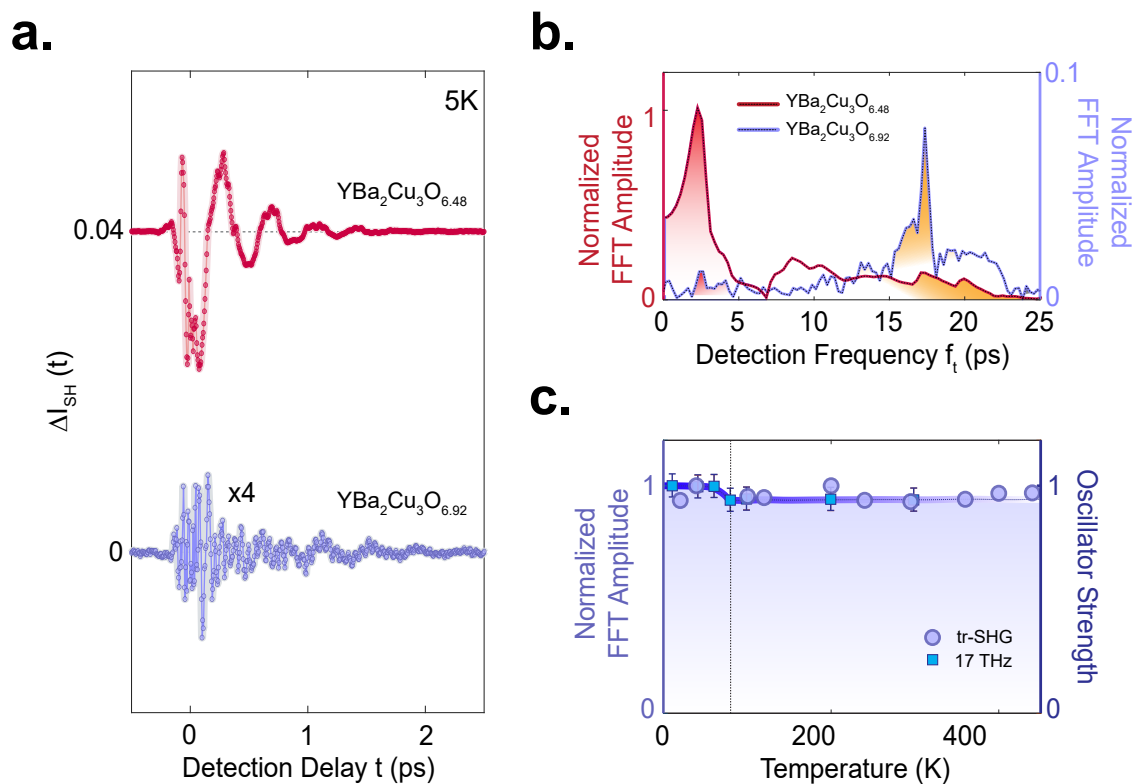


**Figure 4.9:** (a). Mid-IR pump induced changes in second harmonic intensity as a function of detection time delay  $t$  for  $\text{YBa}_2\text{Cu}_3\text{O}_{6.48}$  (red,  $T_c = 48$  K, excitation fluence of  $5 \text{ mJ}\cdot\text{cm}^{-2}$ ) [22] and  $\text{YBa}_2\text{Cu}_3\text{O}_{6.92}$  (blue,  $T_c = 91$  K, approximate excitation fluence of  $43 \text{ mJ}\cdot\text{cm}^{-2}$  nearly eight times higher than the underdoped measurement), both at base temperature of 5K (below  $T_c$ ). (b). Normalized Fourier transform amplitude of the data shown in (a), for  $\text{YBa}_2\text{Cu}_3\text{O}_{6.48}$  (red) and  $\text{YBa}_2\text{Cu}_3\text{O}_{6.92}$  (blue). Both FFTs are normalized to the maximum value of the FFT shown for  $\text{YBa}_2\text{Cu}_3\text{O}_{6.48}$ . The red and yellow shadings indicate the peak at 3 THz and phonon peaks at 17 THz and 20 THz, respectively. (c). Normalized total integrated amplitude of the FFT of the mid-IR pump induced changes in second harmonic intensity of  $\text{YBa}_2\text{Cu}_3\text{O}_{6.92}$  as a function of temperature [199] overlaid on the extracted oscillator strength of the 17 THz phonon mode [192], showing temperature in-dependent behavior.

At this doping, the apical oxygen phonon frequencies are the same as those of

$\text{YBa}_2\text{Cu}_3\text{O}_{6.48}$  but the zero-momentum inter-bilayer Josephson plasma resonance is blue-shifted to 7 THz [48, 135]. Figure 4.9(a) compares the coherent contributions to the single-pump probe tr-SHG intensity for  $\text{YBa}_2\text{Cu}_3\text{O}_{6.48}$  and  $\text{YBa}_2\text{Cu}_3\text{O}_{6.92}$ , measured at a sample temperature of 5 K. Both curves include high-frequency oscillations of the driven phonons, whilst the lower-frequency oscillations are heavily suppressed in  $\text{YBa}_2\text{Cu}_3\text{O}_{6.92}$  compared to  $\text{YBa}_2\text{Cu}_3\text{O}_{6.48}$  (see Fig. 4.9(a)).

As shown also in the Fourier spectrum in Fig. 4.9(b), although in both compounds the peaks appear at the same frequency positions, the relative amplitudes of the other peaks compared to those of the resonantly driven phonons are weaker in the  $\text{YBa}_2\text{Cu}_3\text{O}_{6.92}$  compound. Moreover, the integrated SH intensity measured in the higher doping remained temperature in-dependent for all measured temperatures as shown in Fig. 4.9 (c), emphasizing on the different nature of the low-frequency oscillations observed in  $\text{YBa}_2\text{Cu}_3\text{O}_{6.92}$  compared to those seen in  $\text{YBa}_2\text{Cu}_3\text{O}_{6.48}$ .

## 4.7 Summary and Outlook

The discussion in this Chapter was devoted to the previously reported pump-probe measurements in  $\text{YBa}_2\text{Cu}_3\text{O}_{6.48}$  which aimed at understanding the microscopic physics underlying the formation of the photo-induced superconducting-like state. These experiments were then combined with new measurements in the higher doped compound  $\text{YBa}_2\text{Cu}_3\text{O}_{6.92}$ , to provide a full, detailed comparison.

We began with a detailed review of the single mid-IR pump, polarization rotation experiments, which revealed the coherent dynamics of the symmetry-even modes in both compounds. In these measurements both doping levels showed a very similar response, consisting of oscillations frequencies which coincide with three known fully symmetric  $A_g$  Raman modes.

We then turned to single mid-IR pump, tr-SHG probe experiments which are instead sensitive to the coherent dynamics of the symmetry-odd modes, revealing the amplification of oscillations at a frequency of 3 THz, much lower than the drive frequency. The amplitude of these oscillations was observed to decrease with temperature, becoming negligible at approximately  $T^*$ . These oscillations were attributed to low-frequency finite-momentum Josephson plasmon polaritons (JPPs). A response with similar frequency content was also observed in the new experiments which were carried out in the higher doped compound, however, in this case the low-frequency oscillations were much smaller in magnitude, and displayed no temperature dependence throughout the measured range.

These one-dimensional measurements cannot directly pinpoint the precise microscopic coupling mechanism between the apical oxygen phonon modes and the JPPs. Additionally, the lack of an experimentally controllable phase-stable local oscillator adds an extra degree of uncertainty to the interpretation of these results. In the next chapter, we will describe experiments carried out using a newly-developed form of two-dimensional spectroscopy, which offers a direct observation of the coupling mechanism between these modes, allowing us to significantly improve our understanding of these dynamics, and consequently the underlying physics of the non-equilibrium superconducting-like state in  $\text{YBa}_2\text{Cu}_3\text{O}_{6+x}$ .

# Chapter 5

## Multidimensional Phononics in

## $\text{YBa}_2\text{Cu}_3\text{O}_{6+x}$

### 5.1 Introduction

In Chapter 4 a series of earlier single mid-IR pump-probe experiments were summarized, which revealed the coherent dynamics of both the symmetry-even and odd modes in the photo-induced state of  $\text{YBa}_2\text{Cu}_3\text{O}_{6.48}$  [22, 72]. New complementary measurements carried out on  $\text{YBa}_2\text{Cu}_3\text{O}_{6.92}$ , a higher-doped version of this compound, were also presented. Of particular interest was the observation of large oscillations in the SHG intensity at a frequency of around 3 THz. These oscillations were observed to be comparatively much larger in the under-doped compound, in which they were attributed to amplified JPPs. These amplified JPPs could possibly be the key to understanding the emergence of the photo-induced superconducting-like macroscopic properties in  $\text{YBa}_2\text{Cu}_3\text{O}_{6.48}$  [22]. However, in order to form a full understanding, it is crucial to disentangle the inter-mode coupling terms in the Hamiltonian that describes the driven state.

For this purpose, the single pump-probe experiments are limited, because they do not provide a direct measurement of the nonlinear coupling between different modes of the system which is presumably responsible for the formation of the non-equilibrium state. In recent years, THz spectroscopy has been extended into multiple dimensions by using more than a single pulse to sequentially excite the sample. This technique has many advantages compared to the single-excitation experiments including that the inter-mode couplings can often be directly mapped out in the obtained multi-dimensional frequency map [75–85].

In the study presented in this thesis, we combined the principles of multi-dimensional spectroscopy with the NIR-probing described earlier. We conducted experiments in which we excite the sample twice with CEP stable mid-IR pulses and then probe the dynamics using either tr-polarization rotation or tr-SHG, with the aim of addressing the questions which remained open from the previous one-dimensional experiments. In this chapter, we first introduce the idea of the *two-dimensional mid-IR nonlinear spectroscopy* used in these experiments, before presenting the results obtained by applying these techniques to  $\text{YBa}_2\text{Cu}_3\text{O}_{6+x}$ .

## 5.2 Two-Pulse Excitation

The general idea of a two-pulse excitation experiment can be intuitively understood by considering the motion of a simple harmonic pendulum. In this picture, the displacement of a collective excitation of the system can be represented by the coordinate of such a pendulum. In the absence of the excitation pulse, this pendulum remains stationary in the equilibrium position (neglecting any possible equilibrium fluctuations). Following a single excitation pulse, denoted as  $E_A$  or  $E_B$ , which drives the pendulum impulsively, the pendulum undergoes harmonic oscillations around

its equilibrium position. While it is still oscillating, after a time delay denoted by  $\tau$ , the second pump gives the pendulum a second kick. Depending on the value of  $\tau$ , the pendulum will oscillate with either an increased or reduced amplitude, depending on whether the second pulse arrives in or out of phase with respect to the pendulum oscillation at the instant it arrives. This idea is illustrated visually in Fig.5.1.

In the limit of linear response, the combined response for when both pump pulses act on the pendulum ( $R_{AB}$ ) will be equal to the sum of the responses which would result from each individual pump pulse acting in isolation ( $R_A + R_B$ ):  $R_{AB} - (R_A + R_B) = 0$ . On the other hand, if the pump pulses are intense enough

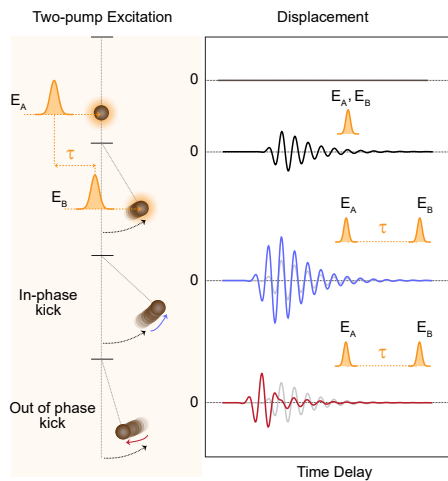


**Figure 5.1:** The two-pulse excitation technique can be likened to a pendulum being driven by timed impulses. Initially, a resonant pulse excites the pendulum, inducing harmonic motion around its equilibrium with a phase offset. After a controlled delay, a second pulse interacts with the already oscillating pendulum. The outcome depends on the synchronization between the second pulse and the pendulum’s motion: an in-phase push amplifies the oscillation, while an out-of-phase interaction suppresses it. By varying the delay between the pulses, a periodic pattern emerges due to the constructive and destructive interference, capturing the interplay of phase and oscillation frequency in the system.

for the motion of the pendulum to enter a nonlinear regime, this will not be the

case, and a nonzero nonlinear response ( $R_{\text{NL}}$ ) can be measured which is defined as  $R_{\text{NL}} = R_{\text{AB}} - (R_{\text{A}} + R_{\text{B}})$ .

One important advantage of the multidimensional spectroscopy techniques lies with the possibility of isolating this nonlinear component of the response, which in fact directly reports on the interesting nonlinear interactions of the system upon two-pump excitation [75, 80–83, 215]. The general pendulum picture discussed here can be extended to any type of excitation and any nonlinear order in the Hamiltonian of the system, and will be used later on in the next chapter when discussing the microscopic dynamics of the phonon-driven state of  $\text{YBa}_2\text{Cu}_3\text{O}_{6+x}$ .

### 5.3 Two-Dimensional Mid-IR Nonlinear Spectroscopy

Two-dimensional mid-IR nonlinear spectroscopy was used to study the driven state of  $\text{YBa}_2\text{Cu}_3\text{O}_{6+x}$ , and in particular  $\text{YBa}_2\text{Cu}_3\text{O}_{6.48}$ , with the aim of unambiguously identifying the inter-mode coupling processes responsible for the amplification of amplified JPPs and hence the formation of photo-induced superconductivity. In these experiments, as sketched in Fig.5.2(a), the two mid-infrared excitation pulses with electric fields denoted by  $E_{\text{A}} \approx 8 \text{ MV.cm}^{-1}$  and  $E_{\text{B}} \approx 5 \text{ MV.cm}^{-1}$ , resonantly drive the c-axis apical oxygen phonon modes at two instants in time, separated by a controllable time delay  $\tau$  which is referred to as the **Excitation delay**.

The subsequent coherent dynamics of the symmetry-even and odd modes were then sampled via either the polarization rotation ( $\Delta E_{\text{PR}}$ ) or SHG ( $I_{\text{SH}}$ ) of the near-infrared probe pulse at a time delay  $t$ , defined relative to the arrival time of the last excitation pulse (depending on the pulse ordering, either  $E_{\text{A}}$  or  $E_{\text{B}}$ ) and referred to

### 5.3. Two-Dimensional Mid-IR Nonlinear Spectroscopy

as the *Detection delay*.

Following the idea of conventional 2D-THz spectroscopy, the cooperative nonlinear contribution to the tr-SHG intensity  $I_{NL}$  from both of the pump pulses was extracted by subtracting the isolated tr-SHG responses  $I_A$  and  $I_B$  (to only pulse  $E_A$  and  $E_B$ , respectively), from the response  $I_{AB}$  (to both the excitation pulses):

$$I_{NL} = I_{AB} - I_A - I_B \quad (5.1)$$

Analogously, the isolated nonlinear contribution to the polarization rotation was

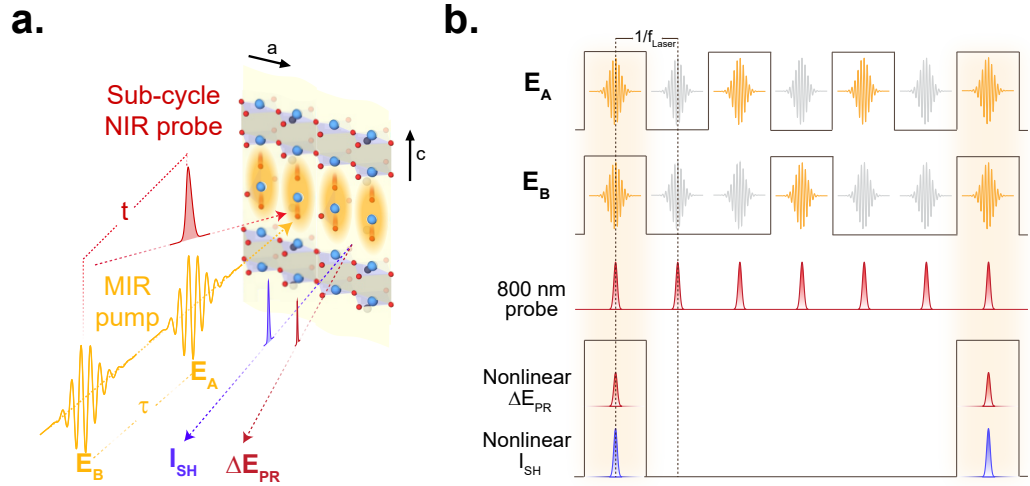


**Figure 5.2:** (a). Schematic of the multidimensional mid-IR nonlinear spectroscopy experiment. Two CEP stable mid-IR pump pulses  $E_A$  and  $E_B$  polarized along the c-axis of  $YBa_2Cu_3O_{6+x}$ , separated by the excitation time delay  $\tau$  resonantly and sequentially excite c-axis apical oxygen phonon modes. The photo-induced dynamics were measured using tr-SHG  $I_{SH}$  and tr-polarization rotation  $\Delta E_{PR}$  of near-infrared probe pulses after time delay  $t$  with respect to the last excitation pulse [199]. (b). Mid-IR pulses chopping scheme which was used to isolate the nonlinear contribution to  $I_{SH}$  and  $\Delta E_{PR}$ . Accordingly, for each pulse, only every second ( $f_{Laser}/2$ ) and every third ( $f_{Laser}/3$ ) pulse of pulses  $E_A$  and  $E_B$ , respectively, were allowed to pass. Consequently, the nonlinear contribution was detected at a frequency of  $f_{Laser}/6 = f_{Laser}/2 \times f_{Laser}/3$ , which corresponds to the intersection of all three pulses— $E_A$ ,  $E_B$ , and the probe—when they coincided.

measured, defined as:

$$\Delta E_{NL} = \Delta E_{AB} - \Delta E_A - \Delta E_B \quad (5.2)$$

Experimentally these nonlinear signals were obtained by mechanically chopping the two excitation pulses at frequencies  $1/2$  and  $1/3$  of the laser repetition rate  $f_{\text{Laser}}$  and measuring the nonlinear contribution at  $f_{\text{Laser}}/6$ . This chopping scheme is shown in Fig.5.2(b) [199].

### 5.3.1 Experimental Setup

Figure 5.3 illustrates the nonlinear two-dimensional spectroscopy experiment. The two separate mid-IR pulses were obtained by splitting the DFG output, which was generated as explained in section 4.2.3, closely behind the GaSe crystal using a gold coated prism, as shown in Fig.5.3(a) and (b). One of the two pulses,  $E_A$ , passed over a delay stage, used to control the excitation time delay  $\tau$ , before being spatially recombined with  $E_B$  and focused onto the sample in a quasi-co-linear geometry. The spot diameters of both beams were  $\approx 100 \mu\text{m}$  on the sample, giving a fluence of  $12 \mu\text{J}$  and  $6 \mu\text{J}$  for  $E_A$  and  $E_B$ , respectively.

Both pulses  $E_A$  and  $E_B$  were individually characterized by electro-optic sampling. Figure 5.3(c) shows that both the time profile and the spectral content were very similar compared to the single pulse used in the one-dimensional experiments which was shown in Fig.4.3(c). The time-delay dependent second harmonic intensity was detected as explained in section 4.4.5. The nonlinear signal was isolated according to the chopping scheme shown in Fig.5.2(b). The time-delay dependent nonlinear polarization rotation of the 800 nm pulses was measured as explained in section 4.2.2 in parallel with the second harmonic intensity [199].

### 5.3. Two-Dimensional Mid-IR Nonlinear Spectroscopy

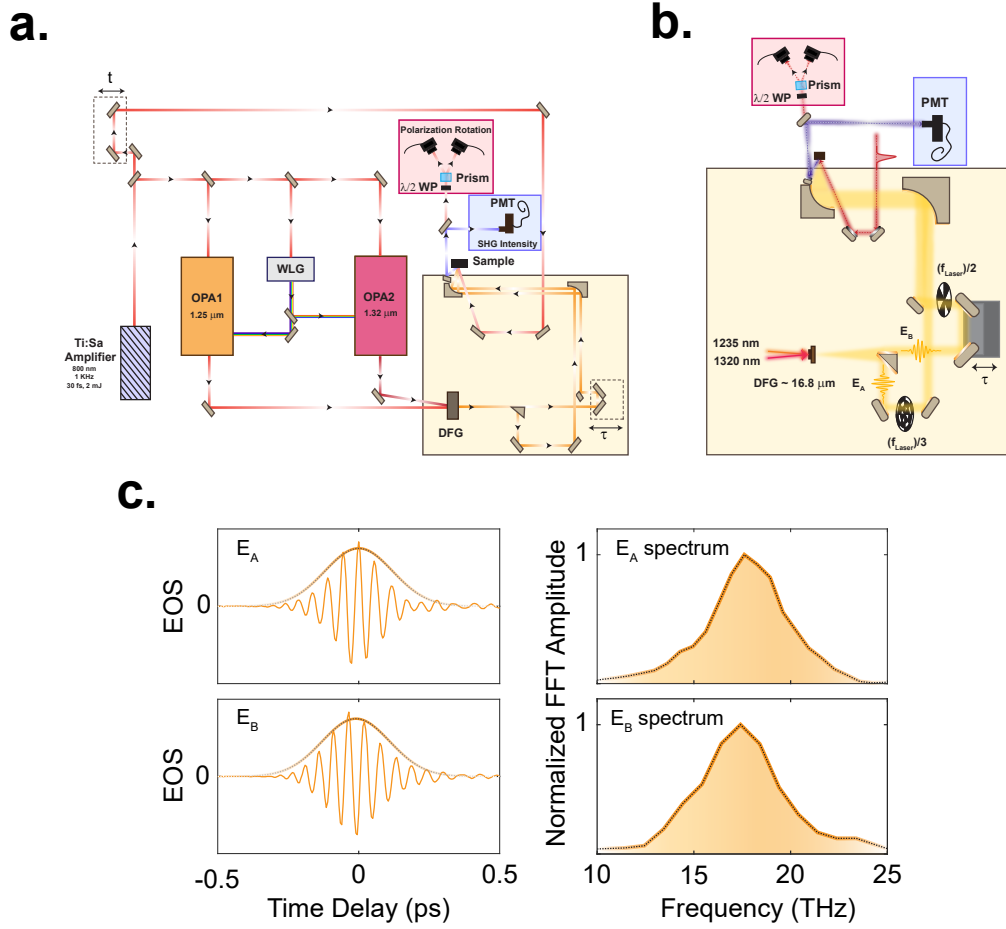


**Figure 5.3:** (a). Same as in Fig.4.3 (a). (b). The generated mid-IR pump pulses were split up to half using a gold coated right-angle prism (shown as  $E_A$  and  $E_B$ ). Before  $E_A$  and  $E_B$  were combined and focused onto the sample, they were delayed and chopped at  $\frac{1}{2}f_{\text{Laser}}$  and  $\frac{1}{3}f_{\text{Laser}}$ , respectively. The photo-induced changes after mid-IR excitation in both the SHG intensity and polarization rotation were detected at  $\frac{1}{6}f_{\text{Laser}}$ , otherwise as described in Fig. 4.3. (c). Electro-optic sampling characterization of the two mid-IR excitation pulses  $E_A$  and  $E_B$  along with their corresponding Fourier amplitudes. The pulses were centered at 17 THz [199].

## 5.4 Multidimensional tr-Polarization Rotation In $\text{YBa}_2\text{Cu}_3\text{O}_{6+x}$

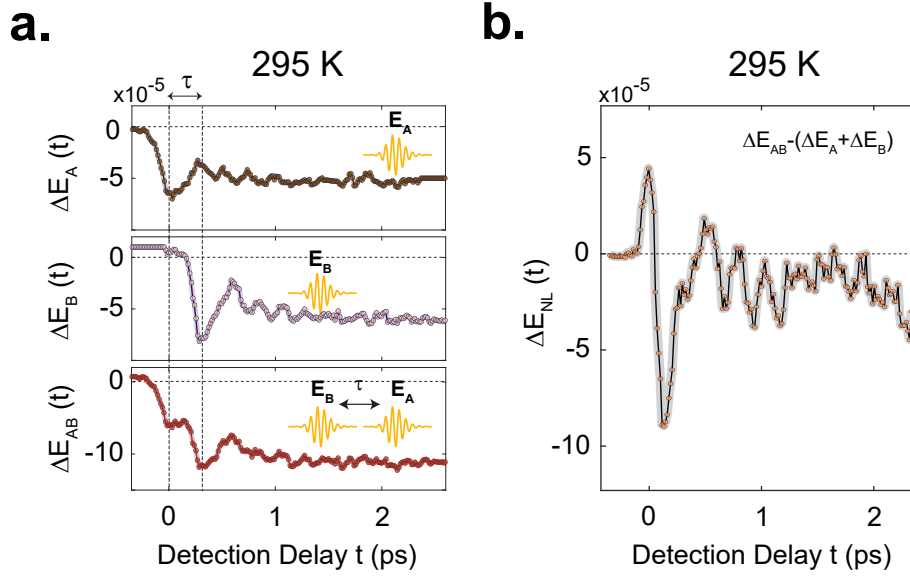
We start by focusing on the time-resolved polarization rotation measurements, which is sensitive to the symmetry-even (Raman) modes. This represents the first direct inspection of the coupling mechanism between the two resonantly driven apical oxygen modes and the symmetry-even  $A_g$  coupled Raman modes which were previously observed to oscillate coherently in the single pump-probe experiment described in section 4.3.

Figure 5.4 summarizes the tr-polarization rotation measured in  $\text{YBa}_2\text{Cu}_3\text{O}_{6.92}$  in three different excitation schemes along with a snapshot of  $\Delta E_{\text{NL}}$  for a fixed excitation delay  $\tau = 0.04$  ps, measured at room temperature. As expected, the measured responses  $\Delta E_{\text{PR,A}}$  and  $\Delta E_{\text{PR,B}}$  resemble the dynamics presented in the one-dimensional experiment in Fig. 4.4 (d) and (f). Moreover, the two sequential minima in  $\Delta E_{\text{PR,AB}}$  (highlighted by the vertical gray lines) imply the arrival of the two excitation pulses at two instants in time which correspond to the excitation delay between  $E_A$  and  $E_B$ .

The corresponding two-dimensional time-delay-dependent map of the nonlinear signal is shown in Fig. 5.5(a). To better visualize how the dynamics along each time-delay axis ( $\tau$  and  $t$ ) appear, snapshots of the nonlinear response along each time delay axis are also shown in Fig. 5.5(a). The nonlinear two-dimensional Fourier spectrum obtained from taking the Fourier transformation along both time axes, labeled as **excitation frequency axis**  $f_\tau$  and **detection frequency axis**  $f_t$ , along  $\tau$  and  $t$ , respectively, is displayed in Fig. 5.5(b).

The time domain snapshots show that the early-delay nonlinear response has a

rectified envelope. Therefore, in order to better observe the coherent oscillations which dominate the signal at later delays, the time domain map was cropped, as plotted in Fig.5.5 (c). The cropping was done by multiplying a smooth error function as written in Eq.5.3 to the measured nonlinear signal along each time axis. The two-dimensional Fourier transform of the cropped data is then shown in panel (d).



**Figure 5.4:** (a). From top to bottom: time-resolved polarization rotation  $\Delta E_{\text{PR},A}$ ,  $\Delta E_{\text{PR},B}$  and  $\Delta E_{\text{PR},AB}$  measured following excitation by only  $E_A$  (approximate fluence  $\approx 12 \text{ mJ.cm}^{-2}$ ), by only  $E_B$  (approximate fluence  $\approx 6 \text{ mJ.cm}^{-2}$ ) after excitation delay  $\tau$  and by both pulses, respectively, at a base temperature of 295 K (above  $T_c$ ). (b). Nonlinear contribution to the time-resolved SHG intensity shown in panel (a), given as  $\Delta E_{\text{PR},AB} - \Delta E_{\text{PR},A} - \Delta E_{\text{PR},B}$ , and for base temperatures of 295 K [199].

$$f_{\text{cropping}} = (1 + \text{erf}(s - s_1)/s_2) \quad (5.3)$$

Here  $s$ ,  $s_1$  and  $s_2$ , refer to time delay axis ( $t$  or  $\tau$ ), cropping time and the rise time of the error function, respectively<sup>1</sup>.

<sup>1</sup>Whilst  $s_2$  was set to 0.1 ps in order not to introduce any artificial oscillations.

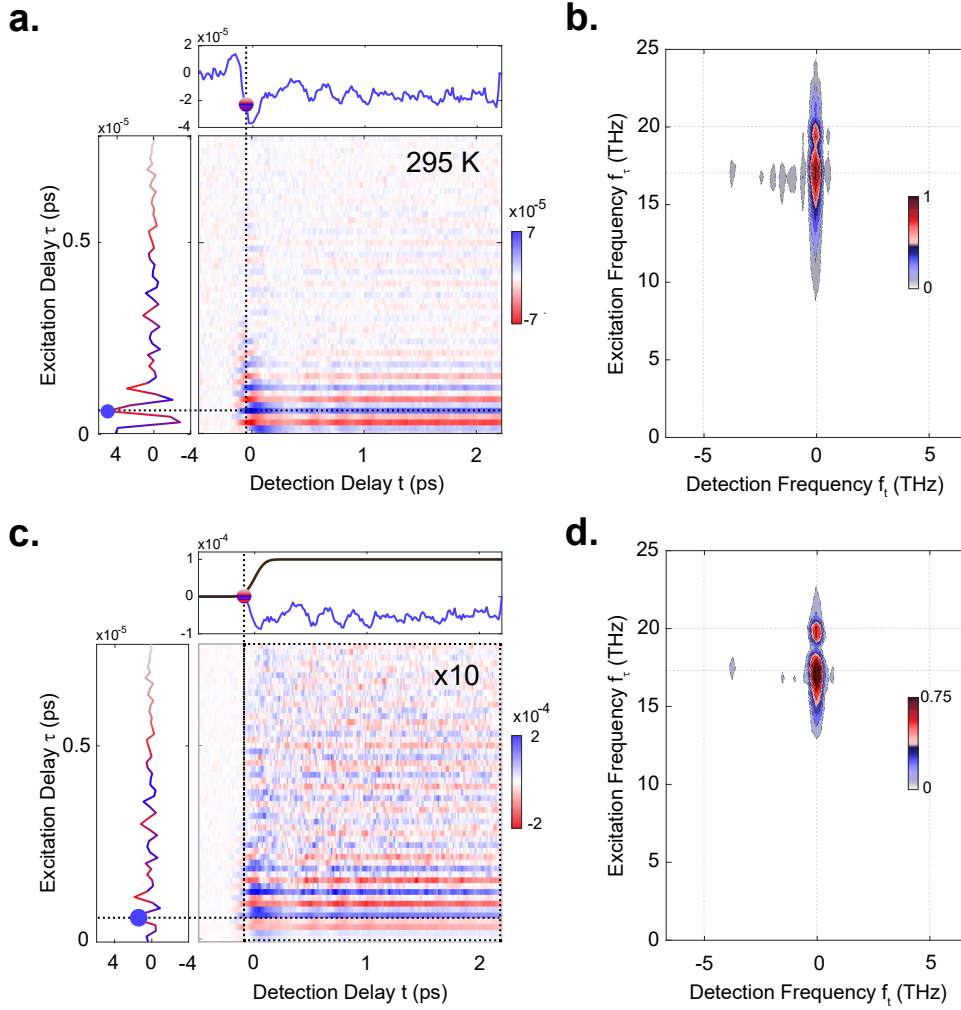


**Figure 5.5:** (a). Central plot: Uncropped nonlinear contributions to the time-resolved polarization rotation measured in  $\text{YBa}_2\text{Cu}_3\text{O}_{6.92}$  at base temperature 295 K above  $T_c$  with vertical (blue-shaded line) and horizontal (red line) slices of the data. Top plot: a horizontal slice of the data showing the nonlinear time-resolved polarization rotation as a function of detection delay ( $t$ ) for a chosen excitation delay ( $\tau = 0.04$  ps). Left plot: a vertical slice of the data showing the nonlinear time-resolved polarization rotation as a function of excitation delay ( $\tau$ ) for a chosen detection delay ( $t = 0.135$  ps). (b). Normalized two-dimensional Fourier transform of the data shown in (a) before cropping. The spectrum is normalized to its own maximum value. (c). Central plot: same data as in (a) after cropping along the detection delay  $t$  axis. Top plot: the same horizontal slice of the data shown in (a) top panel after cropping, with the smooth error function pointed out in Eq.5.3 which is used to crop the data shown in black. Left plot: same vertical slice of the data as in (a) with no cropping. (d). Same as in (b) for (c) after cropping. For comparison, data in (d) are normalized to (b). There are two strong peaks at frequency coordinates ( $f_t; f_\tau$ ): (0; 17) and (0; 20) along with a weaker cross peak at (-3.6; 17), all in units of THz [199].

The resulting nonlinear two-dimensional frequency map clearly reveals two peaks at the frequency coordinates  $(f_t; f_\tau)$ ; (0 THz; 17 THz) and (0 THz; 20 THz) along with a comparatively weaker cross peak at (-3.6 THz; 17 THz). This 2D spectrum directly illustrates the nonlinear coupling between the resonantly driven infrared-active apical oxygen phonons and the Raman-active modes [199]. The specific peak pattern measured here indicates a third-order nonlinear coupling which was discussed in Chapter 1, section 1.6.2 in Eq. 1.25 ( $\propto Q_{\text{IR}}^2 Q_{\text{R}}$ ), and will be explained for the case of  $\text{YBa}_2\text{Cu}_3\text{O}_{6.92}$  in detail in Chapter 6 section 6.6.

## 5.5 Multidimensional tr-SHG In $\text{YBa}_2\text{Cu}_3\text{O}_{6+x}$

In this section we turn to the measurements of the time-resolved SHG, which is sensitive to the symmetry-odd (infrared-active) modes. The cooperative nonlinear contribution to the tr-SHG intensity  $I_{\text{NL}}$  measured in  $\text{YBa}_2\text{Cu}_3\text{O}_{6.48}$  from both of the pump pulses is extracted by subtracting the isolated tr-SHG responses  $I_{\text{A}}$  and  $I_{\text{B}}$  (to only pulse  $E_{\text{A}}$  and  $E_{\text{B}}$ ), respectively, from the response  $I_{\text{AB}}$  (to both the excitation pulses) as pointed out in Eq. 5.1. This procedure is illustrated in Fig. 5.6(a) for an excitation pulse delay  $\tau = 0.5$  ps between  $E_{\text{A}}$  and  $E_{\text{B}}$ .

The individual tr-SHG signals  $I_{\text{A}}$  and  $I_{\text{B}}$  each contain a rectified response due to electric-field induced SHG (EFISH) at early delays (see sections 4.4.3 and 4.4.5), which is then followed by the responses of the coherently driven phonons and the amplified plasmons. After subtraction,  $I_{\text{NL}}$  reveals coherent dynamics due to nonlinear interactions between different modes of the system. This nonlinear response is also observed to be strongly dependent on temperature, as shown for two sample temperatures 20 K and 295 K, shown in Fig. 5.6(b).

Measurements of  $I_{\text{NL}}$  as a function of both  $t$  and  $\tau$ , at a temperature of 20 K, yielded

the two-dimensional time domain map shown in Fig.5.7 (a). The corresponding two-dimensional Fourier spectrum is shown in Fig.5.7 (b). Representative vertical and horizontal slices of the 2D time map along the  $\tau$  and  $t$  axes, respectively, are also shown in order to help visualize the dynamics. From this data, it is clear that the  $\tau$ -axis dynamics are dominated by the resonantly excited phonon modes at 17 THz and 20 THz, similarly to the  $\tau$  axis dynamics plotted in Fig.5.5 for the polarization rotation measurements. This is in contrast to the  $t$ -axis dynamics, which are dominated by the coherent dynamics arising from all non-linearly coupled modes.

The non-linear signal at early time delays along the detection delay  $t$ -axis is dom-

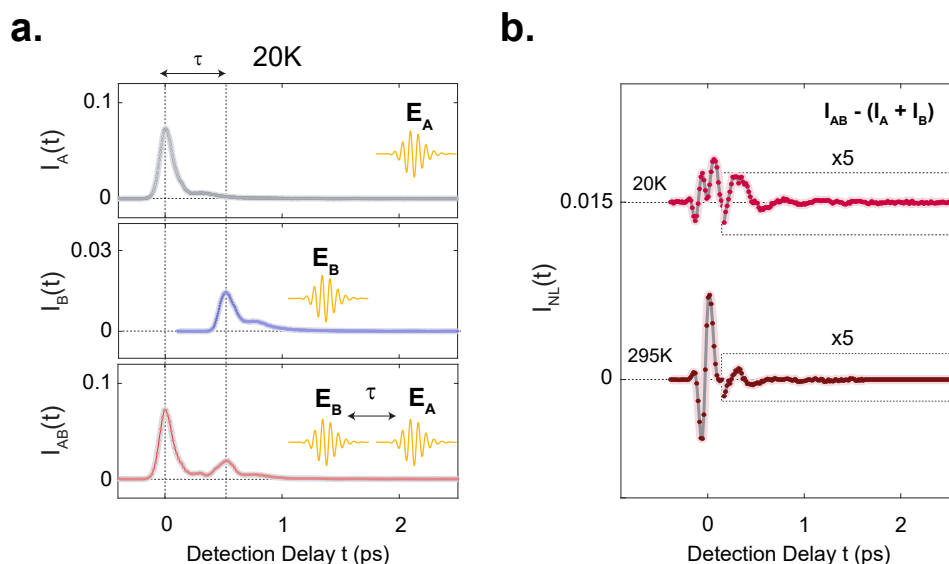


**Figure 5.6:** (a). From top to bottom: time-resolved SHG intensities  $I_A$ ,  $I_B$  and  $I_{AB}$  measured in  $\text{YBa}_2\text{Cu}_3\text{O}_{6.48}$  following excitation by only  $E_A$  (approximate fluence  $\approx 12 \text{ mJ.cm}^{-2}$ ), by only  $E_B$  (approximate fluence  $\approx 6 \text{ mJ.cm}^{-2}$ ) after excitation delay  $\tau$  and by both pulses, respectively, at a base temperature of 20 K (below  $T_c$ ). (b). Nonlinear contribution to the time-resolved SHG intensity shown in panel (a), given as  $(I_{AB} - I_A - I_B)$ , and for base temperatures of 20 K and 295 K (below and above  $T_c$ , respectively). The dashed rectangle frames the data at later time delays, which are enlarged by a factor of 5 for clarity [199].

inated by large rectified components of the homodyne contributions from the individual resonantly-excited modes (as explained in section 4.4.5 and in Eq.4.14), as well as mixing terms proportional to the electric fields  $E_A$  and  $E_B$  of the excitation pulses. More specifically, each pump pulse electric field results in a nonlinear polarization  $P_i(t') = \epsilon_0 \chi^{(3)} E_{\text{pump}}(t') E_{\text{pr}}^2(t' - t)$  which radiates two fields  $E_{A,\text{emit}}$  and  $E_{B,\text{emit}}$  the so-called EFISH as a result of  $E_A$  and  $E_B$ , respectively (see Eq.4.13).

In the second harmonic homodyne detection measurement, these fields are measured as  $I_{\text{SH},A} = |E_{A,\text{emit}}|^2$  for only pulse  $E_A$ ,  $I_{\text{SH},B} = |E_{B,\text{emit}}|^2$  for only pulse  $E_B$  and  $I_{\text{SH},AB} = |E_{A,\text{emit}} + E_{B,\text{emit}}|^2$  for when both excitation pulses  $E_{AB}$  are exciting the sample - neglecting all the other symmetry breaking contributions. From this the nonlinear second harmonic intensity can be derived as  $I_{\text{SH,NL}} = I_{\text{SH},AB} - I_{\text{SH},A} - I_{\text{SH},B} \propto E_{A,\text{emit}} E_{B,\text{emit}}$ . Similarly, the homodyne SHG component of the nonlinear mixing between the resonantly excited apical oxygen phonon modes dominates along the excitation axis  $\tau$ .

In order to enable a clear observation of the contribution to the two-dimensional Fourier spectrum from the longer-lived oscillatory response of the coupled modes, the data was cropped along both time axes. This was carried out by multiplying the raw data (along both time axes) by the same smooth error function given in Eq.5.3, with a rise time of 0.1 ps in all cases. The resulting two-dimensional cropped time-domain data and corresponding Fourier spectrum are shown in Figs.5.8 (c) and (d), which exhibit eight dominant peaks. There are two peaks at zero detection frequency with the corresponding frequency coordinates  $(f_t; f_\tau) = (0 \text{ THz}; 17 \text{ THz})$  and  $(0 \text{ THz}; 20 \text{ THz})$ . These peaks reflect the homodyne-detected nonlinear tr-SHG in response to either of the two apical oxygen phonon modes (as evidenced by their positions along the vertical  $f_\tau$  axis). The positions of the remaining two peaks at  $(-3 \text{ THz}; 17 \text{ THz})$  and  $(3 \text{ THz}; 20 \text{ THz})$  suggest that the dominant  $\approx 3 \text{ THz}$  response ob-

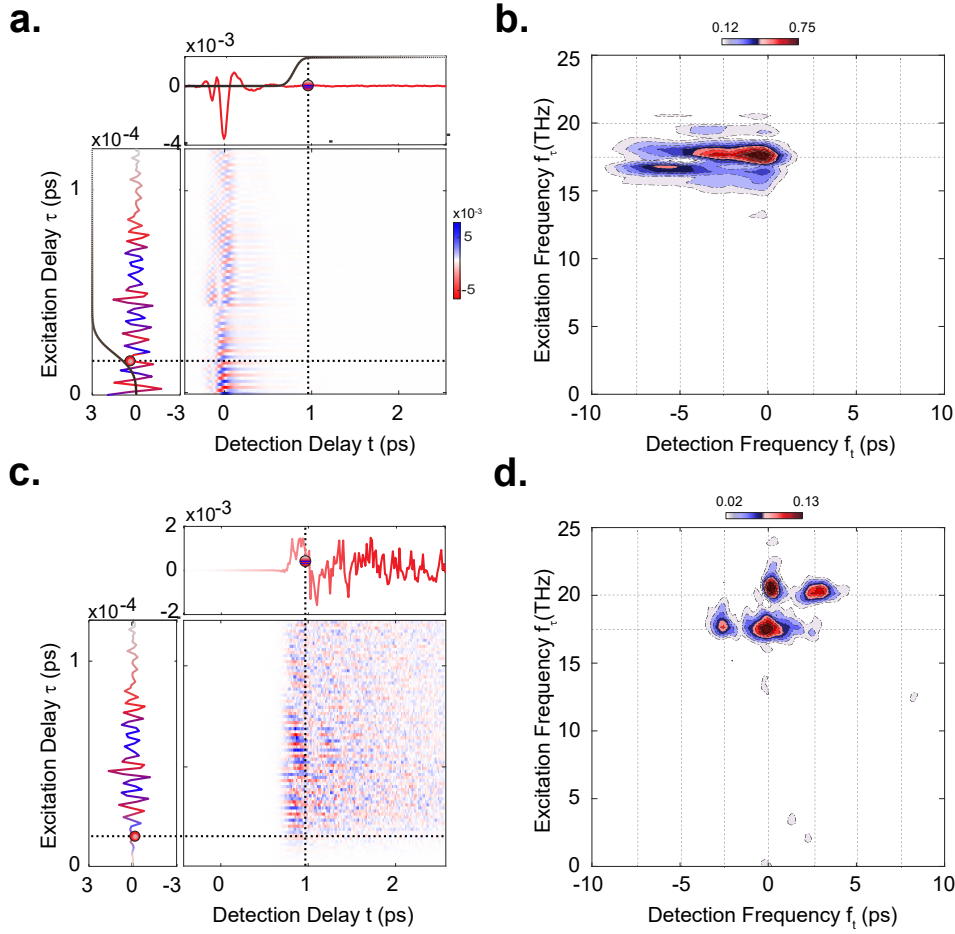


**Figure 5.7:** (a). Central plot: Uncropped nonlinear contributions to the time-resolved SHG intensity measured in  $\text{YBa}_2\text{Cu}_3\text{O}_{6.48}$  at base temperature 20 K below  $T_c$  with vertical (blue-shaded line) and horizontal (red-shaded line) slices of the data. Top plot: a horizontal slice of the data showing the nonlinear time-resolved SHG intensity as a function of detection delay ( $t$ ) for a chosen excitation delay ( $\tau = 0.13$  ps). Left plot: a vertical slice of the data showing the nonlinear time-resolved SHG intensity as a function of excitation delay ( $\tau$ ) for a chosen detection delay ( $t = 0.96$  ps). The black curve in both top and left plots indicates the smooth error function indicated in Eq.5.3 used to crop the data along detection and excitation delay, respectively. (b). Central plot: same data as in (a) after cropping along both time axis. Top plot: the same horizontal slice of the data shown in (a) top panel after cropping, magnified by a factor of 40. Left plot: same vertical slice of the data as in (a) left panel after cropping, magnified by a factor of 5. (c). Normalized two-dimensional Fourier transform of the data shown in (a) before cropping. (d). Same as in (c) for (b) after cropping. For comparison, data in (d) are normalized to (c). There are four peaks in the spectrum at frequency coordinates  $(f_t; f_\tau)$ :  $(-3; 17)$ ,  $(0; 17)$ ,  $(0; 20)$  and  $(3; 20)$ , all in units of THz [199].

served in the pump-probe experiment (see Fig.4.7(d) and reported in ref.[22]) results cooperatively from the excitation of *both* apical oxygen phonon modes [199].

Furthermore, the 2D peak patterns, as shown in Fig.5.8 (c) and (d), exhibit quantitative rather than qualitative differences when measured at low and high temperatures, specifically at 20 K and 295 K. Notably, the structure of the peaks remains consistent at both temperatures, but the peaks broaden as the temperature increases. The temperature-dependent behavior of the 2D response will be discussed in more detail in the following section, section5.6.

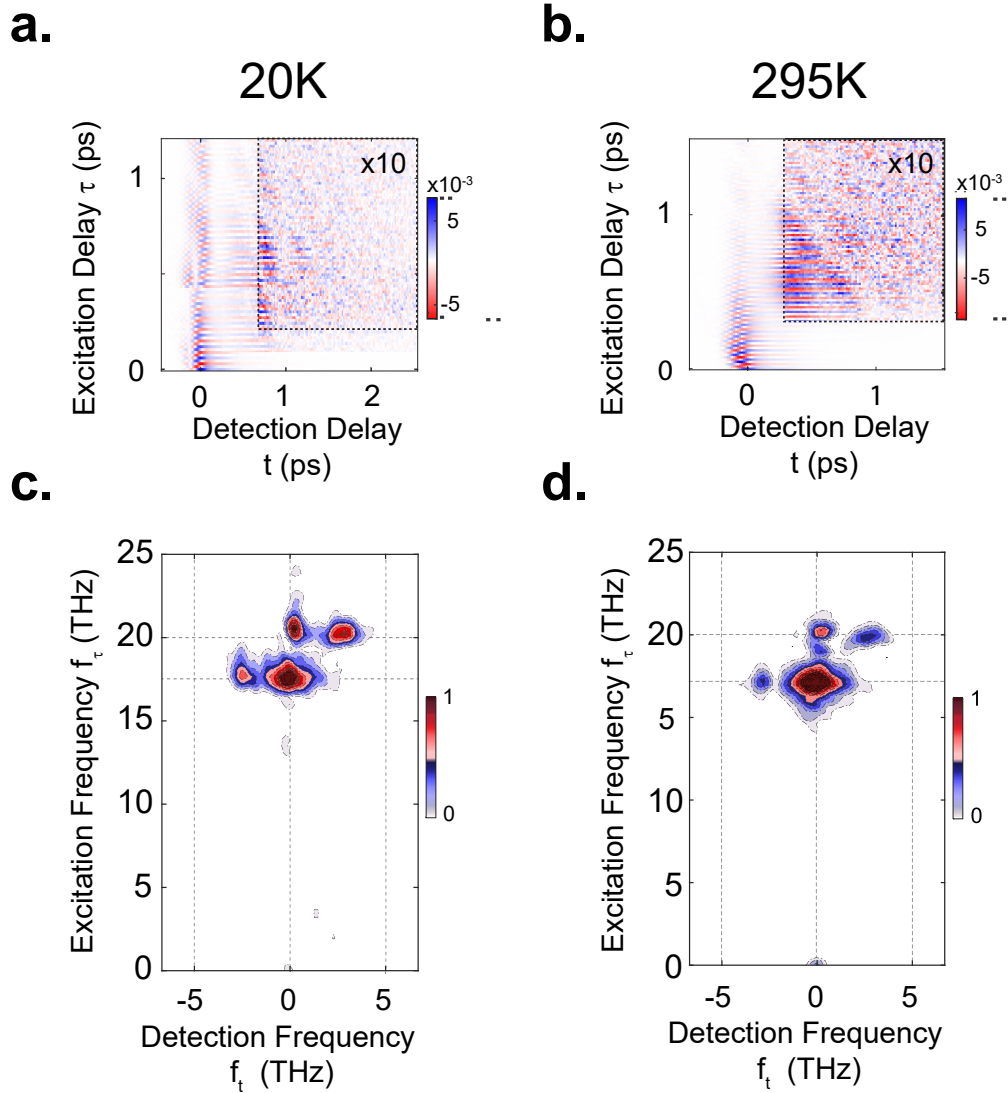


**Figure 5.8:** (a). Nonlinear contributions to the time-resolved SHG intensity (as described in Fig.5.6(b)) with the excitation time delay  $\tau$  changing along the vertical axis, measured at a base temperature of 20 K (below  $T_c$ ). (b). Same as in (a) measured at 295 K (above  $T_c$ ). The data inside the black dashed box are multiplied by 10 for clarity. Data at both temperatures were measured with approximate fluences  $12 \text{ mJ.cm}^{-2}$  and  $6 \text{ mJ.cm}^{-2}$  for  $E_A$  and  $E_B$ , respectively. (c). Normalized two-dimensional Fourier spectrum of the data inside the black dashed box in panel (a). Four strong peaks are found in the 2D spectrum with the corresponding frequency coordinates  $(f_t; f_\tau)$ :  $(-3; 17)$ ,  $(0; 17)$ ,  $(0; 20)$  and  $(3; 20)$ , all in units of THz. (d). Same as (c) for the data shown in panel (b), with the same peak pattern and peak frequency positions as in (c). The Fourier transformation for the two different temperatures are performed in different windows based on the time domain data and each 2D spectrum is normalized to its own maximum [199].

## 5.6 Doping and Temperature Dependence

The two-pump-tr-SHG probe experiments were also carried out in the higher-doped compound  $\text{YBa}_2\text{Cu}_3\text{O}_{6.92}$ , with the aim of further investigating the dynamics of the driven phonon modes and understanding the nature of the temperature independent low-frequency mode at  $\approx 3$  THz which was discussed earlier in section 4.6. Figures 5.9 (c) and (d) compare the nonlinear two-dimensional spectra measured in  $\text{YBa}_2\text{Cu}_3\text{O}_{6.48}$  and  $\text{YBa}_2\text{Cu}_3\text{O}_{6.92}$ , respectively, at a base temperature of 20 K, which is below  $T_c$  for both doping levels. Note that the same time-domain cropping procedure described in the previous section 5.5 was also used here. In both compounds the peaks appear at approximately the same frequency positions, however, the relative amplitudes of the peaks are weaker in the  $\text{YBa}_2\text{Cu}_3\text{O}_{6.92}$  doping, as was also the case in the one-dimensional pump-probe experiments on the two doping levels (see Fig.4.9(a) and (b)).

We also carried out two-dimensional temperature-dependent measurements in both  $\text{YBa}_2\text{Cu}_3\text{O}_{6+x}$  compounds. We then performed 2D Fourier transformations on the uncropped (raw) data measured at each base temperature for each doping. The entire two-dimensional Fourier spectrum was then integrated along both frequency axes and plotted as a function of temperature, displayed here in Figs.5.10 (a) and (b) for  $\text{YBa}_2\text{Cu}_3\text{O}_{6.48}$  and  $\text{YBa}_2\text{Cu}_3\text{O}_{6.92}$ , respectively [199].

The integrated 2D-peak amplitudes measured in  $\text{YBa}_2\text{Cu}_3\text{O}_{6.48}$  was observed to gradually decrease as the temperature increases throughout the pseudogap phase, but never reached zero amplitude within the measured range. Interestingly, the temperature dependence observed here follows the same trend as the temperature dependence of the photo-induced superfluid density extracted from the THz-spectroscopy based measurements in the same compound (shown in Fig.3.8(b)) [64,

65, 81], as well as that of the 3 THz peak observed in the single pump, tr-SHG experiment (shown in Fig.4.8(b)) [22]. In contrast, the integrated 2D-peak amplitudes measured in  $\text{YBa}_2\text{Cu}_3\text{O}_{6.92}$  remained temperature in-dependent across the whole measured temperature range, also consistent with the measured SH intensity in the single pump, tr-SHG probe experiments shown in Fig.4.9(c). This temperature independent response is in good agreement with the previously reported temperature dependence of the apical oxygen phonon modes of the underdoped compound (6.5 doping) in equilibrium (reported in ref.[192] and shown in Fig.3.6(d)) and out of equilibrium (reported in ref.[22] and shown in Fig.4.8 (b)).

The integrated 2D-peak amplitudes measured in  $\text{YBa}_2\text{Cu}_3\text{O}_{6.48}$  can be well-fitted using a fitting function that consists of two components. One is temperature-independent, whilst the other exhibits a mean-field dependence with a characteristic temperature scale of  $T^* = 380$  K:  $\alpha_1 + \alpha_2 \sqrt{1 - T/T^*}$  [199]. The value used for  $T^*$  in the fitting function was chosen to be equal to that reported in ref.[22] in the one dimensional pump-probe experiment and shown in Fig.4.8(b), and is comparable with the pseudogap temperature for this doping level. In contrast, the integrated 2D-peak amplitudes measured in  $\text{YBa}_2\text{Cu}_3\text{O}_{6.92}$  are temperature independent up to at least 450 K, far above  $T^* = 160$  K (the  $T^*$  value was taken from ref.[51]). From these observations, it is evident that the temperature dependence measured in  $\text{YBa}_2\text{Cu}_3\text{O}_{6.48}$  cannot purely be attributed to the phonons, further suggesting the involvement of an additional mode that exhibits temperature sensitivity. This will be discussed thoroughly in the next chapter, section 6.3.

## 5.6. Doping and Temperature Dependence

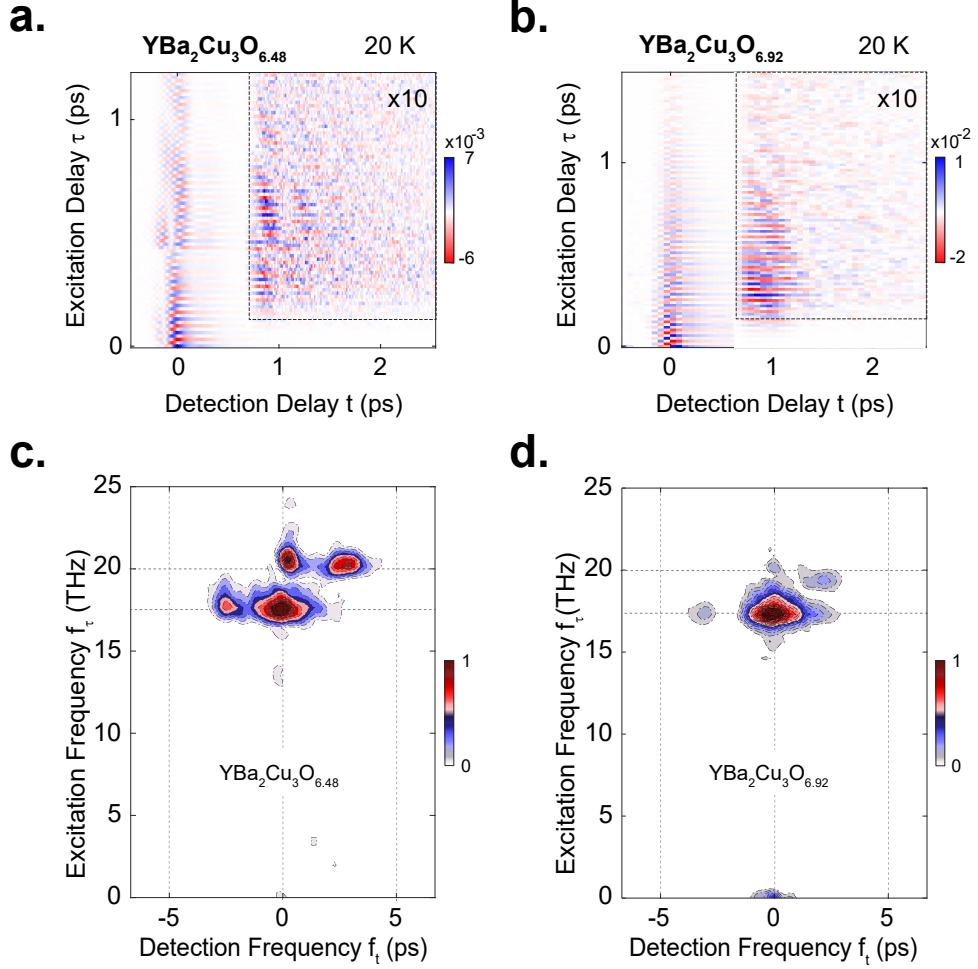


**Figure 5.9:** (a). and (b). Nonlinear contributions to the time-resolved SHG intensity with the excitation time delay  $\tau$  changing along the vertical axis, measured at a base temperature of 20 K (below  $T_c = 48$  K ) in  $\text{YBa}_2\text{Cu}_3\text{O}_{6.48}$  and  $\text{YBa}_2\text{Cu}_3\text{O}_{6.92}$  (below  $T_c = 91$  K ), respectively. The data inside the black dashed box are multiplied by 10 for clarity. (c). Normalized two-dimensional Fourier spectrum of the data inside the black dashed box, respectively, shown in panel (a). The corresponding peaks frequency coordinates  $(f_t; f_\tau)$  are:  $(-3; 17)$ ,  $(0; 17)$ ,  $(0; 20)$  and  $(3; 20)$ , all in units of THz. (d). Normalized two-dimensional Fourier spectrum of the data inside the black dashed box shown in panel (b). The corresponding peaks frequency coordinates are identical to those observed in panel (c) with one extra peak at  $(0; 0)$  also in units of THz. The 2D spectra shown here were normalized to their own maximum value [199].

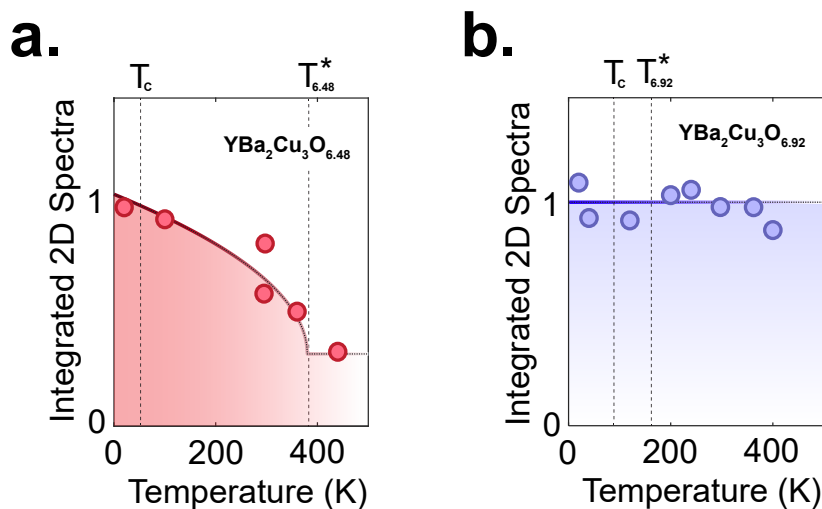


**Figure 5.10:** (a). Normalized frequency-integrated amplitude of nonlinear two-dimensional spectra of  $\text{YBa}_2\text{Cu}_3\text{O}_{6.48}$  shown in Fig.5.9(a) as a function of base temperature (red circles). The thick red line is a fit with a mean-field dependence ( $\alpha_1 + \alpha_2\sqrt{1 - T/T^*}$ ), indicating that this quantity has a dominant contribution that decreases as temperature approaches the pseudogap temperature  $T^*$  (380 K) and a contribution that takes a constant value  $\alpha$  for all measured temperatures. (b). Same as panel (a) for a different doping of  $\text{YBa}_2\text{Cu}_3\text{O}_{6.92}$ . Here, the frequency-integrated nonlinear two-dimensional amplitude does not depend on temperature. Note that the temperature dependent data in each doping are measured under the same excitation fluence and the same two-dimensional time window for consistency in the analysis [199].

---

## 5.7 Summary and Outlook

This chapter presented a new series of experiments conducted on two doping levels of  $\text{YBa}_2\text{Cu}_3\text{O}_{6+x}$  using multidimensional spectroscopy in the mid-infrared region. These experiments provided a direct measurement of the coupling between the symmetry-odd, symmetry-even and symmetry-odd, symmetry-odd modes in the phonon-driven state.

The 2D peak pattern measured for  $\text{YBa}_2\text{Cu}_3\text{O}_{6.92}$  in the tr-polarization rotation channel exhibited peaks along the excitation frequency axis corresponding to the driven

phonon frequencies (17 THz and 20 THz). Additionally, cross-peaks were observed at the frequency of a Raman-active mode, appearing at 3.6 THz.

In the tr-SHG channel, the 2D maps measured for both compounds revealed identical peak patterns, albeit with differing relative amplitudes. The peaks along the excitation frequency axis corresponded to the frequencies of the driven phonons, while cross-peaks emerged at 3 THz. These cross-peaks frequencies observed in the 2D spectra indicate that, for both dopings, the 3 THz oscillations which were observed in the previous one-dimensional experiments arise from a cooperative action of both apical oxygen phonon modes.

Whilst the 2D spectra obtained using tr-SHG probes for both doping levels of  $\text{YBa}_2\text{Cu}_3\text{O}_{6+x}$  revealed similar peak patterns with the same frequency positions, the temperature dependence of the response differed between the doping levels. In the  $\text{YBa}_2\text{Cu}_3\text{O}_{6.48}$  compound, a clear temperature dependence was observed, with the pseudogap temperature  $T^*$  appearing to be the relevant temperature scale (consistent with the THz and one-dimensional pump-probe experiments), above which the amplitude remained constant. In contrast, the response in the  $\text{YBa}_2\text{Cu}_3\text{O}_{6.92}$  compound remained temperature-independent throughout the same temperature range.

Based on the experimental observations laid out in Chapters 3 to 5, Chapter 6 provides numerical simulations which demonstrate that the SHG-based measurements presented here can only be consistent with a four-mode mixing process between the two apical oxygen phonon modes and pairs of phase-fluctuating finite-momentum JPPs in the  $\text{YBa}_2\text{Cu}_3\text{O}_{6.48}$  compound. This mechanism may provide the basis for understanding the formation of phonon-driven photo-induced superconductivity in this compound.

# Chapter 6

## Squeezed Josephson Plasmon Amplification

### 6.1 Introduction

In Chapters 3-5 the experimental observations connected to both the emergence of photo-induced macroscopic superconducting-like properties, and the accompanying coherent microscopic dynamics as probed by both one and two-dimensional techniques, were detailed. In this Chapter, we propose a single theoretical model (including detailed numerical simulations) which can account for many of these experimental observations.

The discussion will initially be focused on the symmetry-odd modes coherent dynamics in  $\text{YBa}_2\text{Cu}_3\text{O}_{6+x}$ . We start by using a simplified Hamiltonian for *only* the driven phonons, describing the observed dynamics in one- and two-dimensional tr-SHG experiments in  $\text{YBa}_2\text{Cu}_3\text{O}_{6.92}$ . Subsequently, this Hamiltonian is expanded to encompass the case of the underdoped  $\text{YBa}_2\text{Cu}_3\text{O}_{6.48}$  compound.

The main emphasis will be placed on how the 2D peak pattern obtained from the new multidimensional experiments on both doping levels of  $\text{YBa}_2\text{Cu}_3\text{O}_{6+x}$  provide a clear picture of the microscopic dynamics in the phonon-driven state of these compounds. We will argue that in the case of  $\text{YBa}_2\text{Cu}_3\text{O}_{6.48}$ , this peak pattern together with the photo-induced reflectivity edge at slightly blue-shifted frequency, points uniquely towards a four-mode mixing interaction between the two resonantly driven apical oxygen phonon modes and pairs of opposite-momentum JPPs. Based on this coupling mechanism, the driven phonons are actually predicted to generate a squeezed state of such pairs.

The discussion finalizes with the description of how the presence of such a squeezed state naturally results in the photo-induced THz reflectivity edge which was observed in earlier experiments and described in chapter 3, representing a significant step towards understanding the formation of the photo-induced superconducting-like state in these compounds.

The chapter concludes with a theoretical discussion (also supported by numerical simulations) on the driven coherent dynamics of the symmetry-even modes, providing a detailed characterization of their coupling mechanisms.

## 6.2 Dynamics of Driven Phonons

In this section we simulate the photo-induced phonon dynamics in the  $\text{YBa}_2\text{Cu}_3\text{O}_{6.92}$  compound, which has two IR-active,  $B_{1u}$ -symmetry apical oxygen phonon modes at frequencies of  $\omega_{\text{IR1}}/2\pi = 17$  THz and  $\omega_{\text{IR2}}/2\pi = 20$  THz. In the experiments, these two modes were resonantly driven to large amplitudes by CEP stable, c-axis polarized excitation pulses. Here we model this process with a lattice potential which includes both harmonic and an-harmonic terms of the driven modes and their

coupling to the mid-IR electric field  $E_{\text{pump}}(t)$ . This potential is given by equation 6.1 [25, 216]:

$$V_{\text{driven-phonons}} = \frac{1}{2}(\omega_{\text{IR1}}^2 Q_{\text{IR1}}^2 + \omega_{\text{IR2}}^2 Q_{\text{IR2}}^2) + \frac{1}{4}(\kappa_{\text{IR1}} Q_{\text{IR1}}^4 + \kappa_{\text{IR2}} Q_{\text{IR2}}^4) + (Z_{\text{IR1}}^* R_{\text{IR1}} + Z_{\text{IR2}}^* R_{\text{IR2}}) E_{\text{pump}}(t) \quad (6.1)$$

Here,  $Q_{\text{IR1}}$  and  $Q_{\text{IR2}}$  represent the time dependent displacements of the two phonon modes with  $\kappa_{\text{IRi}}$  and  $Z_i^*$  being their an-harmonic coefficients and mode effective charges, respectively. The resulting equations of motion are as follows:

$$\begin{aligned} \ddot{Q}_{\text{IR2}} + 2\gamma_{\text{IR2}} \dot{Q}_{\text{IR2}} + \omega_{\text{IR2}}^2 Q_{\text{IR2}}^2 &= Z_2^* E - \kappa_{\text{IR2}} Q_{\text{IR2}}^3 \\ \ddot{Q}_{\text{IR1}} + 2\gamma_{\text{IR1}} \dot{Q}_{\text{IR1}} + \omega_{\text{IR1}}^2 Q_{\text{IR1}}^2 &= Z_1^* E - \kappa_{\text{IR1}} Q_{\text{IR1}}^3 \end{aligned} \quad (6.2)$$

Here  $\gamma_{\text{IRi}}$  accounts for the damping for each mode. To simulate the one- and two-dimensional tr-SHG and tr-PR experiments, these equations of motion were solved first for a single and then for two-pulse excitation, as will be discussed in the following.

### 6.2.1 Single-Pulse Excitation

To simulate the one-dimensional experiments, the pump electric field is represented by a sinusoid centred at frequency  $\omega_{\text{pump}}/2\pi = 18.5$  THz, multiplied by a Gaussian envelope of width  $\sigma_{\text{pump}} = 0.15$  ps as written in Eq.6.3 and shown in Fig.6.1. These values were chosen to be consistent with the experimentally measured values as described in Section 4.4.1.

$$E(t) = E_0 \exp\left(\frac{-t^2}{2\sigma_{\text{pump}}^2}\right) \sin(\omega_{\text{pump}} t) \quad (6.3)$$

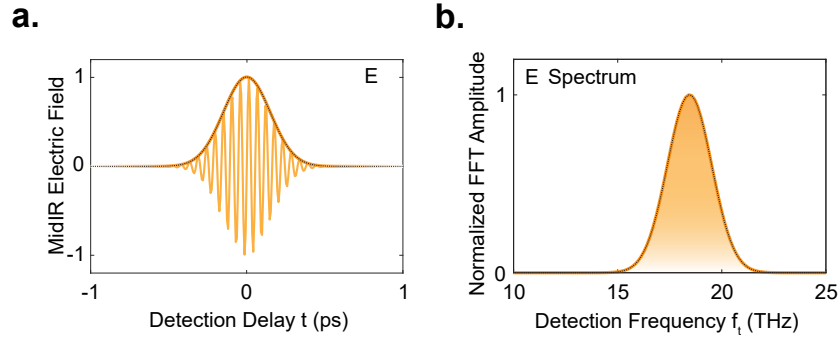


**Figure 6.1:** (a). Mid-infrared pump electric field shown in Eq.6.3, used to solved the equations of motion in Eq.6.2. (b). Normalized Fourier spectrum of (a).

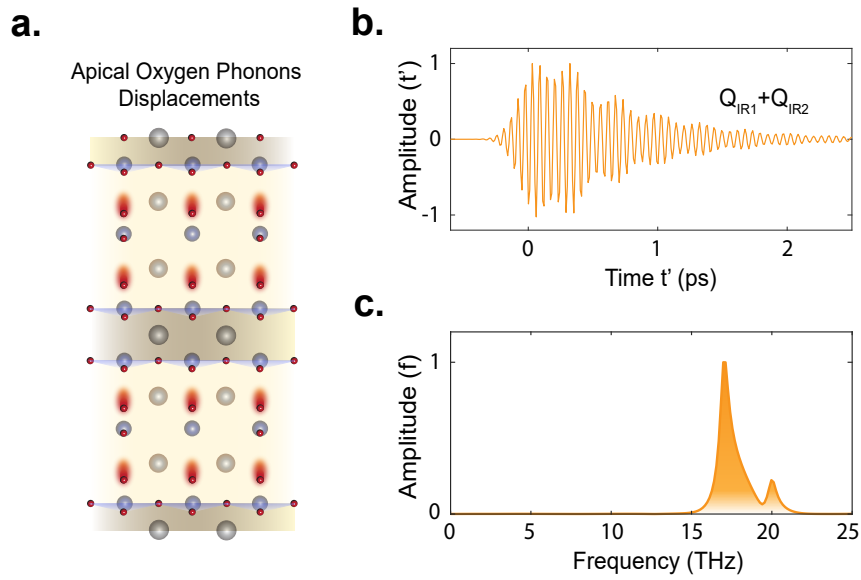


**Figure 6.2:** (a). Illustration of the motion of symmetry-breaking c-axis apical oxygen phonon modes, driven resonantly via mid-IR pump pulses. (b). Normalized time-dependent displacement of phonon modes, simulated using the potential in Eq.6.1. (c). Normalized Fourier amplitude of the driven phonons shown in (a), showing two peaks at the eigenfrequencies of the phonons at 17 THz and 20 THz. [199]

Here  $E_0 = 12$  MV/cm is the peak mid-IR pump electric field strength, which

is comparable with the typical values used in the one-dimensional experiments. The equations of motion given in Eq.6.2 were solved numerically for the electric field in Eq.6.3, to simulate the coherent, resonant displacements of the phonons ( $Q_{\text{IR1}} + Q_{\text{IR2}}$ ) in  $\text{YBa}_2\text{Cu}_3\text{O}_{6.92}$  which are illustrated in Fig.6.2(a). For the full list of parameters used to solve the equations of motion see Appendix D.1.

Following the derivation given in section 4.4.5 and Eq.4.13, the generated hyper-Raman fields are given by:  $E_{\text{SH,IRi}}(t', t) \propto \frac{\partial \chi^{(2)}}{\partial Q_{\text{IRi}}} Q_{\text{IRi}}(t') E_{800}^2(t' - t)$ . The intensity measured by the detector is then calculated using Eq.4.14:

$$I_{\text{SH}}(t) = \int |E_{\text{SH,IR1}}(t', t) + E_{\text{SH,IR2}}(t', t) + E_{\text{SH,pump}}(t', t) + E_{\text{Lo}}(t')|^2 dt' \quad (6.4)$$

Where  $E_{\text{SH,pump}}(t', t)$  is as given in Eq.4.13. Fig.6.3 shows the calculated  $I_{\text{SH}}(t)$  for three different values of  $E_{\text{Lo}}$ , and compares these to the experimentally measured response. This comparison demonstrates that the simulations provided a good agreement with the experimentally measured response in  $\text{YBa}_2\text{Cu}_3\text{O}_{6.92}$ , *only* in the intermediate case of a small, but not negligible local oscillator field.

From Eq.6.4, the measurement of the phonons response at their resonance frequencies 17 THz and 20 THz originates from the interference of their hyper-Raman fields via  $I_{\text{Het}}(t) \propto E_{\text{Lo}}[\cos(\omega_{\text{IR1}}t) + \cos(\omega_{\text{IR2}}t)]$ . The response in the homodyne detection limit, however, appears at frequency components  $\omega_{\text{IR2}} + \omega_{\text{IR1}}$  and  $\omega_{\text{IR2}} - \omega_{\text{IR1}}$  which come from the homodyne mixing of phonons hyper-Raman fields at the detector e.i.  $I_{\text{Hom}}(t) \propto [\cos(\omega_{\text{IR1}}t)\cos(\omega_{\text{IR2}}t)]$ , as already discussed in section 4.4.5. In this case, the small peak at 3 THz (shown in Fig.4.9 (b)) arises from the difference frequency component, whilst the sum frequency component can not be resolved due to the limited probe time resolution. For a full analytical discussion see Appendix E.1.

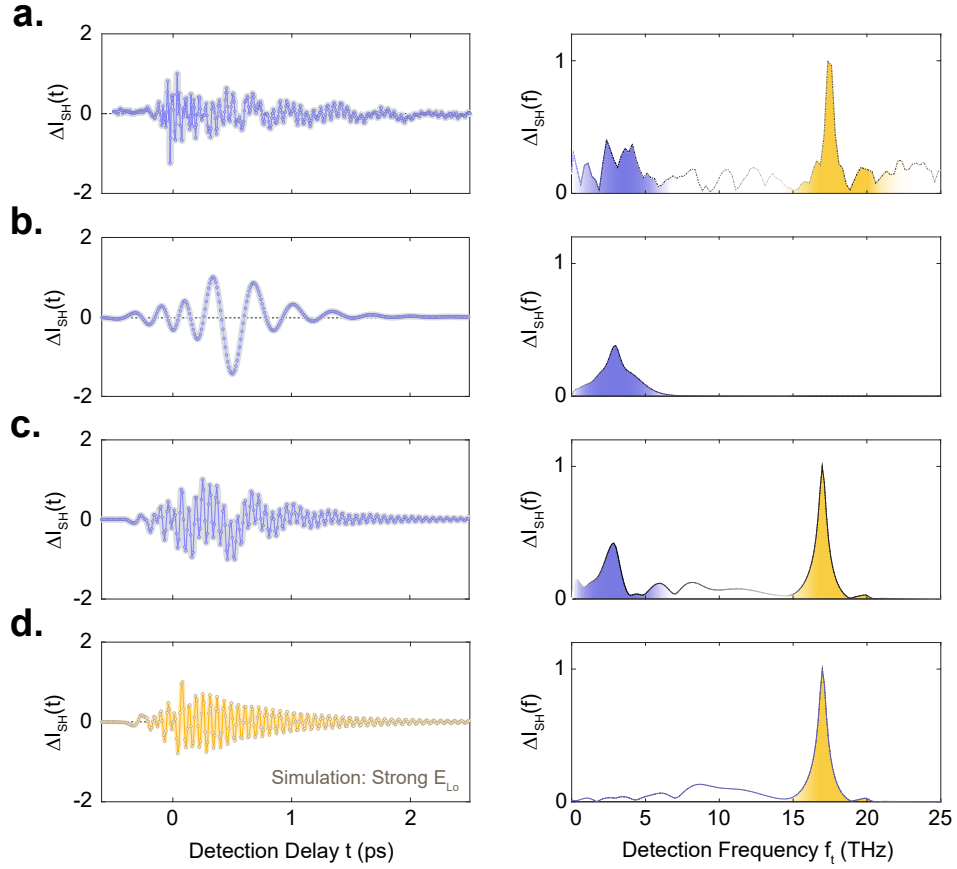


**Figure 6.3:** (a). Left panel: oscillatory contribution of mid-IR pump induced changes in time-resolved SHG intensity as a function of detection time delay  $t$  for  $\text{YBa}_2\text{Cu}_3\text{O}_{6.92}$  at base temperature 5 K below  $T_c$  ( $T_c = 91$  K), at an excitation fluence of  $29 \text{ mJ}\cdot\text{cm}^{-2}$ . Right panel: corresponding Fourier spectrum of the data shown in the left panel, with two peaks at the resonantly excited phonon modes at 17 THz and 20 THz (shaded in yellow) and one smaller peak at the difference frequency of the two phonon modes  $\approx 3$  THz (shaded in blue). (b). Left panel: oscillatory contribution to the changes in the second harmonic intensity, simulated for the lattice potential defined in Equation (2.1), in the homodyne detection limit. Right panel: corresponding Fourier spectrum with the same colour coding as in (a). Only the beating between the two phonon modes at 3 THz contributes to this spectrum. (c). Left panel: same as left panel in (b), now in the intermediate detection limit with a small, but nonzero local oscillator. Right panel: Same as right panel in (b). Here, the two phonon modes also appear at their fundamental frequencies. (d). Left panel: same as left panels in (b) and (c), now in the heterodyne detection limit with a strong local oscillator. Right panel: Same as right panels in (b) and (c). Here, the heterodyne contribution of the two phonon modes dominates the SHG signal [199].

### 6.2.2 Two-Dimensional Nonlinear Spectroscopy

In the two-pulse excitation experiment, the sample was excited sequentially by two mid-IR pulses, with electric fields denoted as  $E_A$  and  $E_B$ , that are separated by the variable excitation time delay  $\tau$  (see Fig.6.4):

$$E_A = E_{A0} \exp\left(\frac{-t^2}{2\sigma_{\text{pump}}^2}\right) \sin(\omega_{\text{pump}}(t - t_0)) \quad (6.5)$$

$$E_B = E_{B0} \exp\left(\frac{((t + \tau) - t_0)^2}{2\sigma_{\text{pump}}^2}\right) \sin(\omega_{\text{pump}}((t + \tau) - t_0)) \quad (6.6)$$

Here the peak electric fields used in the simulations for  $E_{A0}$  and  $E_{B0}$ , were chosen to be comparable with the experimental values,  $4 \text{ MV}\cdot\text{cm}^{-1}$  and  $12 \text{ MV}\cdot\text{cm}^{-1}$ , respectively. The total electric field  $E_{AB}(t + \tau)$  is given by the sum of both electric fields:  $E_{AB}(t, \tau) = E_A(t) + E_B(t + \tau)$ .

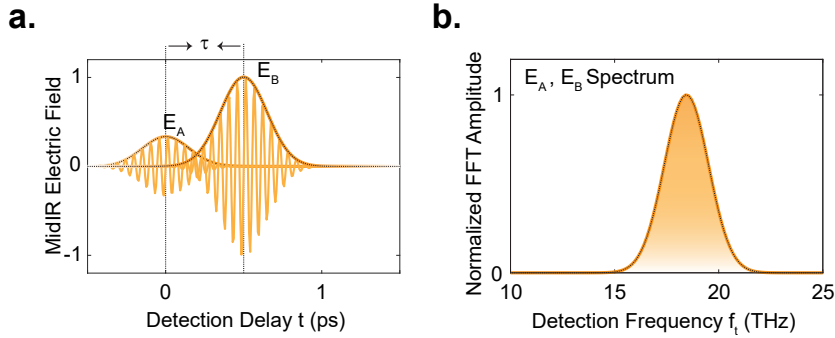


**Figure 6.4:** (a). Mid-infrared pump electric fields of pulse  $E_A$  and  $E_B$ , with  $E_{A0}$  and  $E_{B0}$ ,  $4 \text{ MV}/\text{cm}$  and  $12 \text{ MV}/\text{cm}$ , respectively.  $\tau$  denotes the separation time between  $E_A$  and  $E_B$ . (b). Normalized Fourier spectrum of  $E_A$  and  $E_B$ .

---

In order to reproduce the results of the 2D SHG measurements in  $\text{YBa}_2\text{Cu}_3\text{O}_{6.92}$ , first Eq.6.2 was solved for the case of excitation with only pulse  $E_A$ , then for the case of only pulse  $E_B$  and finally for both excitation pulses together  $E_{AB}$ . Then, the associated SH intensities  $I_A$ ,  $I_B$  and  $I_{AB}$  were calculated using Eq.6.4 and from these

the nonlinear contribution to the SH intensity  $I_{\text{NL}} = I_{\text{AB}} - I_{\text{A}} - I_{\text{B}}$  was extracted. The resulting  $I_{\text{NL}}$  for three different values of  $E_{\text{LO}}$  are shown in panels (a)-(c) with their corresponding two-dimensional Fourier transforms in panels (d)-(f) of Fig.6.5.

As shown in Figs.6.5(d) and (e), seven peaks can be found in the 2D spectra measured in the homodyne ( $I_{\text{Hom}}(f_t, f_\tau)$ ) and intermediate ( $I_{\text{Int}}(f_t, f_\tau)$ ) regimes with the frequency coordinates  $(f_t, f_\tau)$ : (0 THz; 17 THz), (0 THz; 20 THz), (3 THz; 20 THz), (0 THz; 0 THz), (3 THz; -17 THz), (0 THz; -17 THz) and (0 THz; -20 THz). In the heterodyne ( $I_{\text{Het}}(f_t, f_\tau)$ ) limit, however, there are only three strong peaks at frequency coordinates of (0 THz; 17 THz), (17 THz; 17 THz) and (17 THz; -17 THz). For a full analytical derivation of the 2D peak pattern see Appendix E.1.

The peak patterns simulated in the homodyne dominated limit once again provide a good agreement with the experimentally measured 2D peak pattern in  $\text{YBa}_2\text{Cu}_3\text{O}_{6.92}$  (see Fig.5.9(d)), as was also the case for the simulations of the one-dimensional SHG experiment. The simulations of both one- and two-dimensional tr-SHG experiments using the simple potential described in Eq.6.1 therefore successfully explain the presence of a low-frequency SHG peak at 3 THz in  $\text{YBa}_2\text{Cu}_3\text{O}_{6.92}$ , which originates from homodyne mixing of the fields from the driven phonons at the detector. This model also naturally explains the lack of a temperature dependence of the response measured in  $\text{YBa}_2\text{Cu}_3\text{O}_{6.92}$  in both one- and two-dimensional experiments, because the driven phonon amplitudes (which are solely responsible for the measured signal) have been shown to remain constant across such a temperature range [22, 192].

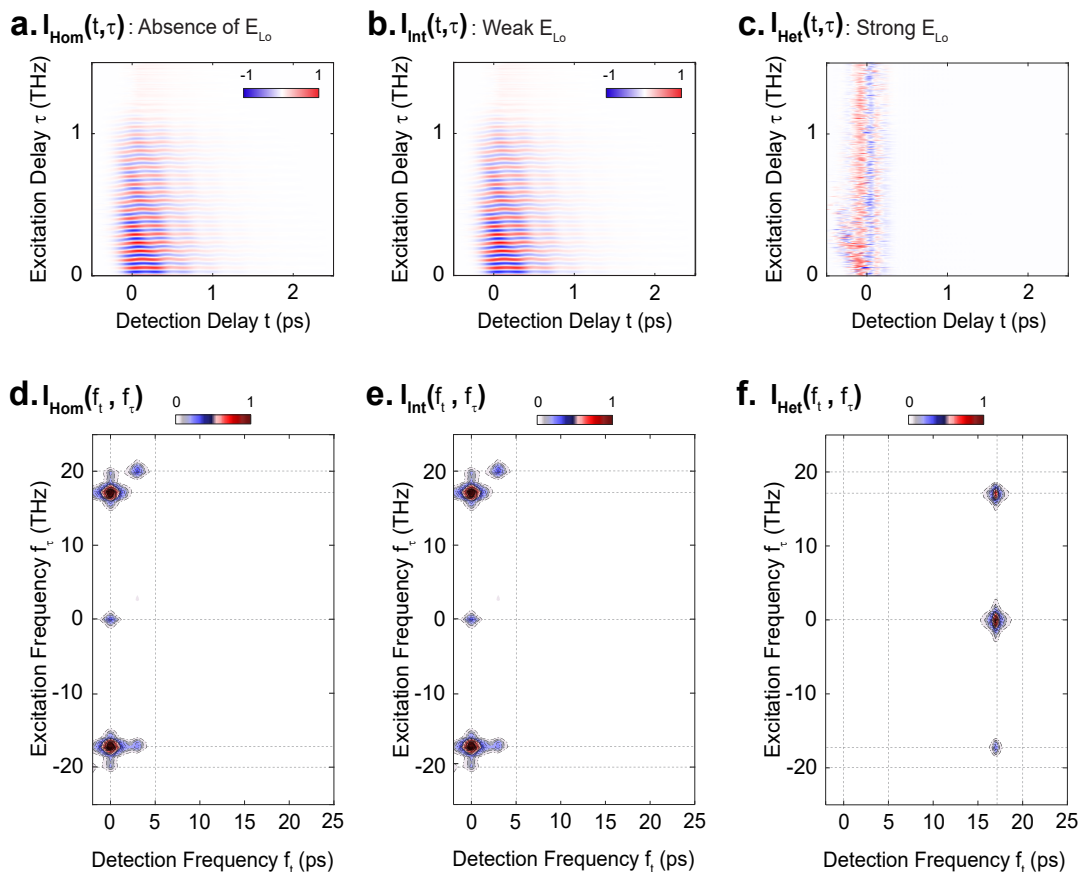


**Figure 6.5:** (a), (b), and (c). tr-SHG two-dimensional intensity map simulated using the lattice potential defined in Eq.6.1 for two-pulse excitation, respectively, in the limit of homodyne ( $E_{L_0} = 0$ ), intermediate (small  $E_{L_0}$ ) and heterodyne (large  $E_{L_0}$ ) detection. (d). Corresponding two-dimensional Fourier spectrum of (a). According to this 2D spectrum, there are seven peaks at frequency coordinates  $(f_t; f_\tau)$ ; (0;17), (0;20), (3;20), (0;-17), (0;-20), (3;-17) and (0;0) all in units of THz. (e). Same as in (d), this time for (b), representing the same peak pattern and frequency coordinates as in (d). (f). Same as in (d) and (e) but for (c). Here, the number of peaks reduced to three peaks with frequency coordinates; (17;0), (17;17) and (17; -17) all in units of THz. All Panels were normalized according to their own maximum values [199].

## 6.3 Phonon-Plasma Polariton Dynamics

The above discussion of the dynamics of the driven phonons can be extended to the underdoped compound of  $\text{YBa}_2\text{Cu}_3\text{O}_{6.48}$ , in which the phonon modes have approximately the same frequency [48, 49, 192] (see also Fig.3.5). Indeed, the identical peak patterns in the 2D maps suggest that similar dynamics are at play in both dopings. However, the temperature dependence of the signal in the 6.48 compound indicates the presence of a further coupled mode, which must explain the observed temperature dependence without altering the positions of the peaks in the 2D spectrum. Here we show that if we introduce a four-mode mixing coupling to a lower frequency mode with an eigenfrequency of 1.5 THz, this does not alter the 2D spectrum other than enhancing the relative amplitudes of the peaks.

We assign this mode to a finite-momentum JPP based on the following arguments. Firstly, this coupled mode must obey a  $T^*$ -related temperature dependence. Secondly, no IR-active phonon mode has been observed at this frequency for both doping levels of  $\text{YBa}_2\text{Cu}_3\text{O}_{6+x}$  compounds [48, 49, 192]. Lastly, in the underdoped compound, the only IR-active mode in the vicinity of this frequency is the equilibrium Josephson plasmon resonance (at the frequency of  $\approx 1$  THz) [48] while for the 6.92 doping is shifted to higher frequencies (at the frequency of 7 THz [48, 192]).

Therefore, the coupled dynamics in  $\text{YBa}_2\text{Cu}_3\text{O}_{6.48}$  can be modeled by the same phonon potential  $V_{\text{driven-phonons}}$  introduced in Eq.6.1, with the addition of a term which considers the phonon-plasmon interaction, given by:

$$V_{\text{phonon-plasmon}} = \beta(Q_{\text{IR1}} + Q_{\text{IR2}})^2 J_{\text{P1},q_x} J_{\text{P1},-q_x} \quad (6.7)$$

This term causes the resonantly driven apical oxygen phonons to parametrically excite pairs of finite-momentum, phase fluctuating Josephson plasmon polaritons  $J_{P1,q_x}$  and  $J_{P1,-q_x}$  via a force proportional to  $(Q_{IR1} + Q_{IR2})^2$ . The subscript  $q_x$  refers to the in-plane momentum of the JPPs and  $\beta$  is the coupling coefficient. The corresponding coupled equations of motion are:

$$\begin{aligned}
 \ddot{Q}_{IR2} + 2\gamma_{IR2}\dot{Q}_{IR2} + \omega_{IR2}^2 &= Z_2^*E - \kappa_{IR2}Q_{IR2}^3 - \beta(Q_{IR2}^2 + 2Q_{IR1}Q_{IR2})J_{P1,q_x}J_{P1,-q_x} \\
 \ddot{Q}_{IR1} + 2\gamma_{IR1}\dot{Q}_{IR1} + \omega_{IR1}^2 &= Z_1^*E - \kappa_{IR1}Q_{IR1}^3 - \beta(Q_{IR1}^2 + 2Q_{IR1}Q_{IR2})J_{P1,q_x}J_{P1,-q_x} \\
 \ddot{J}_{P1,-q_x} + 2\gamma_{JP1}\dot{J}_{P1,-q_x} + \omega_{JP1,-q_x}^2(-q_x)J_{P1,-q_x} &= -\beta(Q_{IR1} + Q_{IR2})^2J_{P1,-q_x} \\
 \ddot{J}_{P1,q_x} + 2\gamma_{JP1}\dot{J}_{P1,q_x} + \omega_{JP1,q_x}^2(q_x)J_{P1,q_x} &= -\beta(Q_{IR1} + Q_{IR2})^2J_{P1,q_x}
 \end{aligned} \tag{6.8}$$

Here  $\gamma_{JP1}$  and  $\omega_{JP1}$  refer to phenomenological damping and frequency of the plasma-polaritons. For details of the derivation with respect to in-plane momentum  $q_x$ , see Appendix A.1. Note that to solve the JPPs equations of motion numerically, the JPPs current coordinates were seeded with a random initial phase.

### 6.3.1 Single-Pulse Excitation

In this section we solve the coupled equations of motion in Eq.6.8 for a single-pulse excitation discussed in Section 6.2.1, in order to replicate the one-dimensional experiment. We begin by showing how the motion of the driven phonon modes provides a parametric force which resonantly amplifies the JPPs, before providing a detailed description of the properties of the JPP dynamics which result. Finally, in Fig.6.9(e) and (f) we show that this model predicts an SHG signal which closely matches that measured experimentally in the appropriate detection limit.

As shown in Figs.6.6 (c) and (d), the beating of the two phonons  $Q_{IR1}Q_{IR2}$ , which acts as the dominant parametric drive for the JPPs, has two frequency components

### 6.3. Phonon-Plasma Polariton Dynamics

at the sum and difference frequencies of the two phonons,  $\omega_{\text{IR}2} + \omega_{\text{IR}1}$  and  $\omega_{\text{IR}2} - \omega_{\text{IR}1}$ , respectively. The terms proportional to  $Q_{\text{IR}i}^2$ , which have been discussed in 1.6.3, can also contribute to the excitation of the JPPs as an impulsive drive but remain subdominant<sup>1</sup>. However, the difference frequency component is the most effective parametric drive for the JPPs with the resonance condition:  $2\omega_{\text{JP}1}(\pm q_x) = \omega_{\text{IR}1} - \omega_{\text{IR}2}$ .

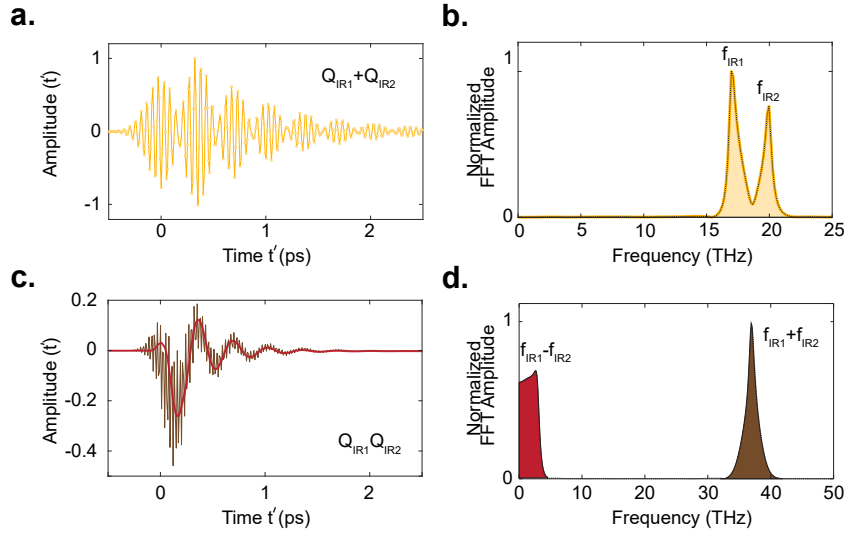


**Figure 6.6:** (a). Normalized time-dependent displacement of phonon modes, simulated using the potential in Eq.6.1 but for  $\text{YBa}_2\text{Cu}_3\text{O}_{6.48}$ . (b). The normalized Fourier spectrum of (a), with the phonon eigenfrequencies indicated as  $f_{\text{IR}1}$  and  $f_{\text{IR}2}$ . (c). The time-dependent force proportional to  $Q_{\text{IR}1} Q_{\text{IR}2}$  mixing term. (d). Normalized FFT amplitude of (c), representing two frequency component at sum and difference frequencies of the driven phonons,  $f_{\text{IR}2} + f_{\text{IR}1}$  and  $f_{\text{IR}2} - f_{\text{IR}1}$ , respectively. The panels (a) and (c) were normalized to the maximum value of (a) [199].

The simulated dynamics of the amplified JPPs are displayed in Figure.6.7. The amplification of the pairs of current coordinates  $J_{\text{P}1, q_x}$  and  $J_{\text{P}1, -q_x}$ , each oscillating at  $\omega_{\text{JP}1, \pm q_x}$ , starts from an in-coherent phase fluctuating state. Because in the experiments discussed in this thesis, each measurement is averaged over thousands of

<sup>1</sup>This will become clear by simulating the 2D spectrum for each coupling term and noting that only the mixing term  $\beta Q_{\text{IR}1} Q_{\text{IR}2}$ , can reproduce the measured 2D spectrum.

pulses, therefore the average value of these fluctuations is zero:  $\langle J_{P1,\pm q_x} \rangle_{\text{equil.}} = 0$ , where the angular bracket indicates the average is taken over many shots and hence over many different initial phases. This is also true for the covariance of these two currents which oscillates at  $2\omega_{JP1,\pm q_x}$ , meaning  $\langle J_{P1,+q_x} J_{P1,-q_x} \rangle_{\text{equil.}} = 0$ .

However, the parametric force dictates the phase of these coordinates to be  $\pi$  or zero after amplification, thus fixing the zero crossings, which results in reducing the fluctuations of the current coordinates at specific instants in time (see Fig.6.7 (a) and (e)). When accumulated over many pulses, the average value of the amplified JPPs remains zero  $\langle J_{P1,\pm q_x} \rangle_{\text{drive}} = 0$ , but the average value of the covariance becomes nonzero  $\langle J_{P1,+q_x} J_{P1,-q_x} \rangle_{\text{drive}} \neq 0$ , as indicated in red in Figs.6.7 (a-d).

The dynamics of the JPPs discussed here are those of a squeezed state in the absence of a coherent background, which was described in Section 1.6.3. In this case the parametric force from the phonons leads to the generation of a squeezed state of pairs of JPPs with in-plane momenta  $\pm q_x$ , which oscillates at  $\omega_{\text{squeezed}} = 2\omega_{JP1,\pm q_x} = \omega_{\text{IR2}} - \omega_{\text{IR1}}$ . For a full theoretical description of the dynamics of the JPPs squeezed state see Appendix F.1.

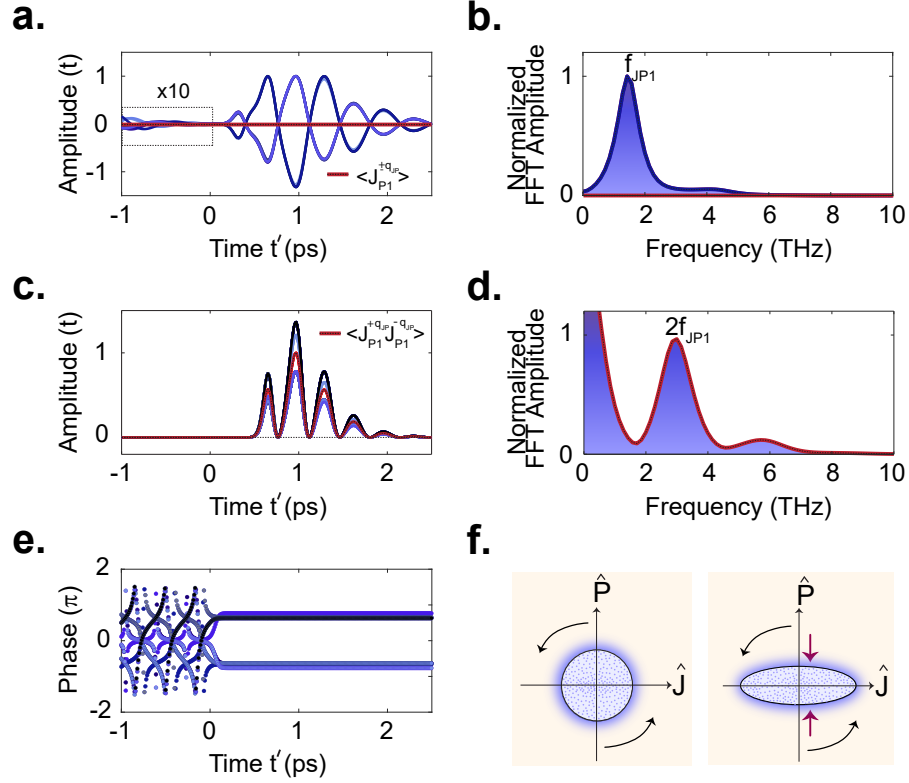


**Figure 6.7:** (a). Time-dependent displacements of the amplified, phase-fluctuating JPPs,  $J_{P1, \pm q_x}$  (in blue) along with their average value  $\langle J_{P1, \pm q_x} \rangle = 0$  (in red), simulated using four-mode mixing mechanism detailed in the text. The dashed-black box indicates the initial fluctuating JPPs current coordinates before amplification and for clarity is multiplied by 10. (b). The normalized FFT amplitude of (a) with the same color coding. The peak represents the finite-momentum frequency of the JPPs  $\omega_{JP1}(\pm q_x) = 1.5$  THz, dictated by the parametric drive. (c). Time-dependent beating of the JPPs at  $\pm q_x$  referred to as squeezed mode  $J_{P1, q_x} J_{P1, -q_x}$  with their *non-zero* average value  $\langle J_{P1, q_x} J_{P1, -q_x} \rangle \neq 0$ , color coded same as in (a). (d). Same as in (b) but for (c). The beating has two contributions, one rectified to zero and one at  $\omega_{squeezed} = 2\omega_{JP, \pm q_x}$ . (e). Time-dependent representation of the phase of the JPPs. Before parametric amplification, the phase of the JPPs are completely random. However, after amplification via the phonons parametric force, the phase is locked to two specific values of 0 or  $\pi$  which is set by the drive. (f). The dynamics of the amplified JPPs discussed here can directly be connected to the generation of squeezed state already discussed in Section 1.7 [199].

## 6.4 Probing Amplified Josephson Plasmon Polari- ton Fluctuations

In this section we explore how the dynamics explained above ultimately give rise to the experimentally-measured signal. According to the four-mode mixing model, and as depicted in Fig.6.8 (a), the two apical oxygen phonon modes excite pairs of phase-fluctuating JPPs, forming the so-called squeezed state. These fluctuating currents  $J_{P1,q_x}$  and  $J_{P1,-q_x}$ , when taken individually, are symmetry-odd, hence break the inversion symmetry and are expected to generate hyper-Raman fields given by  $E_{SH,JP1,q_x} = \frac{\partial \chi^{(2)}}{\partial J_{P1,q_x}} J_{P1,q_x}(t') E_{800}^2(t' - t)$  and  $E_{SH,JP1,-q_x} = \frac{\partial \chi^{(2)}}{\partial J_{P1,-q_x}} J_{P1,-q_x}(t') E_{800}^2(t' - t)$ . On the other hand, the covariance  $J_{P1,q_x} J_{P1,-q_x}$ , is symmetry-even and therefore not hyper-Raman active, hence it neither breaks inversion symmetry nor modulates the SHG intensity. Schematic illustrations of the currents which flow in the sample due to the individual symmetry-breaking modes ( $J_{P1,q_x}$  and  $J_{P1,-q_x}$ ), and the symmetry-even squeezed mode ( $\langle J_{P1,q_x} J_{P1,-q_x} \rangle_{drive}$ ) are given in Fig.6.8(b).

Therefore, the total tr-SHG intensity response resulting from coherent dynamics of all the symmetry-odd modes can be calculated by once again using Eq.4.14:

$$I_{SH}(t) = \int |E_{SH,IR1}(t', t) + E_{SH,IR2}(t', t) + E_{SH,JP1,q_x}(t', t) + E_{SH,JP1,-q_x}(t', t) + E_{Lo}|^2 dt' \quad (6.9)$$

where  $E_{SH,IR1}(t', t)$  and  $E_{SH,IR2}(t', t)$  refer to the hyper-Raman fields generated by the coherent response of the driven phonon modes. Note that in Eq.6.9 and hence Fig.6.9 the nonlinear polarization due to direct mixing of the pump and probe electric fields via  $\chi_3$  is not included.

#### 6.4. Probing Amplified Josephson Plasmon Polariton Fluctuations

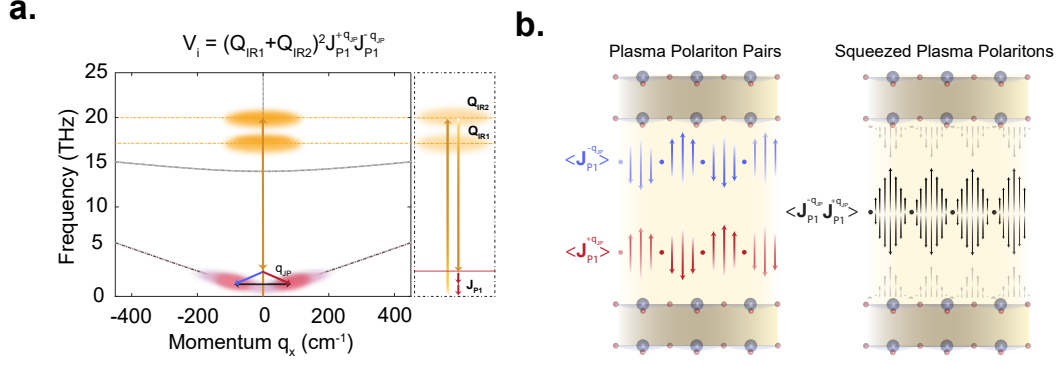


**Figure 6.8:** (a). Left panel: dispersion curves of the two apical oxygen phonon modes ( $Q_{IR1}$  at 17 THz and  $Q_{IR2}$  at 20 THz) and of the inter-bilayer ( $J_{P1}$ ) and intra-bilayer ( $J_{P2}$ ) Josephson plasma polaritons along the in-plane momentum  $q_x$  are shown as yellow and red dashed lines, respectively, for the four-mode mixing model explained in the text. The plasmon-polariton dispersion was calculated as discussed in section.2.6. The mid-IR pump excites the two apical oxygen phonon modes. They parametrically amplify a pair of inter-bilayer Josephson plasmon polaritons ( $J_{P1}$ ) at identical but opposite finite momentum  $\pm q_{JP}$  (illustrated by the red and blue arrows) such that the resonance condition is fulfilled:  $\omega_{IR2} - \omega_{IR1} = 2\omega_{JP1}(\pm q_{JP})$ . The right panel shows the energy level diagram describing the four-mode mixing model. (b). From left to right: Illustration of symmetry-odd, amplified phase-fluctuating inter-bilayer JPP modes at  $q_x$  (in red) and  $-q_x$  (in blue) along with the beating of the two, the symmetry-even, fixed phase squeezed mode (in black). As shown, the red and blue modes each oscillate at  $\omega_{JP1}(\pm q_x)$  while the black mode oscillates at the frequency of  $2\omega_{JP1}(\pm q_x)$  [199].

Figure 6.9 shows the simulated tr-SHG response calculated using Eq.6.9 for three values of  $E_{Lo}$ . In this calculation, the result was averaged over a randomized initial plasmon phase, in order to capture the effect of averaging over many laser shots in the real experiment. As described earlier and shown in Fig.6.7, due to the fluctuating temporal phase of the plasmons, the averaged plasmon amplitude is zero:  $\langle J_{P1, \pm q_x} \rangle_{drive} = 0$ , and hence the response in the heterodyne detection limit is zero. In fact, heterodyne detection is blind to the signatures of  $J_{P1, q_x}$  and  $J_{P1, -q_x}$  fluctuations as well as the covariance  $\langle J_{P1, q_x} J_{P1, -q_x} \rangle_{drive}$  of the two. This means that, in the heterodyne detection limit, only the averaged SHG intensity from the phonon modes is nonzero (see Fig.6.9(c) and (d)).

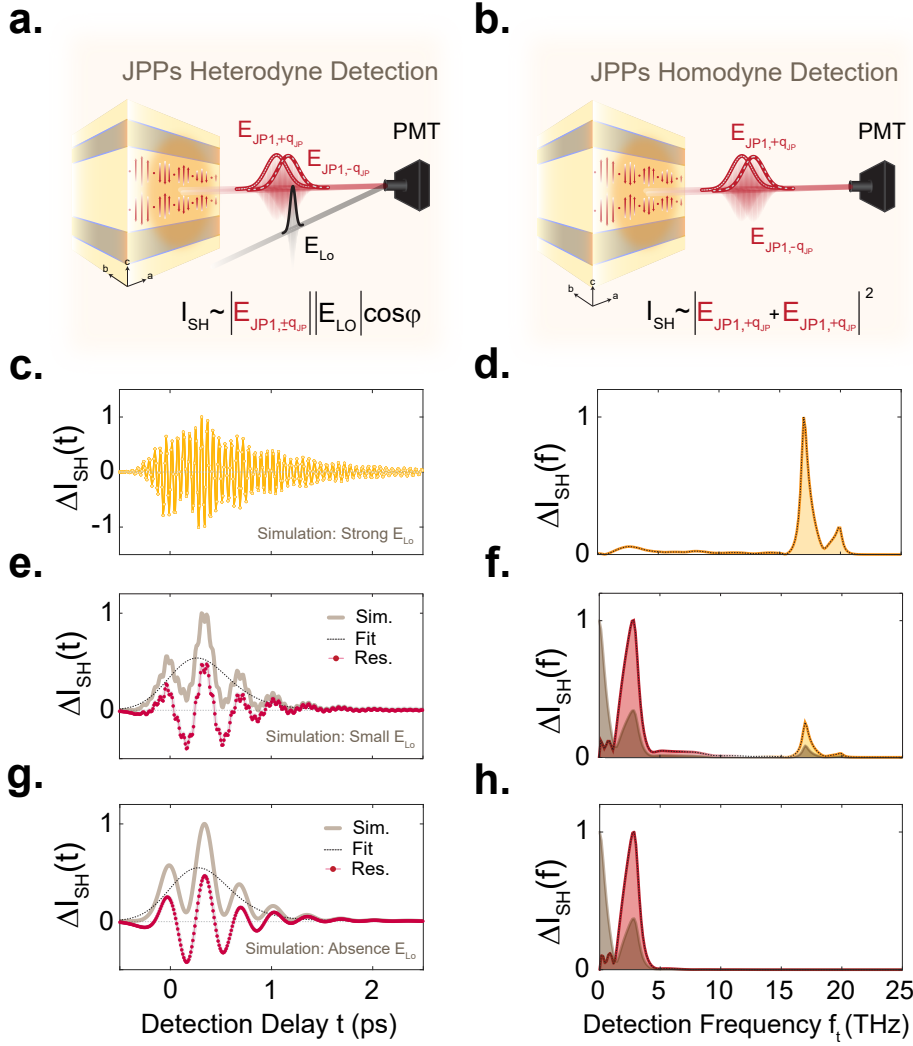


**Figure 6.9:** (a). Schematic of heterodyne detection of the hyper-Raman fields  $E_{\text{JP1},\pm q_x}$  generated from JPPs. (b). Same as in (a) but in the homodyne detection limit, in the absence of  $E_{\text{Lo}}$ . (c). Normalized tr-SHG intensity, simulated calculating the Eq.6.9 in the heterodyne detection limit (large  $E_{\text{Lo}}$ ). As discussed in the main text, the heterodyne detected response from JPPs averages to zero, hence the response is only from the driven phonons coherent dynamics. (d). Normalized FFT amplitude of (c), representing the driven phonons resonant response at 17 THz and 20 THz, convoluted with probe time resolution. (e). Same as in (c), but in the intermediate limit with small but nonzero  $E_{\text{Lo}}$ , before (shaded in brown) and after (red circles) of rectified background subtraction. The fit used to subtract the background is indicated by dashed-black curve and has a functional form of  $F_{\text{fit}} = A(1 + \text{erf}((t - t_0)/s_1)\exp(-(t - t_0)/s_2))$ , where,  $s_1$  and  $s_2$  are the rise and decay time constants, respectively.

## 6.4. Probing Amplified Josephson Plasmon Polariton Fluctuations

---

**Figure 6.9:** (f). Same as in (d), but for (e) before (shaded in brown) and after (shaded in red and yellow) background subtraction. The peaks shaded in yellow represent the resonant response of the driven phonons at 17 THz and 20 THz, while the low frequency peak at 3 THz corresponds to the homodyne contribution originating from the beating of the two as well as the JPPs. (g). Same as in (c) and (e) but in the homodyne detection limit ( $E_{Lo} = 0$ ), again before and after background subtraction same as in (e) with the same color coding. (h). Same as in (d) and (f) but for (g). Here in the homodyne detection limit, the response at 3 THz originates from the beating of the driven phonons and JPPs [199].

---

In the homodyne detection limit however, the detected second harmonic intensity has contributions which are proportional to the products  $\Delta I_{SH, Hom, \pm q_x} \propto \langle E_{JP1, -q_x} E_{JP1, -q_x} \rangle = \langle E_{JP1, \pm q_x} E_{JP1, \mp q_x} \rangle = \langle E_{JP1, q_x} E_{JP1, q_x} \rangle$ , which oscillate at  $2\omega_{JP1}$  and importantly have a fixed phase and therefore remain *nonzero*, even when averaged over many shots of the laser. The homodyne mixing therefore resurrects the dynamics of the squeezed state oscillating at  $2\omega_{JP1} = \omega_{squeezed}$ , meaning that even though the squeezed mode does not generate any hyper-Raman field, its dynamics can be traced back via the homodyne measurement.

Finally, we note that the homodyne mixing of the JPPs appears at the same frequency (3 THz) as the homodyne mixing between the two driven phonons (see section 6.2). As can be seen from the simulation results shown in Fig. 6.7, only the intermediate regime of small  $E_{Lo}$  shows a good agreement with the experimentally measured response (see Fig. 4.7(c)).

### 6.4.1 Two-Dimensional Nonlinear Spectroscopy

The simulations of the coupled phonon-plasmon dynamics via the four-mode mixing model were extended to the case of the two-pulse excitation experiment, using the same procedure described in Section 6.2.2, now with the equations of motion for

the four-mode mixing model given by Eq.6.8. Figure6.10 summarizes the resulting nonlinear two-dimensional simulations of the tr-SHG intensity for three different values of  $E_{LO}$ .

In the strong homodyne ( $I_{Hom}(f_t, f_\tau)$ ) detection limit, six strong peaks emerge, with frequency coordinates  $(f_t, f_\tau)$ ; (0 THz; 17 THz), (0 THz; 20 THz), (3 THz; 20 THz), (0 THz; -17 THz), (0 THz; -20 THz) and (3 THz; -17 THz) and two relatively weaker peaks at (0 THz; 0 THz) and (0 THz; 3 THz). On the other hand, in the strong heterodyne ( $I_{Het}(f_t, f_\tau)$ ) detection limit, the number of peaks is reduced to only five with completely different frequency coordinates  $(f_t, f_\tau)$ ; (17 THz; 0 THz), (20 THz; 0 THz), (17 THz; 17 THz), (20 THz; 20 THz) and (-17 THz; -17 THz).

A comparison between these simulated 2D peak patterns shows that the one calculated in the limit of homodyne-dominated detection provides a good agreement with the experimentally measured 2D peak pattern shown in Fig.5.8 (c) and (d). Moreover, the peak pattern observed from simulating the phonon-plasmon dynamics via the four-mode mixing model is *identical* to the simulated peak pattern arising from homodyne mixing of only the driven-phonons (see Fig.6.5 (d) and (e)). Therefore, all of these peaks include homodyne contributions from the two driven phonons (as their interference produces a difference-frequency response at 3 THz), and from the cooperatively-amplified JPPs. As discussed earlier, the homodyne detection of the amplified JPPs retrieves the non-radiating squeezed Josephson plasmon dynamics.

## 6.4. Probing Amplified Josephson Plasmon Polariton Fluctuations

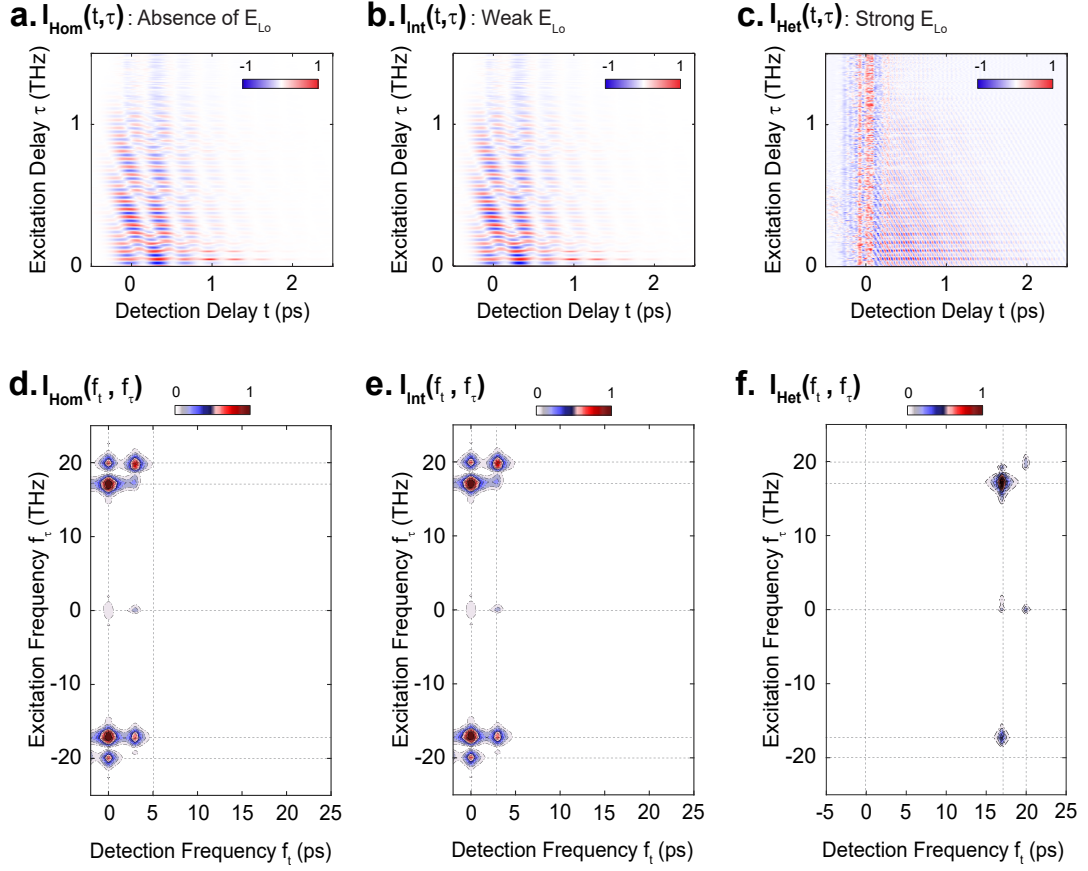


**Figure 6.10:** (a), (b), and (c). Normalized tr-SHG two-dimensional intensity map simulated using the lattice potential defined in Eq.6.7 for two-pulse excitation, respectively, in the limit of homodyne ( $E_{\text{Lo}} = 0$ ), intermediate (small  $E_{\text{Lo}}$ ) and heterodyne (large  $E_{\text{Lo}}$ ) detection. (d). Corresponding two-dimensional Fourier spectrum of (a). According to this 2D spectrum, there are eight strong peaks at frequency coordinates  $(f_t; f_\tau)$ ; (0;17), (0;20), (3;20), (0;-17), (0;-20) and (3;-17) along with two weaker peaks at (0,3) and (0;0) all in units of THz. (e). Same as in (d), this time for (b), representing the same peak pattern and frequency coordinates as in (d). (f). Same as in (d) and (e) but for (c). Here, the number of peaks reduced to four peaks with frequency coordinates; (17;0), (17;17), (20;20) and (17; -17) all in units of THz. The heterodyne detected nonlinear SHG response for the plasmon averages to zero due to the fluctuating seed. All Panels were normalized according to their own maximum values [199].

The results of the numerical simulations also provide an explanation for the two different temperature-dependent behaviors measured in  $\text{YBa}_2\text{Cu}_3\text{O}_{6.48}$  and

$\text{YBa}_2\text{Cu}_3\text{O}_{6.92}$  shown in Fig.5.10(a) and (b), respectively. In the case of  $\text{YBa}_2\text{Cu}_3\text{O}_{6.92}$  as discussed earlier, there is no IR-active, symmetry-odd mode below a frequency of 2 THz [48, 49] and the plasmon drive is far from resonance ( $2\omega_{\text{JP1}} = 14\text{THz} > \omega_{\text{IR2}} - \omega_{\text{IR1}} = 3\text{THz}$ ) [48, 135]. Therefore, the data measured in  $\text{YBa}_2\text{Cu}_3\text{O}_{6.92}$  represents the 2D peak pattern which arises purely from homodyne mixing of the resonantly excited phonon modes. Additionally, the 2D integrated amplitude being temperature independent implies that the excitation of the apical oxygen phonon modes is temperature independent as also reported for the same doping in equilibrium [192] and in the non-equilibrium one-dimensional experiment in this thesis (see Fig.4.9(c)).

Based on this, we can then attribute the temperature-dependent component of the 2D pattern in  $\text{YBa}_2\text{Cu}_3\text{O}_{6.48}$  (in Fig.5.10(a)) to the four-mode mixing nonlinearity of the phonons and amplified JPPs. Here, the plasmon amplification is a resonant process that dominates over the temperature independent phonon homodyne mixing. The relevant temperature scale  $T^*$  is consistent with the idea of finite frequency and momentum JPPs ( $J_{\text{P1},\pm q_x}$ ) fluctuating throughout the pseudo-gap phase as the four-mode amplification process can only take place if there is a fluctuating seed in equilibrium.

## 6.5 Photo-Induced Reflectivity Edge Calculations

The parametric plasmon amplification observed here also provides a possible explanation for the measured superconducting-like features in the non-equilibrium THz reflectivity in  $\text{YBa}_2\text{Cu}_3\text{O}_{6.48}$  (see Fig.3.7) [64–66]. As illustrated in Fig.6.11(a), excitation of apical oxygen phonon modes at 17 THz and 20 THz leads to coherent amplification of pairs of finite momentum inter-bilayer JPPs, where the amplifica-

## 6.5. Photo-Induced Reflectivity Edge Calculations

---

tion is most effective for the value of in-plane momentum  $q_x = q_{JP}$  which ensures that the resonance condition  $2\omega_{JP1}(\pm q_x) = \omega_{IR2} - \omega_{IR1}$  at  $\omega_{JP1} \approx 1.5$  THz is fulfilled. In this section we show that these coherently amplified superconducting modes give rise to a characteristic plasma edge at  $q = 0$ , observed in the reflectivity at a frequency blue-shifted relative to the equilibrium Josephson plasma resonance.

A Fresnel-Floquet formalism was used to calculate the expected reflectivity of  $\text{YBa}_2\text{Cu}_3\text{O}_{6.48}$  under these driven conditions [74, 217]. Based on this, the oscillations at  $\omega_F = \omega_{IR2} - \omega_{IR1}$  produce a Floquet medium. In the signal and idler basis, the eigenstates and eigenvalues of the Floquet medium are found according to the following:

$$\begin{bmatrix} \epsilon_\infty(\omega^2\omega_{JP}^2) + i\frac{\sigma_{DC}}{\epsilon_0}\omega - c^2q_x^2 & A \\ A & \epsilon_\infty((\omega - \omega_F)^2 - \omega_{JP}^2) + i\frac{\sigma_{DC}}{\epsilon_0}(\omega - \omega_F) - c^2q_x^2 \end{bmatrix} \begin{bmatrix} E(\omega) \\ E(\omega - \omega_F) \end{bmatrix} = 0 \quad (6.10)$$

Here,  $\omega$  is the frequency of the probe beam,  $\omega - \omega_F$  is the idler frequency,  $q_x$  is the in-plane momentum,  $E(\omega)$  is the electric field,  $\epsilon_\infty$  is the background material permittivity,  $\sigma_{DC}/\epsilon_0$  is a dissipation term resulting from the quasiparticle contribution to the conductivity,  $c$  is the speed of light and  $A$  captures the amplitude of the  $Q_{IR1}Q_{IR2}$  oscillations. The reflectivity was calculated using the Fresnel-Floquet approach with parameters  $\omega_F/2\pi = 3.8$  THz,  $A = 37.6$  (THz)<sup>2</sup>,  $\sigma_{DC}/\epsilon_0 = 36$  THz,  $(\omega_{JP}/2\pi)^2 = 0.37$  (THz)<sup>2</sup> and  $\epsilon_\infty = 25$ .

The results of this calculation are shown and compared to the experimentally measured reflectivity in Fig.6.11 (b). Starting from a featureless spectrum, a reflectivity edge emerges near 1.5 THz, in good agreement with the experimental data.

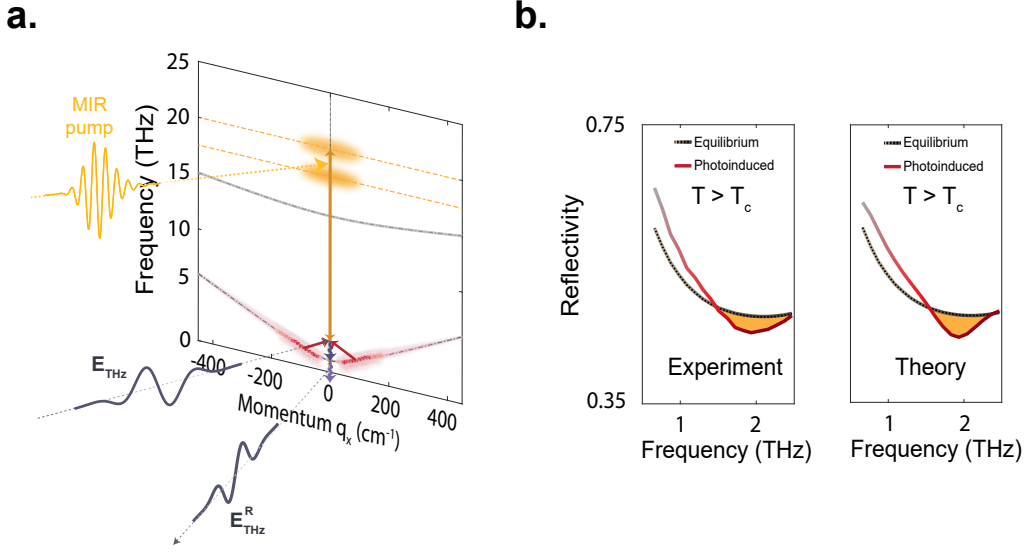


**Figure 6.11:** (a). Illustration of the coupling between phonon-driven amplified Josephson plasmon polaritons, assuming the four-mode mixing model, and the THz probe field, resulting in the observed photo-induced reflectivity edge. The mid-IR excitation pulse (yellow) resonantly excites the two apical oxygen phonon modes  $Q_{\text{IR}1}$  and  $Q_{\text{IR}2}$  (yellow shading) which parametrically amplify pairs of inter-bilayer Josephson plasma polaritons  $J_{\text{P}1}$  at frequencies  $\omega_{J_{\text{P}1}}(\pm q_x)$  (red shading). These excitations renormalize the reflection coefficient, as measured by the THz probe field at  $q_x = 0$  (grey pulses). (b). Comparison between experiment (left [64, 65]) and theory [74]. Dashed black lines show the THz frequency reflectivity above  $T_c$  in equilibrium. Red solid lines are the THz frequency reflectivity following mid-IR excitation. In both plots, the yellow shaded area indicates the photo-induced changes at the photo-induced plasma edge ( $\omega_{\text{JPLI}} < 2$  THz) [199].

## 6.6 Phonon-Phonon Dynamics

In this section, we provide numerical simulations which model the time resolved polarization rotation experiments in  $\text{YBa}_2\text{Cu}_3\text{O}_{6.92}$  in order to develop further insight into the third-order nonlinear coupling between the resonantly-driven IR-active phonon modes, and the Raman-active phonon modes. This is significantly more convincing than previously-reported observations of this coupling from purely one-

dimensional measurements, which relied on arguments based on the quantitative scaling of the signal with other controlled parameters such as fluence and drive-frequency. With this we complete our survey of the dynamics uncovered by the experiments described in this thesis.

We model the resonant excitation of the two infrared-active apical oxygen phonons using the same lattice potential discussed in Eq.6.1 and earlier in section 1.6.2. The nonlinear coupling of these modes to Raman-active phonon modes  $Q_{R,i}(\omega_{R,i})$ , with harmonic potentials  $V_i = \frac{1}{2}\omega_{R,i}^2 Q_{R,i}^2$ , is determined by the phononic interaction potential:

$$V_{\text{phononics}} = \sum_i (g_i Q_{\text{IR}1}^2 + h_i Q_{\text{IR}2}^2) Q_{R,i} \quad (6.11)$$

where  $g_i$  and  $h_i$  are the nonlinear coupling coefficients. The corresponding coupled equations of motion for all the phonon modes are:

$$\begin{aligned} \ddot{Q}_{\text{IR}2} + 2\gamma_{\text{IR}2}\dot{Q}_{\text{IR}2} + \omega_{\text{IR}2}^2 Q_{\text{IR}2} &= Z_2^* - \kappa_{\text{IR}2} Q_{\text{IR}2}^3 \\ \ddot{Q}_{\text{IR}1} + 2\gamma_{\text{IR}1}\dot{Q}_{\text{IR}1} + \omega_{\text{IR}1}^2 Q_{\text{IR}1} &= Z_1^* - \kappa_{\text{IR}1} Q_{\text{IR}1}^3 \\ \ddot{Q}_{R,1} + 2\gamma_{R,1}\dot{Q}_{R,1} + \omega_{R,1}^2 Q_{R,1} &= -g_1 Q_{\text{IR}1}^2 - h_1 Q_{\text{IR}2}^2 \\ \ddot{Q}_{R,2} + 2\gamma_{R,2}\dot{Q}_{R,2} + \omega_{R,2}^2 Q_{R,2} &= -g_2 Q_{\text{IR}1}^2 - h_2 Q_{\text{IR}2}^2 \\ \ddot{Q}_{R,3} + 2\gamma_{R,3}\dot{Q}_{R,3} + \omega_{R,3}^2 Q_{R,3} &= -g_3 Q_{\text{IR}1}^2 - h_3 Q_{\text{IR}2}^2 \end{aligned} \quad (6.12)$$

where  $\gamma_{R,i}$  are the phenomenological damping coefficients. The  $Q_{\text{IR}i}^2$  quadratic force on the Raman modes  $Q_{R,j}$  predicts the latter to move with a rectified component, as well as oscillating at their eigenfrequencies around the transient displacements [22, 23, 26, 30, 31, 72].

The time-delay dependent probe polarization rotation, induced by the three Raman phonon mode coordinates  $Q_{R,i}$ , was then calculated as explained in Section 4.2.2

using equations 4.4 and 4.5:

$$\Delta E_i(t) = A \int \frac{\partial \chi^{(1)}}{\partial Q_{R,i}} Q_{R,i}(t') E_{pr}(t' - t) dt' \quad (6.13)$$

### 6.6.1 Single-Pulse Excitation

The coupled equations of motion in Eq.6.12 were first solved for the case of a single-pulse excitation, in order to reproduce the one-dimensional experiment. Figures 6.12 (a) and (b) show the simulated  $\Delta E_{PR} = \sum_i \Delta E_i(t)$  for the three  $A_g$  Raman-active modes and the corresponding Fourier spectrum, respectively. The simulation

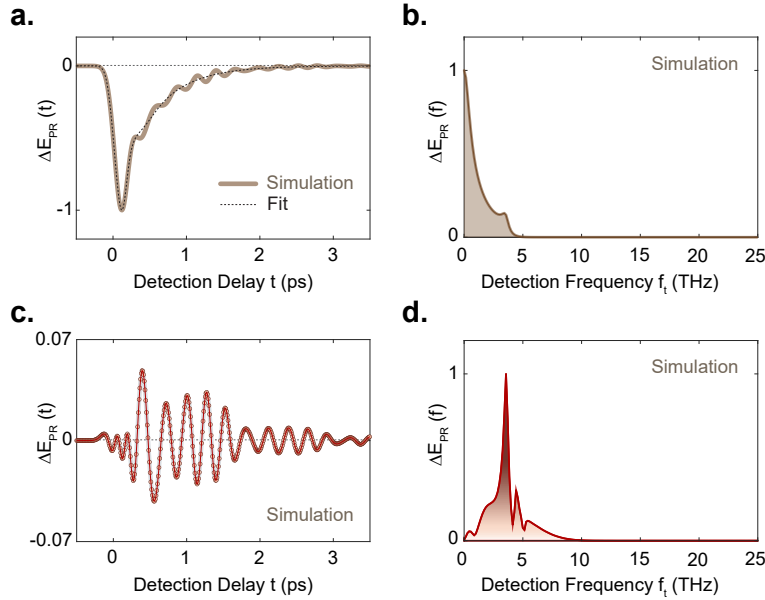


**Figure 6.12:** (a). The normalized polarization rotation response simulated using the lattice potential defined in Eq.6.11 for phonon-phonon coupling in  $YBa_2Cu_3O_{6.92}$ , representing a rectified component along with coherent oscillations of lower frequency Raman-active modes. The dashed-black curve indicates the fit to the data to subtract the rectified envelope. (b). Corresponding Fourier spectrum of (a). (c). Same as in (a) after the rectified envelope was subtracted in order to focus on the coherent oscillations of the Raman-active modes. (d). Same as in (b) but for (c), revealing three  $A_g$  Raman phonon modes at 3.6 THz, 4.4 THz and 5.1 THz [199].

results successfully reproduce the experimental data shown in Figs.4.4 (d) and (c). Note that the dynamics seen here were already explained in detail in Section 1.6.2.

### 6.6.2 Two-Dimensional Nonlinear Spectroscopy

To reproduce the two-pulse excitation experiments, the coupled equations of motion in Eq.6.12 were solved for a drive electric field  $E_{AB}(t, \tau)$  discussed in Section 6.2.2. The time dependent nonlinear contribution to the time-resolved polarization rotation was then calculated following the procedure outlined earlier in Eq.5.2:

$$\Delta E_{PR,NL} = \Delta E_{PR,AB} - \Delta E_{PR,A} - \Delta E_{PR,B}.$$

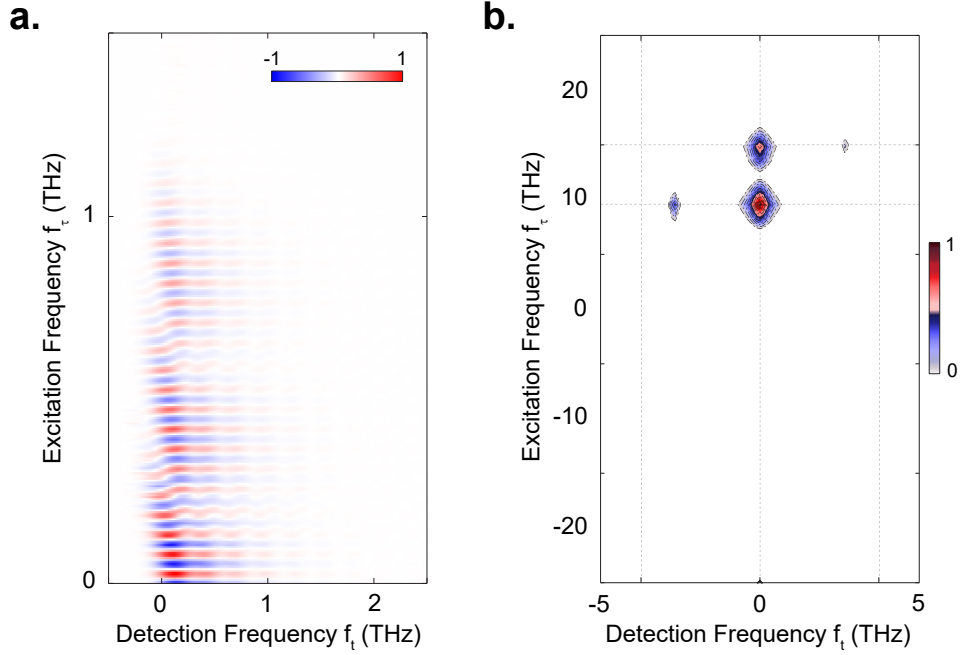


**Figure 6.13:** (a). Simulated, normalized two-dimensional tr-polarization rotation for the lattice potential defined in Eq.6.11. (b). Corresponding normalized nonlinear two-dimensional Fourier spectrum of (a), showing three peaks at frequency coordinates (0,17), (0,20) and (-3.6,17), all in units of THz [199].

Figure 6.13 summarizes the resulting nonlinear two-dimensional dynamics. In the

2D spectrum there appear two strong peaks at the frequency coordinates  $(f_t; f_\tau)$ : (0 THz; 17 THz) and (0 THz; 20 THz) along with a weaker peaks at (-3.6 THz; 17 THz). This peak pattern successfully reproduces the experimental 2D spectrum shown in Fig.5.5(d) and therefore confirms the nature of the third-order nonlinear phonon-phonon coupling. The measurement and the simulation presented here therefore represent the first direct measurement of the third-order nonlinear coupling (displacive excitation) between high-frequency IR-active and low-frequency Raman-active phonon modes using multidimensional spectroscopy.

## 6.7 Summary

This chapter focused on developing a theoretical framework in order to understand the results of the one- and two-dimensional experiments carried out in  $\text{YBa}_2\text{Cu}_3\text{O}_{6+x}$  compounds which were presented in Chapters 3 to 5. The ultimate goal was to propose a microscopic mechanism that can explain the formation of photo-induced superconducting-like properties observed in underdoped  $\text{YBa}_2\text{Cu}_3\text{O}_{6.48}$ , based on the observed photo-induced dynamics.

We began by using a simple Hamiltonian consisting of only the two driven phonon modes. The numerical simulations based on this simple model successfully reproduced the measured dynamics of the one- and two-dimensional tr-SHG experiments in both  $\text{YBa}_2\text{Cu}_3\text{O}_{6.48}$  and  $\text{YBa}_2\text{Cu}_3\text{O}_{6.92}$ .

However, this model alone cannot account for both the large difference in relative amplitudes as well as the temperature dependence of the peaks in the  $\text{YBa}_2\text{Cu}_3\text{O}_{6.48}$  compound. Therefore, to account for these, we extended the model to also include a further mode at a frequency of 1.5 THz. We find that if this mode is coupled to the two driven phonons with a four-mode mixing nonlinear term, it becomes

resonantly amplified and the observed dynamics are well reproduced. Note that due to the peak positions in the 2D tr-SHG spectrum, all other potential coupling mechanisms can be ruled out. The observed temperature dependence of the nonlinear signal, which is unique to the 6.48 compound, can then be understood as arising from the underlying temperature dependence of this mode. Following the arguments in [22], we assign this mode to finite-momentum JPP(s).

We also explored the microscopic consequences of this four-mode mixing process extensively. We found that such a process dictates that the driven phonon modes parametrically amplify pairs of phase-fluctuating, finite-momentum JPPs (at 1.5 THz), generating a squeezed state at a frequency of 3 THz. Even though the squeezed dynamics cannot be measured directly, they can be retrieved by tr-SHG homodyne mixing and hence are visible in our experiment. Fresnel-Floquet calculations show that the formation of the squeezed state through the four-mode mixing model also explains the observation of the photo-induced reflectivity edge at the frequency of 1.5 THz in earlier experiments.

The Chapter concluded by addressing the dynamics of the Raman-coupled modes in  $\text{YBa}_2\text{Cu}_3\text{O}_{6.92}$  which were observed in the tr-polarization rotation measurements. The one- and two-dimensional experiments were successfully reproduced by numerical simulations based on a third-order nonlinear coupling, completing our understanding of the Hamiltonian which governs the interaction between the resonantly-driven apical oxygen phonon modes, and all other lower frequency modes in this system.



# Summary and Outlook

Quantum materials often exhibit extremely rich phase diagrams, in which many exotic phases lie close to each-other in energy. This energetic proximity results in strong fluctuations (quantum or thermal) between the competing orders. Firstly, the study of these fluctuations provides deeper insights into the equilibrium properties of quantum materials, but more importantly it opens up possible pathways through which new phases and hence novel states can be accessed which are beyond the limits of thermal equilibrium [1, 2]. In most cases, these phenomena are closely correlated with the specific arrangement of the atoms in the crystal structure. Selective manipulation of these arrangements can be used to break symmetries and enhance or alter certain interactions, often resulting in the emergence of new functional properties.

In recent years, following major advances in laser technology, mode-selective excitation which targets specific vibrational degrees of freedom through resonant driving has become possible. This approach enables precise control over quantum material properties, which in some cases has been achieved through an apparent effective reduction in fluctuations in favor of magnetic, ferroelectric and superconducting orders [19, 22, 33, 64–67, 194, 195]. In *Chapter 1* an overview was given of some important ways in which light can interact with matter, including both structural (phonons) and electronic (plasmons) degrees of freedom. The first part of

the chapter focused on the linear interactions which govern the materials complex optical properties in equilibrium. In the second part of *Chapter 1*, the framework of nonlinear phononics was reviewed in details, which represents a framework for how mid-infrared light can be used to transiently manipulate material properties through various symmetry-allowed energy pathways [23, 26].

One of the most desirable and yet mysterious orders in quantum materials is superconductivity. *Chapter 2* lays out a brief overview of the fundamental principles of equilibrium superconducting order, firstly in the conventional superconductors and then in the high- $T_c$  Cuprate superconductors. Modeling Cuprate superconductors as a stack of Josephson junctions enabled their c-axis optical properties and the corresponding energy scales to be understood. This approach revealed that these materials host a variety of excitations in the THz to mid-infrared energy range.

The discussions in Chapters 1 and 2 established a foundation for approaching the central goal of this thesis: understanding the dynamics of the mid-IR photoinduced non-equilibrium superconducting-like state in  $\text{YBa}_2\text{Cu}_3\text{O}_{6+x}$ .

The presence of a large pseudogap energy scale (with a temperature  $T^*$ ), which has been associated with above- $T_c$  superconducting fluctuations [41, 43–45, 48, 49, 178], along with certain c-axis IR-active phonon modes which exhibit strong anomalous behaviour close to the superconducting phase transition [43, 49], has made underdoped  $\text{YBa}_2\text{Cu}_3\text{O}_{6+x}$  a strong candidate for inducing or enhancing superconductivity with light. In underdoped  $\text{YBa}_2\text{Cu}_3\text{O}_{6+x}$ , large-amplitude excitation of the c-axis apical oxygen phonon modes using resonant mid-infrared pulses at temperatures far above the transition temperature  $T_c$ , has been shown to induce transient optical properties that are reminiscent of those of an equilibrium superconductor. These experiments were reviewed in *Chapter 3*. These photo-

induced optical properties include a  $1/\omega$  divergence in the imaginary part of the THz-frequency optical conductivity and a reflectivity edge at a frequency of 1.5 THz [64–67]. More recently, this transient state has also been shown to expel static magnetic fields [68]. The temperature scale up to which these photoinduced signatures survive matches the temperature range of the pseudogap phase, drawing a connection to the idea of pre-existing superconducting fluctuations in this energy range even in equilibrium [22, 64–68, 199].

Following these macroscopic observations of photoinduced superconducting-like properties, a series of experiments were carried out in which the same excitation protocol (resonant driving of the apical oxygen phonon modes) was combined with optical probing in order to investigate the microscopic dynamics of the non-equilibrium state [22, 71–73]. The photoinduced symmetry-odd and symmetry-even dynamics, launched by mid-IR photoexcitation, were measured using second harmonic generation (SHG) and polarization rotation of 800 nm-wavelength probe pulses, respectively. *Chapter 4* provided a detailed review of these experiments, which were performed on both doping levels of  $\text{YBa}_2\text{Cu}_3\text{O}_{6.48}$  and  $\text{YBa}_2\text{Cu}_3\text{O}_{6.92}$ . The 6.92 doping level was chosen in order to provide a comparison with a compound in which photo-excitation does not induce macroscopic superconducting-like properties [188].

The key findings from these one-dimensional pump-probe experiments include: the detection of a low-frequency oscillatory response at a frequency of 3 THz in the SHG signal in both doping levels, with a stronger amplitude in the 6.48 compound; the parametric amplification of this mode in the 6.48 compound as a function of the driven phonon mode amplitude; and a temperature-dependent behavior of this component in the 6.48 compound, in contrast to the temperature-independent response in the 6.92 compound. Notably, the temperature dependence of the 3 THz

mode in the 6.48 doping was consistent with that of the other reported photoinduced superconducting-like properties in this doping. Despite the insights gained from these observations, no definitive microscopic mechanism could be pinpointed, in part due to the inherent limitations of one-dimensional experiments in resolving the exact nature of the coupling mechanism.

To address these limitations and to obtain a more complete understanding of the interactions between different modes, which was the main goal of this thesis, a novel form of multidimensional spectroscopy was developed and implemented. This advanced technique allowed for a more detailed mapping of the inter-mode interactions, potentially providing a deeper understanding of the underlying mechanisms that produce the non-equilibrium superconducting-like state in this system.

By combining two sequentially delayed mid-infrared excitation pulses and measuring the subsequent SHG or polarization-rotation of an 800 nm-wavelength probe pulse, this technique extends 2D THz spectroscopy into the mid-infrared frequency range. The details and the application of this technique along with the measured results in  $\text{YBa}_2\text{Cu}_3\text{O}_{6+x}$  were summarized in *Chapter 5*. The homodyne-detected tr-SHG 2D peak patterns measured across both doping levels of  $\text{YBa}_2\text{Cu}_3\text{O}_{6+x}$  revealed identical peak patterns consisting of two center peaks at frequencies positions of  $(f_t; f_\tau)$  (0 THz, 17 THz) and (0 THz, 20 THz) and two cross-peaks at frequencies of (-3 THz, 17 THz) and (3 THz, 20 THz). However, the temperature dependence again differed between the two: whilst the integrated 2D map of the underdoped compound exhibited temperature-dependent behavior consistent with the previous one-dimensional measurements, the higher-doped compound showed a temperature-independent response throughout the entire temperature range.

*Chapter 6* was devoted to presenting a theoretical model drawn from all of the

observations from the THz, one- and two dimensional experiments. This model describes the phonon-driven dynamics in  $\text{YBa}_2\text{Cu}_3\text{O}_{6+x}$ , and also provides an explanation for the photo-induced THz reflectivity edge. To summarize, the observation of homodyne cross-peaks in the two-dimensional spectra at  $\pm 3$  THz, which coincide with the low-frequency mode observed in the one-dimensional experiment, together with the photo-induced reflectivity edge at 1.5 THz, unambiguously point towards a four-mode mixing process.

This four-mode mixing process involves both resonantly excited apical oxygen phonon modes at 17 THz and 20 THz, coupled with a pair JPPs at 1.5 THz, generating a non-classical squeezed state. The  $T^*$  temperature scale of the parametrically amplified state suggests that the pseudo-gap phase hosts fluctuating JPPs which seed these dynamics. The numerical simulations presented in *Chapter 6* using the four-mode mixing model successfully reproduced the experimentally measured one- and two-dimensional responses. Furthermore, this coupling mechanism also quantitatively replicates the photo-induced reflectivity edge observed in the THz experiments.

This thesis has therefore provided significant new insights into the emergence of the non-equilibrium superconducting-like state in  $\text{YBa}_2\text{Cu}_3\text{O}_{6+x}$  through the development of novel multidimensional spectroscopic techniques. The results have significantly advanced our understanding of the interactions between various phonon and plasma polariton modes, and in particular how these interactions may be exploited to reduce fluctuations and induce order in quantum materials.

The generation of squeezed Josephson plasmons presented here draws a connection to the idea that a fluctuating pseudo-gap phase, hosting some form of phase-incoherent superconductivity, could be a pre-requisite for the formation of non-

equilibrium superconductivity. Indeed, the other material systems in which some form of light-induced enhancement of superconducting properties has been observed, namely  $K_3C_{60}$  [32, 34, 218] and  $\kappa$ -BEDT charge transfer salts [194, 195], also exhibit a strong vortex Nernst effect above  $T_c$  [219, 220]. It remains to be understood if some form of mode-squeezing could also be relevant to the light-induced coherence observed in those compounds.

The framework established here has at least three major ingredients which may be exploited in future work: firstly, the generation of a squeezed state may point towards a mechanism for phase stabilization or phase-noise reduction in material systems with strong fluctuations. More broadly, the results may suggest a new pathway towards the engineering of parametrically amplified responses in materials, with potential connections to the physics of time crystals [221–224] and to Floquet quantum matter [225, 226]. Secondly, SHG-homodyne detection was shown to be an effective probe with which the coherent dynamics of the squeezed fluctuations could be reconstructed, due to its sensitivity to the mode variance. However, for further systematic study of the squeezed dynamics and to provide a direct measurement of the phase fluctuations, a phase-stable controllable SH local oscillator should be established. Finally, the findings reported here also demonstrate the potential of this new form of mid-infrared multidimensional spectroscopy to understand inter-mode interactions and their resulting exotic phenomena in other strongly correlated materials, presenting a powerful approach for future experiments in the field.

Returning to the discussion of  $YBa_2Cu_3O_{6+x}$ , future experiments and theoretical work are essential to determine whether the four-mode mixing mechanism proposed here is sufficient to fully explain the possible establishment of superconducting phase rigidity in the non-equilibrium state, or if additional co-existing mechanisms contribute to superconducting phase coherence, with the generation of a

squeezed state being a secondary consequence. Continued investigation in this direction holds the promise of uncovering new pathways for manipulating quantum phases and could ultimately contribute to the design of next-generation quantum materials.

# List of Publications

The work presented in the Chapters 4-6 of this thesis are based on the following publications:

- A. von Hoegen, M. Fechner, M. Först, **N. Taherian**, E. Rowe, A. Ribak, J. Porras, B. Keimer, M. Michael, E. Demler, and A. Cavalleri “*Amplification of superconducting fluctuations in driven  $YBa_2Cu_3O_{6+x}$* ” **Physical Review X** **12**, **031008 (2022)**;
- **N. Taherian**, M. Först, A. Liu, M. Fechner, D. Pavicevic, A. von Hoegen, E. Rowe, Y. Liu, S. Nakata, B. Keimer, E. Demler, M. H. Michael, A. Cavalleri “*Probing amplified Josephson plasmons in  $YBa_2Cu_3O_{6+x}$  by multidimensional spectroscopy*” **npj Quantum Materials** **10**, **1–10 (2025)**;



# Appendices

# Appendix A

## Derivation of Squeezed State EOM

### A.1 Derivation of Squeezed State EOM

To derive the non-classical squeezed state equations of motion, we start from Ehrenfest equation in the simple harmonic oscillator picture which can be derived as follows;

$$\partial_t \tilde{P} = i[\tilde{H}, \tilde{P}] \quad (\text{A.1})$$

Here  $\tilde{H}$  and  $\tilde{P}$  refer to Hamiltonian and momentum operators, respectively. From quantum mechanics the expressions for position and momentum operators  $\tilde{x}$  and  $\tilde{P}$ , respectively, read;

$$\tilde{x} = i\partial_p \quad (\text{A.2})$$

and

$$\tilde{P} = -i\partial_x \quad (\text{A.3})$$

## Appendix A. Derivation of Squeezed State EOM

---

where the commutation relation reads  $[x, P] = i\hbar$  [227]. combining Eqs.A.1 to A.3 from above, the expression for Eq.A.1 reduces to;

$$\partial_t P = i[H, -i\partial_x] = -\partial_x H \quad (\text{A.4})$$

Now this picture can be extended to the general case discussed in section1.6.3 and 6.3 with the aim of deriving an expression for Eq.A.4 for modes corresponding to different values of momentum  $q$ , i.e.  $i[H, P(q)]$  (see Hamiltonian shown in Eq.1.24 and 6.7). To do this, we begin with the definition of the continuous field operator  $Q(x)$  and its conjugate momentum operator  $P(x)$  in the real space;

$$\begin{aligned} Q(x) &= \int \frac{d^3q}{(2\pi)^{(3)}} e^{iqx} Q(q) \\ P(x) &= \int \frac{d^3q}{(2\pi)^{(3)}} e^{iqx} P(q) \end{aligned} \quad (\text{A.5})$$

Note that  $Q^*(q) = Q(-q)$  (where  $*$  denotes the complex conjugate) for  $x$  to be real. Using the definitions above and quantum field theory, it can be shown that for two different positions  $x$  and  $x'$ , the canonical commutation relations reads;

$$\begin{aligned} [Q(x), P(x')] &= i\hbar\delta^3(x - x') \\ [Q(x), Q(x')] &= [P(x), P(x')] = 0 \end{aligned} \quad (\text{A.6})$$

Using the inverse Fourier transformation of the Eq.A.5 for a Fourier mode at  $q$ , we have;

$$\begin{aligned} Q(q) &= \int d^3x e^{-iqx} Q(x) \\ P(q) &= \int d^3x e^{-iqx} P(x) \end{aligned} \quad (\text{A.7})$$

### A.1. Derivation of Squeezed State EOM

---

Similarly, for two different values of  $q$  and  $q'$ , the commutation relation reads;

$$\begin{aligned} [Q(q), P(q')] &= i\hbar\delta^3(q + q') \\ [Q(q), Q(q')] &= [P(q), P(q')] = 0 \end{aligned} \tag{A.8}$$

which implies that for  $x$  to be real,  $q' = -q$ . From this, a generalized expression for Eq.A.3 for the momentum of the mode at  $q$  can be obtained such that:  $P(q) = \frac{\delta H}{\delta Q(-q)}$ , and hence the expression  $\delta_t P(q) = i[H, P(q)] = -\frac{\delta H}{\delta Q(q)}$  can be calculated which derives the equation of motion. This derivation procedure is followed from [228].

# Appendix B

## Nonlinear Circuit Model of Josephson Junction

### B.1 Modeling the Josephson Junction

In a Josephson junction when the bias current exceeds the critical current, the current flowing through the junction is no longer entirely dissipationless and therefore the Josephson equations cannot capture the dissipative dynamics. To account for both the super-carrier tunneling and the quasiparticle dissipation, the Josephson junction can be modeled as a non-linear circuit. This circuit model consists of an inductor ( $L$ ) representing the Josephson non-dissipative tunneling, in parallel with a capacitor ( $C$ ) representing the superconducting electrodes, and a resistor ( $R$ ) representing the quasiparticle dissipative tunneling. This arrangement is known as a resistively and capacitively shunted junction, and commonly referred to as the *RCSJ* model [229, 230], illustrated schematically in Fig.B.1(a). For an applied bias

## B.1. Modeling the Josephson Junction

---

current  $I_{\text{ext}}$ , the total current flowing through this circuit is given by:

$$I_{\text{ext}} = I_c \sin(\Delta\theta^*) + \frac{V}{R} + C \frac{\partial V}{\partial t} \quad (\text{B.1})$$

The first term on the right represents the Josephson current, the second term denotes the ohmic current flowing through the resistor, and the final term corresponds to the current induced by the capacitor. By employing the second Josephson equation, and using the chain rule to write  $\frac{\partial V}{\partial t} = \frac{\partial(\Delta\theta^*)^2}{\partial t^2}$ , Eq.B.1 can be reformulated as a function of  $(\Delta\theta^*)$  as given below:

$$I_{\text{ext}} = \frac{\partial(\Delta\theta^*)^2}{\partial t^2} + \frac{1}{RC} \frac{\partial(\Delta\theta^*)}{\partial t} + \omega_J^2 \sin(\Delta\theta^*) \quad (\text{B.2})$$

Equation B.2 is analogous to the equation of motion for a driven damped harmonic oscillator, where  $\Delta\theta^*$ ,  $\omega_J^2 = \frac{2eI_c}{\hbar C} = \frac{1}{LC}$  and  $\gamma = \frac{1}{RC}$ , denote the coordinate amplitude, resonance frequency, and damping, respectively. The solutions to Eq.B.2 manifest as plasma oscillations of the supercarriers, referred to as **Josephson plasma oscillations**. Note that the generalized version of the Josephson plasma oscillations at finite-momentum was given in Chapter 2, section.2.5.2.

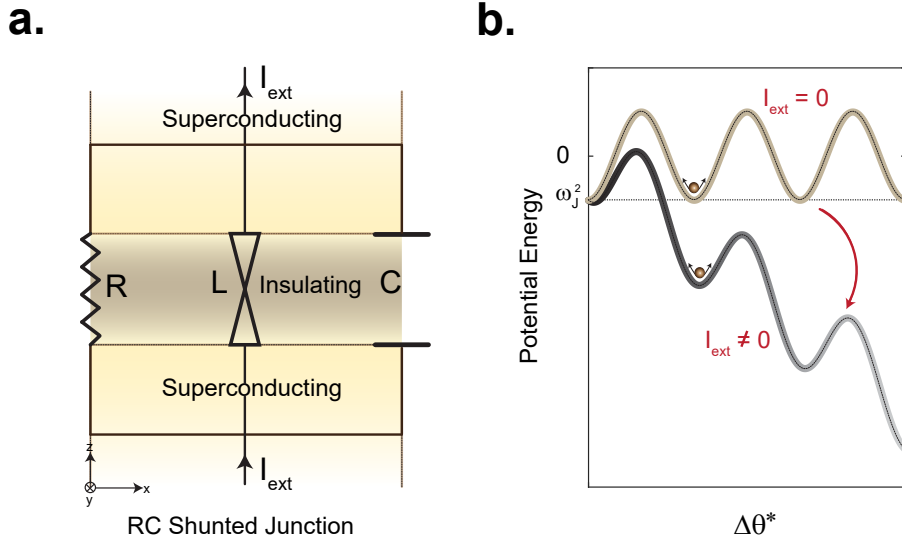


**Figure B.1:** (a). Equivalent circuit of RCSJ model for a Josephson junction. (b). The "tilted washboard" potential representation of the RCSJ model in the presence and absence of  $I_{\text{ext}}$ . Figures and captions of the panels (a) and (b) are adapted from [116].

Returning to the analogy of the damped harmonic oscillator, the particle (which here represents the phase difference across the junction -  $\Delta\theta$ ) oscillates in a potential defined as

$$U(\Delta\theta^*) = I_{\text{ext}}(\Delta\theta^*) - \omega_J^2 \cos(\Delta\theta^*) \quad (\text{B.3})$$

This potential, for the case of  $I_{\text{ext}}(\Delta\theta^*) \neq 0$  is known as **tilted washboard potential**. The oscillation of the phase is illustrated in Fig.B.1(b) for both zero and nonzero values of  $I_{\text{ext}}$ .

# Appendix C

## Establishment of a Local Oscillator

### C.1 Experimental Development of a Local Oscillator

The interpretation of the one- and two-dimensional time-resolved second harmonic generation (tr-SHG) experiments discussed in Chapters 4 and 5 is intricately connected to the detection scheme used in the experimental setup. As discussed in section 4.4.5 depending on the absence or presence of a local oscillator field ( $E_{Lo}$ ) on the detector, the signal is measured in, respectively, homodyne ( $I_{Hom}$ ) or heterodyne ( $I_{Het}$ ) detection limits. Here, we present an experimental attempt of the establishment of the local oscillator as an example and discuss the certain practical challenges.

Figure.C.1(a) shows an experimental schematic for the implementation of a controllable time-resolved SHG heterodyne detection scheme. In this scheme, the probe beam at 800 nm is split into two arms, one of which is incident on the sample (with or without the center of symmetry), which is also photo-excited by a mid-IR pump,

## Appendix C. Establishment of a Local Oscillator

generating a hyper-Raman field ( $E_{\text{SH}}$ ). The other probe arm was sent to a system with broken inversion symmetry (for example  $\text{LiNbO}_3$ ) with nonzero  $\chi^{(2)}$  in order to generate a static SHG field which acts as the local oscillator field ( $E_{\text{Lo}}$ ).

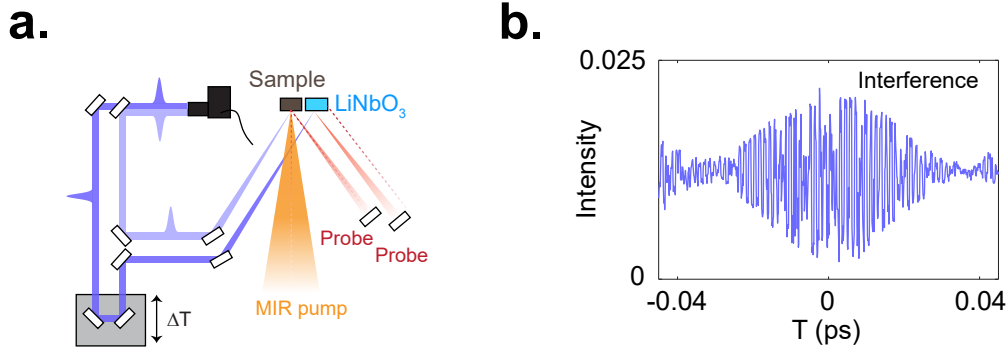


**Figure C.1:** (a). Schematic of an experimental approach for the establishment of the  $E_{\text{Lo}}$  with wavelength centered at 400 nm, detailed in the text. (b). An exemplary interference pattern measured as a function of time delay ( $T$ ) between the  $E_{\text{SH}}$  and  $E_{\text{Lo}}$  fields. The generated  $E_{\text{SH}}$  used in this measurement was generated from a different sample ( $\text{Cr}_2\text{O}_3$ ) and not  $\text{YBa}_2\text{Cu}_3\text{O}_{6+x}$ . By optimizing the spatial and temporal overlap, the interference pattern can be maximized.

Both generated fields at 400 nm were collected in reflection<sup>1</sup> and were sent to the detector, where they were spatially overlapped. To find the temporal overlap of the two fields, they were delayed by time delay  $T$ , using a motorized delay stage in the local oscillator path. To achieve this, the pump-probe delay is first fixed at the peak of the response, then the delay  $T$  between the two SHG fields is scanned in order to find the interference pattern as shown in Fig.C.1(b). Once the interference pattern is optimized, the time delay  $T$  was fixed and then the response was measured as function of pump-probe time delay  $t$ .

Importantly, the heterodyne detection of the tr-SHG signals requires a phase-stable local oscillator field. This is important because the absolute phase of the coherent

<sup>1</sup>In general these experiments can also be carried out in transmission if the sample is transparent.

### *C.1. Experimental Development of a Local Oscillator*

---

oscillations need to be measured. However, even very small fluctuations in the relative path length between the probing and local oscillator arms of the setup, caused by vibrations of the optical setup and the surrounding air, ruin this phase-stability, such that the implementation of this scheme is practically very challenging. The phase-instability along with the sensitivity of the spatial and temporal overlap of the two fields (the field generated from the sample and the local oscillator) are some of the practical difficulties in implementing a controllable heterodyne detection scheme in the experiments discussed in this thesis.

# Appendix D

## Numerical Simulations Parameters

### D.1 Mid-Infrared Electric Field Parameters

The parameters listed in table D.1 represents those used for the mid-IR excitation pulses to solve the equations of motion (Eq.6.2, Eq.6.8 and Eq.??) in one-two dimensional experiments. These parameters were chosen same as experimentally measured values and are fixed for all the numerical simulations presented in this study.

Label	Peak Field (MV/cm)	$\sigma_{\text{pump}}$ (ps)	$\omega_{\text{pump}}/2\pi$ (THz)
$E_A$	4	0.15	18.5
$E_B$	12	0.15	18.5

Table D.1: Caption

### D.2 Time-Resolved SHG Simulations Parameters

The parameters used in the numerical simulations to solve the one- and two-dimensional equations of motion for  $\text{YBa}_2\text{Cu}_3\text{O}_{6.92}$  and  $\text{YBa}_2\text{Cu}_3\text{O}_{6.48}$  systems, are

### D.3. Time-Resolved Polarization Rotation Simulations Parameters

listed in the tables D.2 and D.3 respectively. The parameters used here were chosen within the range of the numbers extracted from DFT calculations. The remaining free parameters which are Hyper-Raman cross-sections  $\frac{\partial\chi^{(2)}}{\partial Q_i}$  for each individual mode  $Q_i$  were chosen such that the simulations fit the experimental data.

Label	$Z^*$ ( $e/\sqrt{\text{u}}$ )	$\omega/2\pi$ (THz)	$\gamma$ (THz)	$\kappa$ (meV/u <sup>2</sup> A <sup>4</sup> )
$Q_{\text{IR}2}$	0.3	20	1.7	0.8
$Q_{\text{IR}1}$	0.4	17	1.7	56

**Table D.2:** Parameters Used in the numerical simulation of one- and two-dimensional tr-SHG experiments in YBa<sub>2</sub>Cu<sub>3</sub>O<sub>6.92</sub> to simulate the driven phonons dynamics.

Label	$Z^*$ ( $e/\sqrt{\text{u}}$ )	$\omega/2\pi$ (THz)	$\gamma$ (THz)	$\kappa$ (meV/u <sup>2</sup> A <sup>4</sup> )
$Q_{\text{IR}2}$	0.33	20	1.3	56
$Q_{\text{IR}1}$	0.34	17	1.5	56
$J_{\text{P}1,q_x}$	-	1.5	2.2	-
$J_{\text{P}1,-q_x}$	-	1.5	2.2	-

**Table D.3:** Parameters Used in the numerical simulation of one- and two-dimensional tr-SHG experiments in YBa<sub>2</sub>Cu<sub>3</sub>O<sub>6.48</sub> to simulate the phonon-plasmon nonlinear dynamics.

## D.3 Time-Resolved Polarization Rotation Simulations Parameters

The parameters used in the numerical simulations to solve the one- and two-dimensional equations of motion for nonlinear phonon-phonon coupling in YBa<sub>2</sub>Cu<sub>3</sub>O<sub>6.92</sub>, are listed in the table D.4. Same as before, the parameters used here were chosen within the range of the numbers extracted from DFT calculations. The remaining free parameters which are Raman cross-sections  $\frac{\partial\chi^{(1)}}{\partial Q_i}$  for each individual mode  $Q_i$  were chosen such that the simulations fit the experimental data.

## Appendix D. Numerical Simulations Parameters

---

Label	$Z^*$ ( $e/\sqrt{u}$ )	$\omega/2\pi$ (THz)	$\gamma$ (THz)	$\kappa$ (meV/u <sup>2</sup> A <sup>4</sup> )
$Q_{\text{IR}2}$	0.3	20	1	0.8
$Q_{\text{IR}1}$	0.4	17	1	56
$Q_{\text{R},1}$	-	3.6	1	-
$Q_{\text{R},2}$	-	4.4	1	-
$Q_{\text{R},3}$	-	5.1	1	-

**Table D.4:** Parameters Used in the numerical simulation of one- and two-dimensional tr-PR experiments in  $\text{YBa}_2\text{Cu}_3\text{O}_{6.92}$  to simulate the phonon-phonon nonlinear dynamics.

In all the numerical simulations the probe pulse duration was used same as the experimentally measured value  $\approx 30$  fs.

# Appendix E

## Analytical Model For Nonlinear Mode Coupling

### E.1 Analytical Model For Nonlinear Mode Coupling

To develop a deeper understanding of the one- and two-dimensional Fourier transformations in both the experiments and the numerical simulations, we developed a perturbative expansion approach to solve the equations of motion analytically. First, this methodology for a single resonantly excited mode with fourth-order nonlinearity is introduced followed by an extension of it to the case of the two driven apical oxygen phonon modes in  $\text{YBa}_2\text{Cu}_3\text{O}_{6.92}$ .

Consider the lattice potential already described in Eq.6.1. For a single IR-active mode  $Q_i$  with resonance frequency  $\omega_i$ , mode effective charge  $Z_i^*$  and fourth order

## Appendix E. Analytical Model For Nonlinear Mode Coupling

---

self-anharmonicity  $\kappa_i$ , driven by an excitation pulse electric field  $E(t)$  as follows;

$$V_i = \frac{1}{2}\omega_i^2 Q_i^2 + \frac{1}{4}\kappa_i Q_i^4 + Z_i^* Q_i E \quad (\text{E.1})$$

The equation of motion for this mode is

$$\ddot{Q}_i + 2\gamma_i \dot{Q}_i + 2\omega_i^2 Q_i = -Z_i^* E - \kappa_i Q_i^3 \quad (\text{E.2})$$

where the damping coefficient  $\gamma_i$  was introduced.

In the perturbative expansion approach, the drive electric field  $E(t)$  is replaced by  $\lambda E(t)$ , where  $\lambda$  changes continuously from zero to unity and determines the strength of the interaction ( $\lambda$  will be set to one at the end).

$$\ddot{Q}_i + 2\gamma_i \dot{Q}_i + 2\omega_i^2 Q_i = -Z_i^* \lambda E - \kappa_i Q_i^3 \quad (\text{E.3})$$

Seeking seek solutions to this equation in the form of a power series of  $\lambda$

$$Q_i = \lambda Q_i^{(1)} + \lambda^2 Q_i^{(2)} + \lambda^3 Q_i^{(3)} + \dots \quad (\text{E.4})$$

and rewrite Eq.E.3 as

$$\begin{aligned} & (\lambda \ddot{Q}_i^{(1)} + \lambda^2 \ddot{Q}_i^{(2)} + \lambda^3 \ddot{Q}_i^{(3)}) + 2\gamma_i (\lambda \dot{Q}_i^{(1)} + \lambda^2 \dot{Q}_i^{(2)} + \lambda^3 \dot{Q}_i^{(3)}) \\ & + \omega_0^2 (\lambda Q_i^{(1)} + \lambda^2 Q_i^{(2)} + \lambda^3 Q_i^{(3)}) = -\lambda Z_i^* E - \kappa_i Q_i^{(1)3} \end{aligned} \quad (\text{E.5})$$

Next, all the terms in the equation above can be reorganized proportional to the powers of  $\lambda$  and separated into equations below

$$\ddot{Q}_i^{(1)} + 2\gamma_i \dot{Q}_i^{(1)} + 2\omega_i^2 Q_i^{(1)} = -Z_i^* \lambda E \quad (\text{E.6})$$

$$\ddot{Q}_i^{(2)} + 2\gamma_i \dot{Q}_i^{(2)} + 2\omega_i^2 Q_i^{(2)} = 0 \quad (\text{E.7})$$

$$\ddot{Q}_i^{(3)} + 2\gamma_i \dot{Q}_i^{(3)} + 2\omega_i^2 Q_i^{(3)} = -\kappa_i Q_i^{(1)3} \quad (\text{E.8})$$

Using this approach, the linear and nonlinear responses are represented by  $Q_i^{(1)}$  and  $Q_i^{(n)}$  for  $n > 1$ , respectively. Hereafter, as an example the driven phonon dynamics in  $\text{YBa}_2\text{Cu}_3\text{O}_{6.92}$  following single and two-pulse excitation are discussed.

## E.2 Single-Pulse Excitation

For a delta function electric field  $E(t) = E_0\delta(t)$ , the first order impulsive response of the driven damped harmonic oscillator  $Q_i^{(1)}$  can be written as

$$Q_i^{(1)}(t) = \begin{cases} 0 & t < t_0 \\ \frac{E_0}{m\Omega_i} e^{-\gamma_i t} \sin(\Omega_i(t)) & t > t_0; \end{cases} \quad (\text{E.9})$$

with  $\Omega_i = \sqrt{\omega_i^2 - \gamma_i^2}$ .

The third-order correction is obtained by substituting  $Q_i^{(1)}(t)$  into Eq.E.8 and finding the analytical solution

$$\begin{aligned} -\kappa_i Q_i^{(1)3} &= -\kappa_i \left( -\frac{Z_i^* E_0}{\Omega_i} e^{\gamma_i t} \sin(\Omega_i t) \right)^3 \\ &= \frac{Z_i^* \kappa_i E_0}{\Omega_i} e^{-3\gamma_i t} \left( \frac{3}{4} \sin(\Omega_i t) - \frac{1}{4} \sin(3\Omega_i t) \right) \end{aligned} \quad (\text{E.10})$$

These two equations show that the linear and non-linear responses contains a term resonating at the fundamental and another term resonating at the third harmonic frequency.

## Appendix E. Analytical Model For Nonlinear Mode Coupling

---

According to Eq.E.9,  $Q_{\text{IR1}}$  and  $Q_{\text{IR2}}$  develop as;

$$Q_{\text{IR1}}(t) = E'_{\text{IR1}} e^{-\gamma_{\text{IR1}} t} \sin(\Omega_{\text{IR1}} t) \quad (\text{E.11})$$

and

$$Q_{\text{IR2}}(t) = E'_{\text{IR2}} e^{-\gamma_{\text{IR2}} t} \sin(\Omega_{\text{IR2}} t) \quad (\text{E.12})$$

with  $\Omega_{\text{IRi}} = \sqrt{\omega_{\text{IRi}}^2 - \gamma_{\text{IRi}}^2}$  and  $E'_{\text{IRi}} = -\frac{Z_{\text{IRi}}^* E_0}{\Omega_{\text{IRi}}}$ . These phonon modes each generate hyper-Raman fields  $E_{\text{HR},i}$ .

The time dependent SHG intensity is again calculated following the equations presented in section 4.4.4. In the limit of homodyne detection with  $I_{\text{Hom}} \propto |\sum_i E_{\text{HR},i}|^2$ , the signal contains frequency components at  $(\Omega_{\text{IR1}} + \Omega_{\text{IR2}})$  and  $(\Omega_{\text{IR1}} - \Omega_{\text{IR2}})$ . In the heterodyne detection, the contributions resulting from the interference term  $I_{\text{Het}} \propto |E_{\text{HR},i}| |E_{\text{Lo}}| \cos\phi$  appear at the phonon modes eigenfrequencies  $\Omega_{\text{IR1}}$  and  $\Omega_{\text{IR2}}$ . These contribution were already discussed in the Chapter 4, section 4.4.5.

### E.3 Two-Dimensional Nonlinear Spectroscopy

The results discussed for the potential in Eq.E.1 can be extended to the case with two pulses exciting the system. Once again, the excitation pulses are in the form of delta functions  $E_{\text{AB}}(t, \tau) = E_{0A}\delta(t) + E_{0B}\delta(t + \tau)$ .

Following excitation with both pulses, the first order response can be rewritten as

$$\begin{aligned} Q_i^{(1)}(t, \tau) &= Q_{iA}^{(1)}(t) + Q_{iB}^{(1)}(t, \tau) \\ &= -\frac{Z_i^* E_{0A}}{\Omega_i} e^{-\gamma_i t} \sin(\Omega_i t) - \frac{Z_i^* E_{0B}}{\Omega_i} e^{-\gamma_i(t+\tau)} \sin(\Omega_i(t + \tau)) \end{aligned} \quad (\text{E.13})$$

### *E.3. Two-Dimensional Nonlinear Spectroscopy*

---

where  $Q_{iA}^{(1)}(t)$  is the first order response to only the excitation pulse  $E_A$  and  $Q_{iB}^{(1)}(t, \tau)$  is the first order response to only the excitation pulse  $E_B$ . The total response in the second harmonic intensity is then obtained by incorporating the time-resolved probing scheme explained in Section 4.4.4 to the response of the coordinates  $Q_{IR1}$  and  $Q_{IR2}$ . For the two-pulse excitation, we again restrict the analytical approach to only the first order response

$$Q_{IRi,AB}(t, \tau) = E'_{IRi} e^{-\gamma_i t} \sin(\Omega_i t) + E'_{IRi} e^{-\gamma_i(t+\tau)} \sin(\Omega_i(t+\tau)) \quad (\text{E.14})$$

For simplicity, it was assumed that  $E_{0,A} = E_{0,B}$ . The time dependent SHG intensity associated with these dynamics is again calculated following the equations presented in Section 4.4.4, considering the two-pulse excitation approach of Section 6.2.2.

As the perturbative solution is restricted to only the first order response, which is linear to the driving electric field, the nonlinear contribution to the SHG intensity in the heterodyne detection limit is zero. In contrast, there is a nonzero response in the nonlinear contribution in the homodyne detection limit, because it is sensitive to mixing terms from the two phonon fields. Equations E.15 and E.16 show the mathematical terms obtained using the analytical approach to the first order response.

$$I_{NL}^{\text{Het}} = I_{AB}^{\text{Het}} - (I_A^{\text{Het}} + I_B^{\text{Het}}) = 0 \quad (\text{E.15})$$

## Appendix E. Analytical Model For Nonlinear Mode Coupling

$$\begin{aligned}
 I_{\text{NL}}^{\text{Hom}}(t, \tau) &= I_{\text{AB}}^{\text{Hom}} - I^{\text{AHom}} - I^{\text{BHom}} \\
 &= \left\{ \begin{aligned}
 &2E''_{\text{IR1,A}} E''_{\text{IR1,B}} \Omega_{\text{IR1}}^2 e^{-\gamma_{\text{IR1}}(2t+\tau)} \cos(\Omega_{\text{IR1}}(t)) \cos(\Omega_{\text{IR1}}(t+\tau)) \\
 &-2E''_{\text{IR1,A}} E''_{\text{IR1,B}} \Omega_{\text{IR1}} \gamma_{\text{IR1}} e^{-\gamma_{\text{IR1}}(2t+\tau)} \sin(\Omega_{\text{IR1}}(t)) \cos(\Omega_{\text{IR1}}(t+\tau)) \\
 &-2E''_{\text{IR1,A}} E''_{\text{IR1,B}} \Omega_{\text{IR1}} \gamma_{\text{IR1}} e^{-\gamma_{\text{IR1}}(2t+\tau)} \sin(\Omega_{\text{IR1}}(t+\tau)) \cos(\Omega_{\text{IR1}}(t)) \\
 &+2E''_{\text{IR1,A}} E''_{\text{IR1,B}} \gamma_{\text{IR1}}^2 e^{-\gamma_{\text{IR1}}(2t+\tau)} \sin(\Omega_{\text{IR1}} t) \sin(\Omega_{\text{IR1}}(t+\tau)) \\
 &+2E''_{\text{IR2,A}} E''_{\text{IR1,B}} \Omega_{\text{IR1}} \Omega_{\text{IR1}} e^{-\gamma_{\text{IR1}}(t+\tau)} e^{-\gamma_{\text{IR2}}(t)} \cos(\Omega_{\text{IR2}} t) \cos(\Omega_{\text{IR1}}(t+\tau)) \\
 &-2E''_{\text{IR1,A}} E''_{\text{IR2,B}} \Omega_{\text{IR1}} \gamma_{\text{IR2}} e^{-\gamma_{\text{IR1}}(t)} e^{-\gamma_{\text{IR2}}(t+\tau)} \sin(\Omega_{\text{IR2}}(t+\tau)) \cos(\Omega_{\text{IR1}}(t)) \\
 &-2E''_{\text{IR2,A}} E''_{\text{IR1,B}} \Omega_{\text{IR1}} \gamma_{\text{IR2}} e^{-\gamma_{\text{IR1}}(t+\tau)} e^{-\gamma_{\text{IR2}}(t)} \sin(\Omega_{\text{IR2}}(t)) \cos(\Omega_{\text{IR1}}(t+\tau)) \\
 &-2E''_{\text{IR1,A}} E''_{\text{IR2,B}} \Omega_{\text{IR2}} \gamma_{\text{IR1}} e^{-\gamma_{\text{IR1}}(t)} e^{-\gamma_{\text{IR2}}(t+\tau)} \sin(\Omega_{\text{IR1}}(t)) \cos(\Omega_{\text{IR2}}(t+\tau)) \\
 &-2E''_{\text{IR1,B}} E''_{\text{IR2,A}} \Omega_{\text{IR2}} \gamma_{\text{IR1}} e^{-\gamma_{\text{IR1}}(t+\tau)} e^{-\gamma_{\text{IR2}}(t)} \sin(\Omega_{\text{IR1}}(t+\tau)) \cos(\Omega_{\text{IR2}}(t)) \\
 &+2E''_{\text{IR1,A}} E''_{\text{IR2,B}} \gamma_{\text{IR1}} \gamma_{\text{IR2}} e^{-\gamma_{\text{IR1}}(t)} e^{-\gamma_{\text{IR2}}(t+\tau)} \sin(\Omega_{\text{IR1}}(t)) \sin(\Omega_{\text{IR2}}(t+\tau)) \\
 &+2E''_{\text{IR2,A}} E''_{\text{IR1,B}} \gamma_{\text{IR1}} \gamma_{\text{IR2}} e^{-\gamma_{\text{IR1}}(t+\tau)} e^{-\gamma_{\text{IR2}}(t)} \sin(\Omega_{\text{IR2}}(t)) \sin(\Omega_{\text{IR2}}(t+\tau)) \\
 &-2E''_{\text{IR2,A}} E''_{\text{IR2,B}} \Omega_{\text{IR2}} \gamma_{\text{IR2}} e^{-\gamma_{\text{IR2}}(2t+\tau)} \sin(\Omega_{\text{IR2}}(t)) \cos(\Omega_{\text{IR2}}(t+\tau)) \\
 &-2E''_{\text{IR2,A}} E''_{\text{IR2,B}} \Omega_{\text{IR2}} \gamma_{\text{IR2}} e^{-\gamma_{\text{IR2}}(2t+\tau)} \sin(\Omega_{\text{IR2}}(t+\tau)) \cos(\Omega_{\text{IR2}}(t)) \\
 &+2E''_{\text{IR2,A}} E''_{\text{IR2,B}} \gamma_{\text{IR2}}^2 e^{-\gamma_{\text{IR2}}(2t+\tau)} \sin(\Omega_{\text{IR2}}(t)) \sin(\Omega_{\text{IR2}}(t+\tau))
 \end{aligned} \right. \quad (\text{E.16})
 \end{aligned}$$

The sixteen terms in this solution give rise to twelve observable peaks in the nonlinear 2D spectrum, with frequency coordinates  $(f_t; f_\tau)$ ;  $((\Omega_{\text{IR2}} - \Omega_{\text{IR1}}); \Omega_{\text{IR2}})$ ,  $((\Omega_{\text{IR1}} - \Omega_{\text{IR2}}); -\Omega_{\text{IR2}})$ ,  $((\Omega_{\text{IR1}} - \Omega_{\text{IR2}}); \Omega_{\text{IR1}})$ ,  $((\Omega_{\text{IR2}} - \Omega_{\text{IR1}}); -\Omega_{\text{IR1}})$ ,  $(0; \pm\Omega_{\text{IR2}})$  and  $(0; \pm\Omega_{\text{IR1}})$ . In addition, there are eight more peaks  $(\pm(\Omega_{\text{IR1}} + \Omega_{\text{IR2}}); \Omega_{\text{IR1}})$ ,  $(\pm(\Omega_{\text{IR1}} + \Omega_{\text{IR2}}); \Omega_{\text{IR2}})$ ,  $(2\Omega_{\text{IR1}}; \pm\Omega_{\text{IR1}})$  and  $(2\Omega_{\text{IR2}}; \pm\Omega_{\text{IR2}})$  which, due to the probe time resolution, are resolved in neither the numerical simulations nor the experiment. This analytically calculated peak pattern, arising from only phonon mode

### E.3. Two-Dimensional Nonlinear Spectroscopy

dynamics, is consistent with both the numerically simulated and experimentally measured 2D spectra of  $\text{YBa}_2\text{Cu}_3\text{O}_{6.92}$ , as shown in Fig.E.1.

Note that in this treatment, the first-order response of the phonon mode coordinates results in a nonzero contribution to the nonlinear SHG intensity only in the homodyne detection whilst the heterodyne detection is zero. Nonlinear responses in the heterodyne detection limit, as for example shown in the numerically simulated two-dimensional spectra in Fig.6.5 (f), occur only if higher-order responses, such as the fourth order nonlinearities of the driven phonons, are taken into account.

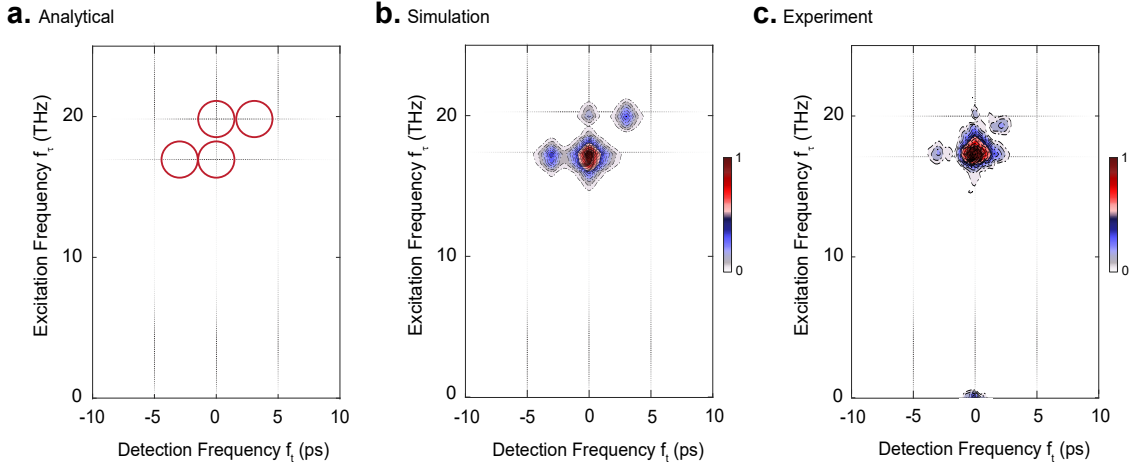


**Figure E.1:** (a). Predicted peak pattern obtained from Eq.E.16, using the two phonon mode coordinates first order response and calculated in the homodyne SHG intensity detection limit. Within the experiment resolution, there are eight peaks with the corresponding frequency coordinates  $(f_t; f_\tau)$ ;  $((\Omega_{\text{IR}2} - \Omega_{\text{IR}1}); \Omega_{\text{IR}2})$ ,  $((\Omega_{\text{IR}1} - \Omega_{\text{IR}2}); -\Omega_{\text{IR}2})$ ,  $((\Omega_{\text{IR}1} - \Omega_{\text{IR}2}); \Omega_{\text{IR}1})$ ,  $((\Omega_{\text{IR}2} - \Omega_{\text{IR}1}); -\Omega_{\text{IR}1})$ ,  $(0; \pm\Omega_{\text{IR}2})$  and  $(0; \pm\Omega_{\text{IR}1})$ , all in units of THz. (b). Two-dimensional Fourier spectrum simulated using the lattice potential defined in Eq.6.1 for two-pulse excitation (considering small excitation fields  $E_{0A} = E_{0B}$  as in the analytical solution) in the limit of homodyne detection. (c). Two-dimensional Fourier spectrum measured in  $\text{YBa}_2\text{Cu}_3\text{O}_{6.92}$  at base temperature 20 K below  $T_c$  shown in Fig.5.9(d). Panels (b) and (c) were normalized according to their own maximum values. The predicted, simulated and measured peak patterns are in good agreement.

# Appendix F

## Squeezed Plasmons Dynamics

### F.1 Squeezed Plasmons Dynamics

As explained, the beating of the fluctuating plasmon polaritons  $\langle J_{P1,q_x} J_{P1,-q_x} \rangle$  forms a squeezed state which oscillates at  $\omega_{\text{squeezed}} = 2\omega_{JP1}(\pm q_{JP})$ . In this section the dynamics of this squeezed mode from a theoretical point of view is discussed. The phonon-plasmon interaction Hamiltonian can be written as follows;

$$\begin{aligned} H_{\text{phonon-plasmon}} = & \sum_{q_x} P_{P1,q_x} P_{P1,-q_x} + (\omega_{JP1}^2 + c^2 q_x^2) J_{P1,q_x} J_{P1,-q_x} \\ & + \beta(Q_{IR1} + Q_{IR2})^2 J_{P1,q_x} J_{P1,-q_x} \end{aligned} \quad (\text{F.1})$$

where  $P_{P1,q_x}$  is the generalized plasmon momentum.

The corresponding coupled equations of motion derived from the Ehrenfest equations  $\frac{\partial O}{\partial t} = i[H, O]$  for the Josephson plasma fluctuations are;

$$\frac{\partial}{\partial t}(J_{P1,q_x} J_{P1,-q_x}) = P_{P1,-q_x} J_{P1,q_x} + P_{P1,q_x} J_{P1,-q_x} \quad (\text{F.2})$$

$$\begin{aligned} \frac{\partial}{\partial t} (P_{P1,-q_x} J_{P1,q_x} + P_{P1,q_x} J_{P1,-q_x}) &= -2(\omega_{JP1}^2 + c^2 q_x^2) J_{P1,q_x} J_{P1,-q_x} \\ &\quad - 2\beta(Q_{IR1} + Q_{IR2})^2 J_{P1,q_x} J_{P1,-q_x} + 2P_{P1,q_x} P_{P1,-q_x} \end{aligned} \quad (F.3)$$

$$\begin{aligned} \frac{\partial}{\partial t} (P_{P1,q_x} P_{P1,-q_x}) &= -(\omega_{JP1}^2 + c^2 q_x^2) (P_{P1,-q_x} J_{P1,q_x} + P_{P1,q_x} J_{P1,-q_x}) \\ &\quad - \beta(Q_{IR1} + Q_{IR2})^2 (P_{P1,-q_x} J_{P1,q_x} + P_{P1,q_x} J_{P1,-q_x}) \end{aligned} \quad (F.4)$$

The time dependent plasma response is obtained by first linearizing the driven current coordinate and momentum fluctuations around their equilibrium values

$$\langle J_{P1,q_x} J_{P1,-q_x} \rangle_{\text{drive}} = \langle J_{P1,q_x} J_{P1,-q_x} \rangle - \langle J_{P1,q_x} J_{P1,-q_x} \rangle_{\text{equil.}} \quad (F.5)$$

and,

$$\langle P_{P1,q_x} P_{P1,-q_x} \rangle_{\text{drive}} = \langle P_{P1,q_x} P_{P1,-q_x} \rangle - \langle P_{P1,q_x} P_{P1,-q_x} \rangle_{\text{equil.}} \quad (F.6)$$

which are related to each other by

$$\begin{aligned} \frac{\partial}{\partial t} \langle J_{P1,q_x} J_{P1,-q_x} \rangle_{\text{equil.}} &= \frac{\partial}{\partial t} \langle P_{P1,q_x} P_{P1,-q_x} \rangle_{\text{equil.}} \\ &= \frac{\partial}{\partial t} \langle P_{P1,q_x} J_{P1,-q_x} + P_{P1,-q_x} J_{P1,q_x} \rangle_{\text{equil.}} \\ &= Q_{IR1} = Q_{IR2} = 0 \end{aligned} \quad (F.7)$$

These conditions lead to the relations  $\langle P_{P1,q_x} J_{P1,-q_x} + P_{P1,-q_x} J_{P1,q_x} \rangle_{\text{equil.}} = 0$  and  $\langle P_{P1,q_x} P_{P1,-q_x} \rangle_{\text{equil.}} = \frac{1}{\omega_{JP1}^2 + c^2 q_x^2} \langle J_{P1,q_x} J_{P1,-q_x} \rangle_{\text{equil.}}$ , finally resulting in the equation of motion for the phonon-driven Josephson plasma polariton fluctuations;

$$\left( \frac{\partial}{\partial t} + 4(\omega_{JP1}^2 + c^2 q_x^2) \right) \langle J_{P1,q_x} J_{P1,-q_x} \rangle = -2\beta(Q_{IR1} + Q_{IR2})^2 \langle J_{P1,q_x} J_{P1,-q_x} \rangle_{\text{equil.}} \quad (F.8)$$

which gives a resonant response when  $2\omega_{JP1}(\pm q_x) = \omega_{IR2} - \omega_{IR1}$  ( $=3$  THz considered here) for an in-plane momentum given by  $c^2 q_{JP}^2 \approx \frac{(\omega_{IR2}^2 - \omega_{IR1}^2)^2}{4} - \omega_{JP1}^2$ . This equation shows that the *equilibrium fluctuations* are crucial for the four-mode mixing

## Appendix F. Squeezed Plasmons Dynamics

---

model. Additionally, it shows that the squeezing dynamics are resonantly excited at  $2\omega_{\text{JP1}}(\pm q_{\text{JP}})$  via the  $Q_{\text{IR1}}Q_{\text{IR2}}$  force and with a phase that is fixed by the phase difference of the two phonons  $\phi_{Q_{\text{IR1}}Q_{\text{IR2}}} = \phi_{Q_{\text{IR2}}} - \phi_{Q_{\text{IR1}}}$ .

From Eq.F.5, and assuming initial thermal fluctuations  $\langle J_{\text{P1},q_x} J_{\text{P1},-q_x} \rangle_{\text{equil.}}$ , we can trace back the non-radiating oscillations of  $\langle J_{\text{P1},q_x} J_{\text{P1},-q_x} \rangle$  at  $2\omega_{\text{JP1}}$  from the SHG measurement in the homodyne detection limit. This intuition is confirmed in the numerical simulations which include dissipation and random phase fluctuations as shown in Fig.6.7(c).



# Acknowledgement

The start was not easy and the path was not smooth but the journey was exciting, educational and the experience, indeed, very valuable. On this journey, there were people to whom I owe a lot for both their emotional and scientific supports.

First and foremost, I would like to sincerely thank my PhD supervisor, Andrea Cavalleri, for giving me the opportunity and supporting me to grow both scientifically and personally. His generous guidance taught me how to persevere and move forward, especially in the moments when I needed it most.

I would like to also thank my PhD co-supervisor Nils Huse for his valuable input and support. My special thanks go to Guido Meier who always deeply cares and truly supports. I am also grateful to Michael Foerst and Michael Fechner for their scientific support throughout my PhD journey.

Although we had our share of challenging moments in the lab at the beginning, Alex von Hoegen, you became one of the very good friends I made during my PhD. I learned a great deal from you, admired your enthusiasm for science, and truly enjoyed working together — especially during our time on the chopper dependence measurements! There are people whose kindness leaves a lasting mark on the timeline of your life. Ankit Disa and Thomas Gebert, you were the first people who made me feel truly at home in the group, and I feel very fortunate that our time

overlapped. I am deeply grateful to Marios H. Michael, with whom I rediscovered the pure joy of physics. You taught me to embrace curiosity, to ask even the most obvious questions without hesitation, and to never feel ashamed when seeking understanding.

A big "thank you" goes to all of the people who made the PhD journey very pleasant and special. I would always remember and acknowledge your hearty support: Joe, Sebastian, Danica, Bo, Gunda, Susmita, Jyoti and many more. I am truly lucky to have known you and worked with you. From our pre-COVID parties and our hilarious over-analysis of the most ridiculous things, to the moments of dancing in the lab after finally finding the pump-probe signal — these memories will always stay with me as a special snapshot of our time together.

*Maman* and *Baba*, you two are the source of my courage, passion and resilience. Your love and support are the two wings which I can fly with. Your kind hearts and guidance always give me the power to make anything impossible, possible. The words fail to express how grateful I am to have your love and support. My dear sister *Elaheh*, your sacrifice and kindness always make everything so colorful for me. Me standing at this point after what we went through would have been impossible if it was not for you and my little shining star *Aram*. Neda Lotfiomran, from the first day that we met you became not just a friend but a caring sister. It would take pages to express my gratitude.

And to you *Edward*, it is not possible to put into words the depth of your impact on both my happiness and my success. Over these past five years, you have been the unwavering support I could always lean on. I know that there were times that I meticulously managed to drive you insane discussing physics with you and also times that if it was not for your love and support, I couldn't have come this far. I

## *Acknowledgements*

---

feel incredibly lucky to have shared every step of this journey with you.

# Bibliography

- <sup>1</sup>D. N. Basov, R. D. Averitt, D. van der Marel, M. Dressel, and K. Haule, “Electrodynamics of correlated electron materials”, *Reviews of Modern Physics* **83**, 471–541 (2011).
- <sup>2</sup>D. N. Basov, R. D. Averitt, and D. Hsieh, “Towards properties on demand in quantum materials”, *Nature Materials* **16**, 1077–1088 (2017).
- <sup>3</sup>B. Keimer, S. A. Kivelson, M. R. Norman, S. Uchida, and J. Zaanen, “From quantum matter to high-temperature superconductivity in copper oxides”, *Nature* **518**, Publisher: Nature Publishing Group, 179–186 (2015).
- <sup>4</sup>J. G. Bednorz and K. A. Müller, “Possible highTc superconductivity in the BaLaCuO system”, *Zeitschrift für Physik B Condensed Matter* **64**, 189–193 (1986).
- <sup>5</sup>J. G. Bednorz, K. A. Müller, and M. Takashige, “Superconductivity in Alkaline Earth-Substituted  $\text{La}_2\text{CuO}_{4-y}$ ”, *Science* **236**, 73–75 (1987).
- <sup>6</sup>M. V. Berry, “Quantal phase factors accompanying adiabatic changes”, *Proceedings of the Royal Society of London. A. Mathematical and Physical Sciences* **392**, 45–57 (1984).
- <sup>7</sup>X.-L. Qi and S.-C. Zhang, “Topological insulators and superconductors”, *Reviews of Modern Physics* **83**, 1057–1110 (2011).

## ***Bibliography***

---

- <sup>8</sup>N. P. Armitage, E. J. Mele, and A. Vishwanath, “Weyl and Dirac semimetals in three-dimensional solids”, *Reviews of Modern Physics* **90**, 015001 (2018).
- <sup>9</sup>J. E. Moore, “The birth of topological insulators”, *Nature* **464**, 194–198 (2010).
- <sup>10</sup>M. Z. Hasan and C. L. Kane, “Colloquium: Topological insulators”, *Reviews of Modern Physics* **82**, 3045–3067 (2010).
- <sup>11</sup>T. H. Hsieh, H. Lin, J. Liu, W. Duan, A. Bansil, and L. Fu, “Topological crystalline insulators in the SnTe material class”, *Nature Communications* **3**, 982 (2012).
- <sup>12</sup>R. M. Lutchyn, J. D. Sau, and S. Das Sarma, “Majorana Fermions and a Topological Phase Transition in Semiconductor-Superconductor Heterostructures”, *Physical Review Letters* **105**, 077001 (2010).
- <sup>13</sup>P. A. Pantazopoulos, J. Feist, F. J. García-Vidal, and A. Kamra, “Unconventional magnetism mediated by spin-phonon-photon coupling”, *Nature Communications* **15**, 4000 (2024).
- <sup>14</sup>R. Fittipaldi, R. Hartmann, M. T. Mercaldo, S. Komori, A. Bjørli, W. Kyung, Y. Yasui, T. Miyoshi, L. a. B. Olde Olthof, C. M. Palomares Garcia, V. Granata, I. Keren, W. Higemoto, A. Suter, T. Prokscha, A. Romano, C. Noce, C. Kim, Y. Maeno, E. Scheer, B. Kalisky, J. W. A. Robinson, M. Cuoco, Z. Salman, A. Vecchione, and A. Di Bernardo, “Unveiling unconventional magnetism at the surface of  $\text{Sr}_2\text{RuO}_4$ ”, *Nature Communications* **12**, 5792 (2021).
- <sup>15</sup>Z. Guguchia, D. J. Gawryluk, S. Shin, Z. Hao, C. Mielke III, D. Das, I. Plokhikh, L. Liborio, J. K. Shenton, Y. Hu, V. Sazgari, M. Medarde, H. Deng, Y. Cai, C. Chen, Y. Jiang, A. Amato, M. Shi, M. Z. Hasan, J.-X. Yin, R. Khasanov, E. Pomjakushina, and H. Luetkens, “Hidden magnetism uncovered in a charge ordered bilayer kagome material  $\text{ScV}_6\text{Sn}_6$ ”, *Nature Communications* **14**, 7796 (2023).

- <sup>16</sup>D. S. Wei, D. Saykin, O. Y. Miller, S. Ran, S. R. Saha, D. F. Agterberg, J. Schmalian, N. P. Butch, J. Paglione, and A. Kapitulnik, “Interplay between magnetism and superconductivity in  $\text{UTe}_2$ ”, *Physical Review B* **105**, 024521 (2022).
- <sup>17</sup>P. Lacorre, J. B. Torrance, J. Pannetier, A. I. Nazzal, P. W. Wang, and T. C. Huang, “Synthesis, crystal structure, and properties of metallic  $\text{PrNiO}_3$ : Comparison with metallic  $\text{NdNiO}_3$  and semiconducting  $\text{SmNiO}_3$ ”, *Journal of Solid State Chemistry* **91**, 225–237 (1991).
- <sup>18</sup>J. B. Torrance, P. Lacorre, A. I. Nazzal, E. J. Ansaldo, and C. Niedermayer, “Systematic study of insulator-metal transitions in perovskites  $\text{RNiO}_3$  ( $\text{R}=\text{Pr},\text{Nd},\text{Sm},\text{Eu}$ ) due to closing of charge-transfer gap”, *Physical Review B* **45**, 8209–8212 (1992).
- <sup>19</sup>A. S. Disa, J. Curtis, M. Fechner, A. Liu, A. von Hoegen, M. Först, T. F. Nova, P. Narang, A. Maljuk, A. V. Boris, B. Keimer, and A. Cavalleri, “Photo-induced high-temperature ferromagnetism in  $\text{ytio}_3$ ”, *Nature* **617**, 73–78 (2023).
- <sup>20</sup>M. Fechner, M. Först, G. Orenstein, V. Krapivin, A. S. Disa, M. Buzzi, A. von Hoegen, G. de la Pena, Q. L. Nguyen, R. Mankowsky, M. Sander, H. Lemke, Y. Deng, M. Trigo, and A. Cavalleri, “Quenched lattice fluctuations in optically driven  $\text{SrTiO}_3$ ”, *Nature Materials* **23**, 363–368 (2024).
- <sup>21</sup>T. F. Nova, A. Cartella, A. Cantaluppi, M. Först, D. Bossini, R. V. Mikhaylovskiy, A. V. Kimel, R. Merlin, and A. Cavalleri, “An effective magnetic field from optically driven phonons”, *Nature Physics* **13**, 10.1038/nphys3925 (2017).
- <sup>22</sup>A. von Hoegen, M. Fechner, M. Först, N. Taherian, E. Rowe, A. Ribak, J. Porras, B. Keimer, M. Michael, E. Demler, and A. Cavalleri, “Amplification of superconducting fluctuations in driven  $\text{YBa}_2\text{Cu}_3\text{O}_{6+x}$ ”, *Physical Review X* **12**, 031008 (2022).

## **Bibliography**

---

- <sup>23</sup>A. Subedi, A. Cavalleri, and A. Georges, “Theory of nonlinear phononics for coherent light control of solids”, *Physical Review B* **89**, 220301 (2014).
- <sup>24</sup>P. G. Radaelli, “Breaking symmetry with light: Ultrafast ferroelectricity and magnetism from three-phonon coupling”, *Physical Review B* **97**, 085145 (2018).
- <sup>25</sup>D. M. Juraschek, M. Fechner, and N. A. Spaldin, “Ultrafast Structure Switching through Nonlinear Phononics”, *Physical Review Letters* **118**, 054101 (2017).
- <sup>26</sup>M. Först, C. Manzoni, S. Kaiser, Y. Tomioka, Y. Tokura, R. Merlin, and A. Cavalleri, “Nonlinear phononics as an ultrafast route to lattice control”, *Nature Physics* **7**, 854–856 (2011).
- <sup>27</sup>A. S. Disa, T. F. Nova, and A. Cavalleri, “Engineering crystal structures with light”, *Nature Physics* **17**, 1087–1092 (2021).
- <sup>28</sup>R. Mankowsky, M. Först, and A. Cavalleri, “Non-equilibrium control of complex solids by nonlinear phononics”, *Reports on Progress in Physics* **79**, 064503 (2016).
- <sup>29</sup>R. Mankowsky, A. von Hoegen, M. Först, and A. Cavalleri, “Ultrafast Reversal of the Ferroelectric Polarization”, *Physical Review Letters* **118**, 197601 (2017).
- <sup>30</sup>M. Först, R. Mankowsky, and A. Cavalleri, “Mode-Selective Control of the Crystal Lattice”, *Accounts of Chemical Research* **48**, 380–387 (2015).
- <sup>31</sup>M. Först, R. Mankowsky, H. Bromberger, D. M. Fritz, H. Lemke, D. Zhu, M. Chollet, Y. Tomioka, Y. Tokura, R. Merlin, J. P. Hill, S. L. Johnson, and A. Cavalleri, “Displacive lattice excitation through nonlinear phononics viewed by femtosecond X-ray diffraction”, *Solid State Communications* **169**, 24–27 (2013).
- <sup>32</sup>M. Budden, T. Gebert, M. Buzzi, G. Jotzu, E. Wang, T. Matsuyama, G. Meier, Y. Laplace, D. Pontiroli, M. Riccò, F. Schlawin, D. Jaksch, and A. Cavalleri, “Evidence for metastable photo-induced superconductivity in  $K_3C_{60}$ ”, *Nature Physics* **17**, 611–618 (2021).

- <sup>33</sup>T. F. Nova, A. S. Disa, M. Fechner, and A. Cavalleri, “Metastable ferroelectricity in optically strained SrTiO<sub>3</sub>”, *Science* **364**, 1075–1079 (2019).
- <sup>34</sup>E. Rowe, B. Yuan, M. Buzzi, G. Jotzu, Y. Zhu, M. Fechner, M. Först, B. Liu, D. Pontiroli, M. Riccò, and A. Cavalleri, “Resonant enhancement of photo-induced superconductivity in K<sub>3</sub>C<sub>60</sub>”, *Nature Physics* **19**, 1821–1826 (2023).
- <sup>35</sup>G. Khaliullin and S. Okamoto, “Theory of orbital state and spin interactions in ferromagnetic titanates”, *Physical Review B* **68**, 205109 (2003).
- <sup>36</sup>C. Ulrich, G. Khaliullin, S. Okamoto, M. Reehuis, A. Ivanov, H. He, Y. Taguchi, Y. Tokura, and B. Keimer, “Magnetic Order and Dynamics in an Orbitally Degenerate Ferromagnetic Insulator”, *Physical Review Letters* **89**, 167202 (2002).
- <sup>37</sup>M. Tsubota, F. Iga, T. Takabatake, N. Kikugawa, T. Suzuki, I. Oguro, H. Kawanaka, and H. Bando, “Low-field magnetic anisotropy in Mott-insulating ferromagnet Y<sub>1-x</sub>Ca<sub>x</sub>TiO<sub>3</sub> ( $x \leq 0.1$ )”, *Physica B: Condensed Matter* **281-282**, 622–624 (2000).
- <sup>38</sup>T. Sakudo and H. Unoki, “Dielectric Properties of SrTiO<sub>3</sub> at Low Temperatures”, *Physical Review Letters* **26**, 851–853 (1971).
- <sup>39</sup>A. Yamanaka, M. Kataoka, Y. Inaba, K. Inoue, B. Hehlen, and E. Courtens, “Evidence for competing orderings in strontium titanate from hyper-Raman scattering spectroscopy”, *Europhysics Letters* **50**, 688 (2000).
- <sup>40</sup>Y. L. Li, S. Choudhury, J. H. Haeni, M. D. Biegalski, A. Vasudevarao, A. Sharan, H. Z. Ma, J. Levy, V. Gopalan, S. Trolier-McKinstry, D. G. Schlom, Q. X. Jia, and L. Q. Chen, “Phase transitions and domain structures in strained pseudocubic (100) SrTiO<sub>3</sub> thin films”, *Physical Review B* **73**, 184112 (2006).

## Bibliography

---

- <sup>41</sup>A. Dubroka, M. Rössle, K. W. Kim, V. K. Malik, D. Munzar, D. N. Basov, A. A. Schafgans, S. J. Moon, C. T. Lin, D. Haug, V. Hinkov, B. Keimer, T. Wolf, J. G. Storey, J. L. Tallon, and C. Bernhard, “Evidence of a precursor superconducting phase at temperatures as high as 180 in  $\text{R}\text{Ba}_2\text{Cu}_3\text{O}_{7-\delta}$  ( $\text{R} = \text{Y}, \text{Gd}, \text{Eu}$ ) superconducting crystals from infrared spectroscopy”, *Physical Review Letters* **106**, 047006 (2011).
- <sup>42</sup>T. Sato, H. Matsui, S. Nishina, T. Takahashi, T. Fujii, T. Watanabe, and A. Matsuda, “Low Energy Excitation and Scaling in  $\text{Bi}_2\text{Sr}_2\text{Ca}_{n-1}\text{Cu}_n\text{O}_{2n+4}$  ( $n=1-3$ ): Angle-Resolved Photoemission Spectroscopy”, *Physical Review Letters* **89**, 067005 (2002).
- <sup>43</sup>D. Munzar, C. Bernhard, A. Golnik, J. Humlíček, and M. Cardona, “Anomalies of the infrared-active phonons in underdoped  $\text{YBa}_2\text{Cu}_3\text{O}_y$  as evidence for the intrabilayer Josephson effect”, *Solid State Communications* **112**, 365–369 (1999).
- <sup>44</sup>M. Takigawa, A. P. Reyes, P. C. Hammel, J. D. Thompson, R. H. Heffner, Z. Fisk, and K. C. Ott, “Cu and O NMR studies of the magnetic properties of  $\text{YBa}_2\text{Cu}_3\text{O}_{6.63}$  ( $T_c = 62 \text{ K}$ )”, *Physical Review B* **43**, 247–257 (1991).
- <sup>45</sup>L. Zhao, C. A. Belvin, R. Liang, D. A. Bonn, W. N. Hardy, N. P. Armitage, and D. Hsieh, “A global inversion-symmetry-broken phase inside the pseudogap region of  $\text{YBa}_2\text{Cu}_3\text{O}_y$ ”, *Nature Physics* **13**, 250–254 (2017).
- <sup>46</sup>C. Bernhard, L. Yu, A. Dubroka, K. W. Kim, M. Rössle, D. Munzar, J. Chaloupka, C. T. Lin, and T. Wolf, “Broad-band infrared ellipsometry measurements of the  $c$ -axis response of underdoped  $\text{YBa}_2\text{Cu}_3\text{O}_7$ : Spectroscopic distinction between the normal-state pseudogap and the superconducting gap”, *Journal of Physics and Chemistry of Solids, SNS2007* **69**, 3064–3069 (2008).

- <sup>47</sup>D. Mihailovic, B. Podobnik, J. Demsar, G. Wagner, and J. Evetts, “Divergence of the quasiparticle lifetime with doping and evidence for pre-formed pairs below  $T^*$  in  $\text{YBa}_2\text{Cu}_3\text{O}_7$ ”, *Journal of Physics and Chemistry of Solids* **59**, 1937–1941 (1998).
- <sup>48</sup>C. C. Homes, T. Timusk, R. Liang, D. A. Bonn, and W. N. Hardy, “Optical conductivity of  $c$  axis oriented  $\text{YBa}_2\text{Cu}_3\text{O}_{6.70}$ : evidence for a pseudogap”, *Physical Review Letters* **71**, 1645–1648 (1993).
- <sup>49</sup>C. C. Homes, T. Timusk, D. A. Bonn, R. Liang, and W. N. Hardy, “Optical phonons polarized along the  $c$  axis of  $\text{YBa}_2\text{Cu}_3\text{O}_{6+x}$  for  $x = 0.5 \rightarrow 0.95$ ”, *Canadian Journal of Physics* **73**, 663 (1995).
- <sup>50</sup>T. Kondo, Y. Hamaya, A. D. Palczewski, T. Takeuchi, J. S. Wen, Z. J. Xu, G. Gu, J. Schmalian, and A. Kaminski, “Disentangling Cooper-pair formation above the transition temperature from the pseudogap state in the cuprates”, *Nature Physics*, 21–25 (2011).
- <sup>51</sup>O. Cyr-Choinière, R. Daou, F. Laliberté, C. Collignon, S. Badoux, D. LeBoeuf, J. Chang, B. J. Ramshaw, D. A. Bonn, W. N. Hardy, R. Liang, J.-Q. Yan, J.-G. Cheng, J.-S. Zhou, J. B. Goodenough, S. Pyon, T. Takayama, H. Takagi, N. Doiron-Leyraud, and L. Taillefer, “Pseudogap temperature  $T^*$  of cuprate superconductors from the Nernst effect”, *Physical Review B* **97**, 064502 (2018).
- <sup>52</sup>T. Ito, K. Takenaka, and S. Uchida, “Systematic deviation from  $T$ -linear behavior in the in-plane resistivity of  $\text{YBa}_2\text{Cu}_3\text{O}_{7-y}$ : Evidence for dominant spin scattering”, *Physical Review Letters* **70**, 3995–3998 (1993).
- <sup>53</sup>Y. Ando, S. Komiyama, K. Segawa, S. Ono, and Y. Kurita, “Electronic phase diagram of high- $t_c$  cuprate superconductors from a mapping of the in-plane resistivity curvature”, *Physical Review Letters* **93**, 267001 (2004).

## ***Bibliography***

---

- <sup>54</sup>S. H. Naqib, M. Borhan Uddin, and J. R. Cole, “Modeling of the out-of-plane resistivity of cuprate superconductors”, *Physica C: Superconductivity* **471**, 1598–1601 (2011).
- <sup>55</sup>A. Damascelli, Z. Hussain, and Z.-X. Shen, “Angle-resolved photoemission studies of the cuprate superconductors”, *Reviews of Modern Physics* **75**, 473–541 (2003).
- <sup>56</sup>R. Daou, J. Chang, D. Leboeuf, O. Cyr-Choinière, F. Laliberté, N. Doiron-Leyraud, B. J. Ramshaw, R. Liang, D. A. Bonn, W. N. Hardy, and L. Taillefer, “Broken rotational symmetry in the pseudogap phase of a high- $T(c)$  superconductor”, *Nature* **463**, 519–522 (2010).
- <sup>57</sup>B. Fauqué, Y. Sidis, V. Hinkov, S. Pailhès, C. T. Lin, X. Chaud, and P. Bourges, “Magnetic Order in the Pseudogap Phase of High- $T_C$  Superconductors”, *Physical Review Letters* **96**, 197001 (2006).
- <sup>58</sup>H. A. Mook, Y. Sidis, B. Fauqué, V. Balédent, and P. Bourges, “Observation of magnetic order in a superconducting  $\text{YBa}_2\text{Cu}_3\text{O}_{6.6}$  single crystal using polarized neutron scattering”, *Physical Review B* **78**, 020506 (2008).
- <sup>59</sup>L. Mangin-Thro, Y. Sidis, A. Wildes, and P. Bourges, “Intra-unit-cell magnetic correlations near optimal doping in  $\text{YBa}_2\text{Cu}_3\text{O}_{6.85}$ ”, *Nature Communications* **6**, 7705 (2015).
- <sup>60</sup>Y. Lubashevsky, L. Pan, T. Kirzhner, G. Koren, and N. P. Armitage, “Optical Birefringence and Dichroism of Cuprate Superconductors in the THz Regime”, *Physical Review Letters* **112**, 147001 (2014).
- <sup>61</sup>J. Xia, E. Schemm, G. Deutscher, S. A. Kivelson, D. A. Bonn, W. N. Hardy, R. Liang, W. Siemons, G. Koster, M. M. Fejer, and A. Kapitulnik, “Polar Kerr-Effect Measurements of the High-Temperature  $\text{YBa}_2\text{Cu}_3\text{O}_{6+x}$  Superconductor: Evidence

- for Broken Symmetry near the Pseudogap Temperature”, *Physical Review Letters* **100**, 127002 (2008).
- <sup>62</sup>S. Blanco-Canosa, A. Frano, E. Schierle, J. Porras, T. Loew, M. Minola, M. Bluschke, E. Weschke, B. Keimer, and M. Le Tacon, “Resonant x-ray scattering study of charge-density wave correlations in  $\text{YBa}_2\text{Cu}_3\text{O}_{6+x}$ ”, *Physical Review B* **90**, 054513 (2014).
- <sup>63</sup>M. Hücker, N. B. Christensen, A. T. Holmes, E. Blackburn, E. M. Forgan, R. Liang, D. A. Bonn, W. N. Hardy, O. Gutowski, M. v. Zimmermann, S. M. Hayden, and J. Chang, “Competing charge, spin, and superconducting orders in underdoped  $\text{YBa}_2\text{Cu}_3\text{O}_y$ ”, *Physical Review B* **90**, 054514 (2014).
- <sup>64</sup>W. Hu, S. Kaiser, D. Nicoletti, C. R. Hunt, I. Gierz, M. C. Hoffmann, M. Le Tacon, T. Loew, B. Keimer, and A. Cavalleri, “Optically enhanced coherent transport in  $\text{YBa}_2\text{Cu}_3\text{O}_{6.5}$  by ultrafast redistribution of interlayer coupling”, *Nature Materials* **13**, 705–711 (2014).
- <sup>65</sup>S. Kaiser, C. R. Hunt, D. Nicoletti, W. Hu, I. Gierz, H. Y. Liu, M. Le Tacon, T. Loew, D. Haug, B. Keimer, and A. Cavalleri, “Optically induced coherent transport far above  $T_c$  in underdoped  $\text{YBa}_2\text{Cu}_3\text{O}_{6+\delta}$ ”, *Physical Review B* **89**, 184516 (2014).
- <sup>66</sup>B. Liu, M. Först, M. Fechner, D. Nicoletti, J. Porras, T. Loew, B. Keimer, and A. Cavalleri, “Pump frequency resonances for light-induced incipient superconductivity in  $\text{YBa}_2\text{Cu}_3\text{O}_{6.5}$ ”, *Physical Review X* **10**, 011053 (2020).
- <sup>67</sup>A. Ribak, M. Buzzi, D. Nicoletti, R. Singla, Y. Liu, S. Nakata, B. Keimer, and A. Cavalleri, “Two-fluid dynamics in driven  $\text{YBa}_2\text{Cu}_3\text{O}_{6.48}$ ”, *Physical Review B* **107**, 104508 (2023).

## Bibliography

---

- <sup>68</sup>S. Fava, G. De Vecchi, G. Jotzu, M. Buzzi, T. Gebert, Y. Liu, B. Keimer, and A. Cavalleri, “Magnetic field expulsion in optically driven  $\text{YBa}_2\text{Cu}_3\text{O}_{6.48}$ ”, *Nature*, 1–6 (2024).
- <sup>69</sup>J. B. Curtis, A. Disa, M. Fechner, A. Cavalleri, and P. Narang, “Dynamics of photoinduced ferromagnetism in oxides with orbital degeneracy”, *Physical Review Research* **5**, 013204 (2023).
- <sup>70</sup>A. S. Disa, M. Fechner, T. F. Nova, B. Liu, M. Först, D. Prabhakaran, P. G. Radaelli, and A. Cavalleri, “Polarizing an antiferromagnet by optical engineering of the crystal field”, *Nature Physics* **16**, 937–941 (2020).
- <sup>71</sup>R. Mankowsky, A. Subedi, M. Först, S. O. Mariager, M. Chollet, H. T. Lemke, J. S. Robinson, J. M. Glowia, M. P. Minitti, A. Frano, M. Fechner, N. A. Spaldin, T. Loew, B. Keimer, A. Georges, and A. Cavalleri, “Nonlinear lattice dynamics as a basis for enhanced superconductivity in  $\text{YBa}_2\text{Cu}_3\text{O}_{6.5}$ ”, *Nature* **516**, 71–73 (2014).
- <sup>72</sup>R. Mankowsky, M. Först, T. Loew, J. Porras, B. Keimer, and A. Cavalleri, “Coherent modulation of the  $\text{YBa}_2\text{Cu}_3\text{O}_{6+x}$  atomic structure by dispersive stimulated ionic Raman scattering”, *Physical Review B* **91**, 094308 (2015).
- <sup>73</sup>R. Mankowsky, M. Fechner, M. Först, A. von Hoegen, J. Porras, T. Loew, G. L. Dakovski, M. Seaberg, S. Möller, G. Coslovich, B. Keimer, S. S. Dhesi, and A. Cavalleri, “Optically induced lattice deformations, electronic structure changes, and enhanced superconductivity in  $\text{YBa}_2\text{Cu}_3\text{O}_{6.48}$ ”, *Structural Dynamics* **4**, 044007 (2017).
- <sup>74</sup>M. H. Michael, A. von Hoegen, M. Fechner, M. Först, A. Cavalleri, and E. Demler, “Parametric resonance of Josephson plasma waves: a theory for optically amplified

- interlayer superconductivity in  $\text{YBa}_2\text{Cu}_3\text{O}_{6+x}$ ”, *Physical Review B* **102**, 174505 (2020).
- <sup>75</sup>S. Mukamel, *Principles of Nonlinear Optical Spectroscopy*, Revised edition (Oxford University Press, New York, 1999).
- <sup>76</sup>L. Luo, M. Mootz, J. H. Kang, C. Huang, K. Eom, J. W. Lee, C. Vaswani, Y. G. Collantes, E. E. Hellstrom, I. E. Perakis, C. B. Eom, and J. Wang, “Quantum coherence tomography of light-controlled superconductivity”, *Nature Physics* **19**, 201–209 (2023).
- <sup>77</sup>T. G. H. Blank, K. A. Grishunin, K. A. Zvezdin, N. T. Hai, J. Wu, S.-H. Su, J.-C. A. Huang, A. K. Zvezdin, and A. V. Kimel, “Two-Dimensional Terahertz Spectroscopy of Nonlinear Phononics in the Topological Insulator  $\text{MnBi}_2\text{Te}_4$ ”, *Physical Review Letters* **131**, 026902 (2023).
- <sup>78</sup>S. Mukamel, Y. Tanimura, and P. Hamm, “Coherent Multidimensional Optical Spectroscopy”, *Accounts of Chemical Research* **42**, 1207–1209 (2009).
- <sup>79</sup>Z. Zhang, F. Y. Gao, J. B. Curtis, Z.-J. Liu, Y.-C. Chien, A. von Hoegen, M. T. Wong, T. Kurihara, T. Suemoto, P. Narang, E. Baldini, and K. A. Nelson, “Terahertz field-induced nonlinear coupling of two magnon modes in an antiferromagnet”, *Nature Physics* **20**, 801–806 (2024).
- <sup>80</sup>Z. Zhang, F. Y. Gao, Y.-C. Chien, Z.-J. Liu, J. B. Curtis, E. R. Sung, X. Ma, W. Ren, S. Cao, P. Narang, A. von Hoegen, E. Baldini, and K. A. Nelson, “Terahertz-field-driven magnon upconversion in an antiferromagnet”, *Nature Physics* **20**, 788–793 (2024).
- <sup>81</sup>A. Liu, *Multidimensional Terahertz Probes of Quantum Materials*, arXiv:2409.03719, 2024.

## Bibliography

---

- <sup>82</sup>A. Liu, D. Pavićević, M. H. Michael, A. G. Salvador, P. E. Dolgirev, M. Fechner, A. S. Disa, P. M. Lozano, Q. Li, G. D. Gu, E. Demler, and A. Cavalleri, “Probing inhomogeneous cuprate superconductivity by terahertz Josephson echo spectroscopy”, *Nature Physics*, 1–6 (2024).
- <sup>83</sup>C. L. Johnson, B. E. Knighton, and J. A. Johnson, “Distinguishing Nonlinear Terahertz Excitation Pathways with Two-Dimensional Spectroscopy”, *Physical Review Letters* **122**, 073901 (2019).
- <sup>84</sup>C. Somma, G. Folpini, K. Reimann, M. Woerner, and T. Elsaesser, “Two-Phonon Quantum Coherences in Indium Antimonide Studied by Nonlinear Two-Dimensional Terahertz Spectroscopy”, *Physical Review Letters* **116**, 177401 (2016).
- <sup>85</sup>E. A. Mashkovich, K. A. Grishunin, R. M. Dubrovin, A. K. Zvezdin, R. V. Pisarev, and A. V. Kimel, “Terahertz light-driven coupling of antiferromagnetic spins to lattice”, *Science* **374**, 1608–1611 (2021).
- <sup>86</sup>M. Fox and M. Fox, *Optical Properties of Solids*, Second Edition, Second Edition, Oxford Master Series in Physics (Oxford University Press, Oxford, New York, 2010).
- <sup>87</sup>N. W. Ashcroft and N. D. Mermin, *Solid State Physics* (Holt, Rinehart and Winston, 1976).
- <sup>88</sup>J. D. Patterson and B. C. Bailey, *Solid-State Physics: Introduction to the Theory* (Springer International Publishing, 2018).
- <sup>89</sup>Charles Kittel-8th Edition, *Introduction to Solid State Physics* ().
- <sup>90</sup>S. H. Simon, *The Oxford Solid State Basics* (Oxford : Oxford University Press, 2013).
- <sup>91</sup>J.-X. Cheng and X. S. Xie, eds., *Coherent Raman Scattering Microscopy* (CRC Press, 2012).

- <sup>92</sup>M. T. Dove and M. T. Dove, *Structure and Dynamics: An Atomic View of Materials*, Oxford Master Series in Physics (Oxford University Press, Oxford, New York, 2003).
- <sup>93</sup>J. P. ( P. Elliott, *Symmetry in physics* (New York : Oxford University Press, 1979).
- <sup>94</sup>M. S. Dresselhaus, G. Dresselhaus, and A. Jorio, *Group Theory: Application to the Physics of Condensed Matter* (Springer Science & Business Media, 2007).
- <sup>95</sup>A. v. Hoegen, “Probing nonlinear dynamics in strongly driven quantum materials”, PhD thesis (University of Hamburg, 2021).
- <sup>96</sup>Z. Zeng, M. Först, M. Fechner, M. Buzzi, E. Amuah, C. Putzke, P. J. W. Moll, D. Prabhakaran, P. Radaelli, and A. Cavalleri, *Breaking symmetry with light: photo-induced chirality in a non-chiral crystal*, 2024.
- <sup>97</sup>A. Cartella, T. F. Nova, M. Fechner, R. Merlin, and A. Cavalleri, “Parametric amplification of optical phonons”, [Proceedings of the National Academy of Sciences](#) **115**, 12148–12151 (2018).
- <sup>98</sup>M. Henstridge, M. Först, E. Rowe, M. Fechner, and A. Cavalleri, “Nonlocal nonlinear phononics”, [Nature Physics](#) **18**, 457–461 (2022).
- <sup>99</sup>A. von Hoegen, R. Mankowsky, M. Fechner, M. Först, and A. Cavalleri, “Probing the interatomic potential of solids with strong-field nonlinear phononics”, [Nature](#) **555**, 79–82 (2018).
- <sup>100</sup>M. Even Tzur, M. Birk, A. Gorlach, M. Krüger, I. Kaminer, and O. Cohen, “Photon-statistics force in ultrafast electron dynamics”, [Nature Photonics](#) **17**, 10.1038/s41566-023-01209-w (2023).
- <sup>101</sup>R. Schnabel, “Squeezed states of light and their applications in laser interferometers”, [Physics Reports, Squeezed states of light and their applications in laser interferometers](#) **684**, 1–51 (2017).

## ***Bibliography***

---

- <sup>102</sup>G. A. Garrett, A. G. Rojo, A. K. Sood, J. F. Whitaker, and R. Merlin, “Vacuum Squeezing of Solids: Macroscopic Quantum States Driven by Light Pulses”, *Science* **275**, 1638–1640 (1997).
- <sup>103</sup>G. A. Garrett, J. F. Whitaker, A. K. Sood, and R. Merlin, “Ultrafast optical excitation of a combined coherent-squeezed phonon field in SrTiO<sub>3</sub>”, *Optics Express* **1**, 385–389 (1997).
- <sup>104</sup>Y. Zhang, M. Menotti, K. Tan, V. D. Vaidya, D. H. Mahler, L. G. Helt, L. Zatti, M. Liscidini, B. Morrison, and Z. Vernon, “Squeezed light from a nanophotonic molecule”, *Nature Communications* **12**, 2233 (2021).
- <sup>105</sup>R. W. Boyd, A. L. Gaeta, and E. Giese, “Nonlinear optics”, in *Springer handbook of atomic, molecular, and optical physics* (Springer, 2008), pp. 1097–1110.
- <sup>106</sup>R. Merlin, “Generating coherent THz phonons with light pulses”, *Solid State Communications, Highlights in Condensed Matter Physics and Materials Science* **102**, 207–220 (1997).
- <sup>107</sup>R. W. Terhune, P. D. Maker, and C. M. Savage, “Measurements of Nonlinear Light Scattering”, *Physical Review Letters* **14**, 681–684 (1965).
- <sup>108</sup>D. A. Long, “The raman effect”, *The Raman Effect: A Unified Treatment of the Theory of Raman Scattering by Molecules* (2002).
- <sup>109</sup>K. Inoue, N. Asai, and T. Sameshima, “Experimental Study of the Hyper-Raman Scattering Due to Raman Inactive Lattice Vibration in SrTiO<sub>3</sub>”, *Journal of the Physical Society of Japan* **50**, 1291–1300 (1981).
- <sup>110</sup>V. N. Denisov, B. N. Mavrin, and V. B. Podobedov, “Hyper-Raman scattering by vibrational excitations in crystals, glasses and liquids”, *Physics Reports* **151**, 1–92 (1987).

- <sup>111</sup>H. Vogt, J. A. Sanjurjo, and G. Rossbroich, “Soft-mode spectroscopy in cubic BaTiO<sub>3</sub> by hyper-Raman scattering”, *Physical Review B* **26**, 5904–5910 (1982).
- <sup>112</sup>H. Vogt, “Coherent and hyper-raman techniques”, in *Light Scattering in Solids II: Basic Concepts and Instrumentation* (Springer, Berlin, Heidelberg, 1982), pp. 207–244.
- <sup>113</sup>H. Vogt and G. Neumann, “Observation of infrared active and silent modes in cubic crystals by hyper-Raman scattering”, *Phys. Status Solidi (b); (German Democratic Republic)* **92:1**, 10.1002/pssb.2220920107 (1979).
- <sup>114</sup>J. F. Annett and J. F. Annett, *Superconductivity, Superfluids and Condensates*, Oxford Master Series in Physics (Oxford University Press, Oxford, New York, 2004).
- <sup>115</sup>K. O. H, “The resistance of pure mercury at helium temperatures”, *Commun. Phys. Lab. Univ. Leiden*, b **120** (1911).
- <sup>116</sup>M. Tinkham, *Introduction to Superconductivity: Second Edition* (Courier Corporation, 2004).
- <sup>117</sup>J. Bardeen, L. N. Cooper, and J. R. Schrieffer, “Microscopic Theory of Superconductivity”, *Physical Review* **106**, 162–164 (1957).
- <sup>118</sup>V. J. Emery and S. A. Kivelson, “Importance of phase fluctuations in superconductors with small superfluid density”, *Nature* **374**, 434–437 (1995).
- <sup>119</sup>V. L. Ginzburg and L. D. Landau, “On the Theory of superconductivity”, *Zh. Eksp. Teor. Fiz.* **20**, 1064–1082 (1950).
- <sup>120</sup>L. P. Gor’kov, “Microscopic derivation of the Ginzburg–Landau equations in the theory of superconductivity”, *Sov. Phys. - JETP (Engl. Transl.); (United States)* (1959).

## ***Bibliography***

---

- <sup>121</sup>R. Gross, A. Marx, and F. Deppe, *Applied Superconductivity: Josephson Effect and Superconducting Electronics* (Walter De Gruyter Incorporated, 2016).
- <sup>122</sup>F. London, H. London, and F. A. Lindemann, “The electromagnetic equations of the supraconductor”, *Proceedings of the Royal Society of London. Series A - Mathematical and Physical Sciences* **149**, 71–88 (1997).
- <sup>123</sup>F. London, *Superfluids* (New York, Dover Publications [1961-64], 1961).
- <sup>124</sup>B. D. Josephson, “Possible new effects in superconductive tunnelling”, *Physics Letters* **1**, 251–253 (1962).
- <sup>125</sup>B. D. JOSEPHSON, “Coupled Superconductors”, *Reviews of Modern Physics* **36**, 216–220 (1964).
- <sup>126</sup>B. Josephson, “Supercurrents through barriers”, *Advances in Physics* **14**, 419–451 (1965).
- <sup>127</sup>X. Hu and S.-Z. Lin, “Phase dynamics in a stack of inductively coupled intrinsic Josephson junctions and terahertz electromagnetic radiation”, *Superconductor Science and Technology* **23**, 10.1088/0953-2048/23/5/053001 (2010).
- <sup>128</sup>S. Savel’ev, V. A. Yampol’skii, A. L. Rakhmanov, and F. Nori, “Terahertz Josephson plasma waves in layered superconductors: spectrum, generation, nonlinear and quantum phenomena”, *Reports on Progress in Physics* **73**, 026501 (2010).
- <sup>129</sup>R. Kleiner and P. Müller, “Intrinsic Josephson effects in high- $T_c$  superconductors”, *Physical Review B* **49**, 1327–1341 (1994).
- <sup>130</sup>L. N. Bulaevskii, D. Domínguez, M. P. Maley, A. R. Bishop, and B. I. Ivlev, “Collective mode and the  $c$ -axis critical current of a Josephson-coupled superconductor at high parallel magnetic fields”, *Physical Review B* **53**, 14601–14610 (1996).
- <sup>131</sup>A. v. Hoegen, “Probing nonlinear dynamics in strongly driven quantum materials”, PhD thesis (University of Hamburg, 2021).

- <sup>132</sup>D. van der Marel and A. Tsvetkov, “Transverse optical plasmons in layered superconductors”, *Czechoslovak Journal of Physics* **46**, 3165–3168 (1996).
- <sup>133</sup>D. van der Marel and A. A. Tsvetkov, “Transverse-optical Josephson plasmons: Equations of motion”, *Physical Review B* **64**, 024530 (2001).
- <sup>134</sup>K. Tamasaaku, Y. Nakamura, and S. Uchida, “Charge dynamics across the CuO<sub>2</sub> planes in La<sub>2-x</sub>Sr<sub>x</sub>CuO<sub>4</sub>”, *Physical Review Letters* **69**, 1455–1458 (1992).
- <sup>135</sup>M. Grüninger, D. van der Marel, A. A. Tsvetkov, and A. Erb, “Observation of Out-of-Phase Bilayer Plasmons in YBa<sub>2</sub>Cu<sub>3</sub>O<sub>7-δ</sub>”, *Physical Review Letters* **84**, 1575–1578 (2000).
- <sup>136</sup>S. V. Dordevic, E. J. Singley, J. H. Kim, M. B. Maple, S. Komiyama, S. Ono, Y. Ando, T. Rõõm, R. Liang, D. A. Bonn, W. N. Hardy, J. P. Carbotte, C. C. Homes, M. Strongin, and D. N. Basov, “Signatures of bilayer splitting in the c-axis optical conductivity of double layer cuprates”, *Physical Review B* **69**, 094511 (2004).
- <sup>137</sup>T. Koyama, “Josephson Plasma Resonances and Optical Properties in High-Tc Superconductors with Alternating Junction Parameters”, *Journal of the Physical Society of Japan* **71**, 2986–2993 (2002).
- <sup>138</sup>T. Koyama, “Quantum Charge Dynamics in an Array of Intrinsic Josephson Junctions”, *Journal of the Physical Society of Japan* **70**, 2114 (2001).
- <sup>139</sup>T. Timusk and C. C. Homes, “The role of magnetism in forming the c-axis spectral peak at 400 cm<sup>-1</sup> in high temperature superconductors”, *Solid State Communications, Proceedings of the High-Tc Superconductivity Workshop* **126**, 63–69 (2003).
- <sup>140</sup>T. Timusk, “The mysterious pseudogap in high temperature superconductors: an infrared view”, *Solid State Communications* **127**, 337–348 (2003).
- <sup>141</sup>N. Plakida, *High-Temperature Cuprate Superconductors: Experiment, Theory, and Applications* (Springer Science & Business Media, 2010).

## ***Bibliography***

---

- <sup>142</sup>M. K. Wu, J. R. Ashburn, C. J. Torng, P. H. Hor, R. L. Meng, L. Gao, Z. J. Huang, Y. Q. Wang, and C. W. Chu, “Superconductivity at 93 K in a new mixed-phase Y-Ba-Cu-O compound system at ambient pressure”, *Physical Review Letters* **58**, 908–910 (1987).
- <sup>143</sup>S. N. Putilin, E. V. Antipov, and M. Marezio, “Superconductivity above 120 K in  $\text{HgBa}_2\text{CaCu}_2\text{O}_{6+}$ ”, *Physica C: Superconductivity* **212**, 266–270 (1993).
- <sup>144</sup>J. Rossat-Mignod, L. P. Regnault, C. Vettier, P. Bourges, P. Burlet, J. Bossy, J. Y. Henry, and G. Lapertot, “Neutron scattering study of the  $\text{YBa}_2\text{Cu}_3\text{O}_{6+x}$  system”, *Physica C: Superconductivity* **185-189**, 86–92 (1991).
- <sup>145</sup>P. Dai, H. A. Mook, and F. Doğan, “Incommensurate Magnetic Fluctuations in  $\text{YBa}_2\text{Cu}_3\text{O}_{6.6}$ ”, *Physical Review Letters* **80**, 1738–1741 (1998).
- <sup>146</sup>P. Dai, H. A. Mook, R. D. Hunt, and F. Doğan, “Evolution of the resonance and incommensurate spin fluctuations in superconducting  $\text{YBa}_2\text{Cu}_3\text{O}_{6+x}$ ”, *Physical Review B* **63**, 054525 (2001).
- <sup>147</sup>P. Dai, H. A. Mook, S. M. Hayden, G. Aeppli, T. G. Perring, R. D. Hunt, and F. Doğan, “The Magnetic Excitation Spectrum and Thermodynamics of High- $T_c$  Superconductors”, *Science* **284**, 1344–1347 (1999).
- <sup>148</sup>H. A. Mook, P. Dai, R. D. Hunt, and F. Doğan, “NEURON SCATTERING STUDIES OF THE MAGNETIC FLUCTUATIONS IN  $\text{YBa}_2\text{Cu}_3\text{O}_7$ ”, *Journal of Physics and Chemistry of Solids* **59**, 2140–2144 (1998).
- <sup>149</sup>H. A. Mook, P. Dai, S. M. Hayden, G. Aeppli, T. G. Perring, and F. Doğan, “Spin fluctuations in  $\text{YBa}_2\text{Cu}_3\text{O}_{6.6}$ ”, *Nature* **395**, 580–582 (1998).
- <sup>150</sup>S. M. Hayden, G. Aeppli, P. Dai, H. A. Mook, T. G. Perring, S. -. Cheong, Z. Fisk, F. Doğan, and T. E. Mason, “Absolute measurements of the high-frequency magnetic dynamics in High- $T_c$  superconductors”, *Physica B: Condensed Matter*,

Proceedings of the International Conference on Neutron Scattering **241-243**, 765–772 (1997).

- <sup>151</sup>S.-W. Cheong, G. Aeppli, T. E. Mason, H. Mook, S. M. Hayden, P. C. Canfield, Z. Fisk, K. N. Clausen, and J. L. Martinez, “Incommensurate magnetic fluctuations in  $\text{La}_{2-x}\text{Sr}_x\text{CuO}_4$ ”, *Physical Review Letters* **67**, 1791–1794 (1991).
- <sup>152</sup>R. J. Birgeneau, Y. Endoh, K. Kakurai, Y. Hidaka, T. Murakami, M. A. Kastner, T. R. Thurston, G. Shirane, and K. Yamada, “Static and dynamic spin fluctuations in superconducting  $\text{La}_{2-x}\text{Sr}_x\text{CuO}_4$ ”, *Physical Review B* **39**, 2868–2871 (1989).
- <sup>153</sup>H. Yoshizawa, S. Mitsuda, H. Kitazawa, and K. Katsumata, “An Incommensurate Magnetic Diffuse Scattering in Superconducting  $\text{La}_{1.92}\text{Sr}_{0.08}\text{CuO}_4$ ”, *Journal of the Physical Society of Japan* **57**, 3686–3689 (1988).
- <sup>154</sup>J. M. Tranquada, P. M. Gehring, G. Shirane, S. Shamoto, and M. Sato, “Neutron-scattering study of the dynamical spin susceptibility in  $\text{YBa}_2\text{Cu}_3\text{O}_{6.6}$ ”, *Physical Review B* **46**, 5561–5575 (1992).
- <sup>155</sup>B. J. Sternlieb, J. M. Tranquada, G. Shirane, M. Sato, and S. Shamoto, “Q dependence of the dynamic susceptibility (“q”) in superconducting  $\text{YBa}_2\text{Cu}_3\text{O}_{6.6}$   $T_c = 46$  K”, *Physical Review B* **50**, 12915–12919 (1994).
- <sup>156</sup>H. F. Fong, B. Keimer, P. W. Anderson, D. Reznik, F. Doğan, and I. A. Aksay, “Phonon and Magnetic Neutron Scattering at 41 meV in  $\text{YBa}_2\text{Cu}_3\text{O}_7$ ”, *Physical Review Letters* **75**, 316–319 (1995).
- <sup>157</sup>H. F. Fong, B. Keimer, D. Reznik, D. L. Milius, and I. A. Aksay, “Polarized and unpolarized neutron-scattering study of the dynamical spin susceptibility of  $\text{YBa}_2\text{Cu}_3\text{O}_7$ ”, *Physical Review B* **54**, 6708–6720 (1996).

## ***Bibliography***

---

- <sup>158</sup>H. F. Fong, B. Keimer, D. L. Milius, and I. A. Aksay, “Superconductivity-Induced Anomalies in the Spin Excitation Spectra of Underdoped  $\text{YBa}_2\text{Cu}_3\text{O}_{6+x}$ ”, *Physical Review Letters* **78**, 713–716 (1997).
- <sup>159</sup>P. Bourges, L. P. Regnault, Y. Sidis, and C. Vettier, “Inelastic-neutron-scattering study of antiferromagnetic fluctuations in  $\text{YBa}_2\text{Cu}_3\text{O}_{6.97}$ ”, *Physical Review B* **53**, 876–885 (1996).
- <sup>160</sup>P. Bourges, H. F. Fong, L. P. Regnault, J. Bossy, C. Vettier, D. L. Milius, I. A. Aksay, and B. Keimer, “High-energy spin excitations in  $\text{YBa}_2\text{Cu}_3\text{O}_{6.5}$ ”, *Physical Review B* **56**, R11439–R11442 (1997).
- <sup>161</sup>P. Dai, M. Yethiraj, H. A. Mook, T. B. Lindemer, and F. Doğan, “Magnetic Dynamics in Underdoped  $\text{YBa}_2\text{Cu}_3\text{O}_{7-x}$ : Direct Observation of a Superconducting Gap”, *Physical Review Letters* **77**, 5425–5428 (1996).
- <sup>162</sup>V. J. Emery, “Theory of high- $t_c$  superconductivity in oxides”, *Physical Review Letters* **58**, 2794–2797 (1987).
- <sup>163</sup>C. M. Varma, S. Schmitt-Rink, and E. Abrahams, “Charge transfer excitations and superconductivity in “ionic” metals”, *Solid State Communications* **62**, 681–685 (1987).
- <sup>164</sup>C. C. Tsuei and J. R. Kirtley, “Pairing symmetry in cuprate superconductors”, *Reviews of Modern Physics* **72**, 969–1016 (2000).
- <sup>165</sup>M. S. Colclough, C. E. Gough, M. Keene, C. M. Muirhead, N. Thomas, J. S. Abell, and S. Sutton, “Radio-frequency SQUID operation using a ceramic high-temperature superconductor”, *Nature* **328**, 47–48 (1987).
- <sup>166</sup>C. C. Tsuei, J. R. Kirtley, C. C. Chi, L. S. Yu-Jahnes, A. Gupta, T. Shaw, J. Z. Sun, and M. B. Ketchen, “Pairing Symmetry and Flux Quantization in a Tricrystal

- Superconducting Ring of  $\text{YBa}_2\text{Cu}_3\text{O}_{7-\delta}$ ”, *Physical Review Letters* **73**, 593–596 (1994).
- <sup>167</sup>D. A. Wollman, D. J. Van Harlingen, W. C. Lee, D. M. Ginsberg, and A. J. Leggett, “Experimental determination of the superconducting pairing state in YBCO from the phase coherence of YBCO-Pb dc SQUIDS”, *Physical Review Letters* **71**, 2134–2137 (1993).
- <sup>168</sup>W. E. Lawrence and S. Doniach, “THEORY OF LAYER-STRUCTURE SUPERCONDUCTORS.”, in (1971).
- <sup>169</sup>C. E. Gough, M. S. Colclough, E. M. Forgan, R. G. Jordan, M. Keene, C. M. Muirhead, A. I. M. Rae, N. Thomas, J. S. Abell, and S. Sutton, “Flux quantization in a high-Tc superconductor”, *Nature* **326**, 855–855 (1987).
- <sup>170</sup>C. Timm, D. Manske, and K. H. Bennemann, “Phase diagram of underdoped cuprate superconductors: Effects of Cooper-pair phase fluctuations”, *Physical Review B* **66**, 094515 (2002).
- <sup>171</sup>D. J. Scalapino, “The Cuprate Pairing Mechanism”, *Science* **284**, 1282–1283 (1999).
- <sup>172</sup>Ø. Fischer, M. Kugler, I. Maggio-Aprile, C. Berthod, and C. Renner, “Scanning tunneling spectroscopy of high-temperature superconductors”, *Reviews of Modern Physics* **79**, 353–419 (2007).
- <sup>173</sup>M. Hashimoto, I. M. Vishik, R.-H. He, T. P. Devereaux, and Z.-X. Shen, “Energy gaps in high-transition-temperature cuprate superconductors”, *Nature Physics* **10**, 483–495 (2014).
- <sup>174</sup>I. M. Vishik, W. S. Lee, R.-H. He, M. Hashimoto, Z. Hussain, T. P. Devereaux, and Z.-X. Shen, “ARPES studies of cuprate Fermiology: superconductivity, pseudogap and quasiparticle dynamics”, *New Journal of Physics* **12**, 105008 (2010).

## Bibliography

---

- <sup>175</sup>Q. Gao, J. M. Bok, P. Ai, J. Liu, H. Yan, X. Luo, Y. Cai, C. Li, Y. Wang, C. Yin, H. Chen, G. Gu, F. Zhang, F. Yang, S. Zhang, Q. Peng, Z. Zhu, G. Liu, Z. Xu, T. Xiang, L. Zhao, H.-Y. Choi, and X. J. Zhou, “ARPES detection of superconducting gap sign in unconventional superconductors”, *Nature Communications* **15**, 4538 (2024).
- <sup>176</sup>S. Hübner, M. A. Hossain, A. Damascelli, and G. A. Sawatzky, “Two gaps make a high-temperature superconductor?”, *Reports on Progress in Physics* **71**, 10.1088/0034-4885/71/6/062501 (2008).
- <sup>177</sup>B. Wuyts, V. V. Moshchalkov, and Y. Bruynseraede, “Resistivity and Hall effect of metallic oxygen-deficient  $\text{YBa}_2\text{Cu}_3\text{O}_x$  films in the normal state”, *Physical Review B* **53**, 9418–9432 (1996).
- <sup>178</sup>O. Cyr-Choinière, D. LeBoeuf, S. Badoux, S. Dufour-Beauséjour, D. A. Bonn, W. N. Hardy, R. Liang, D. Graf, N. Doiron-Leyraud, and L. Taillefer, “Sensitivity of  $T_c$  to pressure and magnetic field in the cuprate superconductor  $\text{YBa}_2\text{Cu}_3\text{O}_y$ : Evidence of charge-order suppression by pressure”, *Physical Review B* **98**, 064513 (2018).
- <sup>179</sup>G. Homann, M. H. Michael, J. G. Cosme, and L. Mathey, “Dissipationless Counterflow Currents above  $T_c$  in Bilayer Superconductors”, *Physical Review Letters* **132**, 096002 (2024).
- <sup>180</sup>C. T. Lin, B. Liang, and H. C. Chen, “Top-seeded solution growth of Ca-doped YBCO single crystals”, *Journal of Crystal Growth, The thirteenth international conference on Crystal Growth in conjunction with the eleventh international conference on Vapor Growth and Epitaxy* **237-239**, 778–782 (2002).
- <sup>181</sup>A. Simon, K. Trübenbach, and H. Borrmann, “Single Crystal X-Ray Structure Analysis of  $\text{YBa}_2\text{Cu}_3\text{O}_{6.5}$ ”, *Journal of Solid State Chemistry* **106**, 128–133 (1993).

- <sup>182</sup>R. J. Cava, B. Batlogg, C. H. Chen, E. A. Rietman, S. M. Zahurak, and D. Werder, “Single-phase 60-K bulk superconductor in annealed  $\text{Ba}_2\text{YCu}_3\text{O}_{7-\delta}$  ( $0.3 \leq \delta \leq 0.4$ ) with correlated oxygen vacancies in the Cu-O chains”, *Physical Review B* **36**, 5719–5722 (1987).
- <sup>183</sup>J. D. Jorgensen, B. W. Veal, A. P. Paulikas, L. J. Nowicki, G. W. Crabtree, H. Claus, and W. K. Kwok, “Structural properties of oxygen-deficient  $\text{YBa}_2\text{Cu}_3\text{O}_{7-\delta}$ ”, *Physical Review B* **41**, 1863–1877 (1990).
- <sup>184</sup>D. H. Lu, D. L. Feng, N. P. Armitage, K. M. Shen, A. Damascelli, C. Kim, F. Ronning, Z.-X. Shen, D. A. Bonn, R. Liang, W. N. Hardy, A. I. Rykov, and S. Tajima, “Superconducting Gap and Strong In-Plane Anisotropy in Untwinned  $\text{YBa}_2\text{Cu}_3\text{O}_{7-\delta}$ ”, *Physical Review Letters* **86**, 4370–4373 (2001).
- <sup>185</sup>E. Polturak, G. Koren, D. Cohen, and E. Aharoni, “Measurements of the anisotropy and temperature dependence of the in-plane energy gap in  $\text{YBa}_2\text{Cu}_3\text{O}_{7-\delta}$  using Andreev reflections”, *Physical Review B* **47**, 5270–5274 (1993).
- <sup>186</sup>M. F. Limonov, A. I. Rykov, S. Tajima, and A. Yamanaka, “Raman Scattering Study on Fully Oxygenated  $\text{YBa}_2\text{Cu}_3\text{O}_7$  Single Crystals: x–y Anisotropy in the Superconductivity-Induced Effects”, *Physical Review Letters* **80**, 825–828 (1998).
- <sup>187</sup>K. Nakayama, T. Sato, K. Terashima, T. Arakane, T. Takahashi, M. Kubota, K. Ono, T. Nishizaki, Y. Takahashi, and N. Kobayashi, “Doping dependence of the gap anisotropy of the high-temperature  $\text{YBa}_2\text{Cu}_3\text{O}_{7-\delta}$  superconductor”, *Physical Review B* **79**, 140503 (2009).
- <sup>188</sup>C. R. Hunt, D. Nicoletti, S. Kaiser, D. Pröpper, T. Loew, J. Porras, B. Keimer, and A. Cavalleri, “Dynamical decoherence of the light induced interlayer coupling in  $\text{YBa}_2\text{Cu}_3\text{O}_{6+\delta}$ ”, *Physical Review B* **94**, 224303 (2016).

## Bibliography

---

- <sup>189</sup>C. R. Hunt, D. Nicoletti, S. Kaiser, T. Takayama, H. Takagi, and A. Cavalleri, “Two distinct kinetic regimes for the relaxation of light-induced superconductivity in  $\text{La}_{1.675}\text{Eu}_{0.2}\text{Sr}_{0.125}\text{CuO}_4$ ”, *Physical Review B* **91**, 020505 (2015).
- <sup>190</sup>S. D. Brorson, R. Buhleier, I. E. Trofimov, J. O. White, C. Ludwig, F. F. Balakirev, H.-U. Habermeier, and J. Kuhl, “Electrodynamics of high-temperature superconductors investigated with coherent terahertz pulse spectroscopy”, *JOSA B* **13**, 1979–1993 (1996).
- <sup>191</sup>R. D. Averitt, G. Rodriguez, A. I. Lobad, J. L. W. Siders, S. A. Trugman, and A. J. Taylor, “Nonequilibrium superconductivity and quasiparticle dynamics in  $\text{YBa}_2\text{Cu}_3\text{O}_{7-\delta}$ ”, *Physical Review B* **63**, 140502 (2001).
- <sup>192</sup>J. Schützmann, S. Tajima, S. Miyamoto, Y. Sato, and R. Hauff, “Doping and temperature dependence of  $c$ -axis optical phonons in  $\text{YBa}_2\text{Cu}_3\text{O}_y$  single crystals”, en, *Physical Review B* **52**, 13665–13673 (1995).
- <sup>193</sup>K. Katsumi, M. Nishida, S. Kaiser, S. Miyasaka, S. Tajima, and R. Shimano, “Near-infrared light-induced superconducting-like state in underdoped  $\text{YBa}_2\text{Cu}_3\text{O}_y$  studied by  $c$ -axis terahertz third-harmonic generation”, *Physical Review B* **107**, 214506 (2023).
- <sup>194</sup>M. Buzzi, D. Nicoletti, S. Fava, G. Jotzu, K. Miyagawa, K. Kanoda, A. Henderson, T. Siegrist, J. A. Schlueter, M.-S. Nam, A. Ardavan, and A. Cavalleri, “Phase diagram for light-induced superconductivity in  $\kappa$ - $(\text{ET}) - 2\text{-x}$ ”, *Physical Review Letters* **127**, 197002 (2021).
- <sup>195</sup>M. Buzzi, M. Först, R. Mankowsky, and A. Cavalleri, “Probing dynamics in quantum materials with femtosecond X-rays”, en, *Nature Reviews Materials* **3**, 299–311 (2018).

- <sup>196</sup>D. Fausti, R. I. Tobey, N. Dean, S. Kaiser, A. Dienst, M. C. Hoffmann, S. Pyon, T. Takayama, H. Takagi, and A. Cavalleri, “Light-Induced Superconductivity in a Stripe-Ordered Cuprate”, *Science* **331**, 189–191 (2011).
- <sup>197</sup>T.-H. Chou, M. Först, M. Fechner, M. Henstridge, S. Roy, M. Buzzi, D. Nicoletti, Y. Liu, S. Nakata, B. Keimer, and A. Cavalleri, “Ultrafast raman thermometry in driven  $\text{YBa}_2\text{Cu}_3\text{O}_{6.48}$ ”, *Physical Review B* **109**, 195141 (2024).
- <sup>198</sup>M. H. Michael, D. D. Santis, E. A. Demler, and P. A. Lee, *Giant Dynamical Paramagnetism in the driven pseudogap phase of  $\text{YBa}_2\text{Cu}_3\text{O}_{6+x}$* , Oct. 2024.
- <sup>199</sup>N. Taherian, M. Först, A. Liu, M. Fechner, D. Pavicevic, A. von Hoegen, E. Rowe, Y. Liu, S. Nakata, B. Keimer, E. Demler, M. H. Michael, and A. Cavalleri, “Probing amplified Josephson plasmons in  $\text{YBa}_2\text{Cu}_3\text{O}_{6+x}$  by multidimensional spectroscopy”, *npj Quantum Materials* **10**, 1–10 (2025).
- <sup>200</sup>V. M. Agranovich and V. Ginzburg, *Crystal Optics with Spatial Dispersion, and Excitons* (Springer Science & Business Media, 2013).
- <sup>201</sup>Y.-X. Yan, E. B. Gamble Jr., and K. A. Nelson, “Impulsive stimulated scattering: General importance in femtosecond laser pulse interactions with matter, and spectroscopic applications”, *The Journal of Chemical Physics* **83**, 5391–5399 (1985).
- <sup>202</sup>H. Nyquist, “Certain Topics in Telegraph Transmission Theory”, *Transactions of the American Institute of Electrical Engineers* **47**, 617–644 (1928).
- <sup>203</sup>C. Manzoni, M. Först, H. Ehrke, and A. Cavalleri, “Single-shot detection and direct control of carrier phase drift of midinfrared pulses”, *Optics Letters* **35**, 757–759 (2010).
- <sup>204</sup>R. W. Boyd, *Nonlinear optics* (Boston : Academic Press, 1992).

## ***Bibliography***

---

- <sup>205</sup>M. Fiebig, V. V. Pavlov, and R. V. Pisarev, “Second-harmonic generation as a tool for studying electronic and magnetic structures of crystals: review”, *JOSA B* **22**, 96–118 (2005).
- <sup>206</sup>Y. M. Chang, L. Xu, and H. W. K. Tom, “Observation of Coherent Surface Optical Phonon Oscillations by Time-Resolved Surface Second-Harmonic Generation”, *Physical Review Letters* **78**, 4649–4652 (1997).
- <sup>207</sup>H. B. Zhao, Y. Fan, G. Lüpke, A. T. Hanbicki, C. H. Li, and B. T. Jonker, “Detection of coherent acoustic phonons by time-resolved second-harmonic generation”, *Physical Review B* **83**, 212302 (2011).
- <sup>208</sup>T. Hogan, L. Bjaalie, L. Zhao, C. Belvin, X. Wang, C. G. Van de Walle, D. Hsieh, and S. D. Wilson, “Structural investigation of the bilayer iridate  $\text{Sr}_3\text{Ir}_2\text{O}_7$ ”, *Physical Review B* **93**, 134110 (2016).
- <sup>209</sup>D. H. Torchinsky, H. Chu, L. Zhao, N. B. Perkins, Y. Sizyuk, T. Qi, G. Cao, and D. Hsieh, “Structural Distortion-Induced Magnetoelastic Locking in  $\text{Sr}_2\text{IrO}_4$  Revealed through Nonlinear Optical Harmonic Generation”, *Physical Review Letters* **114**, 096404 (2015).
- <sup>210</sup>M. Nývlt, F. Bisio, and J. Kirschner, “Second harmonic generation study of the antiferromagnetic  $\text{NiO}(001)$  surface”, *Physical Review B* **77**, 014435 (2008).
- <sup>211</sup>D. Hsieh, J. W. McIver, D. H. Torchinsky, D. R. Gardner, Y. S. Lee, and N. Gedik, “Nonlinear Optical Probe of Tunable Surface Electrons on a Topological Insulator”, *Physical Review Letters* **106**, 057401 (2011).
- <sup>212</sup>R. Stolle, G. Marowsky, E. Schwarzberg, and G. Berkovic, “Phase measurements in nonlinear optics”, *Applied Physics B* **63**, 491–498 (1996).

- <sup>213</sup>P. J. Nowakowski, D. A. Woods, C. D. Bain, and J. R. R. Verlet, “Time-resolved phase-sensitive second harmonic generation spectroscopy”, *The Journal of Chemical Physics* **142**, 084201 (2015).
- <sup>214</sup>A. L. Tyson, D. A. Woods, and J. R. R. Verlet, “Time-resolved second harmonic generation with single-shot phase sensitivity”, *The Journal of Chemical Physics* **149**, 204201 (2018).
- <sup>215</sup>J. Zhang and R. D. Averitt, “Dynamics and Control in Complex Transition Metal Oxides”, *Annual Review of Materials Research* **44**, 19–43 (2014).
- <sup>216</sup>M. Fechner and N. A. Spaldin, “Effects of intense optical phonon pumping on the structure and electronic properties of yttrium barium copper oxide”, *Physical Review B* **94**, 134307 (2016).
- <sup>217</sup>M. H. Michael, M. Först, D. Nicoletti, S. R. U. Haque, Y. Zhang, A. Cavalleri, R. D. Averitt, D. Podolsky, and E. Demler, “Generalized Fresnel-Floquet equations for driven quantum materials”, *Physical Review B* **105**, 174301 (2022).
- <sup>218</sup>M. Mitrano, A. Cantaluppi, D. Nicoletti, S. Kaiser, A. Perucchi, S. Lupi, P. Di Pietro, D. Pontiroli, M. Riccò, S. R. Clark, D. Jaksch, and A. Cavalleri, “Possible light-induced superconductivity in  $K_3C_{60}$  at high temperature”, *Nature* **530**, 461–464 (2016).
- <sup>219</sup>G. Jotzu, G. Meier, A. Cantaluppi, A. Cavalleri, D. Pontiroli, M. Riccò, A. Ardavan, and M.-S. Nam, “Superconducting fluctuations observed far above  $T_c$  in the isotropic superconductor  $K_3C_{60}$ ”, *Physical Review X* **13**, 021008 (2023).
- <sup>220</sup>M.-S. Nam, A. Ardavan, S. J. Blundell, and J. A. Schlueter, “Fluctuating superconductivity in organic molecular metals close to the Mott transition”, *Nature* **449**, 584–587 (2007).

## ***Bibliography***

---

- <sup>221</sup>M. Lyubarov, Y. Lumer, A. Dikopoltsev, E. Lustig, Y. Sharabi, and M. Segev, “Amplified emission and lasing in photonic time crystals”, *Science (New York, N.Y.)* **377**, 425–428 (2022).
- <sup>222</sup>X. Wang, M. S. Mirmoosa, V. S. Asadchy, C. Rockstuhl, S. Fan, and S. A. Tretyakov, “Metasurface-based realization of photonic time crystals”, *Science Advances* **9**, eadg7541 (2023).
- <sup>223</sup>M. H. Michael, S. R. U. Haque, L. Windgatter, S. Latini, Y. Zhang, A. Rubio, R. D. Averitt, and E. Demler, “Photonic time-crystalline behaviour mediated by phonon squeezing in  $\text{Ta}_2\text{NiSe}_5$ ”, *Nature Communications* **15**, 3638 (2024).
- <sup>224</sup>S. R. U. Haque, M. H. Michael, J. Zhu, Y. Zhang, L. Windgatter, S. Latini, J. P. Wakefield, G.-F. Zhang, J. Zhang, A. Rubio, J. G. Checkelsky, E. Demler, and R. D. Averitt, “Terahertz parametric amplification as a reporter of exciton condensate dynamics”, *Nature Materials* **23**, 796–802 (2024).
- <sup>225</sup>Y. H. Wang, H. Steinberg, P. Jarillo-Herrero, and N. Gedik, “Observation of Floquet-Bloch States on the Surface of a Topological Insulator”, *Science* **342**, 453–457 (2013).
- <sup>226</sup>T. Oka and S. Kitamura, “Floquet Engineering of Quantum Materials”, *Annual Review of Condensed Matter Physics* **10**, 387–408 (2019).
- <sup>227</sup>J. Binney and D. Skinner, *The Physics of Quantum Mechanics* (OUP Oxford, 2014).
- <sup>228</sup>M. E. Peskin, *An Introduction To Quantum Field Theory* (CRC Press, Boca Raton, 2018).
- <sup>229</sup>W. C. Stewart, “CURRENT-VOLTAGE CHARACTERISTICS OF JOSEPHSON JUNCTIONS”, *Applied Physics Letters* **12**, 277–280 (1968).

- <sup>230</sup>D. E. McCumber, “Effect of ac Impedance on dc Voltage-Current Characteristics of Superconductor Weak-Link Junctions”, *Journal of Applied Physics* **39**, 3113–3118 (1968).